

**The Investigation of Gas-Phase Ion-Molecule Reactions with
Fourier Transform Ion Cyclotron Resonance Mass
Spectrometry**

Thesis by
Kevin C. Crellin

In Partial Fulfillment of the Requirements
for the Degree of
Doctor of Philosophy

California Institute of Technology
Pasadena, California
1997
(Submitted May 15, 1997)

© 1997

Kevin C. Crellin

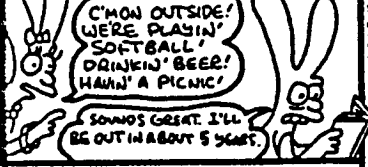
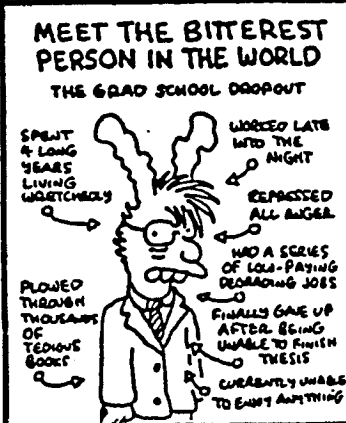
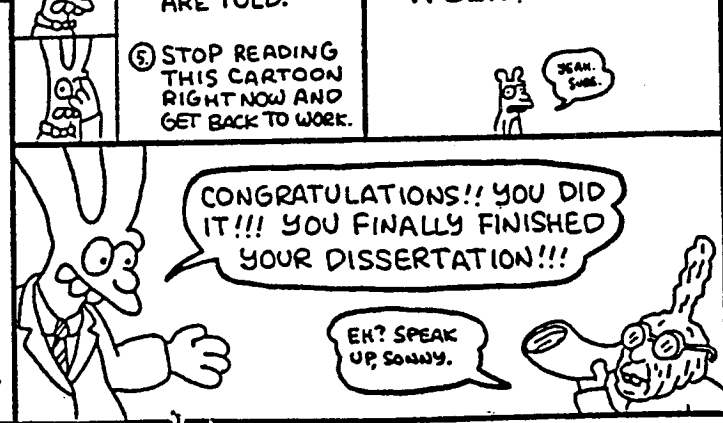
All rights reserved

To my parents and Kenny,
and especially to my wife, Nancy

FOREWORD

LIFE IN HELL

©1987 BY MATT GROENING

<p>SCHOOL IS HELL BUT IT BEATS WORKING</p>	<p>LESSON 19: GRAD SCHOOL— SOME PEOPLE NEVER LEARN</p>	
<p>SHOULD YOU GO TO GRAD SCHOOL? A WEE TEST</p> <p><input type="checkbox"/> <input type="checkbox"/> I AM A COMPULSIVE NEUROTIC.</p> <p><input type="checkbox"/> <input type="checkbox"/> I LIKE MY IMAGINATION CRUSHED INTO DUST.</p> <p><input type="checkbox"/> <input type="checkbox"/> I ENJOY BEING A PROFESSOR'S SLAVE.</p> <p><input type="checkbox"/> <input type="checkbox"/> MY IDEA OF A GOOD TIME IS USING JARGON AND CITING AUTHORITIES.</p> <p><input type="checkbox"/> <input type="checkbox"/> I FEEL A DEEP NEED TO CONTINUE THE PROCESS OF AVOIDING LIFE.</p>	<p>THE 5 SECRETS OF GRAD SCHOOL SUCCESS</p> <ol style="list-style-type: none"> 1 DO NOT ANNOY THE PROFESSOR. 2 BE CONSISTENTLY .MEDIocre. 3 AVOID ANYTHING SMACKING OF ORIGINALITY. 4 DO EXACTLY WHAT YOU ARE TOLD. 5 STOP READING THIS CARTOON RIGHT NOW AND GET BACK TO WORK. 	<p>THE SIMPLE WAY TO AVOID THE STOMACH-CHURNING AGONY OF HAVING TO FINISH YOUR THESIS</p> <p>READ ANOTHER BOOK.</p> <p>REPEAT WHEN NECESSARY.</p> <p>WILL YOUR RESEARCH MAKE THE WORLD A BETTER PLACE?</p> <p>JEAN. SURE.</p>
<p>MEET THE BITTEREST PERSON IN THE WORLD THE GRAD SCHOOL DROPOUT</p>  <p>SLEPT 4 LONG YEARS LIVING WRETCHEDLY</p> <p>WROTE LATE INTO THE NIGHT</p> <p>EXPRESSED ALL ANGER</p> <p>HAD A SERIES OF LOW-PAYING DEGRADING JOBS</p> <p>FINALLY GAVE UP AFTER BEING UNABLE TO FINISH HIS THESIS</p> <p>CURRENTLY UNABLE TO ENJOY ANYTHING</p> <p>PLOWED THROUGH THOUSANDS OF TECHNICAL BOOKS</p>		

THE FLEASMS FROM THE 6-26-87

ACKNOWLEDGMENTS AND PREFACE

Before I start the serious business of acknowledging all those who contributed to the completion of this thesis, I have to say that it is hard for me to believe that all this time and work has passed by and that I actually made it through! However, I am pinching myself and I am not waking up, so I figure I must really have made it. I don't particularly like The Grateful Dead, but I think they had a true understanding of a graduate student's journey to their doctorate when they said, "What a long, strange trip it's been." But the words of Nietzsche are perhaps more applicable: "That which does not destroy me makes me stronger." Without a doubt, the first song I play in my CD player after my thesis seminar will be *Escape* by Alice Cooper. Nothing could be more appropriate.

Even though this thesis has my name on it, obviously the help of many other people has made this possible. First I must thank my advisor, Professor J. L. (Jack) Beauchamp, for his assistance and guidance. His knowledge of chemistry is seemingly boundless, and from him I have learned how best to think about chemical problems. We did not always see eye-to-eye on issues, but I must thank him for letting me follow my interests and work on several different projects. I am especially grateful for his extravagant tolerance in letting me follow my heart and teach freshman chemistry at Harvey Mudd College for one year while still working at Caltech and finishing my thesis. Professor M. Okumura graciously gave me the chance to do some experiments involving stratospheric chemistry (which are reported in Chapter 6), for which I am extremely grateful. Professor W. A. Goddard III was also a source of guidance and encouragement. From his lectures and informal discussions I learned a great deal about the nature of chemical bonding and the application of quantum chemical calculations to chemical problems. He contributed a lot of good advice about how best to perform the theoretical work in Chapter 5. I should also thank the members of my examining

committee, which includes Professor J. E. Bercaw and Professor R. C. Flagan in addition to Professor Beauchamp and Professor Okumura, for their efforts.

Sherrie Campbell gave me my first lesson in the use of a Fourier transform ion cyclotron resonance (FT-ICR) mass spectrometer, and always had good advice concerning the diagnosis of malfunctions (which occurred often) as I slowly gained experience with an old, often balky instrument. Srihari Murthy was also available with helpful advice in my first year and a half at Caltech. However, it was from Dr. Serge Geribaldi (All the way from Nice, France!) that I learned the most about the mechanics of performing experiments with an FT-ICR instrument. My collaborations with him through my first two summers at Caltech were extremely fruitful, and truly got me started with this thesis. It was also a lot of fun communicating with him: I speak no French, and he spoke little English. But we devised an interesting form of “pig-franglais” which worked well for us (now my wife can translate for me instead). And he did teach me some “interesting” (to say the least) French phrases which I can’t repeat here.

In addition to Dr. Geribaldi, Dr. Marcel Widmer was another French-speaking member of the group with whom I collaborated. Our work together resulted in the heated sample introduction probe assembly used in the work of chapters 7 and 8. His contribution to the building of this modification to the instrument was fundamental, and without his presence the completion of the probe apparatus would have taken much longer than it did.

During my last year here I was able to collaborate once again with Dr. Nathan Dalleska (we co-authored a paper with Professor P. B. Armentrout while we were both at the University of Utah, he as a graduate student and I as an undergraduate). He operated the sector mass spectrometer in the Keck laboratory, and we did an accurate mass measurement on it that turned out to be crucial in understanding the data presented in Chapter 8.

While on the subject of my colleagues, I should properly give credit to my fellow (and now former in some cases) Beauchamp group members (in no particular order): Jim Smith, Hakno Lee, Sangwon Lee, Dmitri Kossakovski, Elaine Marzluff, Jon (Caribou) McDunn, Maria (Bananaslug) Satterwhite, Jamie (Peanutman) Walls and Steve O'Connor. All of them contributed in their own way to making the Beauchamp group the lively place that it is. In addition, I should thank Bob Tebreuggen (we served together as the chemistry demonstration assistants for freshman chemistry) for all the fun and for being the cautious one. And I would be remiss if I did not express my appreciation to Brian Hathorn for all the good lunchtime sports (especially baseball) discussions and political arguments while reading the newspaper in the Marcus group common room.

Though Dr. Goddard was instrumental in getting me started with quantum chemistry computations, I must also express my gratitude to Dr. Jason Perry and Francesco "Cecco" Faglioni. Jason did some theoretical work instrumental to the understanding of the chemistry presented in chapters 2-4, and both Jason and Cecco were always available (even in the weight room in Jason's case) to discuss all the questions (both chemical and procedural) that would come up while performing calculations. Cecco's advice concerning the calculations performed in Chapters 5 and 7 was especially helpful.

I must give thanks to my FT-ICR instrument for actually continuing to work during the last five years, even if it did break down quite often. No matter how frustrating it may be to keep an old instrument running, one still develops an attachment to it over time, and the instrument has been kind to me when it mattered most. I must admit that I would not have learned as much about the nuts and bolts of how FT-ICR instruments work if I had not had to repair it so often. I must also at this point express my gratitude for the help and expertise of Tom Dunn of the electronics shop and Guy Duremberg of the machine shop. It was with their assistance that I was able to get the

instrument fixed when electrical or mechanical parts broke down. I would also like to thank Rick Gerhart for his glassblowing skills. He produced all of the glassware required for handling the gases used in FT-ICR experiments, including the vacuum line used to fill bulbs with reagent gases and the glass inlet line used in the experiments of Chapter 6.

In addition to performing research, I have been fortunate to have many chances to hone my teaching skills while here at Caltech. I have always loved teaching chemistry, and I must express my deep gratitude to Professor J. D. Baldeschwieler, Professor V. B. McKoy and Jack for giving me the opportunity to teach in their physical chemistry classes when they were out of town on business. Professor Baldeschwieler has been especially supportive of my efforts to become the most effective teacher I can. I also wish to thank Professor Nathan S. Lewis and Professor Jacqueline K. Barton for their support of my teaching as a teaching assistant in freshman chemistry.

Of course, surviving graduate school requires more than just the mechanical performance of experiments. One also has to make it through the administrative red tape that is invariably associated with the running of a university. Dian Buchness, the divisional secretary, could answer any question one might have about the administrative workings of the chemistry division and the Institute as a whole. And if she didn't know the answer to a question, she knew who did. I would like to thank Priscilla Boon, Jack's secretary, for all of her help when it came to dealing with administrative matters within our research group. Steve Gould, Elly Noe, and Ruth de la Pineda were also extremely helpful in procuring commercial materials that were required for my experiments.

Also instrumental to success in graduate school is the acquisition of a network of friends and a maintenance of outside interests and activities to provide balance (and maybe even some sanity) to one's existence. Weightlifting has been critically important as a stress outlet during my sojourn at Caltech, starting in the old "weight lean-to" on the fenced porch of the old gym and continuing in the present weight room. I have met

some good friends there. I must thank Don Thomas, Mark Meloon, Tim Johann and Nikki Takarabe (the weight room regulars) for all the good days of pumping iron. Furthermore, the weight room provided the setting where I met my wife, Nancy. Thank heavens her father, Craig Maxwell, is a Caltech alumnus. Otherwise, she might never have started coming to the Caltech weight room!

While at Caltech I had the good fortune to serve as Secretary of the Graduate Review Board (GRB). It was a responsibility that I thoroughly enjoyed, due in great part to the fact that I was able to work with Daniel Maskit, the chair of the GRB. One of the best things about Caltech is the honor system, and it was a wonderful experience to be able to work in tandem with another student who cared as much about the honor system as I do. I should also thank GRB members Bobby Bodenheimer, Jean Andino, Geoffrey Burr, Jennifer Herek and Maneesh Sihani for their comradery and good spirits during evening board meetings (which often ran until 2:00 a. m. or longer).

An activity which kept me in touch with the outside world was umpiring baseball games. I must thank John Magallenes from the Caltech mailroom for introducing me to the profession. The umpiring was a wonderful excuse to get out on a grassy field for a few hours during Saturday mornings in spring. Unfortunately, the uniform made it hard to get a tan while out on the field.

In the days when I lived in the Catalina apartments, Ruth Ann Bertsch and her husband Tim McPhillips graciously invited me over to dinner on a regular basis. I have many fond memories of the food and the discussions. Ruth Ann also gave me some wonderfully thoughtful and thorough feedback on my candidacy report and research propositions. Consideration of her comments almost invariably improved the manuscripts.

Even though this list may seem quite exhaustive, I am sure there are a few associates who made contributions to this work that I have not remembered during the writing of this preface. For those I may have forgotten I ask forgiveness. And last (but

certainly not least) I must thank my family for their love and support through this time of my life. Without the encouragement and love of my parents, Terry and Janice Crellin, and my late brother, Kenny, I would never have had even the opportunity to attend Caltech. It is with their guidance that I have become the person I am today. But I owe the most gratitude and love to Nancy (who swore she would never date a “Techer,” and therefore married one instead), just for being in my life. Her love and support give me strength and keep me young. Had it not been for her, this thesis would probably never have been completed.

ABSTRACT

The gas-phase chemistry of several chemical systems have been investigated with Fourier transform ion cyclotron resonance (FT-ICR) mass spectrometry. The emphasis of these experiments is on organoscandium ion chemistry, but inorganic and organic systems have also been examined. Furthermore, quantum mechanical calculations have been performed on selected systems to help in the interpretation of the experimental data or guide the experiments.

Chapter 1 is a brief review of the experimental aspects of FT-ICR mass spectrometry. The history of the development of FT-ICR is given, and the instrumentation required to perform FT-ICR mass spectrometry is described. The mathematical description of ion motion is discussed, and applied to the description of the excitation and detection of ions. A short explanation of how these aspects are combined to form a standard experimental event sequence is then presented.

Chapters 2-5 present the results of our investigations of the reactivity of organoscandium ions with alkanes and alcohols. In Chapter 2 we examine the reactions of $\text{Sc}(\text{CH}_3)_2^+$ with methane, ethane, [2,2- D_2]-propane, [1,1,1,4,4,4- D_6]-*n*-butane and [2- D]-isobutane, while in Chapter 3 the reactions of $\text{CH}_3\text{ScCH}_2\text{CH}_3^+$ with methane, ethane, [2,2- D_2]-propane, [1,1,1,4,4,4- D_6]-*n*-butane, [2- D]-isobutane and *n*-pentane are observed. In both systems σ -bond metathesis reactions similar to those observed in liquid-phase systems are seen. Site selectivity with the larger alkanes is also observed with the aid of deuterium labeling. In Chapter 4 we return to the $\text{Sc}(\text{CH}_3)_2^+$ ion and investigate its reactivity with cyclopentane and cyclohexane. Once again, σ -bond metathesis reactions are observed, this time with secondary C-H bonds rather than primary C-H bonds (as seen with the straight- and branched-chain hydrocarbons). We then change our focus in Chapter 5 to the σ -bond metathesis reactions of $\text{Sc}(\text{OCD}_3)_2^+$ with water, ethanol and 1-propanol. Again, σ -bond metathesis reactions were seen.

However, in this case ligand exchange equilibria were observed via σ -bond metathesis and used to evaluate the relative bond energies of various Sc^+ -alkoxide bonds.

Chapters 6-8 move away from organoscandium systems and into various inorganic and organic systems. In chapter 6 the reaction of Cl^- with ClONO_2 is examined. This reaction was found to be fast and efficient in the gas phase, which raises the possibility that Cl^- might react directly with ClONO_2 on water ice films on the surface of type II polar stratospheric cloud particles. Chapter 7 investigates the reactions of nitrobenzene and the explosives 2,4,6-trinitrotoluene (TNT) and 1,3,5-trinitro-1,3,5-triazacyclohexane (RDX) with $\text{Si}(\text{CH}_3)_3^+$. Adduct formation and small amounts of characteristic fragmentation (with the TNT and RDX adducts) is observed, suggesting that these types of reactions could be useful as a detection scheme for common explosives. Chapter 8 extends this work to the explosives EGDN (ethylene glycol dinitrate) and PETN (pentaerythritol tetranitrate). These nitrate ester explosives do react with $\text{Si}(\text{CH}_3)_3^+$, but no molecular adduct is seen in the FT-ICR mass spectrometer. However, characteristic fragment ions are seen and the PETN- $\text{Si}(\text{CH}_3)_3^+$ adduct can be seen in a sector mass spectrometer. The differences in the reactivity of nitro explosives and nitrate ester explosives are also discussed.

CONTENTS

Dedication	iii
Foreword	iv
Acknowledgments and Preface	v
Abstract	xi
Table of Contents	xiii
List of Tables	xiv
List of Figures	xvii
Chapter 1. An Introduction to Fourier Transform Ion Cyclotron Resonance Mass Spectrometry	1
Chapter 2. Site Selective σ -Bond Metathesis Reactions of $\text{Sc}(\text{CD}_3)_2^+$ with [2,2-D ₂]-Propane, [1,1,1,4,4,4-D ₆]- <i>n</i> -Butane and [2-D]-Isobutane	42
Chapter 3. Group and Site Selective σ -Bond Metathesis Reactions of $\text{CH}_3\text{ScCH}_2\text{CH}_3^+$ with [2,2-D ₂]-Propane, [1,1,1,4,4,4-D ₆]- <i>n</i> -Butane, 2-D]-Isobutane and <i>n</i> -Pentane	58
Chapter 4. σ -Bond Metathesis Reactions of $\text{Sc}(\text{CD}_3)_2^+$ with Secondary C-H Bonds: Reactivity with Cyclohexane and Cyclopentane	98
Chapter 5. σ -Bond Metathesis Reactions of $\text{Sc}(\text{OCD}_3)_2^+$ with Ethanol, 1-Propanol, and 2-Propanol: Measurements of Equilibrium Constants and Relative Bond Strengths	124
Chapter 6. Reaction of Chloride Ions with Chlorine Nitrate and Its Implications for Stratospheric Chemistry	187
Chapter 7. Chemical Ionization of TNT and RDX with Trimethylsilyl Cation	210
Chapter 8. Chemical Ionization of the Nitrate Ester Explosives EGDN and PETN by Trimethylsilyl Cation and Comparison of the Reactivity of Nitrate Ester and Nitro Explosives Toward Trimethylsilyl Cation	274

LIST OF TABLES

Chapter 1.	Principal Ions Produced by EI Ionization of PFK with 40 eV	
	Electrons	8
Chapter 3.	Summary of the Observed Reactivity of $\text{CH}_3\text{ScCH}_2\text{CH}_3^+$ with the	
	Small Alkanes Examined in this Study	83
	Predicted Reaction Enthalpy for the σ -Bond Metathesis Reaction	
	$\text{ScR}^+ + \text{R}'\text{H} \rightarrow \text{ScR}'^+ + \text{RH}$	86
Chapter 4.	Gas-Phase Heats of Formation at 298 K for Chemical Species	
	Relevant to this Work	116
	Gas-Phase Bond Energies at 298 K for Chemical Species Relevant	
	to this Work	118
Chapter 5.	Summary of Observed Ligand Exchange Equilibria	154
	Calculated Total Energies, Zero-Point Energies (ZPE) 0 K to 298 K	
	Enthalpy Correction ($H_{298} - H_0$) and Absolute Entropies	158
	Calculated ΔH_{298} , ΔS_{298} and ΔG_{298} for Reactions 28-30	159
	Gas-Phase Bond Energies at 298 K for Chemical Species Relevant	
	to this Work	161
	Gas-Phase Bond Energies of Sc^+ -Alkoxide Bonds Relative to	
	Sc^+ - OCD_3	163
	Gas-Phase Sc^+ -Oxygen Bond Energies at 298 K	163
	Gas-Phase Heats of Formation at 298 K for Chemical Species	
	Relevant to this Work	166
	LMP2-Optimized Bond Distances (\AA) and Angles (deg) for the	
	Lowest Energy Conformation of H_2O	175
	LMP2-Optimized Bond Distances (\AA) and Angles (deg) for the	
	Lowest Energy Conformation of CH_3OH	176

	LMP2-Optimized Bond Distances (Å) and Angles (deg) for the Lowest Energy Conformation of CH ₃ CH ₂ OH	177
	LMP2-Optimized Bond Distances (Å) and Angles (deg) for the Lowest Energy Conformation of Sc(OH) ₂ ⁺	179
	LMP2-Optimized Bond Distances (Å) and Angles (deg) for the Lowest Energy Conformation of CH ₃ OScOH ⁺	180
	LMP2-Optimized Bond Distances (Å) and Angles (deg) for the Lowest Energy Conformation of Sc(OCH ₃) ₂ ⁺	182
	LMP2-Optimized Bond Distances (Å) and Angles (deg) for the Lowest Energy Conformation of CH ₃ OScOCH ₂ CH ₃ ⁺	184
Chapter 7.	HF-Optimized Bond Distances (Å) and Angles (deg) for the Lowest Energy Conformation of CH ₂ NNO ₂	257
	HF-Optimized Bond Distances (Å) and Angles (deg) for the Lowest Energy Conformation of (CH ₂ NNO ₂) ₂	258
	HF-Optimized Bond Distances (Å) and Angles (deg) for the Lowest Energy Conformation of RDX	261
	PM3-Optimized Bond Distances (Å) and Angles (deg) for the Lowest Energy Conformation of Si(CH ₃) ₃ ⁺	264
	PM3-Optimized Bond Distances (Å) and Angles (deg) for the Lowest Energy Conformation of CH ₂ NNO ₂ -Si(CH ₃) ₃ ⁺	266
	PM3-Optimized Bond Distances (Å) and Angles (deg) for the Lowest Energy Conformation of (CH ₂ NNO ₂) ₂ -Si(CH ₃) ₃ ⁺	268
	PM3-Optimized Bond Distances (Å) and Angles (deg) for the Lowest Energy Conformation of RDX-Si(CH ₃) ₃ ⁺	271
Chapter 8.	PM3-Heats of Formation of Species Involved in Reaction of Si(CH ₃) ₃ ⁺ with EGDN and PETN	302

PM3-Optimized Bond Distances (Å) and Angles (deg) for the Lowest Energy Conformation of $\text{Si}(\text{CH}_3)_3^+$	316
PM3-Optimized Bond Distances (Å) and Angles (deg) for the Lowest Energy Conformation of EGDN	318
PM3-Optimized Bond Distances (Å) and Angles (deg) for the Lowest Energy Conformation of EGDN- $\text{Si}(\text{CH}_3)_3^+$	320
PM3-Optimized Bond Distances (Å) and Angles (deg) for the Lowest Energy Conformation of $\text{Si}(\text{CH}_3)_3\text{ONO}_2$	322
PM3-Optimized Bond Distances (Å) and Angles (deg) for the Lowest Energy Conformation of $\text{C}_2\text{H}_4\text{NO}_3^+$	324
PM3-Optimized Bond Distances (Å) and Angles (deg) for the Lowest Energy Conformation of PETN	326
PM3-Optimized Bond Distances (Å) and Angles (deg) for the Lowest Energy Conformation of PETN- $\text{Si}(\text{CH}_3)_3^+$	328
PM3-Optimized Bond Distances (Å) and Angles (deg) for the Lowest Energy Conformation of $\text{C}_5\text{H}_8\text{N}_3\text{O}_9^+$	331

LIST OF FIGURES

Chapter 1.	The typical cubic ion trap	5
	The trajectory of an ion in a homogeneous magnetic field	10
	The electrostatic trapping field of a cubic ICR trap	13
	Two-dimensional isopotential contours of a quadrupolar excitation potential	16
	The cyclotron and magnetron motions of an ion	20
	Fundamental modes of ion motion in an ICR trap	22
	Ion motion during the RF dipolar excitation of an ion's cyclotron motion	25
	The frequency domain magnitude spectra of single frequency and frequency sweep excitation	28
	The frequency domain magnitude spectra of frequency sweep excitation	31
	Illustration of how the induced charge (and image current) is generated on the detection plates	34
	Simplified illustration of the typical experimental event sequence	36
Chapter 2.	Products of the reaction of $\text{Sc}(\text{CD}_3)_2^+$ with [2,2-D ₂]-propane and [1,1,1,4,4,4-D ₆]- <i>n</i> -butane	47
	Products of the reaction of $\text{Sc}(\text{CD}_3)_2^+$ with [2-D]-isobutane and [1,1,1,4,4,4-D ₆]- <i>n</i> -butane	50
	Schematic of a general potential energy surface	53
Chapter 3.	Products of the reaction of Sc^+ with <i>n</i> -pentane and a semilog plot of the decay of Sc^+ abundance with time	64
	A semilog plot of the decay of the $\text{CH}_3\text{ScCH}_2\text{CH}_3^+$ abundance with time	67

	A semilog plot of the decay of the $\text{CH}_3\text{ScC}_5\text{H}_{11}^+$ abundance with time	70
	Isolation of the $\text{CH}_3\text{ScCH}_2\text{CH}_3^+$ ion and products of the reaction of $\text{CH}_3\text{ScCH}_2\text{CH}_3^+$ with <i>n</i> -pentane	73
	Products of the reaction of $\text{CH}_3\text{ScCH}_2\text{CH}_3^+$ and $\text{CH}_3\text{ScCH}_2\text{CH}_3^+$ with a mixture of <i>n</i> -pentane and $[\text{D}_{12}]$ - <i>n</i> -pentane	75
	Products of the reaction of $\text{CH}_3\text{ScCH}_2\text{CH}_3^+$ with $[2,2\text{-D}_2]$ -propane and $[1,1,1,4,4,4\text{-D}_6]$ - <i>n</i> -butane	78
	Products of the reaction of $\text{CH}_3\text{ScCH}_2\text{CH}_3^+$ with $[2\text{-D}]$ -isobutane	81
	Schematic of a general potential energy surface showing how the nature of the ligand being lost can affect the electrostatic potential well	87
	Schematic of a general potential energy surface showing how the initial electrostatic potential well can affect the height of a barrier relative to the energy of the reactants	91
Chapter 4.	Products of the reaction of $\text{Sc}(\text{CH}_3)_2^+$ with cyclohexane and the CID of $\text{CH}_3\text{Sc}(\eta^3\text{-C}_6\text{H}_9)^+$	103
	Spectrum of the products from the CID of isolated $\text{CH}_3\text{Sc}(\eta^3\text{-C}_6\text{H}_9)^+$	106
	Products of the reaction of $\text{Sc}(\text{CH}_3)_2^+$ with cyclopentane	108
	Schematic of the potential energy surface for the reaction of cyclohexane with $\text{Sc}(\text{CH}_3)_2^+$	114
Chapter 5.	Reaction of $\text{Sc}(\text{OCD}_3)_2^+$ with a $\text{H}_2\text{O}/\text{CD}_3\text{OH}$ mixture	130
	Time plot of the relative abundance of $\text{Sc}(\text{OCD}_3)_2^+$ and $\text{CD}_3\text{OScOH}^+$ versus time	132
	Reaction of $\text{CD}_3\text{OScOCH}^+$ with a $\text{H}_2\text{O}/\text{CD}_3\text{OH}$ mixture	134

Time plot of the relative abundance of $\text{CD}_3\text{OScOH}^+$ and $\text{Sc}(\text{OH})_2^+$ versus time	136
Reaction of $\text{Sc}(\text{OCD}_3)_2^+$ with a $\text{CD}_3\text{OH} / \text{CH}_3\text{CH}_2\text{OH}$ mixture	140
Time plot of the relative abundance of $\text{Sc}(\text{OCD}_3)_2^+$ and $\text{CD}_3\text{OScOCH}_2\text{CH}_3^+$ versus time	142
Reaction of $\text{CD}_3\text{OScOCH}_2\text{CH}_3^+$ with a $\text{CD}_3\text{OH} / \text{CH}_3\text{CH}_2\text{OH}$ mixture	144
Time plot of the relative abundance of $\text{CD}_3\text{OScOCH}_2\text{CH}_3^+$ and $\text{Sc}(\text{OCH}_2\text{CH}_3)_2^+$ versus time	146
Reaction of $\text{Sc}(\text{OCD}_3)_2^+$ with a $\text{CD}_3\text{OH} / \text{CH}_3(\text{CH}_2)_2\text{OH}$ mixture	149
Time plot of the relative abundance of $\text{Sc}(\text{OCD}_3)_2^+$ and $\text{CD}_3\text{OScO}(\text{CH}_2)_2\text{CH}_3^+$ versus time	151
LMP2-optimized lowest energy geometry for $\text{Sc}(\text{OH})_2^+$, $\text{CH}_3\text{OScOH}^+$, $\text{Sc}(\text{OCD}_3)_2^+$ and $\text{CH}_3\text{OScOCH}_2\text{CH}_3^+$	156
Illustration of reaction energetics for processes resulting from the interaction of $\text{CH}_3\text{CH}_2\text{OH}$ with $\text{Sc}(\text{OCD}_3)_2^+$	167
Chapter 6. Isolation of Cl^- and formation of NO_3^- from the reaction $\text{Cl}^- +$ $\text{ClONO}_2 \rightarrow \text{Cl}_2 + \text{NO}_3^-$	193
Observed decay of the Cl^- abundance with time	195
Ab initio structure of the $\text{Cl}_2 \cdot \text{NO}_3^-$ complex	199
Reaction coordinate diagram for $\text{Cl}^- + \text{ClONO}_2 \rightarrow \text{Cl}_2 + \text{NO}_3^-$	201
Chapter 7. Schematic of the complete probe inlet/internal source apparatus	216
Schematic of the assembly of the heated probe tip	218
Isolation of $\text{Si}(\text{CH}_3)_3^+$ and products of the reaction of $\text{Si}(\text{CH}_3)_3^+$ with nitrobenzene	221
A semilog plot of the decay of the $\text{Si}(\text{CH}_3)_3^+$ abundance with time	223

Isolation of $\text{Si}(\text{CH}_3)_3^+$ and products of the reaction of $\text{Si}(\text{CH}_3)_3^+$ with TNT	226
Isolation of the TNT- $\text{Si}(\text{CH}_3)_3^+$ adduct and products of the CID of TNT- $\text{Si}(\text{CH}_3)_3^+$	228
Isolation of $\text{Si}(\text{CH}_3)_3^+$ and products of the reaction of $\text{Si}(\text{CH}_3)_3^+$ with RDX	230
Isolation of the RDX- $\text{Si}(\text{CH}_3)_3^+$ adduct and products of the CID of RDX- $\text{Si}(\text{CH}_3)_3^+$	232
HF-optimized geometries of the lowest energy conformations of CH_2NNO_2 , $(\text{CH}_2\text{NNO}_2)_2$ and RDX	236
PM3-optimized geometries of the lowest energy conformations of $\text{Si}(\text{CH}_3)_3^+$ and the $\text{CH}_2\text{NNO}_2\text{-Si}(\text{CH}_3)_3^+$, $(\text{CH}_2\text{NNO}_2)_2\text{-Si}(\text{CH}_3)_3^+$, and RDX- $\text{Si}(\text{CH}_3)_3^+$ adducts	239
Reaction coordinate diagram for the decomposition of RDX	246
Chapter 8. Isolation of $\text{Si}(\text{CH}_3)_3^+$ and products of the reaction of $\text{Si}(\text{CH}_3)_3^+$ with EGDN	280
A semilog time plot of the products of the reaction of $\text{Si}(\text{CH}_3)_3^+$ with EGDN	282
Isolation of $\text{CO}_2\text{Si}(\text{CH}_3)_3^+$ and products of the CID of $\text{CO}_2\text{Si}(\text{CH}_3)_3^+$	284
Isolation of $\text{Si}(\text{CH}_3)_3^+$ and products of the reaction of $\text{Si}(\text{CH}_3)_3^+$ with PETN	287
A semilog time plot of the products of the reaction of $\text{Si}(\text{CH}_3)_3^+$ with PETN	289
Isolation of $\text{C}_5\text{H}_8\text{N}_3\text{O}_9^+$ and products of the CID of $\text{C}_5\text{H}_8\text{N}_3\text{O}_9^+$	292
Spectrum of the products of the reaction of $\text{Si}(\text{CH}_3)_3^+$ with EGDN in a magnetic sector mass spectrometer	294

Spectrum of the products of the reaction of $\text{Si}(\text{CH}_3)_3^+$ with PETN in a magnetic sector mass spectrometer	297
Reaction coordinate diagram for the reaction of EGDN with $\text{Si}(\text{CH}_3)_3^+$	303
Reaction coordinate diagram for the reaction of PETN with $\text{Si}(\text{CH}_3)_3^+$	305

Chapter 1

AN INTRODUCTION TO FOURIER TRANSFORM ION CYCLOTRON RESONANCE MASS SPECTROMETRY

Kevin C. Crellin

Arthur Amos Noyes Laboratory of Chemical Physics, California Institute of
Technology, Pasadena, CA 91125

Abstract

The experimental aspects of Fourier transform ion cyclotron resonance (FT-ICR) mass spectrometry are briefly reviewed. A short history of the development of FT-ICR mass spectrometry is given, followed by a section describing the instrumentation required to perform FT-ICR experiments. We then discuss the mathematical description of the ion motion within the ICR cell and use this framework to discuss how excitation and detection of ions is achieved. A short description of how these aspects are combined into a general standard experimental event sequence is then presented. This discussion provides an introduction to the experimental techniques used to perform the experiments described in the balance of this dissertation.

Introduction

Today the technique of FT-ICR mass spectrometry is one of the most powerful methods of performing mass spectrometry. It is capable of ultrahigh mass resolution, precise mass measurement over a large mass range, multistage experiments, simultaneous detection of all ions present and long ion storage time. These capabilities are the result of the tremendously fast periodic circular ion motion (ion cyclotron motion) induced by the magnetic field. The intrinsic accuracy and precision in measurements of the average cyclotron motion frequencies (which are inversely proportional to the mass of the ion) lead to the ultrahigh resolution and accuracy in FT-ICR mass measurements.

Historical Development

Cyclotron motion was first used for the generation of high energy (on the order of 10^6 eV) light charged particles without a high electrostatic potential field. These high energy ions were used for nuclear studies.¹ With the introduction of frequency selective cyclotron motion acceleration by a radio frequency (RF) field, the measurement of the collected current of accelerated ions generated a cyclotron frequency spectrum which could be converted to a mass spectrum. This showed the analytical possibilities of ion

selection with RF resonance detection based on the ion's mass-to-charge (m/z) ratio.² Unfortunately, the instrument based on this phenomenon (the omegatron mass spectrometer) suffered from a limited mass range and low resolution. In 1963 a cyclotron based on marginal-oscillator detection was devised, where the detector responds to the power absorbed by resonant ions during a magnetic field sweep rather than to the resonant ion current from a collector electrode.³ This avoided collisional effects that degraded the performance of omegatrons, but this new cyclotron did not attract much attention.

At this time, Baldeschwieler and Llewellyn produced the first ICR spectrometer to investigate gas-phase ion chemistry, and this technique was quickly established and recognized as a valuable mass spectrometric method.⁴ Several instrumental developments have subsequently occurred. The introduction of superconducting magnets with high, constant and extremely homogeneous fields has improved the resolution, mass range and ion storage efficiency of ICR spectrometers.⁵ The development of pulsed mode operation⁶ for the trapping cell allows one to control experiments without spatially separating the ion production and ion mass analysis region. In conjunction with pulsed mode operation, the automation of the experimental procedure sequence with computer control accelerates the collection of data and performance of experiments. Last but not least, the introduction of Fourier transform methods⁷ allows for the simultaneous detection of all ions (further accelerating the rate at which data can be obtained) and further increases the resolution and mass range of the ICR technique, enhancing the applicability of ICR mass spectrometry to various practical problems.

Instrumentation

Before experiments on the reactivity of ions can be performed, the ions must be generated. Several ways of making ions exist: electron impact (EI) ionization,⁸ laser desorption ionization (LDI) and matrix assisted LDI (MALDI),⁹ chemical ionization

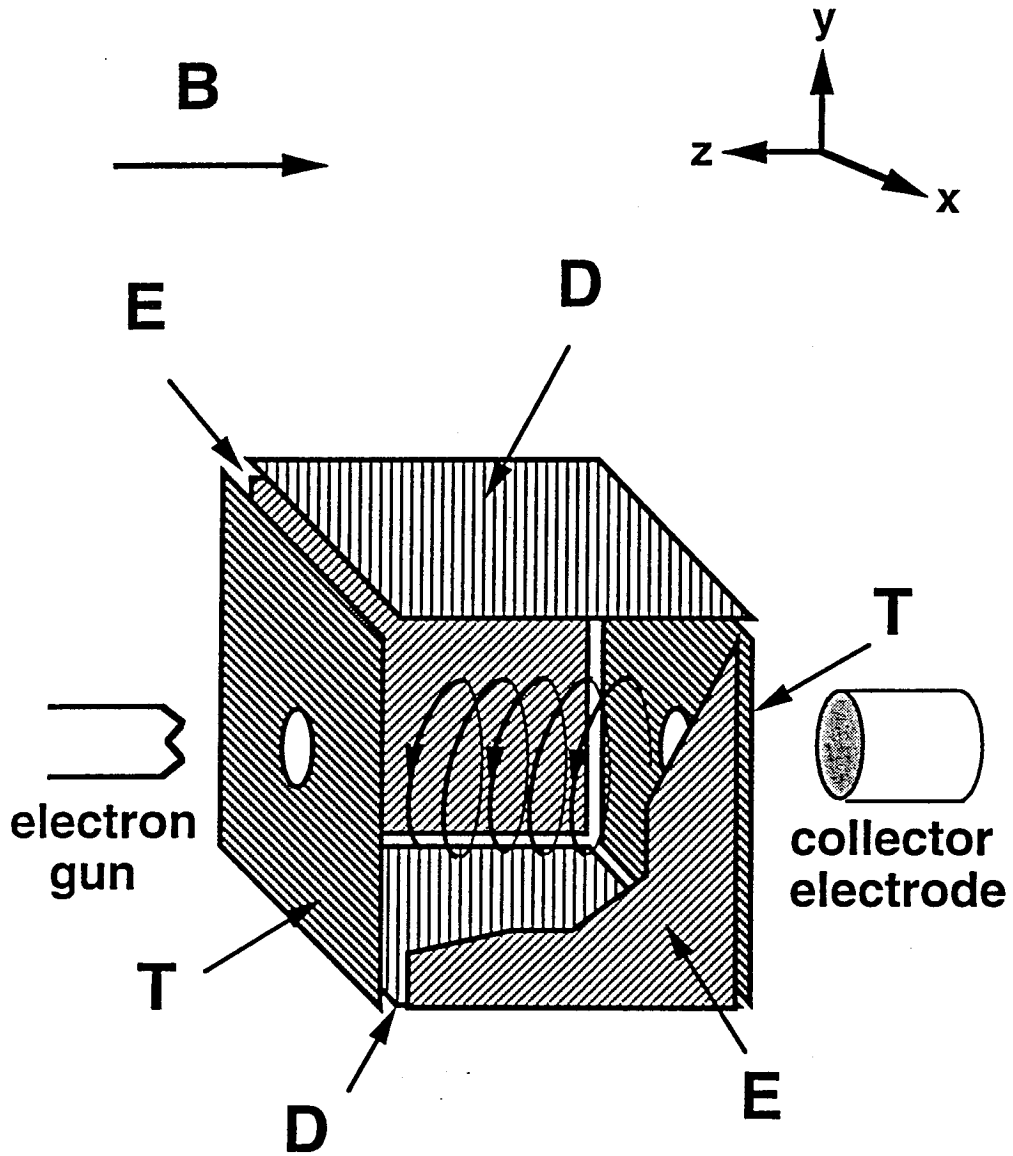
(CI),¹⁰ multiphoton ionization (MPI),¹¹ fast atom bombardment (FAB) ionization,¹² electrospray (ES) ionization,¹³ glow discharge (GD) ionization¹⁴ and surface ionization (SI),¹⁵ to name a few. The experiments in this thesis used EI ionization, LDI and CI exclusively for the formation of ions. The ions are then captured within the trapping cell by the use of combined electrostatic and magnetic fields. Our ion trap, like most,¹⁶ has a cubic geometry consisting of six square, nonmagnetic metal plates attached to ceramic mounts which keep the plates insulated and separated from each other. This geometry is shown in Figure 1.¹⁷

All FT-ICR experiments are conducted in the ICR trapping cell which is enclosed in a high vacuum chamber to minimize collisional damping of ion motions. Our instrument is equipped with a vertical-bore Varian 15-in. electromagnet. The magnetic field is maintained between 1 and 2 T. The cell is located in the central field region where the magnetic field will be as homogeneous as possible.

The magnetic field constrains the ions to move radially in the xy plane, while the electrostatic potential of the trapping plates holds the ions in the middle of the trap with respect to the z axis. The stored ions rotate around the z axis due to their cyclotron motion, but the phase of the ion motions is randomly distributed unless the ions are forced to circulate with the same phase by the application of a resonant RF electric field. This RF potential is applied on the pair of electrodes perpendicular to the x axis as shown in Figure 1. The excitation of the cyclotron motion in this fashion will increase the cyclotron radius of the ions enough to produce large image charges on the detection plates. We should note that the excitation pulse forces the ions to circulate with the same phase: otherwise, the average image charge would remain zero.

After the RF excitation the coherent ion motion produces an image current from the detection plates (which are perpendicular to the y axis in Figure 1). This current is converted to a voltage via a resistor, and this voltage is then amplified to produce the oscillating time domain signal (transient), which decays with time. Fourier

Figure 1. The typical cubic ion trap: Ions are generated by electron impact, excited by RF excitation from the excitation plates and detected with the detector plates by measurement of the induced current amplitude from the ion motion.



E: Excitation D: Detection T: Trapping

transformation of this transient results in a frequency domain spectrum with all the superimposed frequencies present decomposed to show the individual cyclotron motions from which it was made. The mass of each ion is approximately inversely proportional to the cyclotron frequency associated with it. However, this spectrum must be calibrated¹⁸ with a compound that produces well-characterized ions, since the reciprocal relationship is only approximate and the magnetic field can vary slightly with time. In our experiments perfluorokerosene (PFK) was often used as the calibration standard. Table 1 shows the principal ions produced by EI of PFK with 40 eV electrons. The approximate relative abundances of the peaks are also shown. Neutral gases (such as PFK) are introduced to the system through a stainless steel inlet system with ultrahigh vacuum (UHV) leak valves to control the amount of gas released to the chamber. Pressures of the neutral gases are measured with a Schultz-Phelps (SP) ion gauge, which produces an ion current output that is directly proportional to the amount of gas present. An MKS 390 HA-00001SP05 capacitance manometer is used to calibrate the SP gauge. The graph of ion current versus manometer pressure is fit to a straight line (using the least squares algorithm) to determine the relationship between ion current and pressure. This procedure must be followed to determine the calibration constant for each gas used.

EI ionization is accomplished by shooting electrons across the cell. As shown in Figure 1, the electron gun is a filament that typically carries a current of approximately $0.3 \mu\text{A}$. The collector electrode on the other side of the cell is held at a positive voltage to draw the electrons across the cell. Holes in the trapping plates allow the electrons to pass through the cell, and the energy of the electrons can be adjusted by varying the potential on the collector electrode. To allow for LDI experiments, the excitation plates have holes of approximately 0.5 cm diameter in the center of each plate. On one side a metal target is mounted next to the orifice, while on the other side the orifice is in line with a quartz window, allowing a laser to be shone through the cell to the target. Irradiation of the target then desorbs reactant ions directly into the cell. Both the

Table 1. Principal Ions Produced by EI Ionization of PFK with 40 eV Electrons.

Ion	<i>m/z</i> Ratio	Relative Abundance (%)
CF ₃ ⁺	69.01	20
C ₃ F ₅ ⁺	131.03	60
C ₄ F ₆ ⁺	162.03	25
C ₄ F ₇ ⁺	181.03	100
C ₅ F ₉ ⁺	231.04	65
C ₆ F ₉ ⁺	243.05	60
C ₆ F ₁₀ ⁺	262.05	20
C ₆ F ₁₁ ⁺	281.05	30
C ₇ F ₁₁ ⁺	293.06	20
C ₇ F ₁₃ ⁺	331.06	25
C ₈ F ₁₅ ⁺	381.06	25

electron beam and the laser beam can be pulsed to avoid the continuous desorption of ions, and these pulses are controlled by the pulse sequence program of the data collection electronics.

Mathematical Description of the Ion Motions

To give the reader a greater appreciation of how the ions are trapped by an ICR cell, we will now give a general description of the ion motion within an ICR trap. In all the discussion that follows, the magnetic field is always directed parallel to the z axis and the electric and magnetic fields are symbolized by \mathbf{E} and \mathbf{B} , respectively (the bold face type indicates vector quantities).

Static Magnetic Field. In this case the ion with charge q and mass m moves in a circular fashion around the magnetic field axis (see Figure 2). The radius r_c of this circular path is determined by the ion's velocity \mathbf{v} , which has magnitude $v = r_c \omega_c$ (ω_c is the associated angular velocity). Note that no work is done along this path, since the Lorentz force is always perpendicular to the ion motion. Mathematically, this cyclotron motion can be described by the equation of motion in equation 1. Each Cartesian

$$m\mathbf{v}' = q(\mathbf{v} \times \mathbf{B}) \quad (1)$$

component of this vector equation can be described by equations 2a-2c, where B is the

$$v'_x = \left(\frac{qB}{m} \right) v_y \quad (2a)$$

$$v'_y = \left(\frac{qB}{m} \right) v_x \quad (2b)$$

$$v'_z = 0 \quad (2c)$$

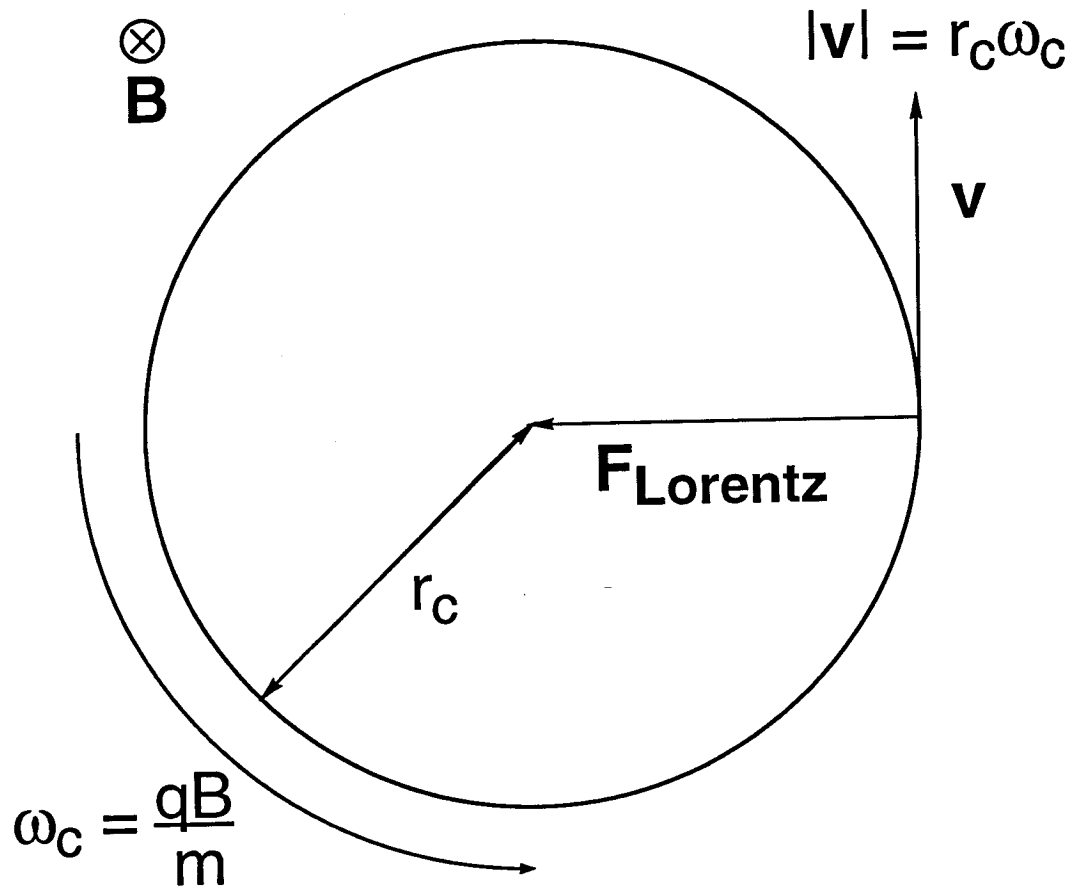
magnitude of \mathbf{B} . The solution to these coupled differential equations, given in equations 3a-3d, describes the trajectory of an ion in a static magnetic field. By defining the new

$$x = r_c \cos(\omega_c t + \phi) \quad (3a)$$

$$y = r_c \sin(\omega_c t + \phi) \quad (3b)$$

$$z = (v_z)_0 t + z_0 \quad (3c)$$

Figure 2. The trajectory of an ion in a homogeneous magnetic field. The ion circulates around the magnetic field axis with the cyclotron frequency ω_c and cyclotron radius r_c .



$$\omega_c = \frac{qB}{m} \quad (3d)$$

coordinate $r = x + iy$ equations 3a and 3b can be combined to give equation 4. Writing

$$r = r_c e^{i(\omega_c t + \phi)} \quad (4)$$

the trajectory in this complex form shows more directly that the ion circulates around the magnetic field axis with the cyclotron frequency ω_c and cyclotron radius r_c . We can also derive the value of r_c by assuming that the ion is at thermal equilibrium at a temperature T . From the kinetic molecular theory and the theory of equipartition of energy, we can write equation 5, where k is the Boltzmann constant. Substituting $r_c \omega_c$

$$\frac{mv^2}{2} = kT \quad (5)$$

for v and solving for r_c gives us equation 6. From this we can see that the cyclotron

$$r_c = \frac{\sqrt{2mkT}}{qB} \quad (6)$$

radius decreases with increasing magnetic field and increasing ion charge.

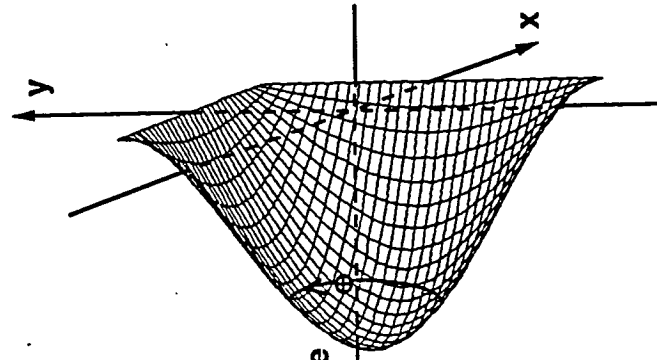
Static Magnetic Field and Static Electric Field. In this case we can qualitatively see that an ion will move in a circular fashion around the magnetic field axis and will also oscillate in the z direction within the harmonic potential well generated by the DC voltage (which has the same sign as the ions to be trapped) applied to both trapping plates (see Figure 3¹⁹). This trapping voltage removes the freedom of motion present in equation 3c. However, a full solution of the equations of motion is required to calculate quantitative trajectories. This full solution will also show that our qualitative look at the ion motion missed one of the modes of motion present.

As before, we will start our derivation with the equation of motion. From equation 7, we can represent that equation of motion with equation 8. To solve this we

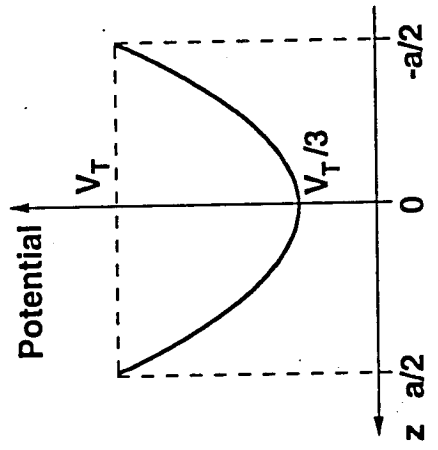
$$\mathbf{E} = -\nabla\Phi = -\left(\frac{\partial}{\partial x} + \frac{\partial}{\partial y} + \frac{\partial}{\partial z}\right)\Phi \quad (7)$$

$$m\mathbf{v}' = q(\mathbf{E} + \mathbf{v} \times \mathbf{B}) = q(-\nabla\Phi + \mathbf{v} \times \mathbf{B}) \quad (8)$$

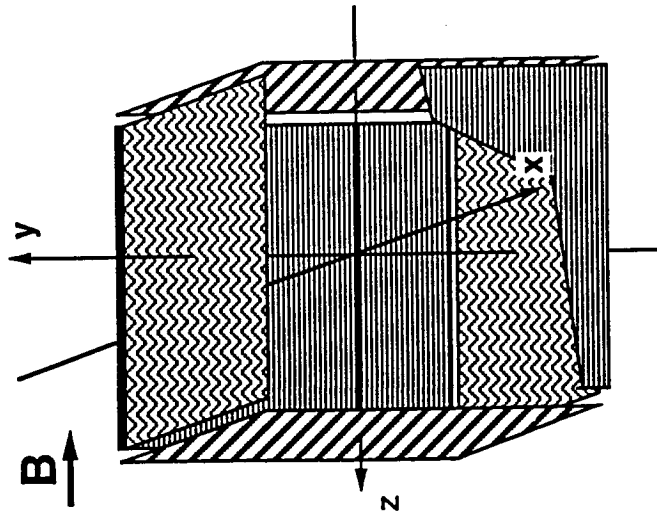
Figure 3. The electrostatic trapping field of a cubic ICR trap (left), showing the parabolic potential well in the z direction for $x = y = 0$ (middle) and the radial, bell-shaped potential in the xy plane for $z = 0$ (right).



Potential
in $z = 0$ plane



$x = 0, y = 0$



must know the electrostatic potential, which can be found with Laplace's equation (equation 9), and the boundary conditions. For a cubic trap of length a , with a DC

$$\nabla^2\Phi = \left(\frac{\partial^2}{\partial^2x} + \frac{\partial^2}{\partial^2y} + \frac{\partial^2}{\partial^2z} \right)\Phi = 0 \quad (9)$$

potential V_t , applied at the trapping plates, the boundary conditions are given by equations 10a and 10b. If a separation of variables is performed on equation 9 and the

$$\Phi\left(\pm\frac{a}{2}, y, z\right) = \Phi\left(x, \pm\frac{a}{2}, z\right) = 0 \quad (10a)$$

$$\Phi\left(x, y, \pm\frac{a}{2}\right) = V_t \quad (10b)$$

symmetry of the boundary conditions exploited, the solution of equation 9 can be given as the Fourier series of equation 11,²⁰ which is shown graphically in Figure 3. To

$$\Phi = \frac{16V_t}{\pi^2} \sum_{m=0}^{\infty} \sum_{n=0}^{\infty} \frac{(-1)^{m+n} \cosh\left(\frac{k_{mn}\pi z}{a}\right) \cos\left[\frac{(2m+1)\pi y}{a}\right] \cos\left[\frac{(2n+1)\pi x}{a}\right]}{(2m+1)(2n+1) \cosh\left(\frac{k_{mn}\pi}{2}\right)}, \quad (11)$$

$$k_{mn} = \sqrt{(2m+1)^2 + (2n+1)^2}$$

simplify this behavior, a Taylor expansion of equation 11 through third order in x , y and z about the center of the cell ($x = y = z = 0$) can be used to approximate the electric potential near the center of the cell as a quadrupolar potential. This approximate potential is described in equation 12, and shown graphically in Figure 4.¹⁹ The

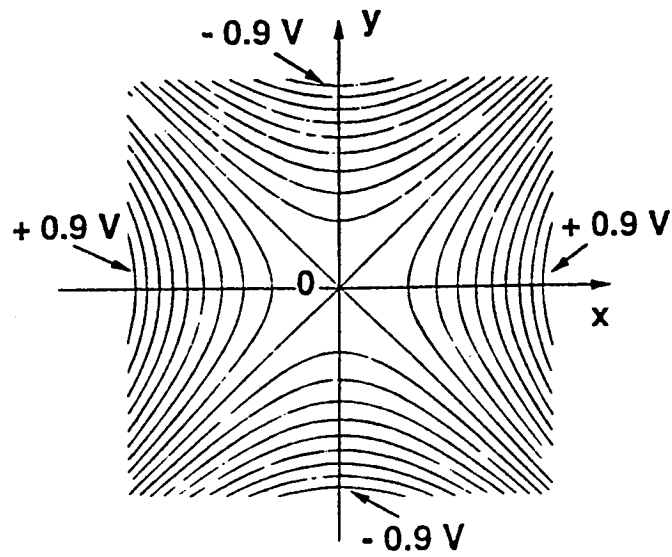
$$\Phi_{\text{quad}} \approx V_t \left[\gamma - \frac{\alpha}{2a^2} (x^2 + y^2 - 2z^2) \right] \quad (12)$$

constants α and γ are both determined by the geometry of the cell; for a cubic cell $\alpha = 2.77373$ and $\gamma = 1/3$. Substitution of the expression for Φ_{quad} into equation 7 yields the equation of motion for each Cartesian component as described in equations 13a-13c.

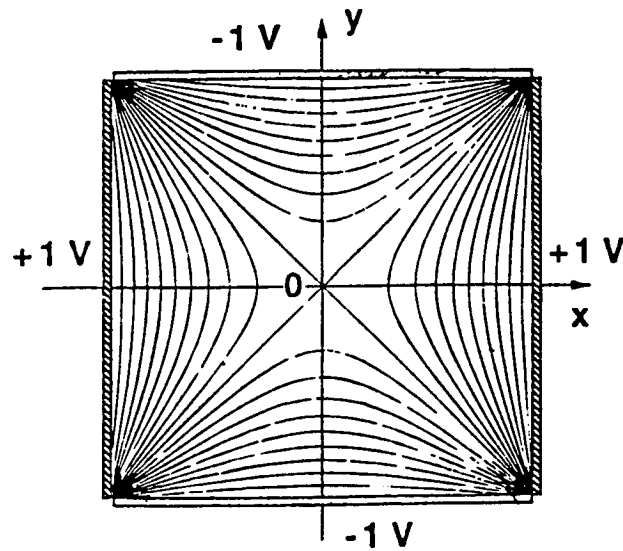
$$v'_x = \left(\frac{\alpha q V_t}{a^2 m} \right) x + \left(\frac{qB}{m} \right) v_y \quad (13a)$$

$$v'_y = \left(\frac{\alpha q V_t}{a^2 m} \right) y - \left(\frac{qB}{m} \right) v_x \quad (13b)$$

Figure 4. Two-dimensional isopotential contours of a quadrupolar excitation potential: the upper drawing shows the contours for a perfect azimuthal quadrupolar excitation potential, while the lower drawing shows the numerically calculated contours that exist at the midplane of a cubic ICR cell. Note that near the center of the trap, the potential closely approximates the pure quadrupole potential.



Azimuthal Pure Quadrupolar
Potential ($x^2 - y^2$)



Simulated Azimuthal
Quadrupolar Potential
for a Cubic Trap; $z = 0$

$$v'_z = -2\left(\frac{\alpha q V_t}{a^2 m}\right)z \quad (13c)$$

Equation 13c is immediately seen to be the equation for a one-dimensional harmonic oscillator and its trajectory can be represented as written in equations 14a and 14b,

$$z = z_0 \cos(\omega_z t + \phi) \quad (14a)$$

$$\omega_z = \sqrt{\frac{2\alpha q V_t}{a^2 m}} \quad (14b)$$

where ω_z is the frequency of the axial oscillation of the ion between the trapping plates. We can also derive the value of z_0 , the amplitude of the axial oscillation, by assuming that the ion is at thermal equilibrium at a temperature T . Again, from both the kinetic molecular theory and the theory of equipartition of energy, we can write equation 15.

$$\frac{mv_z^2}{2} = \frac{kT}{2} \quad (15)$$

The evaluation of v_z^2 is not as straightforward as the evaluation of v^2 in equation 5, since the magnitude of v_z is continually changing. However, since $v_z(t)$ is known, the average value of v_z^2 can be calculated and is found to be $z_0^2 \omega_z^2 / 2$. Substituting this for v_z^2 and solving for z_0 , we obtain equation 16. This trapping amplitude increases with

$$z_0 = \sqrt{\frac{a^2 kT}{\alpha q V_t}} \quad (16)$$

increasing temperature or decreasing ion charge or decreasing trapping potential, but is independent of the ion's mass.

If we now use substitutions from equations 3d and 14b and define the new coordinate $r = x + iy$, we can simplify equations 13a and 13b to equation 17, which

$$r'' + i\omega_c r' - \frac{1}{2}\omega_z^2 r = 0 \quad (17)$$

describes the overall trajectory resulting from the x and y components of the equations of motion. The solution of this differential equation is shown in equations 18a and 18b.

$$r = r_+ e^{-i\omega_+ t} + r_- e^{-i\omega_- t} \quad (18a)$$

$$\omega_{\pm} = \frac{1}{2} \left(\omega_c \pm \sqrt{\omega_c^2 - 2\omega_z^2} \right) \quad (18b)$$

From equation 18a we see that the trajectory of the ion in the xy plane is a superposition of two separate circular motions. The ion still rotates around the z axis with a cyclotron radius r_+ (the distance from the cyclotron rotation center) and a reduced cyclotron frequency of ω_+ (which is approximately equal to ω_c). However, the center of the cyclotron motion also rotates, following an equipotential line in the radial electrostatic field (see Figure 3) with a magnetron frequency ω_- and a magnetron radius r_- . These two superimposed motions are illustrated in Figure 5.²¹ It is interesting to note that this motion is reminiscent of the planetary epicycles of Ptolemy. We can also use equation 18b to derive the limiting mass that can be trapped, since the periodic nature of the cyclic motions require ω_+ and ω_- to be real. For these frequencies to be real, inequality 19 must hold. Substituting for ω_c and ω_z from equation 3d and 14b, the critical mass

$$\omega_c^2 - 2\omega_z^2 \geq 0 \quad (19)$$

m_c can be calculated as shown in equation 20. This critical mass tells us the upper mass

$$m_c = \frac{qa^2 B^2}{4\alpha V_t} \quad (20)$$

limit that can be trapped with the given conditions: an ion can be trapped only if $m \leq m_c$. The overall trajectory of these three independent oscillations (the axial, cyclotron and magnetron oscillations) is shown in Figure 6.¹⁹

Static Magnetic Field with Static and Dynamic Electric Fields. In this case the absorbed resonant energy from the dynamic RF electric field will have an additional influence on the ion motion. The electric field can excite any mode of motion as long it is applied at the proper resonance frequency. There are various modes and methods of exciting ions,²² but the most popular method is dipolar excitation.

In dipolar excitation, an RF electric field is applied to the opposing excitation plates, with each plate being given opposing phases. We can calculate the postexcitation

Figure 5. The cyclotron and magnetron motions of an ion in the xy plane are shown in the upper drawing. r_+ and ω_+ are the cyclotron radius and reduced cyclotron frequency, while r_- and ω_- are the magnetron radius and magnetron frequency. The lower drawing shows the overall trajectory resulting from the combination of these two modes of motion.

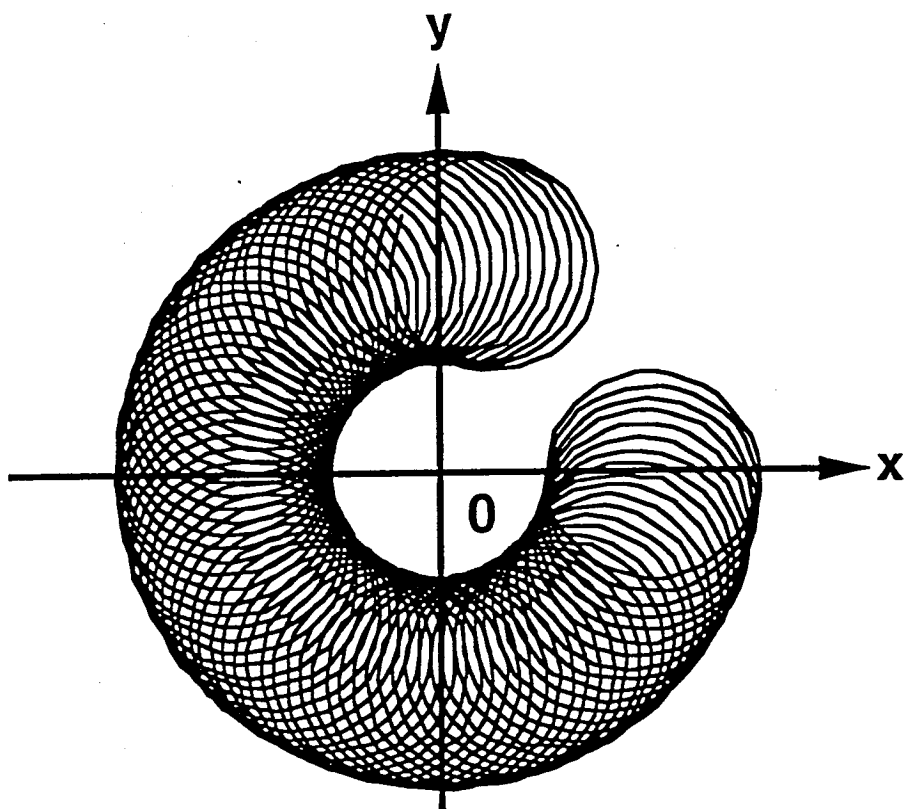
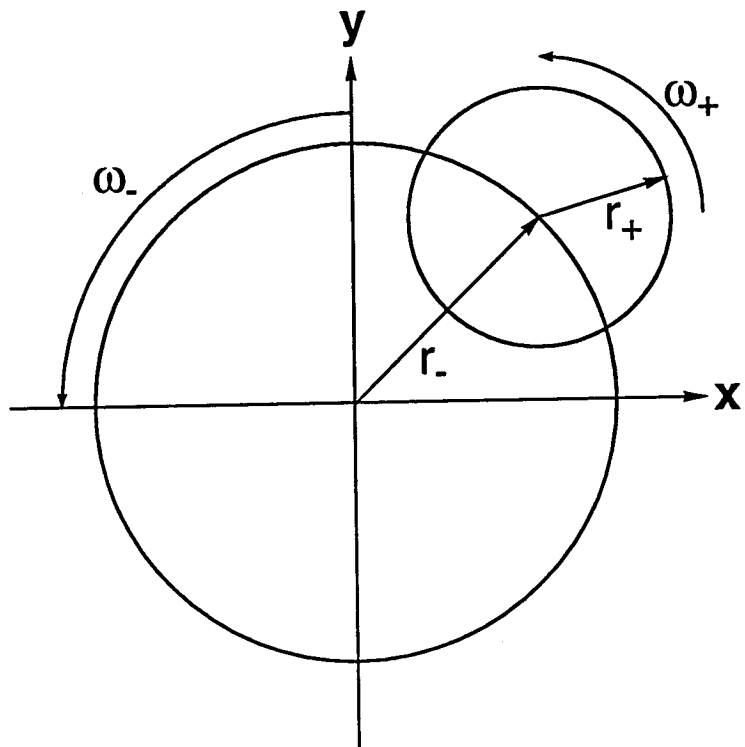
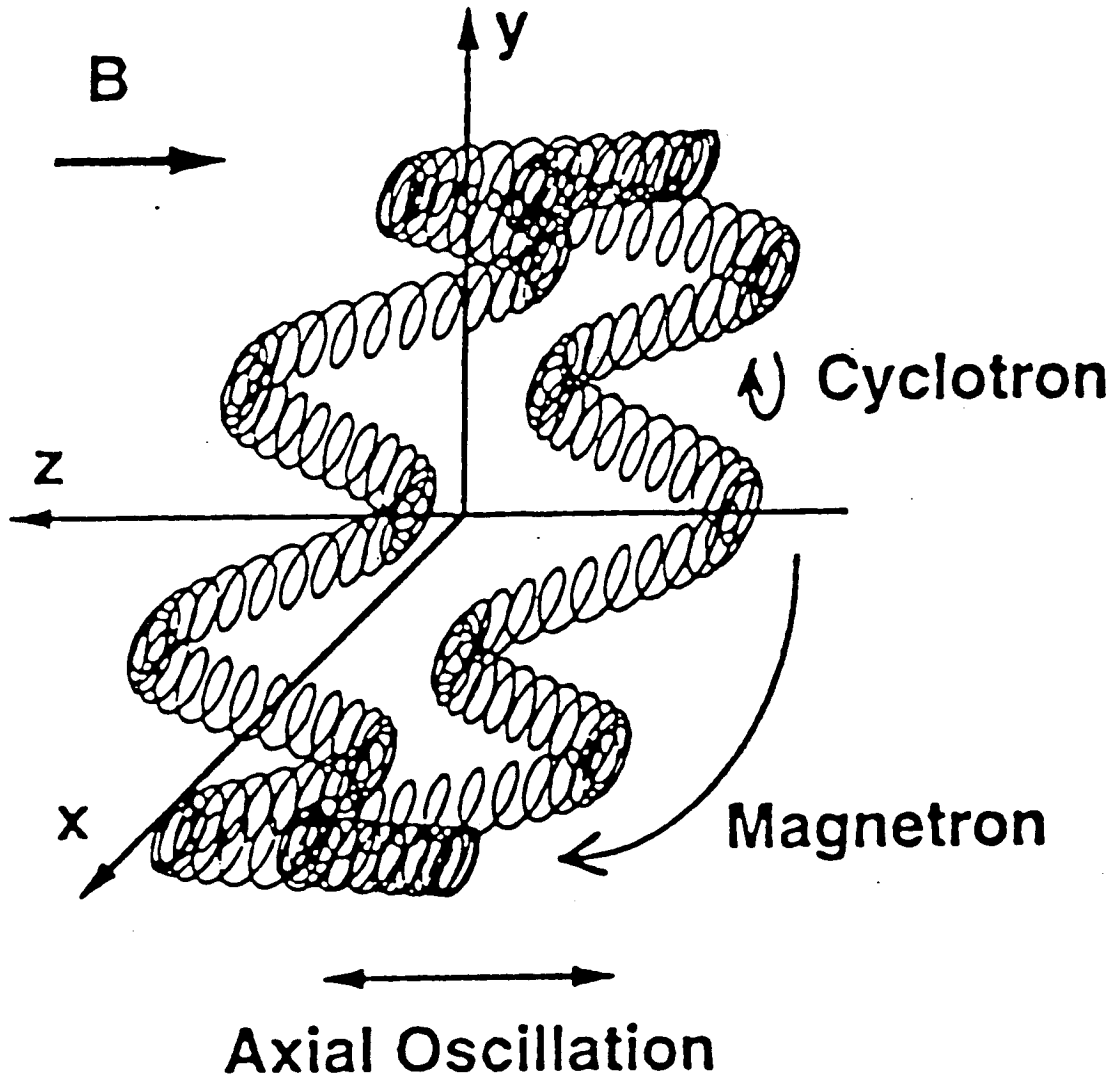


Figure 6. Fundamental modes of ion motion in an ICR trap: the cyclotron motion, the magnetron motion and the axial oscillation. The combination of these three modes gives the overall trajectory.



ion motion with equation 21 by equating the instantaneous single frequency power

$$P = \frac{dU}{dt} \quad (21)$$

absorption by an ion, averaged over one cycle of its oscillation, to the time derivative of the ion energy U (evaluated from the ion's position in the quadrupolar trapping potential). The average power P of RF excitation for a cubic trap has been described in an approximate form for reduced cyclotron motion in equation 22,^{22c} where $\beta = 0.72167$

$$P = \frac{q\beta V_{pp} r_+ \omega_+}{2a} \quad (22)$$

and V_{pp} is the peak-to-peak voltage of the RF electric field. The energy U_+ of the reduced cyclotron motion (shown in equation 23, where $\omega_p = \omega_+ - \omega_-$) has been derived

$$U_+ = \frac{m}{2} \omega_p \omega_+ r_+^2 \quad (23)$$

using classical mechanics.²³ Relating equations 22 and 23 through equation 21, we obtain the differential equation of motion in equation 24. Assuming the initial cyclotron

$$m\omega_p r_+' = \frac{q\beta V_{pp}}{2a} \quad (24)$$

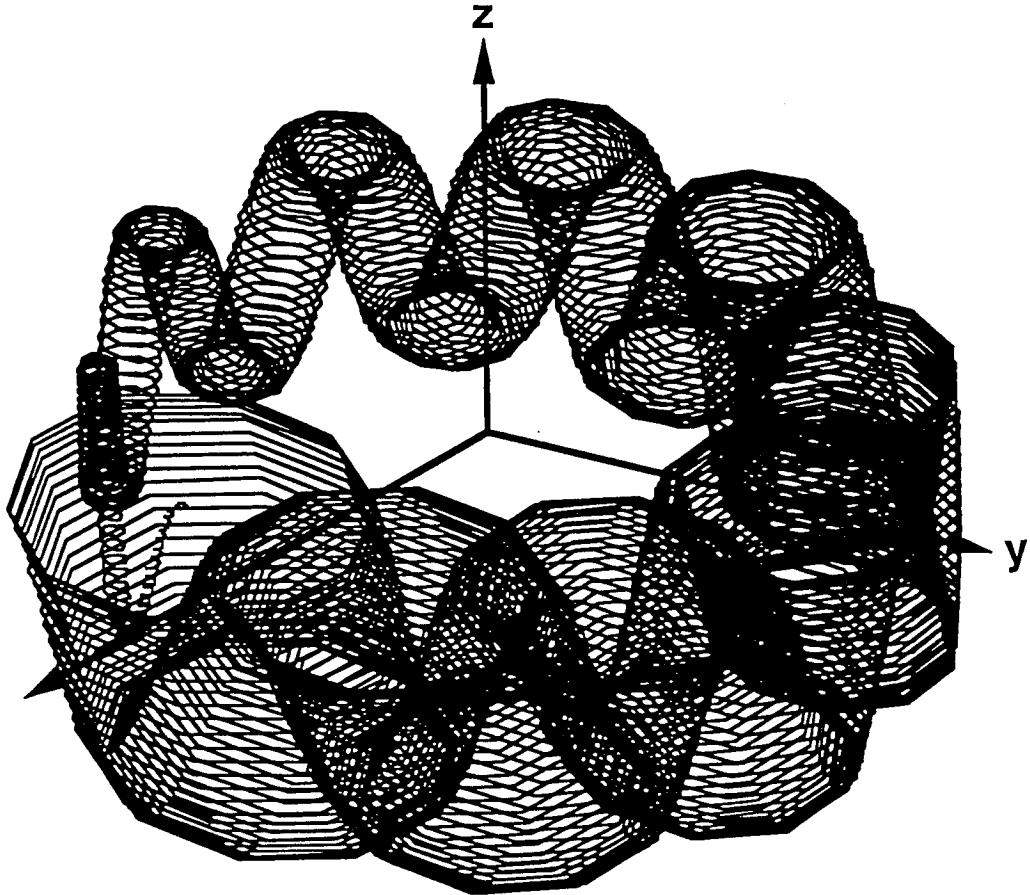
radius is negligible ($r_+(0) = 0$), we can write the solution to the equation of motion in equation 25. Substitution of equation 25 into equation 18a yields equation 26, which

$$r_+ = \frac{q\beta V_{pp} t}{2ma\omega_p} \cong \frac{\beta V_{pp} t}{2aB} \quad (25)$$

$$r = \frac{q\beta V_{pp} t}{2ma\omega_p} e^{-i\omega_+ t} + r_- e^{-i\omega_- t} \quad (26)$$

describes the xy component of the ions postexcitation trajectory. Along with equation 14a for the z component of the ion's motion, this gives a complete (though approximate) representation of the postexcitation ion motion. Figure 7¹⁷ shows a plot of the resultant motion.

Figure 7. Ion motion during the RF dipolar excitation of an ion's cyclotron motion.



Dipolar excitation can also be used to excite the magnetron mode of motion. This is accomplished by using ω_- as the excitation frequency instead of ω_+ . The trajectory that results is given in equation 27. However, the use of magnetron excitation

$$r_- = r_-(0) - \frac{q\beta V_{pp}t}{2ma\omega_p} \quad (27)$$

can often lead to the unintentional ejection of ions, and as a consequence it is not often used. We should note that both the cyclotron and magnetron modes of motion increase linearly with the duration of the excitation.

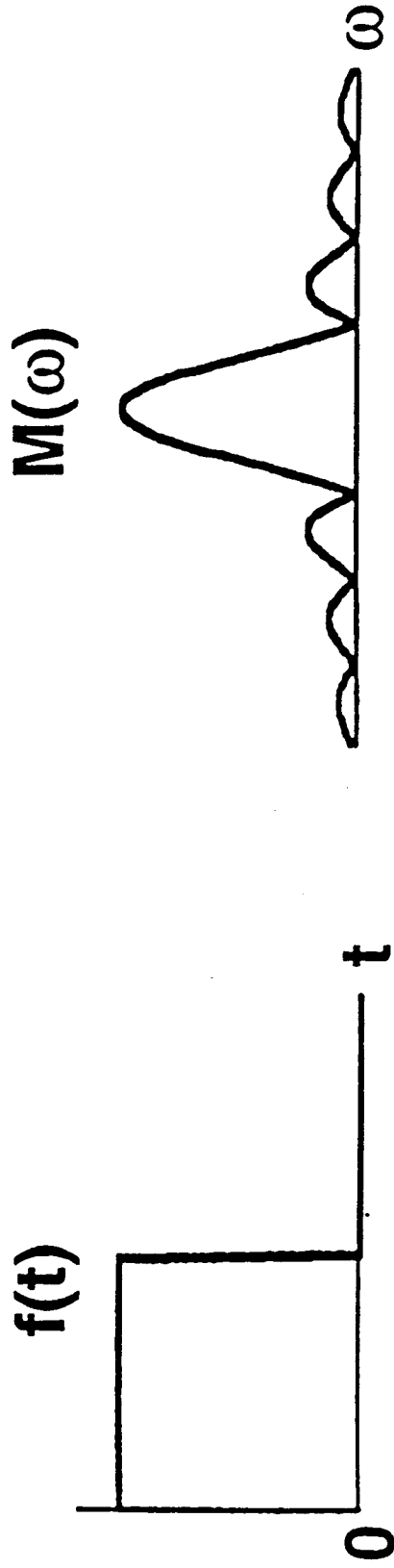
Excitation and Detection of Ions

Excitation of ions is accomplished by applying a RF electric field to the trapping plates. When the RF frequency matches the frequency of any of the natural cyclic motions of the ion, the energy of the field is resonantly absorbed and that specific motion will be excited. From equation 25, we can see that the final ion radius is directly proportional to the excitation amplitude and independent of the ion mass and charge. Therefore, if we are able to provide an excitation that is uniform in magnitude at each frequency, all ions will be coherently excited to the same radius. This excitation can be done at single frequencies, but is most commonly done with a frequency sweep.

Single frequency (or single-pulse) excitation was the first method used with FT-ICR mass spectrometry.⁷ A single frequency pulse of duration t will produce in the frequency domain a sine function centered at the frequency of excitation with a full-width-at-half-maximum (FWHM) value of approximately $1.2/t$ Hz (see Figure 8²¹). Such pulses are useful for detection at a single mass or ejections at a single mass (if the field amplitude and/or time duration of the pulse is large enough).

However, to take spectra with single frequency pulses is extremely time consuming. To remedy this and allow for the excitation of ions over a wide frequency range, frequency sweep excitation was introduced.²⁴ This frequency sweep or “chirp” excitation is the most commonly used excitation method in FT-ICR mass spectrometry.

Figure 8. The time domain excitation waveform (left) and frequency domain magnitude spectrum (right) of single frequency excitation.



In this method the RF field is scanned linearly with time over the frequency range of interest as described in equation 28a and 28b, where ζ is the frequency sweep rate and

$$f(t) = e^{i\left(\omega_0 t + \frac{\zeta t^2}{2}\right)}, 0 \leq t \leq T \quad (28a)$$

$$f(t) = 0, t < 0 \text{ or } t > T \quad (28b)$$

ω_0 is the initial frequency at $t = 0$. The final frequency ω_f at $t = T$ is given by equation 29. Although broadband excitation is possible, there is still a problem: the excitation

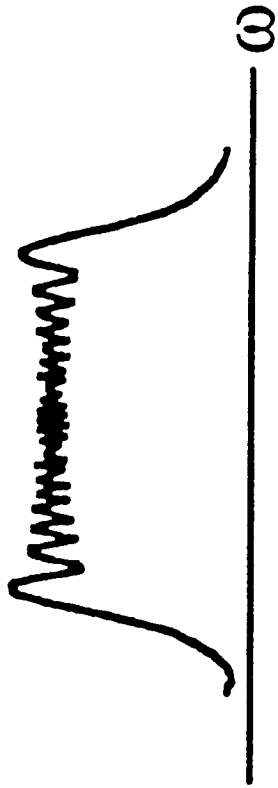
$$\omega_f = \omega_0 + \zeta T \quad (29)$$

amplitudes are not constant over the frequency range. Variations in amplitude of $\pm 25\%$ are observed in the frequency spectrum with linear sweep excitation, making quantification of absolute ion intensities difficult (see Figure 9²¹). By slowing the frequency sweep it is possible to flatten the power spectrum and decrease the amplitude variation in the excitation. Even so, it is best to keep the mass peaks of interest near the center of the mass range where the power spectrum is flatter. Frequency sweeps are simple, but they should be used with care, especially for quantitative work. Furthermore, as with single frequency excitation, frequency sweep excitations can be used to eject ions in a given mass range if the field amplitude and/or time duration of the pulse is large enough.

The ability of single frequency and frequency sweep excitation to eject ions from the cell allows for the selective ejection of unwanted ions. This provides us with a convenient way to isolate the ions of interest from unwanted ions for further study of their subsequent chemistry. Since most methods of ion formation produce more than just the ions of interest, we are rather lucky that excitation methods can also be used to eject ions.

The detected ICR signal can be derived with Comisarow's signal model²⁵ once the ion motion has been properly described. From Comisarow's signal model and equations 25 and 26, the induced charge generated by the ion motion can be derived as

Figure 9. The time domain excitation waveform (left) and frequency domain magnitude spectrum (right) of frequency sweep excitation.



written in equation 30, where $Q(t)$ is the induced charge on the plates, N is the number

$$Q(t) = -\frac{Nq}{d}[r_+\cos(\omega_+t) + r_-\cos(\omega_-t)] \quad (30)$$

of ions present, q is the charge of each ion and d is the distance between the plates. This description is valid for magnetic and electrostatic trapping fields in a cubic cell, as shown in Figure 10,¹⁷ and was derived by assuming the detection plates are extended to infinity in the xy plane and that nothing interferes with detection of the ion by the detection plates.

Equation 30 shows that both cyclotron and magnetron frequencies can be detected and that the signal amplitude for each mode is proportional to the postexcitation radius of each mode. Since the cyclotron mode is usually excited in an ICR experiment, $r_+ \gg r_-$ after excitation and the detected signal will show mostly the cyclotron resonant frequency. We could also excite the magnetron motion to a larger radius, but this is rarely done for reasons discussed in the previous section. The conversion from induced charge to an induced voltage is discussed by Comisarow.²⁵

Standard Experimental Event Sequence

Examination of the standard experimental event sequence shows how the various aspects of ICR experiments are combined to collect the data necessary to obtain a mass spectrum. Figure 11²¹ illustrates in a simplified form the experimental procedure in the proper sequential order. Ions are initially formed with a specified ionization method and then isolated if necessary with various combinations of single frequency or frequency sweep excitations of high enough power to eject undesired ions. After isolation of the ions of interest, a time delay is provided to allow the ions to undergo either unimolecular reactions or bimolecular ion-molecule processes. The ions at the end of this delay period are then simultaneously excited with another sweep excitation, and this excited cyclotron motion is detected through the image currents these ions produce on the detection plates. This current is then converted to a voltage and amplified. After detection, the resulting

Figure 10. Illustration of how the induced charge (and image current) is generated on the detection plates by an ion circulating inside an ICR cell with a homogeneous magnetic field of strength B .

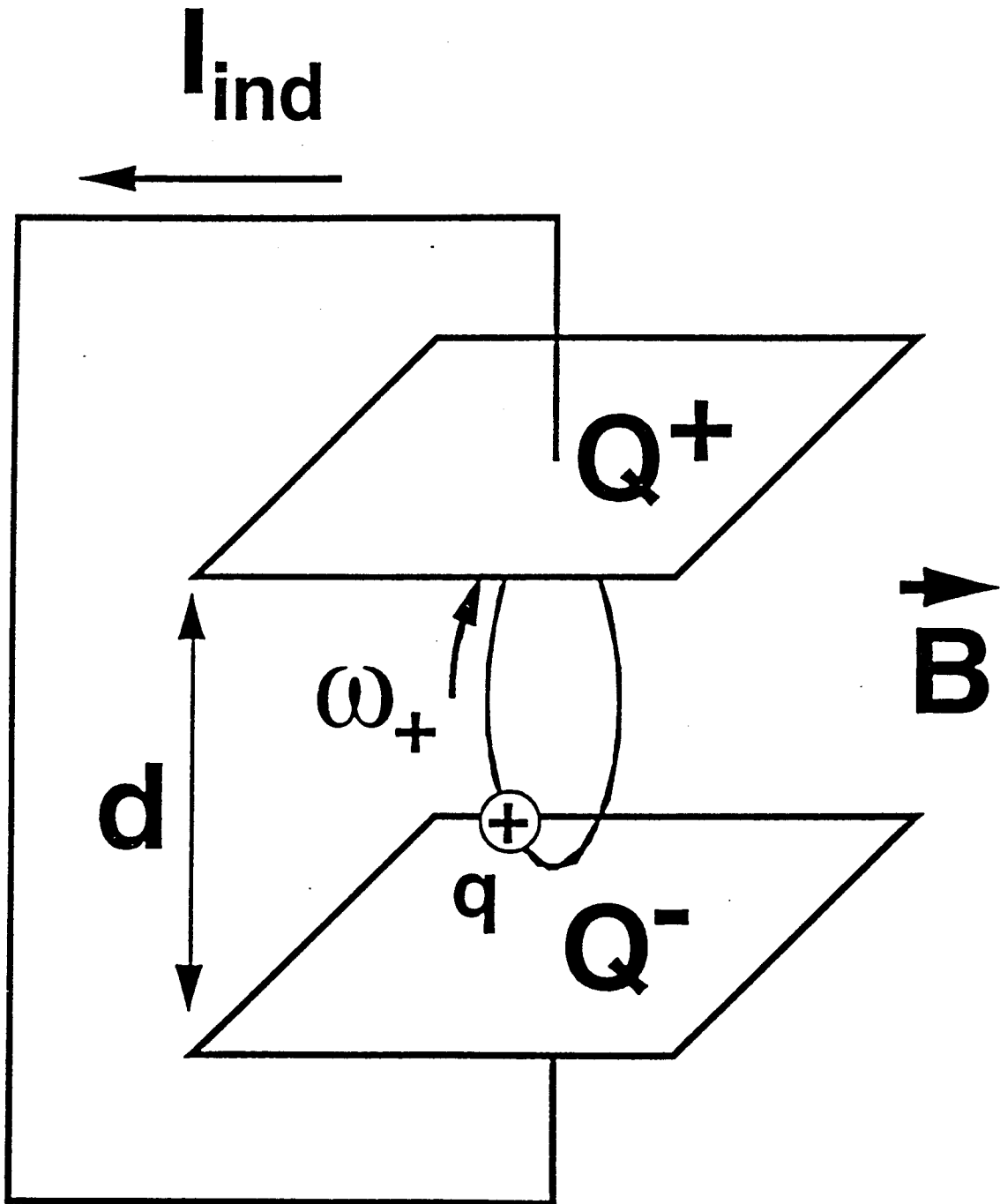
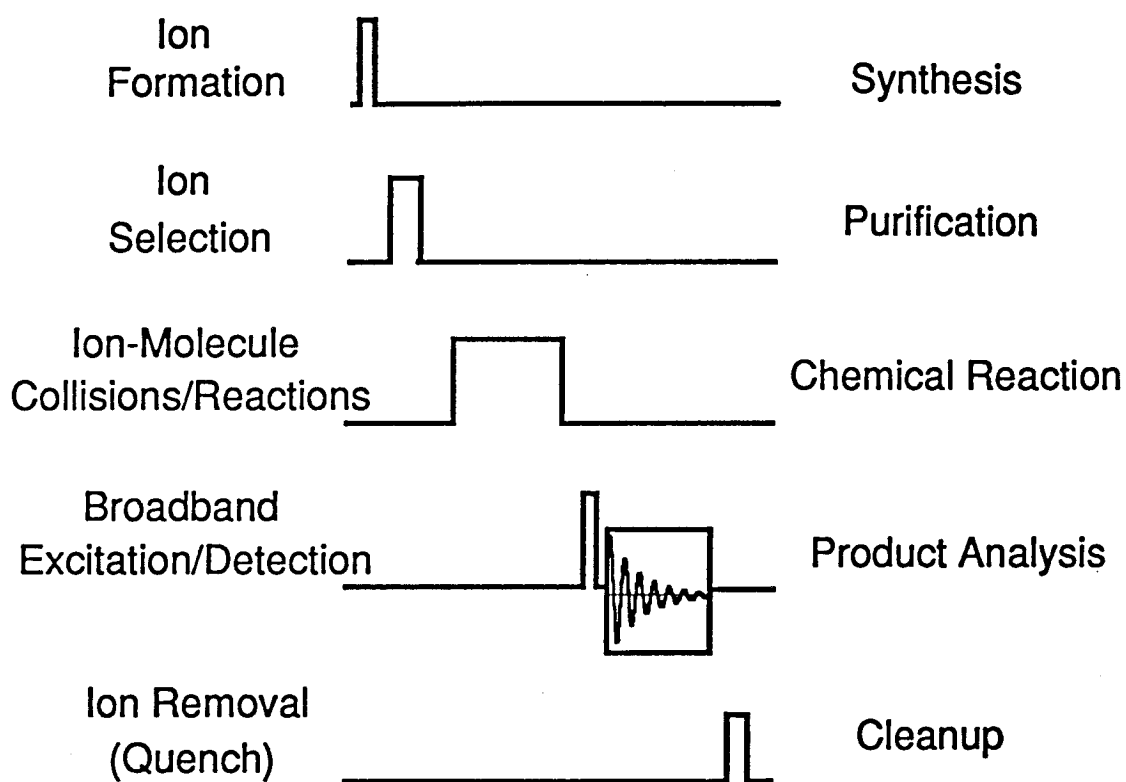


Figure 11. Simplified illustration of the typical experimental event sequence, with the conventional chemical manipulations listed at right.



spectrum is then stored as a digital transient signal and a quench RF pulse covering the whole mass range is applied to rid the cell of all ions in preparation for the next cycle of events. The various pulses required to perform an experiment are controlled by the data collection software.

We should note here that the initial kinetic energy of the ions immediately after their formation can vary greatly depending on the method of formation. For example, LDI leads to ions with high kinetic energies, while EI ionization produces ions of low kinetic energy. The high velocity ions can be cooled (either collisionally or radiatively) by allowing for more time between the ionization and excitation event and usually results in higher spectral resolution. For this reason, longer delay times between the ionization and excitation events are often introduced when ionization methods that produce high kinetic energy ions are used.

Conclusions

The experimental aspects of FT-ICR mass spectrometry have been briefly reviewed. The developmental history of FT-ICR mass spectrometry was briefly discussed and the specific instrumentation needed to perform FT-ICR experiments was described. The mathematical description of ion motion, excitation and detection within the ICR cell has been considered and the way in which these various aspects of FT-ICR mass spectrometry are combined into a standard experimental event sequence was presented. This review should provide the necessary background information required to understand the experimental techniques used to perform the experiments described throughout the rest of this dissertation.

References

- ¹Lawrence, E. O.; Livingston, M. S. *Phys. Rev.* **1932**, *40*, 19.
- ²(a) Hipple, J. A.; Sommer, H.; Thomas, H. A. *Phys. Rev.* **1949**, *76*, 1877. (b) Sommer, H.; Thomas, H. A. *Phys. Rev.* **1950**, *78*, 806.
- ³(a) Wobschall, D.; Graham, J. R.; Malone, D. P. *Phys. Rev.* **1963**, *131*, 1565. (b) Wobschall, D. *Rev. Sci. Instrum.* **1965**, *36*, 466.
- ⁴(a) Baldeschwieler, J. D.; Benz, H.; Llewellyn, P. M. *Adv. Mass Spectrom.* **1968**, *4*, 113. (b) Baldeschwieler, J. D. *Science* **1968**, *159*, 263. (c) Baldeschwieler, J. D.; Beauchamp, J. L.; Llewellyn, P. M. Fr. Patent 1,531,956; *Chem. Abstr.* **1969**, *71*, 413. (d) Baldeschwieler, J. D.; Woodgate, S. S. *Acc. Chem. Res.* **1971**, *4*, 114.
- ⁵(a) Comisarow, M. B. *Anal. Chim. Acta.* **1985**, *178*, 1. (b) Marshall, A. G.; Verdun, F. R. *Fourier Transforms in NMR, Optical, and Mass Spectrometry: A User's Handbook*, 1990, Elsevier, Amsterdam.
- ⁶McIver, R. T., Jr. *Rev. Sci. Instrum.* **1970**, *41*, 555.
- ⁷Comisarow, M. B.; Marshall, A. G. *Chem. Phys. Lett.* **1974**, *25*, 282.
- ⁸(a) Itikawa, Y.; Takayanagi, K.; Iwai, T. *At. Data Nucl. Data Tables*, **1984**, *31*, 215. (b) *Electron Impact Ionization*, T. D. Mark and G. H. Dunn, Eds., 1985, Springer-Verlag, New York-Berlin. (c) Tawara, H.; Kato, T. *At. Data Nucl. Data Tables*, **1987**, *36*, 167.
- ⁹(a) Cody, R. B.; Burnier, R. C.; Reents, W. D., Jr.; Carlin, T. J.; McCrery, D. A.; Lengel, R. K.; Freiser, B. S. *Int. J. Mass Spectrom. Ion Phys.* **1980**, *33*, 37. (b) *Lasers and Mass Spectrometry*, D. M. Lubman, Ed., 1990, Oxford University Press, New York. (c) Castoro, J. A.; Köster, C.; Wilkins, C. *Rapid Commun. Mass Spectrom.* **1992**, *6*, 239. (d) Azzaro, M.; Breton, S.; Decouzon, M.; Geribaldi, S. *Int. J. Mass Spectrom. Ion Proc.* **1987**, *78*, 53. (e) Karas, M.; Bachmann, D.; Bahr, U.; Hillenkamp, F. *Int. J. Mass Spectrom. Ion Proc.* **1993**, *128*, 1. (f) Juhasz, P.; Costello, C. E.; Biemann, K. J. *J. Am. Soc. Mass Spectrom.* **1993**, *4*, 399.
- ¹⁰(a) Zitrin, S. *Org. Mass Spectrom.* **1982**, *17*, 74. (b) Stillwell, R. N.; Carroll, D. I.; Nowlin, J. G.; Horning, E. C. *Anal. Chem.* **1983**, *55*, 1313, and references contained therein. (c) Clemens, D.; Munson, B. *Anal. Chem.* **1985**, *57*, 2022. (d) Orlando, R.; Munson, B. *Anal. Chem.* **1986**, *58*, 2788. (e) Yinon, J.; Fraise, D.; Dagley, I. J. *Org. Mass Spectrom.* **1991**, *26*, 867. (f) Wood, T. D.; Marshall, A. G. *J. Am. Soc. Mass Spectrom.* **1991**, *2*, 299. (g) Hogan, J. D.; Laude, D. A., Jr. *Anal. Chem.* **1991**, *63*, 2105. (h) Burrows, E. P. *Org. Mass Spectrom.* **1994**, *29*, 315.
- ¹¹(a) Meyer, K. F.; Jasinski, J. M.; Rosenfield, R. N.; Brauman, J. I. *J. Am. Chem. Soc.* **1982**, *104*, 663. (b) Thorne, L. R.; Beauchamp, J. L. *Gas Phase Ion Chemistry*, Vol. 3, M. T. Bowers, Ed., 1984, Academic Press, New York. (c) Hanratty, M. A.; Paulsen, C. M.; Beauchamp, J. L. *J. Am. Chem. Soc.* **1985**, *107*, 5074. (d) Zimmerman, J. A.; Watson, H. C.; Eyler, J. R. *Anal. Chem.* **1991**, *63*, 361. (e) Surjasasmita, P. I.; Freiser, B. S. *J. Am. Soc. Mass Spectrom.* **1993**, *4*, 135.

¹²(a) Barber, M.; Bordoli, R. S.; Sedgwick, R. D.; Tyler, A. N. *J. Chem. Soc. Chem. Commun.* **1981**, 325. (b) *Mass Spectrometry of Biological Materials*, C. McEwan and B. Larson, Eds., 1990, Marcel Dekker, Inc., New York. (c) Watson, C. H.; Kruppa, G. Wronka, J.; Laukien, F. H. *Rapid Commun. Mass Spectrom.* **1991**, *5*, 249. (d) Shinohara, H.; Sato, H.; Saito, Y.; Takayama, M.; Izuoka, A.; Sugawara, T. *J. Phys. Chem.* **1991**, *95*, 8449.

¹³(a) Hofstadler, S. A.; Schmidt, E.; Guan, Z.; Laude, D. A., Jr. *J. Am. Soc. Mass Spectrom.* **1993**, *4*, 168. (b) Light-Wahl, K. J.; Springer, D. L.; Winger, B. E.; Edmonds, C. G.; Camp, D. G.; Thrall, B. D.; Smith, R. D. *J. Am. Chem. Soc.* **1993**, *115*, 803. (c) Michael, S. M.; Chien, B. M.; Lubman, D. M. *Anal. Chem.* **1993**, *65*, 2614. (d) Bruce, J. E.; Anderson, G. A.; Hofstadler, S. A.; Van Orden, S. L.; Sherman, M. S.; Rockwood, A. L.; Smith, R. D. *Rapid Commun. Mass Spectrom.* **1993**, *7*, 914. (e) Hofstadler, S. A.; Beu, S. C.; Laude, D. A., Jr. *Anal. Chem.* **1993**, *65*, 312. (f) Winger, B. E.; Hofstadler, S. A.; Bruce, J. E.; Udseth, H. R.; Smith, R. D. *J. Am. Soc. Mass Spectrom.* **1993**, *4*, 566.

¹⁴(a) Chapman, B. *Glow Discharge Processes: Sputtering and Plasma Etching*, 1980, Wiley, New York. (b) Barshick, C. M.; Eyler, J. R. *J. Am. Soc. Mass Spectrom.* **1992**, *3*, 122. (c) Limbach, P. A.; Marshall, A. G.; Wang, M. *Int. J. Mass Spectrom. Ion Proc.* **1993**, *125*, 135.

¹⁵(a) Sunderlin, L. S.; Armentrout, P. B. *J. Phys. Chem.* **1988**, *92*, 1209. (b) Suzuki, T.; Takahashi, K.; Nomura, M.; Fujii, Y.; Okamoto, M. *Jpn. J. Applied Phys.* **1994**, *33*, 4247. (c) Clemmer, D. E.; Chen, Y.-M.; Khan, F. A.; Armentrout, P. B. *J. Phys. Chem.* **1994**, *98*, 6522. (d) Takayama, M.; Hiraoka, K.; Nakata, H. *Int. J. Mass Spectrom. Ion Proc.* **1995**, *148*, L11. (e) Kickel, B. L.; Armentrout, P. B. *J. Am. Chem. Soc.* **1995**, *117*, 4057.

¹⁶Comisarow, M. B. *Int. J. Mass Spectrom. Ion Phys.* **1981**, *37*, 251.

¹⁷This figure is reproduced from: Kim, H. S., Ph.D. Thesis, The Ohio State University, 1994.

¹⁸Mass calibration is performed with a fitting function of the form $m/z = A\nu^1 + B\nu^2 + C\nu^3$, where $\nu = \omega/2\pi$. The constants A , B and C are determined by fitting a particular set of peak frequencies (at least three) for ions of known m/z . If more than three peaks are used, an overdetermined system results. For additional information, see Reference 5b.

¹⁹This figure is reproduced from the following article: Guan, S.; Kim, H. S.; Marshall, A. G.; Wahl, M. C.; Wood, T. D.; Xiang, X. *Chem. Rev.* **1994**, *94*, 2161.

²⁰(a) Sharp, T. E.; Eyler, J. R.; Li, E. *Int. J. Mass Spectrom. Ion Phys.* **1972**, *9*, 421. (b) Jackson, J. D. *Classical Electrodynamics*, 1975, Wiley, New York. (c) Reference 5b.

²¹This figure is reproduced from Reference 5b.

²²(a) Grosshans, P. B.; Marshall, A. G. *Anal. Chem.* **1991**, *63*, 2057. (b) Grosshans, P. B.; Marshall, A. G. *Int. J. Mass Spectrom. Ion Proc.* **1990**, *100*, 347. (c) Schweikhard, L.; Marshall, A. G. *J. Am. Soc. Mass Spectrom.* **1993**, *4*, 433.

²³Brown, L. S.; Gabrielse, G. *Rev. Mod. Phys.* **1986**, *58*, 233.

²⁴(a) Comisarow, M. B.; Marshall, A. G. *Chem. Phys. Lett.* **1974**, *26*, 489. (b)
Marshall, A. G.; Roe, D. C. *J. Chem. Phys.* **1980**, *73*, 1581.

²⁵Comisarow, M. B. *J. Chem. Phys.* **1978**, *69*, 4097.

Chapter 2

**SITE SELECTIVE σ -BOND METATHESIS REACTIONS OF $\text{Sc}(\text{CD}_3)_2^+$
WITH [2,2-D₂]-PROPANE, [1,1,1,4,4,4-D₆]-*n*-BUTANE AND [2-D]-ISOBUTANE**

Kevin C. Crellin, Serge Geribaldi and J. L. Beauchamp

Contribution No. 8895, Arthur Amos Noyes Laboratory of Chemical Physics,
California Institute of Technology, Pasadena, CA 91125

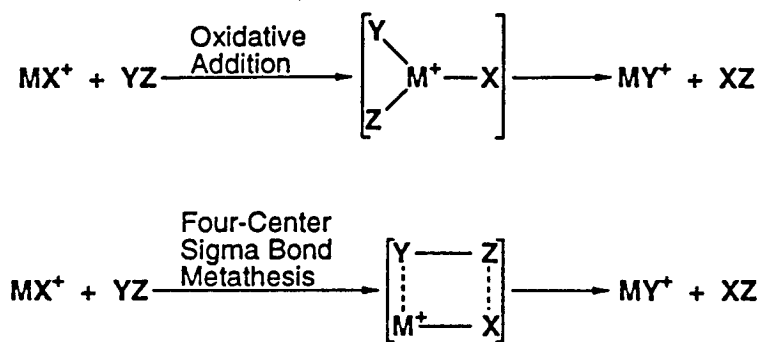
Published as a note in *Organometallics*, **1994**, *13*, 3733-3736.

Abstract

Fourier transform ion cyclotron resonance mass spectrometry has been used to examine the reactions of $\text{Sc}(\text{CD}_3)_2^+$ with methane, ethane, [2,2-D₂]-propane, [1,1,1,4,4,4-D₆]-*n*-butane and [2-D]-isobutane. $\text{Sc}(\text{CD}_3)_2^+$ is not observed to react with methane but for ethane, propane, *n*-butane and isobutane σ -bond metathesis with methane elimination is the initial and dominant reaction observed, with further dehydrogenation of the resulting products occurring as additional reaction channels. For propane, *n*-butane and isobutane the initial σ -bond metathesis occurs predominantly at the primary position. These processes are facile at room temperature and occur with little or no activation energy. Measured total bimolecular rate constants with ethane, [2,2-D₂]-propane, [1,1,1,4,4,4-D₆]-*n*-butane and [2-D]-isobutane are 4.7×10^{-11} , 1.5×10^{-10} , 4.4×10^{-10} and $4.3 \times 10^{-10} \text{ cm}^3 \text{ s}^{-1} \text{ molecule}^{-1}$, respectively. The total reaction rate of $\text{Sc}(\text{CH}_3)_2^+$ with unlabeled *n*-butane was measured to be $4.3 \times 10^{-10} \text{ cm}^3 \text{ s}^{-1} \text{ molecule}^{-1}$. With the butanes a second intramolecular metathesis reaction follows the bimolecular process to yield a metallacycle product. In accordance with earlier theoretical predictions these metathesis reactions appear to proceed via an allowed four-center mechanism similar to that of a $2\sigma + 2\sigma$ cycloaddition. The observed site selectivity also agrees with theoretical predictions.

Introduction

Steigerwald and Goddard have predicted that the degenerate hydrogen exchange reaction of D_2 with transition metal complexes such as Cl_2MH ($M = Sc, Ti, Ti^+$) can occur via a four-center mechanism similar to $2\sigma + 2\sigma$ cycloaddition (Scheme I). They



Scheme I

found that these reactions can proceed at low energies with small barriers and that the barriers decreased as the Lewis acid character of the metal increased.¹ These predictions have interesting implications with regard to the reactivity of $Sc(CD_3)_2^+$ with alkanes. This ion has an extremely acidic metal center and should therefore be capable of reacting via a four-center mechanism. Also, since Sc^+ has only two valence electrons, it is capable of forming no more than two strong σ bonds,^{2,3} while oxidative addition mechanisms for reactions of $Sc(CD_3)_2^+$ with alkanes require the formation of four σ bonds (see Scheme I). This suggests that $Sc(CD_3)_2^+$ must react via a four-center mechanism if it is to react at all.

Exceptional reactivity in other scandium complexes has also been observed. Thompson et al. have observed σ -bond metathesis reactions with permethylscandocene derivatives,^{4a} and they invoked a four-center mechanism for this process. Huang et al. have observed σ -bond metathesis reactions of $Sc(CH_3)_2^+$ with alkenes,^{4b} and such reactivity has also been observed in other transition metal systems.^{4c,5-7} It might be thought that $Sc(CH_3)_2^+$ could exhibit such σ -bond metathesis reactions with alkanes. We have used labeled compounds to investigate the reactions of $Sc(CD_3)_2^+$ with small

alkanes to see if any site selectivity is observed, as previous studies have found that attack can occur at both primary and secondary C-H bonds in hydrocarbons.⁷⁻⁹ In this study we report the results of the reaction of $\text{Sc}(\text{CD}_3)_2^+$ with ethane, [2,2-D₂]-propane, [1,1,1,4,4,4-D₆]-*n*-butane and [2-D]-isobutane.

Experimental

Reactions were investigated with Fourier transform ion cyclotron resonance (FT-ICR) mass spectrometry, of which a number of reviews are available.¹⁰ A 1-in. cubic trapping cell is located between the poles of a Varian 15-in. electromagnet maintained at 1.0 T. Pressures were measured with a Schultz-Phelps ion gauge calibrated against an MKS 390 HA-00001SP05 capacitance manometer. Uncertainties in the absolute pressure limit rate constants to an accuracy of $\pm 20\%$. Labeled [2,2-D₂]-propane (98% D), [1,1,1,4,4,4-D₆]-*n*-butane (98% D) and [2-D]-isobutane (98% D) were obtained commercially from Merck, Sharp and Dohme and purified by freeze-pump-thaw cycling.

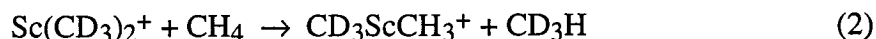
Sc^+ ions were produced by laser ablation of a scandium metal target with a N_2 laser at 337.1 nm. The reactant ion was generated by reaction 1² and unwanted ions



were ejected from the cell using double resonance techniques¹¹ and/or frequency sweep excitation.¹² Reactions of isolated $\text{Sc}(\text{CD}_3)_2^+$ were first examined with labeled *n*-butane. Methane, ethane, labeled propane or labeled isobutane were then added along with the labeled *n*-butane and reactions due to the additional alkane were observed. In order to determine if any kinetic isotope effects were present, the reaction of isolated $\text{Sc}(\text{CH}_3)_2^+$ (made via reaction 1 using unlabeled *n*-butane) with unlabeled *n*-butane was examined. Rate constants were determined in a straightforward manner, from slopes of semilog plots of the decay of reactant ion abundance versus time, with various pressures of the neutral reactants.

Results

Reaction with Methane. The thermoneutral exchange reaction of $\text{Sc}(\text{CD}_3)_2^+$ with



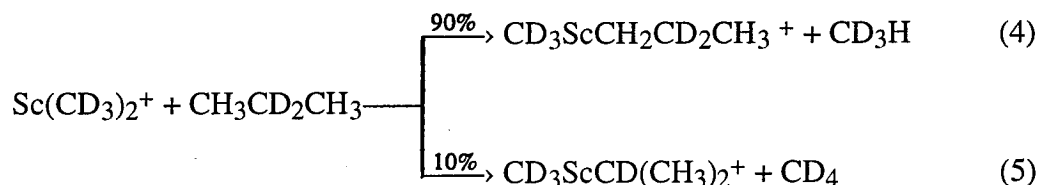
CH_4 (reaction 2) was not observed. For reaction 2 we estimate that $k \leq 1 \times 10^{-11} \text{ cm}^3\text{s}^{-1} \text{ molecule}^{-1}$.

Reaction with Ethane. The only process observed is reaction 3. For reaction 3



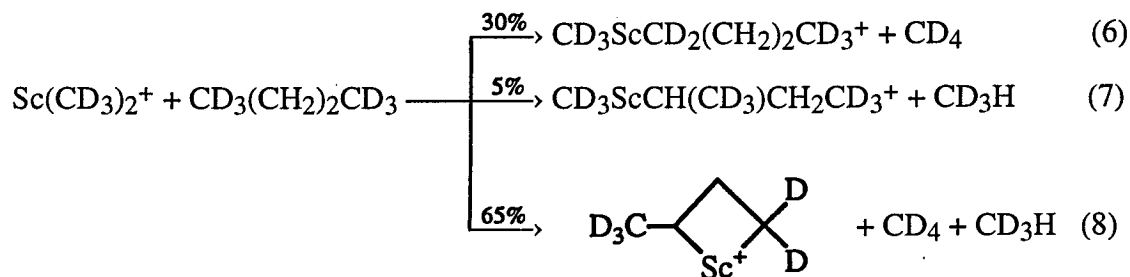
$k = 4.7 \times 10^{-11} \text{ cm}^3\text{s}^{-1} \text{ molecule}^{-1}$ and the reaction efficiency $k/k_{\text{Langevin}} = 0.045$.

Reaction with Propane. The main process observed with the labeled propane is



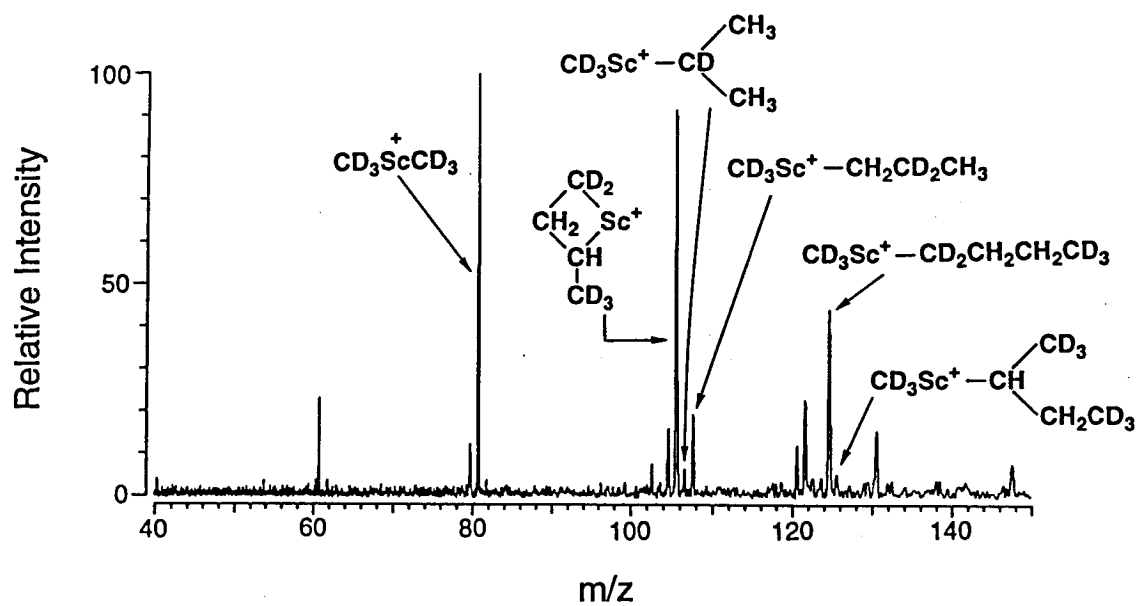
the metathesis reaction 4. Reaction 5 is a minor pathway (see Figure 1). For the reaction of $\text{Sc}(\text{CD}_3)_2^+$ with labeled propane the total bimolecular rate constant $k = 1.5 \times 10^{-10} \text{ cm}^3\text{s}^{-1} \text{ molecule}^{-1}$ and the reaction efficiency $k/k_{\text{ADO}} = 0.14$.¹³

Reaction with *n*-Butane. Reactions 6-8 are observed with labeled *n*-butane (see Figure 1). Unlabeled *n*-butane shows the same product distribution, but without labeling we are unable to differentiate between the *n*-butyl and *sec*-butyl products. It is postulated that reaction 8 occurs when the vibrationally excited product of reaction 6 has enough energy for a second intramolecular metathesis reaction, resulting in the



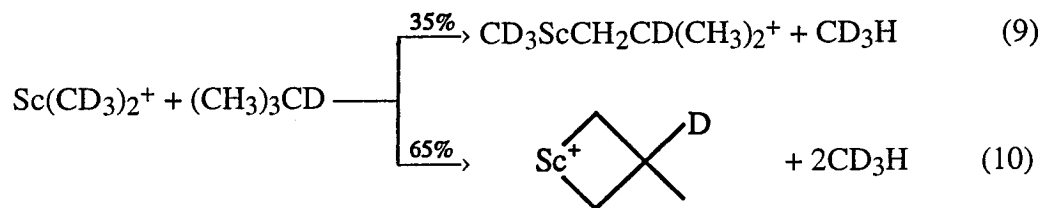
metallacycle product. For the reaction of $\text{Sc}(\text{CD}_3)_2^+$ with labeled *n*-butane the total bimolecular rate constant $k = 4.4 \times 10^{-10} \text{ cm}^3\text{s}^{-1} \text{ molecule}^{-1}$ and the reaction efficiency

Figure 1. Products of reaction of $\text{Sc}(\text{CD}_3)_2^+$ with $[2,2\text{-D}_2]\text{-propane}$ and $[1,1,1,4,4,4\text{-D}_6]\text{-}n\text{-butane}$. Spectrum was taken 140 ms after isolation of $\text{Sc}(\text{CD}_3)_2^+$. The main peaks above m/z 130 correspond to ScR_2^+ , R = alkyl. Peaks at m/z 61 and 79 correspond to ScO^+ and $\text{Sc}(\text{OH})_2^+$, respectively.



k/k_{ADO} is 0.39.¹³ For the reaction of $\text{Sc}(\text{CH}_3)_2^+$ with unlabeled *n*-butane the total bimolecular rate constant $k = 4.3 \times 10^{-10} \text{ cm}^3 \text{ s}^{-1} \text{ molecule}^{-1}$ and the reaction efficiency k/k_{ADO} is 0.37.¹³

Reaction with Isobutane. Reactions 9 and 10 are observed with labeled isobutane (see Figure 2). Reaction 10 occurs when the vibrationally excited product of reaction 9 has enough energy for a second metathesis reaction to yield the metallacycle product.



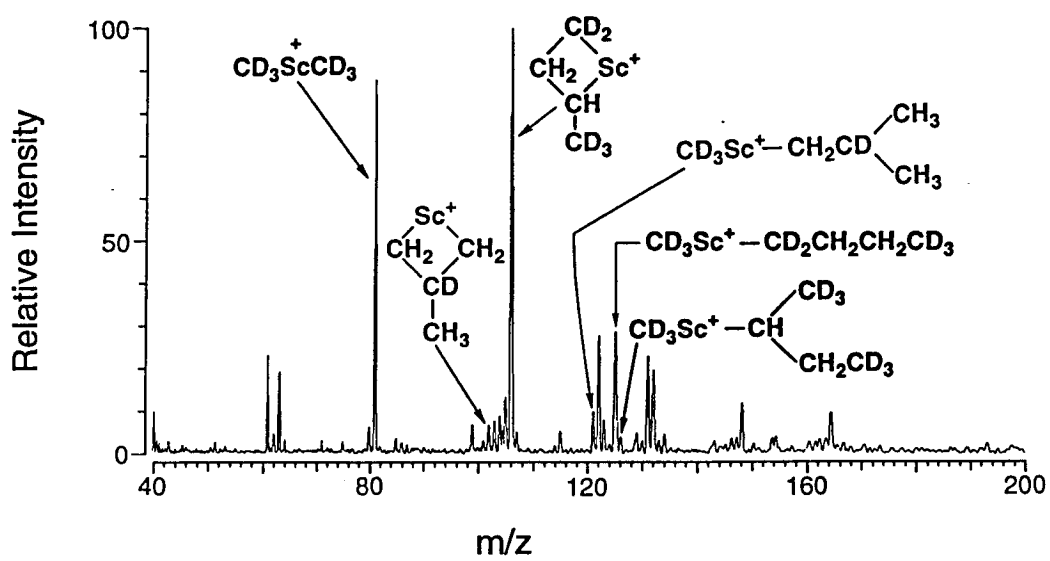
For the reaction of $\text{Sc}(\text{CD}_3)_2^+$ with labeled isobutane the total bimolecular rate constant $k = 4.3 \times 10^{-10} \text{ cm}^3 \text{ s}^{-1} \text{ molecule}^{-1}$ and the reaction efficiency k/k_{ADO} is 0.37.¹³

Discussion

With ethane, propane, *n*-butane and isobutane σ -bond metathesis reactions occur where a methyl group of $\text{Sc}(\text{CD}_3)_2^+$ is replaced by either a ethyl, propyl, *n*-butyl or isobutyl group. Indeed, in the reaction with *n*-butane and isobutane, the *n*-butyl and isobutyl groups appear to undergo a second intramolecular σ -bond metathesis reaction (reactions 8 and 10) to form four-membered metallacycles. The metathesis reactions could proceed via an oxidative addition/reductive elimination pathway or via a four-center intermediate (see Scheme 1). Again, since Sc^+ has only two valence electrons with which to form strong σ bonds,^{2,3} we favor a four-center mechanism for these metathesis reactions. The high kinetic efficiencies observed indicate low barriers for these metathesis reactions, in accordance with the predictions of Steigerwald and Goddard.¹

All of the labeled hydrocarbons we used contained hydrogen at their primary positions except the labeled *n*-butane, which was deuterated at its primary positions. Since the deuterium labels of *n*-butane could affect the measured total bimolecular rate

Figure 2. Products of reaction of $\text{Sc}(\text{CD}_3)_2^+$ with [2-D]-isobutane and [1,1,1,4,4,4-D₆]-*n*-butane. Spectrum was taken 400 ms after isolation of $\text{Sc}(\text{CD}_3)_2^+$. The main peaks above m/z 130 correspond to ScR_2^+ , R = alkyl. Peaks at m/z 61 and 63 correspond to ScO^+ and ScOH_2^+ , respectively.

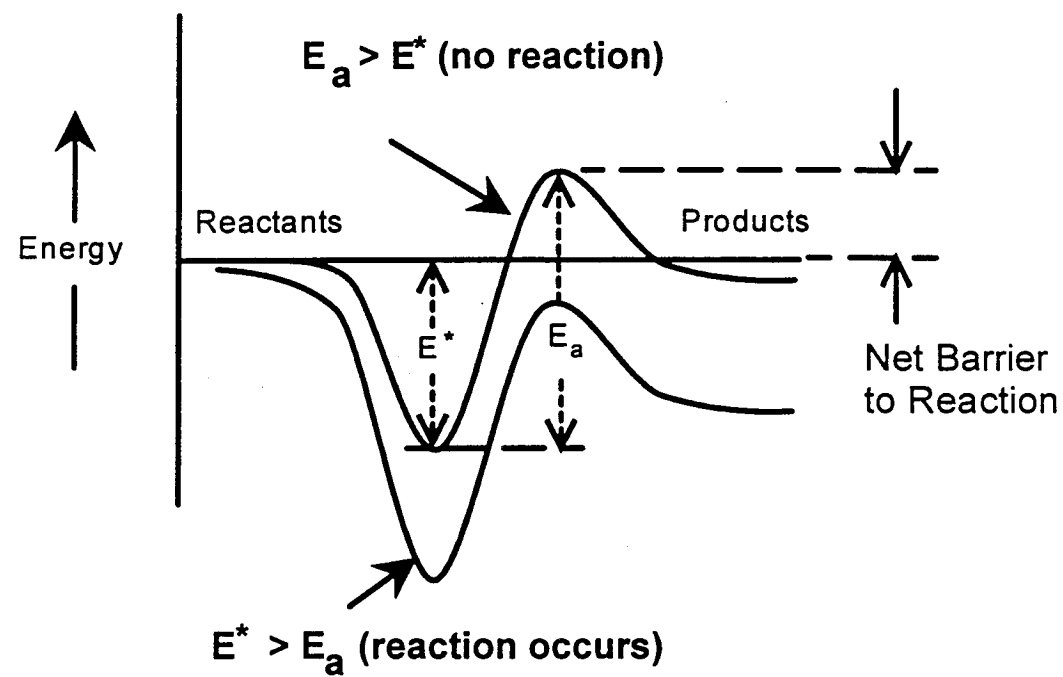


constant, we observed the reaction of $\text{Sc}(\text{CH}_3)_2^+$ with unlabeled *n*-butane to see if kinetic isotope effects were present. The total bimolecular rate constants measured for labeled and unlabeled *n*-butane were practically identical ($k_{\text{H}}/k_{\text{D}} = 0.98$). Thus we conclude that little or no isotope effect exists.

The rate constants for the reaction of $\text{Sc}(\text{CD}_3)_2^+$ with *n*-butane and isobutane are almost the same and are about 2.9 times as large as that for reaction with propane. In contrast, ethane is only a tenth as reactive as the butanes and methane is not observed to react at all with $\text{Sc}(\text{CD}_3)_2^+$. The latter observation agrees with the theoretical predictions of Perry and Goddard¹⁴ that the degenerate metathesis reaction of methane with $\text{Sc}(\text{CH}_3)_2^+$ has a net barrier of approximately 12 kcal mol⁻¹. The higher kinetic efficiencies seen for the reactions of $\text{Sc}(\text{CD}_3)_2^+$ with the butanes and propane can be accounted for by the deeper potential wells which result from the increased polarizabilities of the larger alkanes. This makes it easier to overcome the intrinsic barrier to σ -bond metathesis. These results are reminiscent of the reactions of Co^+ with hydrocarbons, where larger hydrocarbons deepen the electrostatic potential well for the Co^+ -alkane adduct, more strongly binding the alkane to Co^+ and lowering the barrier to bond insertion below the energy of the reactants^{9,15} (see Figure 3).

Site specificity was observed for the reactions of $\text{Sc}(\text{CD}_3)_2^+$ with propane, *n*-butane and isobutane (see Figures 1 and 2). For propane and *n*-butane, the initial metathesis reactions (reactions 4-7) show a marked preference for attack at primary rather than secondary C-H bonds. For isobutane the initial metathesis reaction (reaction 9) occurs *only* at primary C-H bonds. No attack is seen at the tertiary site. These are interesting results considering that secondary and tertiary C-H bonds are weaker than primary C-H bonds.¹⁶ For $\text{Sc}(\text{CH}_3)_2^+$, steric effects are not likely to be important at the uncrowded metal center, even in the four-center transition state for σ -bond metathesis. Perry and Goddard¹⁴ have recently presented a theoretical study of the reactions of

Figure 3. Schematic of a general potential energy surface showing how the initial electrostatic potential well can affect the height of a barrier relative to the energy of the reactants. Deepening the initial electrostatic well can lower the barrier to reaction below the energy of the reactants. The upper curve would be appropriate for the reaction of $\text{Sc}(\text{CD}_3)_2^+$ with methane, which is predicted to have a barrier of 12 kcal mol^{-1} (reference 14). The lower curve would correspond to the reaction with ethane, propane and the isomeric butanes.



$\text{Sc}(\text{CH}_3)_2^+$ with alkanes and found that the differences in bond strengths for $\text{Sc}^+\text{-R}$ for the series $\text{R} = \text{CH}_3, \text{C}_2\text{H}_5, i\text{-C}_3\text{H}_7$ and $t\text{-C}_4\text{H}_9$ match closely the differences in bond strengths for H-R . This suggests that the exchange reaction $\text{Sc}^+\text{-R} + \text{R}'\text{-H} \rightarrow \text{Sc}^+\text{-R}' + \text{R-H}$ should be thermoneutral for this series. However, alkyl groups larger than ethyl are able to bend around and interact with the Sc^+ center. The additional interaction or "solvation" with the alkyl group further stabilizes the Sc^+ center by about 3 kcal mol^{-1} in the case of the *n*-propyl substituent.¹⁴ This stabilization explains the observed preference for reaction at primary sites with the larger alkanes in this investigation. While reaction at the secondary position of propane is thermoneutral, reaction at the primary position is exothermic by approximately 5 kcal mol^{-1} . Reaction at primary C-H bonds may also be favored by the structure of the most stable $\text{Sc}^+\text{-alkyl}$ adduct. Perry et al. have found that the $\text{Co}^+\text{-propane}$ adduct is more stable when it exhibits η^4 coordination to the two primary carbons than when it exhibits η^2 coordination to the secondary carbon.¹⁵ $\text{Sc}(\text{CH}_3)_2^+$ may show similar behavior when it forms an adduct with propane.

Our results in this system contrast with results obtained by Weinberg and Sun,⁸ who find that in the case of propane reacting with a Pt surface attack at secondary C-H bonds is preferred over attack at primary C-H bonds. However, reactions of iridium complexes in solution⁷ and Co^+ with propane⁹ in the gas phase have shown a preference for attack at primary C-H bonds.

Though numerous examples of four-center σ -bond metathesis reactions of have been documented,⁴⁻⁷ to our knowledge the present results comprise the first example of alkanes showing such reactivity with such a comparatively simple metal complex and the first case where a larger alkyl group replaces a smaller alkyl group at the metal center. Previous studies⁴⁻⁷ used experimentally measured equilibrium constants for σ -bond metathesis reactions to evaluate relative metal-X bond strengths for a series of complexes. This method of evaluating relative metal-X bond strengths may also prove

to be useful in the present system for evaluating *absolute* Sc⁺-R bond strengths, since the absolute value of the Sc⁺-CH₃ and CH₃Sc⁺-CH₃ bond energies are known.¹⁷ It might also prove possible to extend these experiments to different series of ligands and different metals. We are currently conducting experiments in our laboratory along these lines.

Acknowledgments

We wish to thank J. K. Perry and Professor W. A. Goddard III for their theoretical work on this system. This work was supported by the National Science Foundation under grant CHE-9108318 and by a grant from AMOCO.

References

- ¹Steigerwald, M. L.; Goddard, W. A. III *J. Am. Chem. Soc.* **1984**, *106*, 308.
- ²Tolbert, M. A.; Beauchamp, J. L. *J. Am. Chem. Soc.* **1984**, *106*, 8117.
- ³Beauchamp, J. L.; van Koppen, P. A. M. *Energetics of Organometallic Species*, J. A. M. Simoes, Ed., 1992, Kluwer Academic Publishers, The Netherlands.
- ⁴(a) Thompson, M. E.; Baxter, S. M.; Bulls, A. R.; Burger, B. J.; Nolan, M. C.; Santarsiero, B. D.; Schaefer, W. P.; Bercaw, J. E. *J. Am. Chem. Soc.* **1987**, *109*, 203. (b) Huang, Y.; Hill, Y. D.; Sodupe, M.; Bauschlicher, C. W., Jr.; Freiser, B. S. *J. Am. Chem. Soc.* **1992**, *114*, 9106. (c) Bryndza, H. E.; Fong, L. K.; Paciello, R. A.; Tam, W.; Bercaw, J. E. *J. Am. Chem. Soc.* **1987**, *109*, 1444.
- ⁵Uppal, J. S.; Douglas, D. E.; Staley, R. H. *J. Am. Chem. Soc.* **1981**, *103*, 508.
- ⁶Christ, C. S.; Eyler, J. R.; Richardson, D. E. *J. Am. Chem. Soc.* **1988**, *110*, 4038.
- ⁷(a) Wax, M. J.; Stryker, J. M.; Buchanan, J. M.; Kovac, C. A.; Bergman, R. G. *J. Am. Chem. Soc.* **1984**, *106*, 1121. (b) Buchanan, J. M.; Stryker, J. M.; Bergman, R. G. *J. Am. Chem. Soc.* **1986**, *108*, 1537.
- ⁸Weinberg, W. H.; Sun, Y. *Science* **1991**, *253*, 542.
- ⁹van Koppen, P. A. M.; Brodbelt-Lustig, J.; Bowers, M. T.; Dearden, D. V.; Beauchamp, J. L.; Fisher, E. R.; Armentrout, P. B. *J. Am. Chem. Soc.* **1991**, *113*, 2359.
- ¹⁰(a) Marshall, A. G. *Acc. Chem. Res.* **1985**, *18*, 316. (b) Comisarow, M. B. *Anal. Chim. Acta.* **1985**, *178*, 1.
- ¹¹(a) Anders, L. R.; Beauchamp, J. L.; Dunbar, R. C.; Baldeschwieler, J. D. *J. Chem Phys.* **1966**, *45*, 1062.
- ¹²Comisarow, M. B.; Marshall, A. G. *Chem. Phys. Lett.* **1974**, *26*, 489.
- ¹³Collision rates are calculated using average dipole orientation (ADO) theory: Su, T.; Bowers, M. T. *Int. J. Mass Spectrom. Ion Phys.* **1973**, *12*, 347.
- ¹⁴Perry, J. K.; Goddard, W. A. III *J. Am. Chem. Soc.* **1994**, *116*, 5013.
- ¹⁵Perry, J. K.; Ohanessian, G.; Goddard, W. A. III *J. Phys. Chem.* **1993**, *97*, 5238.
- ¹⁶McMillen, D. F.; Golden, D. M. *Ann. Rev. Phys. Chem.* **1982**, *33*, 493.
- ¹⁷(a) Armentrout, P. B.; Georgiadis, R. *Polyhedron* **1988**, *7*, 1573. (b) Elkind, J. L.; Armentrout, P. B. *J. Phys. Chem.* **1987**, *91*, 2037.

Chapter 3

**GROUP AND SITE SELECTIVE σ -BOND METATHESIS REACTIONS OF
CH₃ScCH₂CH₃⁺ WITH [2,2-D₂]-PROPANE, [1,1,1,4,4,4-D₆]-*n*-BUTANE, [2-D]-
ISOBUTANE AND *n*-PENTANE**

Kevin C. Crellin, Serge Geribaldi, M. Widmer and J. L. Beauchamp

Contribution No. 9052, Arthur Amos Noyes Laboratory of Chemical Physics,
California Institute of Technology, Pasadena, CA 91125

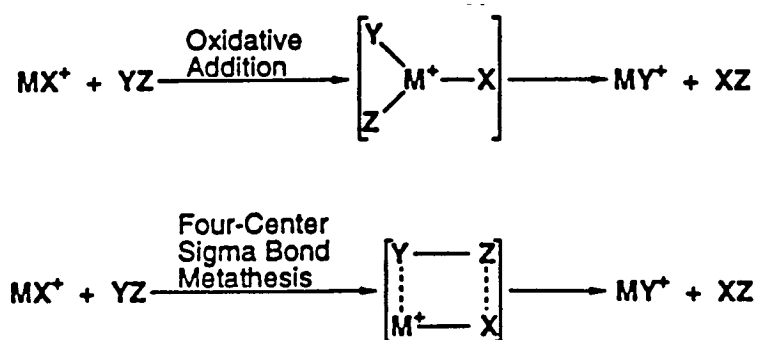
Published as an article in *Organometallics*, **1995**, *14*, 4366-4373.

Abstract

Fourier transform ion cyclotron resonance mass spectrometry has been used to examine the reactions of $\text{CH}_3\text{ScCH}_2\text{CH}_3^+$ with $[\text{D}_4]$ -methane, ethane, $[\text{2,2-D}_2]$ -propane, $[\text{1,1,1,4,4,4-D}_6]$ -*n*-butane, $[\text{2-D}]$ -isobutane, *n*-pentane and $[\text{D}_{12}]$ -*n*-pentane. $\text{CH}_3\text{ScCH}_2\text{CH}_3^+$ is not observed to react with methane or ethane but for propane, *n*-butane, isobutane and *n*-pentane σ -bond metathesis with ethane elimination is the initial and dominant reaction observed, with further dehydrogenation of the resulting products occurring as additional reaction channels. For propane, *n*-butane and isobutane no methane elimination is observed. For *n*-pentane methane elimination is a minor reaction channel. For propane, *n*-butane and isobutane the initial σ -bond metathesis involves predominantly the primary C-H bonds of the hydrocarbon. These processes are facile at room temperature and occur with little or no activation energy. Measured total bimolecular rate constants with $[\text{2,2-D}_2]$ -propane, $[\text{1,1,1,4,4,4-D}_6]$ -*n*-butane, $[\text{2-D}]$ -isobutane and *n*-pentane are 0.87×10^{-10} , 0.98×10^{-10} , 1.7×10^{-10} and $6.4 \times 10^{-10} \text{ cm}^3 \text{ s}^{-1} \text{ molecule}^{-1}$, respectively. With the butanes and pentane a second intramolecular metathesis reaction follows the initial addition to yield a metallacycle product. In accordance with earlier theoretical predictions these metathesis reactions appear to proceed via an allowed four-center mechanism similar to that of a $2\sigma + 2\sigma$ cycloaddition. The higher reactivity of the metal-ethyl bond compared to the metal-methyl bond and the observed C-H bond specificity are also in agreement with theoretical predictions.

Introduction

Previous studies in our laboratory have revealed the exceptional reactivity of $\text{Sc}(\text{CD}_3)_2^+$ with small alkanes.¹ A four-center cycloaddition mechanism was invoked for σ -bond metathesis occurring at the metal center (Scheme I), in accord with the

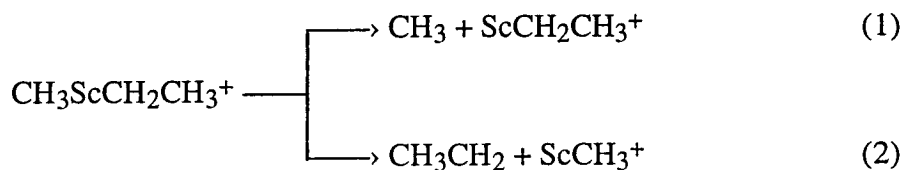


Scheme I

prediction of Steigerwald and Goddard that certain organometallic systems containing an extremely acidic (in the Lewis sense) metal center should exhibit this kind of reactivity.² These reactions of $\text{Sc}(\text{CD}_3)_2^+$ with small alkanes do not involve oxidative addition mechanisms since Sc^+ has only two valence electrons, which precludes the formation of more than two strong σ bonds.³ The reactions also exhibit a high degree of site specificity, with attack at the primary position of a small alkane favored over attack at secondary or tertiary positions.¹ This result agrees well with theoretical predictions of the enthalpies of these reactions as calculated by Perry and Goddard.⁴ Similar site specificity has also been observed for reactions of Co^+ with propane in the gas phase⁵ and for reactions of iridium complexes in solution.⁶

Though the reactivity of $\text{Sc}(\text{CD}_3)_2^+$ has been investigated, no studies have yet been done on the reactivity of mixed ligand systems such as $\text{CH}_3\text{ScCH}_2\text{CH}_3^+$. By examining the reactions of $\text{CH}_3\text{ScCH}_2\text{CH}_3^+$, we can investigate how the reactivity changes as larger ligands are introduced to the metal center. We can also attempt to elucidate the factors that favor the reactivity of one ligand over that of another ligand, and observe the effect that a second and larger ligand might have on the selectivity

previously seen in smaller systems.¹ The focus of the present work is to examine the relative reactivities of the metal-methyl and metal-ethyl bonds. Theoretical results of Perry and Goddard indicate that the Sc⁺-C bond in Sc⁺-CH₃ is approximately 5 kcal mol⁻¹ stronger than the Sc⁺-C bond in Sc⁺-CH₂CH₃.⁴ From this we can estimate that the process shown in reaction 1 should be about 5 kcal mol⁻¹ more endothermic than the



process shown in reaction 2. This suggests that the methyl and ethyl groups should behave differently for reactions of CH₃ScCH₂CH₃⁺ with small alkanes. It might also be suspected that replacement of one of the methyl groups by an ethyl group could affect the reactivity of the remaining methyl group compared to the reactivity observed for methyl groups in Sc(CD₃)₂⁺. Synergistic effects of one ligand upon another metal-ligand bond strength within the same complex have been observed in the gas phase even for linear, two-ligand metal complexes.⁷ Thus it is possible that CH₃ScCH₂CH₃⁺ may exhibit a trans influence,⁸ with the ethyl group affecting the bond energy or other properties of the remaining Sc⁺-CH₃ bond. Since Sc(CD₃)₂⁺ shows a preference for attack at the primary positions of small alkanes,¹ we have used labeled compounds to see if any site selectivity is observed in the reactions of CH₃ScCH₂CH₃⁺ with hydrocarbons. In this study we report the results of the reaction of CH₃ScCH₂CH₃⁺ with [D₄]-methane, ethane, [2,2-d₂]-propane, [1,1,1,4,4,4-d₆]-*n*-butane, [2-D]-isobutane and *n*-pentane.

Experimental

Reactions were investigated with Fourier transform ion cyclotron resonance (FT-ICR) mass spectrometry, of which a number of reviews are available.⁹ Only details relevant to these experiments are outlined here. A 1-in. cubic trapping cell is located between the poles of a Varian 15-in. electromagnet maintained at 1.0 T. Data collection

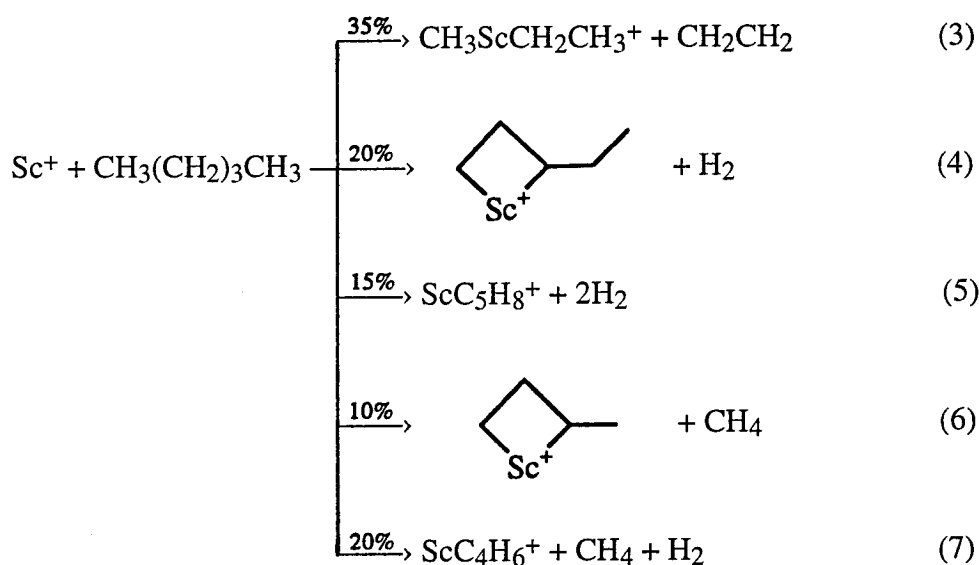
is accomplished with an IonSpec Omega 386 FT-ICR data system and associated electronics. Neutral gases are introduced into the cell by separate leak valves and their pressures are measured with a Schultz-Phelps ion gauge calibrated against an MKS 390 HA-00001SP05 capacitance manometer. Uncertainties in absolute pressures are estimated to be $\pm 20\%$. Labeled [2,2-D₂]-propane (98% D), [1,1,1,4,4,4-d₆]-*n*-butane (98% D) and [2-D]-isobutane (98% D) were obtained commercially from Merck, Sharp and Dohme. Labeled [D₄]-methane (99% D) and labeled [D₁₂]-*n*-pentane (98% D) were obtained commercially from Cambridge Isotope Laboratories. All reactant gases utilized were purified by freeze-pump-thaw cycling.

Sc⁺ ions were produced by laser ablation of a scandium metal target with a N₂ laser at 337.1 nm.^{1,10} The reactant ion was generated by reaction of Sc⁺ with *n*-pentane and unwanted ions were ejected from the cell using double resonance techniques¹¹ and/or frequency sweep excitation.¹² Reactions of isolated CH₃ScCH₂CH₃⁺ with *n*-pentane were examined first. Some experiments were performed with mixed samples of *n*-pentane and [D₁₂]-*n*-pentane in order to confirm the presence of certain structures. These mixed reagent experiments will be discussed in more detail in the results and discussion sections. The pentane pressures used in these experiments were in the range (2-3) $\times 10^{-7}$ Torr. Labeled methane, ethane, labeled propane, labeled *n*-butane or labeled isobutane were then added along with the *n*-pentane and reactions due to the additional alkane were observed. The pressure of the additional methane or ethane used was about 1×10^{-6} Torr, while the pressure of the additional alkanes larger than ethane were typically in the range (3-7) $\times 10^{-7}$ Torr. Rate constants were determined in a straightforward manner, from slopes of semilog plots of the decay of reactant ion abundance versus time and the pressure of the neutral reactant. The reported rate constants are averages of several different sets of experimental data taken at different pressures of the neutral gases. Errors are estimated to be $\pm 20\%$ due to uncertainties in absolute pressure determination. All experiments were performed at ambient

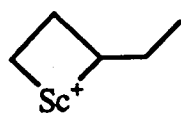
temperature. To insure accurate product distributions, all distributions given in the next section were determined at short reaction times, before any subsequent secondary reactivity could affect the observed product distribution.

Results

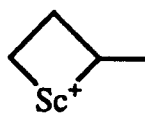
Reaction of Sc⁺ with *n*-Pentane - Generation of CH₃ScCH₂CH₃⁺. A typical mass spectrum showing the products of the reaction of Sc⁺ with *n*-pentane is presented in Figure 1a. Figure 1b shows a typical semilog plot of the decay of the Sc⁺ abundance with time and the temporal variation of product ion abundances following the isolation of Sc⁺. The initial processes observed are reactions 3-7. The metallacycle product of



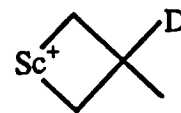
reaction 6, ion **II**, has been previously observed.^{1,3a} Studies of the reaction of Sc⁺ with labeled *n*-butane show that 1,3 dehydrogenation of the *n*-butane to form ScC₄H₈⁺ is observed, which is consistent with the formation of **II**.^{3a} In addition, the previously observed reaction of labeled isobutane with Sc(CD₃)₂⁺ leads to the formation of ion **III**, which is the only structure consistent with the observed mass peak.¹ The postulated



I



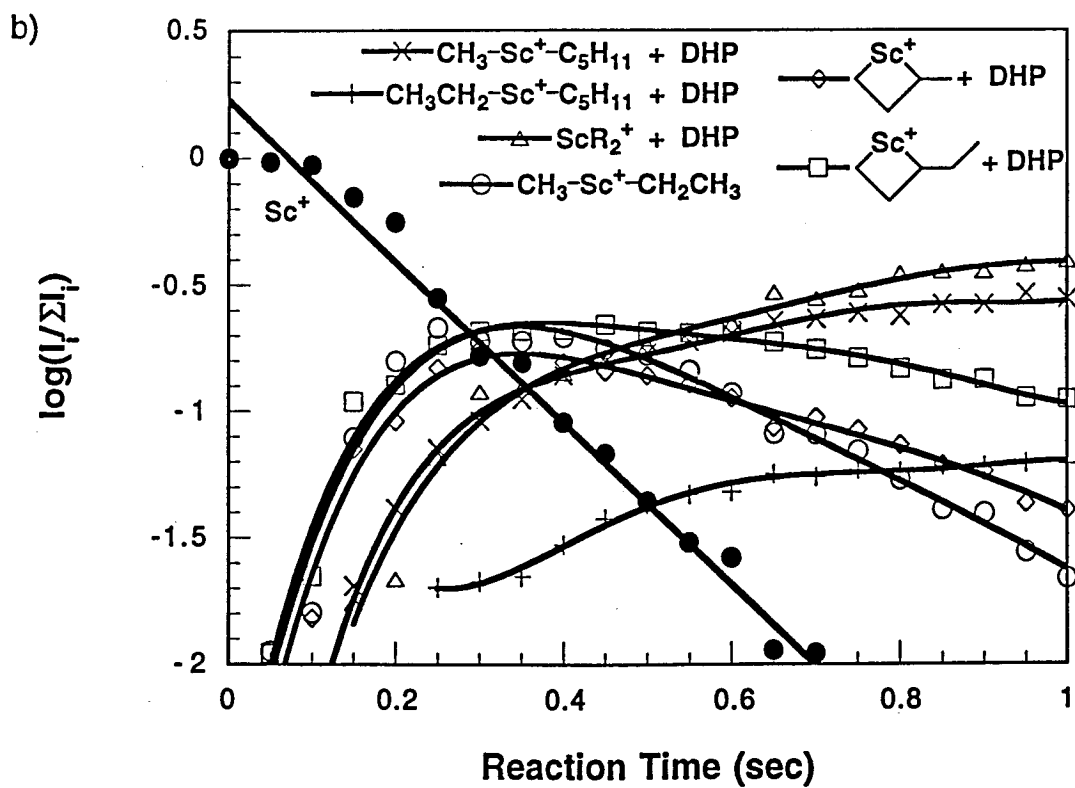
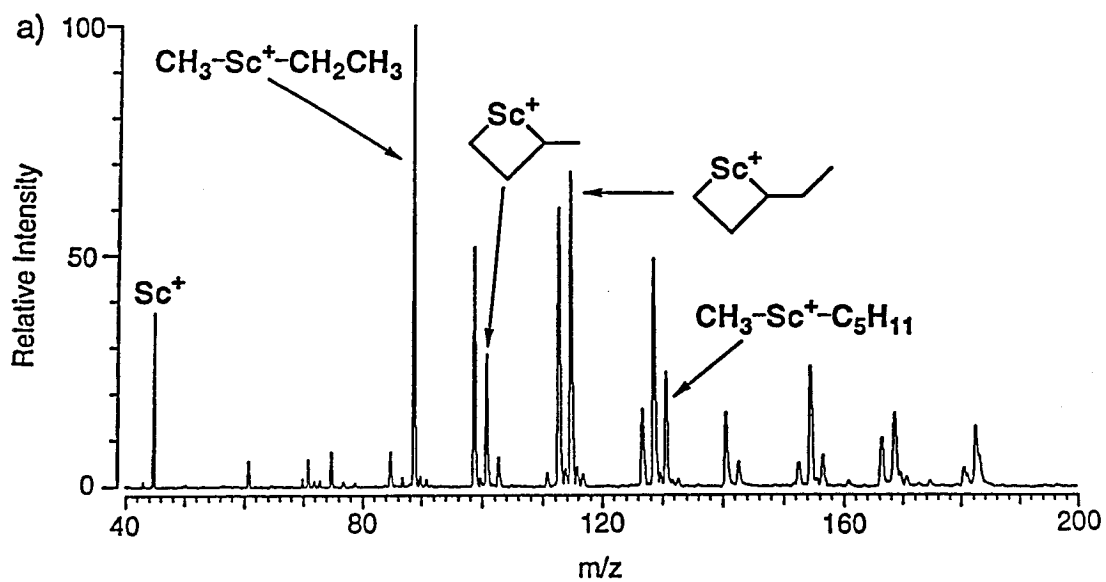
II



III

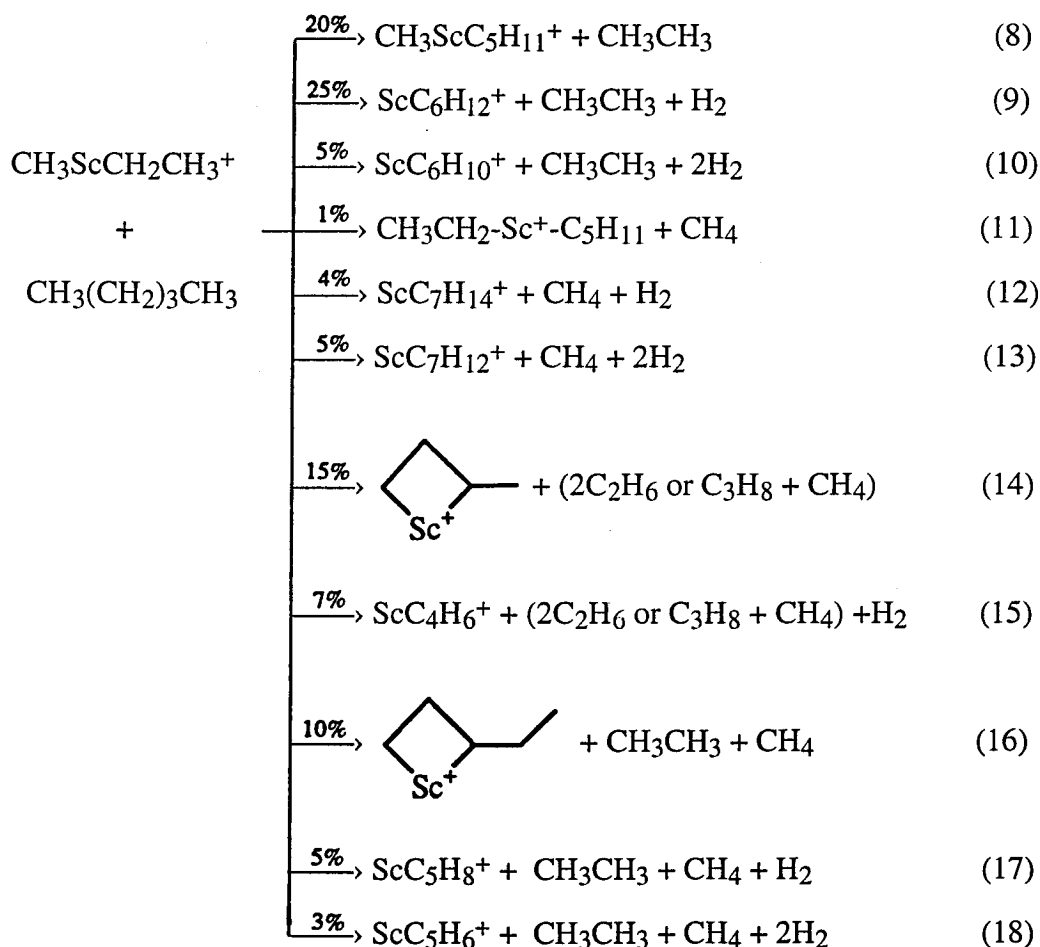
Figure 1a. Products of the reaction of Sc^+ with *n*-pentane. Spectrum was taken 450 ms after isolation of Sc^+ . Peaks at m/z 141 and 143 correspond to dehydrogenated $\text{CH}_3\text{CH}_2\text{ScC}_5\text{H}_{11}^+$. The main peaks above m/z 145 correspond to ScR_2^+ , R = alkyl. The peaks at m/z 61 and 103 correspond to ScO^+ and $\text{ScOC}_3\text{H}_6^+$, respectively. The peaks at m/z 71, 75 and 85 correspond to ScC_2H_2^+ , $\text{Sc}(\text{CH}_3)_2^+$ and $\text{CH}_3\text{ScCCH}^+$, respectively.

Figure 1b. A semilog plot of the decay of the Sc^+ abundance with time for a single experimental run. The line is a fit to the data. The constant Sc^+ abundance observed in the first 100 ms "induction period" is most likely due to translationally excited Sc^+ ions that must cool down before they can react. The temporal variation of the product ion distribution for the reaction of Sc^+ with *n*-pentane is also shown. The relative intensities of the Sc^+ -alkyl products involving *n*-pentane include the contribution from secondary dehydrogenated products which are associated with the main Sc^+ -alkyl peaks and formed by subsequent unimolecular reactions of the primary Sc^+ -alkyl products. Note the lack of deviation from linearly for the data, which suggests that little or no excited Sc^+ is present.



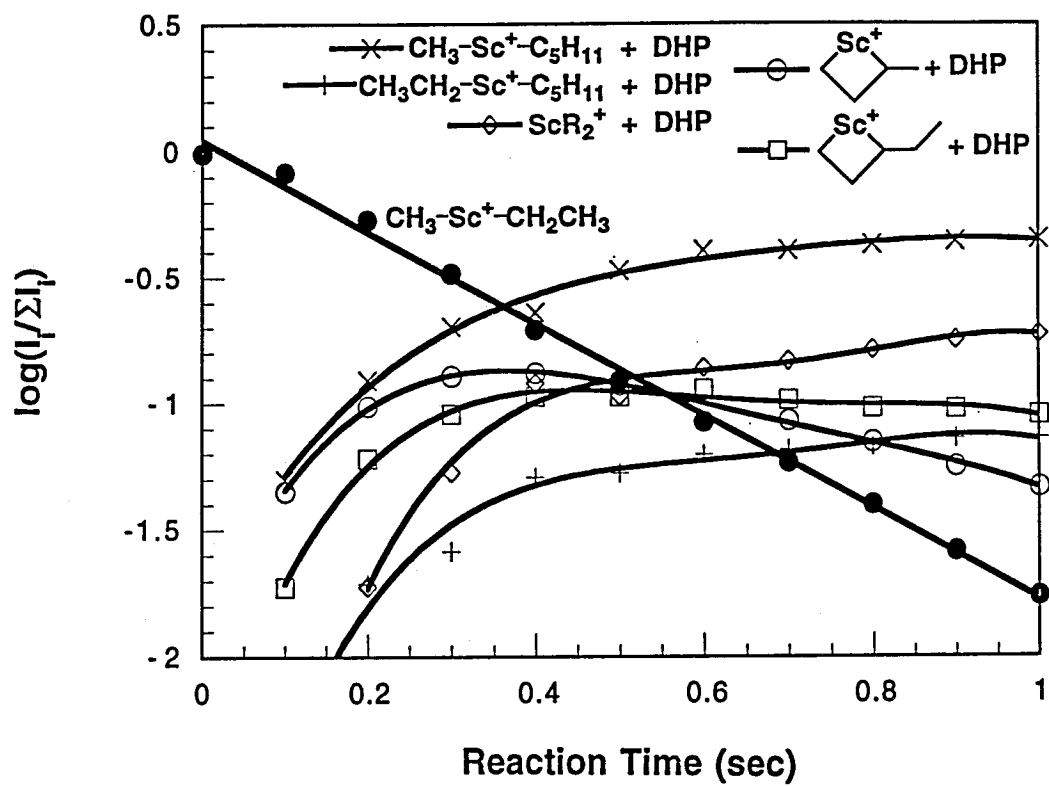
metallacycle product of reaction 4, ion I, is analogous to the metallacycle formed in reaction 6 and ion III. Reactions 5 and 7 are observed when the nascent products of reactions 4 and 6 dehydrogenate. For the reaction of Sc^+ with *n*-pentane the total bimolecular rate constant $k = 1.2 \times 10^{-9} \text{ cm}^3 \text{ s}^{-1} \text{ molecule}^{-1}$ and the reaction efficiency k/k_{ADO} is 0.85.¹³

$\text{CH}_3\text{ScCH}_2\text{CH}_3^+$ can react further with *n*-pentane as shown in reactions 8-18. A typical semilog plot of the decay of the $\text{CH}_3\text{ScCH}_2\text{CH}_3^+$ abundance with time and the temporal variation of product ion abundances following the isolation of $\text{CH}_3\text{ScCH}_2\text{CH}_3^+$ is shown in Figure 2. It is postulated that reaction 16 occurs when the



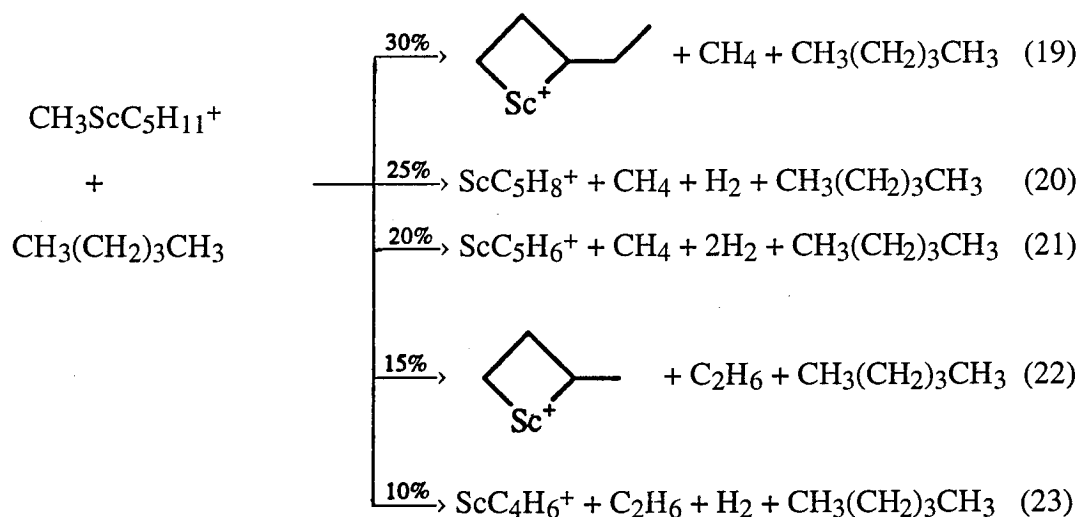
vibrationally excited products of reactions 8 or 11 have enough energy for a second intramolecular metathesis reaction, resulting in the observed metallacycle product. The neutral products of reactions 14 and 15 are uncertain. Reactions 9, 10, 12, 13, 15, 17 and

Figure 2. A semilog plot of the decay of the $\text{CH}_3\text{ScCH}_2\text{CH}_3^+$ abundance with time for a single experimental run. The line is a fit to the data. The temporal variation of the product ion distribution for the reaction of $\text{CH}_3\text{ScCH}_2\text{CH}_3^+$ with *n*-pentane is also shown. The relative intensities of the Sc^+ -alkyl products involving *n*-pentane include the contribution from secondary dehydrogenated products which are associated with the main Sc^+ -alkyl peaks and formed by subsequent unimolecular reactions of the primary Sc^+ -alkyl products. Note the lack of deviation from linearly for the data, which suggests that little or no excited $\text{CH}_3\text{ScCH}_2\text{CH}_3^+$ is present.



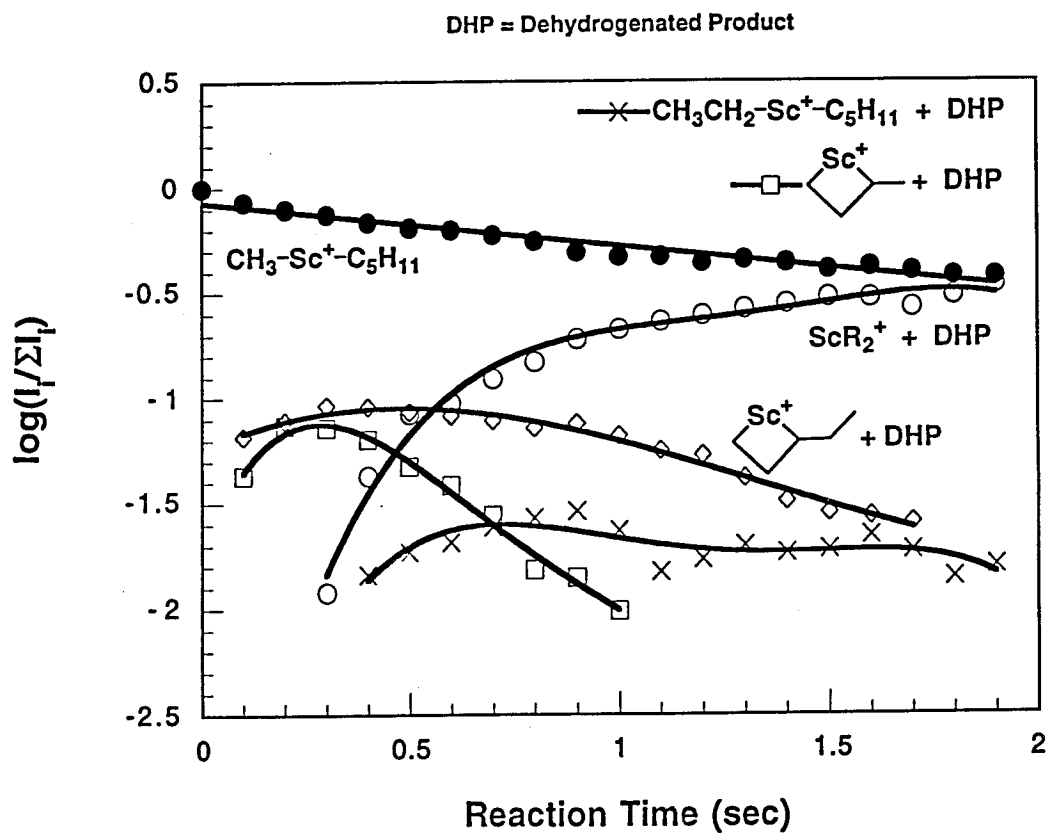
18 are observed when the nascent products of reactions 8, 11, 14 and 16 dehydrogenate. The reaction of $\text{CH}_3\text{ScCH}_2\text{CH}_3^+$ with *n*-pentane will be discussed in more detail in the next section.

Since $\text{CH}_3\text{ScC}_5\text{H}_{11}^+$ is the predominant product of the reaction of $\text{CH}_3\text{ScCH}_2\text{CH}_3^+$ with *n*-pentane, it was also isolated so that its reactivity with *n*-pentane could be examined. A semilog plot of the temporal variation of ion abundances following the isolation of $\text{CH}_3\text{ScC}_5\text{H}_{11}^+$ is shown in Figure 3. Reactions 19-23 are the initial processes observed, and it appears that adduct formation with the neutral *n*-pentane generates enough energy to either collisionally or chemically activate the $\text{CH}_3\text{ScC}_5\text{H}_{11}^+$ ion. This strongly suggests that $\text{CH}_3\text{ScC}_5\text{H}_{11}^+$ is in fact a precursor to



the metallacycle species and supports our postulate that the metallacycle of reaction 16 results from vibrationally excited $\text{CH}_3\text{ScC}_5\text{H}_{11}^+$ ions. At longer reaction times the abundance of both metallacycle products decrease and the formation of ScC_nH_m^+ products with $n \geq 7$ and $m \geq 12$ is observed. Reactions 20, 21 and 23 are observed when the nascent products of reactions 19 and 22 dehydrogenate. For the reaction of $\text{CH}_3\text{ScC}_5\text{H}_{11}^+$ with *n*-pentane the total bimolecular rate constant $k = 1.6 \times 10^{-10} \text{ cm}^3\text{s}^{-1} \text{ molecule}^{-1}$ and the reaction efficiency k/k_{ADO} is 0.15.¹³

Figure 3. A semilog plot of the decay of the $\text{CH}_3\text{ScC}_5\text{H}_{11}^+$ abundance with time for a single experimental run. The line is fit to the data. The temporal variation of the product ion distribution for the reaction of $\text{CH}_3\text{ScC}_5\text{H}_{11}^+$ with *n*-pentane is also shown. The relative intensities of the Sc^+ -alkyl products involving *n*-pentane include the contribution from secondary dehydrogenated products which are associated with the main Sc^+ -alkyl peaks and formed by subsequent unimolecular reactions of the primary Sc^+ -alkyl products.

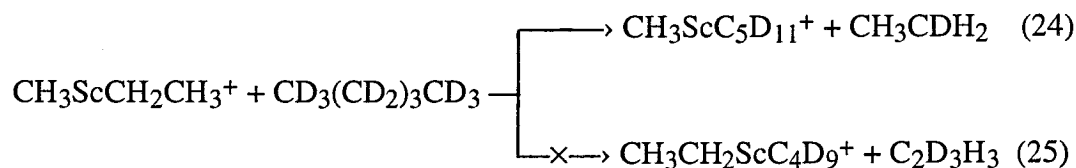


Reaction 3 was utilized to generate the $\text{CH}_3\text{ScCH}_2\text{CH}_3^+$ ion, which was then isolated as shown in Figure 4a for further study of its reactivity.

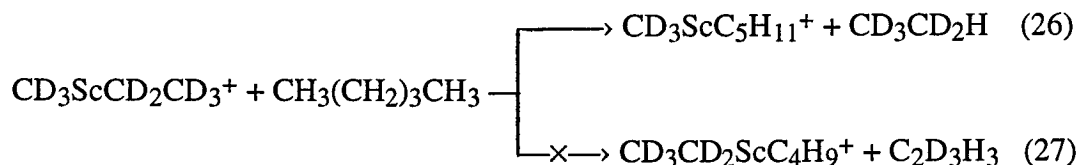
Reaction of $\text{CH}_3\text{ScCH}_2\text{CH}_3^+$ with *n*-Pentane - Elucidation of Structures.

Reactions 8-18 are observed with *n*-pentane (see Figures 2 and 4b). Single and multiple loss of hydrogen is observed from all the nascent products of reactions 8, 11, 14 and 16. For the reaction of $\text{CH}_3\text{ScCH}_2\text{CH}_3^+$ with *n*-pentane the total bimolecular rate constant $k = 6.4 \times 10^{-10} \text{ cm}^3\text{s}^{-1} \text{ molecule}^{-1}$ and the reaction efficiency k/k_{ADO} is 0.55.¹³ In order to determine if an isotope effect is present we also observed the reaction of $\text{CD}_3\text{ScCD}_2\text{CD}_3^+$ with $[\text{D}_{12}]$ -*n*-pentane. The reaction with labeled *n*-pentane shows the same product distribution as in the unlabeled case, and the total bimolecular rate constant $k = 6.5 \times 10^{-10} \text{ cm}^3\text{s}^{-1} \text{ molecule}^{-1}$ and the reaction efficiency k/k_{ADO} is 0.56.¹³

Reactions of $\text{CH}_3\text{ScCH}_2\text{CH}_3^+$ and $\text{CD}_3\text{ScCD}_2\text{CD}_3^+$ with *n*-pentane/ $[\text{D}_{12}]$ -*n*-pentane mixtures were also observed to provide corroborating evidence that the major product is in fact $\text{CH}_3\text{ScC}_5\text{H}_{11}^+$ and not $\text{CH}_3\text{CH}_2\text{ScC}_4\text{H}_9^+$, both of which have the same mass. When $\text{CH}_3\text{ScCH}_2\text{CH}_3^+$ was isolated and reacted with labeled *n*-pentane, only reaction 24 was observed. Reaction 25 was not seen (Figure 5a). Analogously, when



$\text{CD}_3\text{ScCD}_2\text{CD}_3^+$ was isolated and reacted with unlabeled *n*-pentane, only reaction 26



was observed. Reaction 27 did not occur (Figure 5b). These observations support our assertion that the major product of the reaction between $\text{CH}_3\text{ScCH}_2\text{CH}_3^+$ and *n*-pentane is $\text{CH}_3\text{ScC}_5\text{H}_{11}^+$.

Figure 4a. Demonstration of our ability to isolate the $\text{CH}_3\text{ScCH}_2\text{CH}_3^+$ ion from unwanted products of the reaction of Sc^+ with *n*-pentane. Spectrum was taken 400 ms after generation of Sc^+ .

Figure 4b. Products of the reaction of $\text{CH}_3\text{ScCH}_2\text{CH}_3^+$ with *n*-pentane. Spectrum was taken 400 ms after the isolation of $\text{CH}_3\text{ScCH}_2\text{CH}_3^+$. Peaks at m/z 141 and 143 correspond to dehydrogenated $\text{CH}_3\text{CH}_2\text{ScC}_5\text{H}_{11}^+$. The main peaks above m/z 145 correspond to ScR_2^+ , R = alkyl. The peaks at m/z 61 and 103 correspond to ScO^+ and $\text{ScOC}_3\text{H}_6^+$, respectively. The peaks at m/z 71, 75 and 85 correspond to ScC_2H_2^+ , $\text{Sc}(\text{CH}_3)_2^+$ and $\text{CH}_3\text{ScCCH}^+$, respectively.

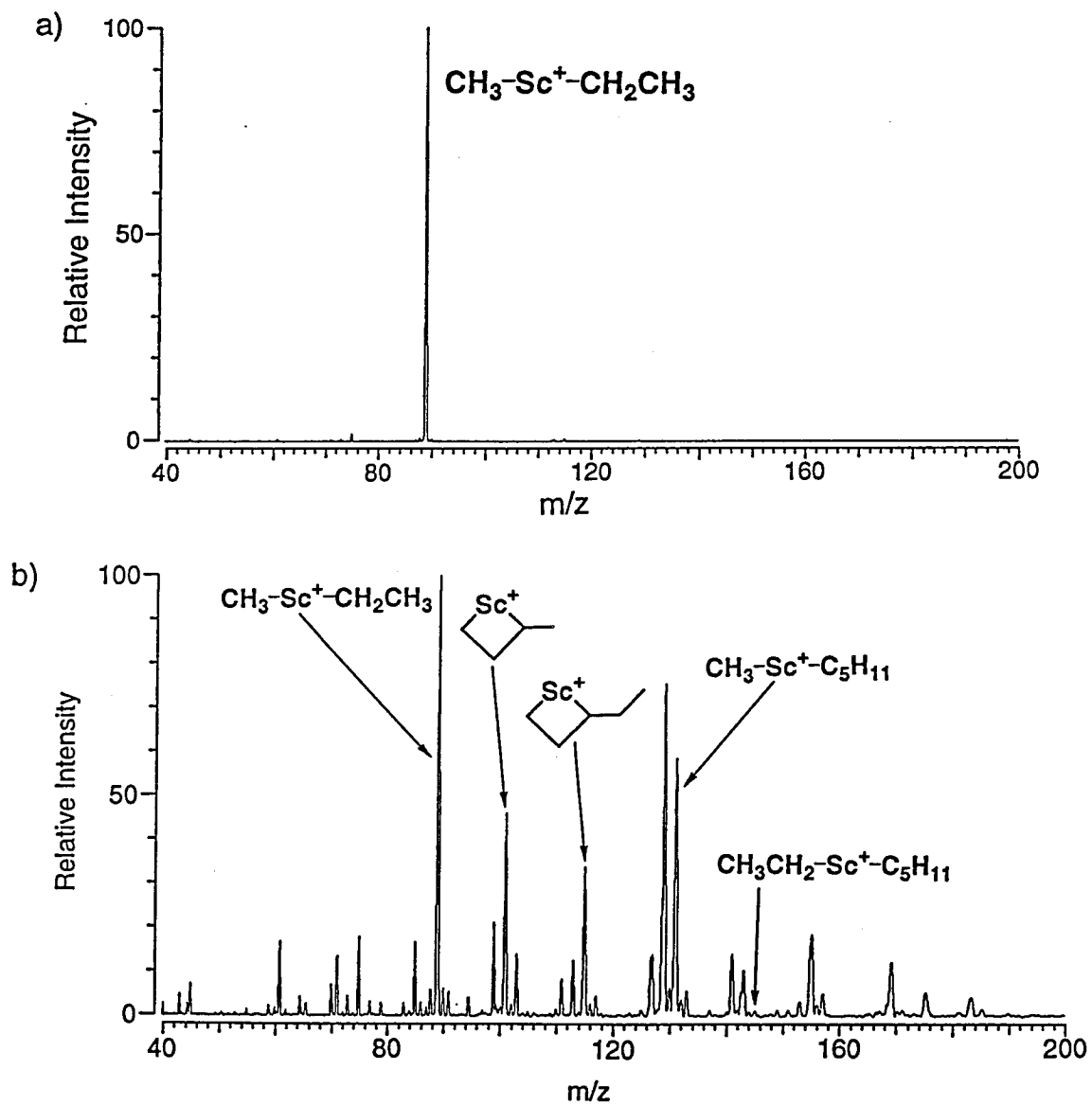
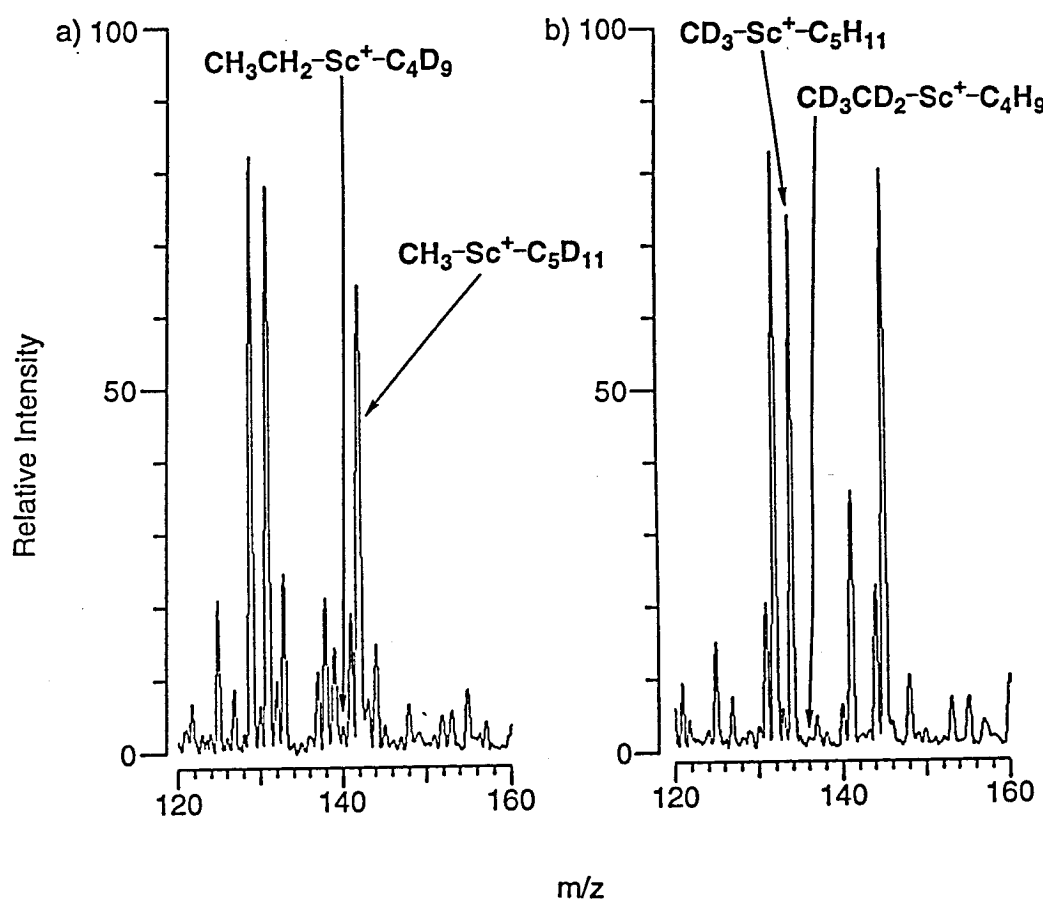


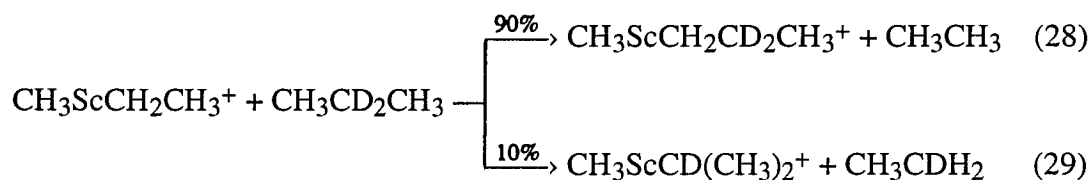
Figure 5a. Products of the reaction of $\text{CH}_3\text{ScCH}_2\text{CH}_3^+$ with a mixture of *n*-pentane and $[\text{D}_{12}]$ -*n*-pentane between m/z 120 and 160. Spectrum was taken 600 ms after the isolation of $\text{CH}_3\text{ScCH}_2\text{CH}_3^+$. Note the absence of any $\text{CH}_3\text{CH}_2\text{ScC}_4\text{D}_9^+$ product.

Figure 5b. Products of the reaction of $\text{CD}_3\text{ScCD}_2\text{CD}_3^+$ with a mixture of *n*-pentane and $[\text{D}_{12}]$ -*n*-pentane between m/z 120 and 160. Spectrum was taken 700 ms after the isolation of $\text{CD}_3\text{ScCD}_2\text{CD}_3^+$. Note the absence of any $\text{CD}_3\text{CD}_2\text{ScC}_4\text{H}_9^+$ product.



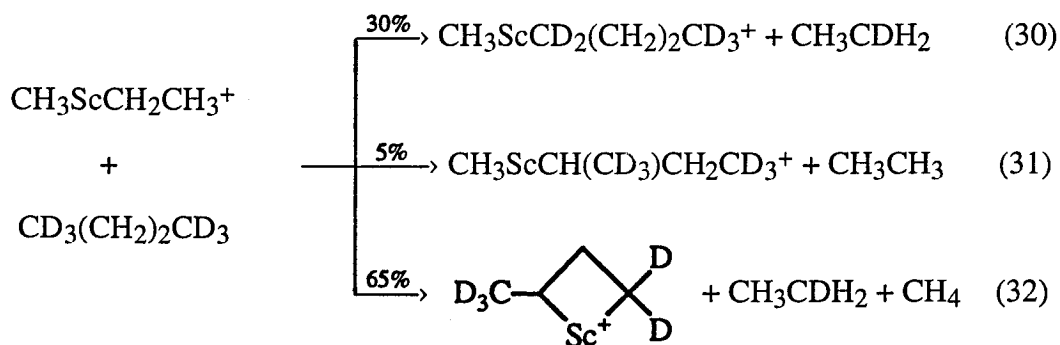
Reaction of $\text{CH}_3\text{ScCH}_2\text{CH}_3^+$ with Methane and Ethane. The possible exchange reactions of $\text{CH}_3\text{ScCH}_2\text{CH}_3^+$ with CD_4 were not observed. We estimate that for the reaction of $\text{CH}_3\text{ScCH}_2\text{CH}_3^+$ with methane the total bimolecular rate constant $k \leq 1 \times 10^{-12} \text{ cm}^3\text{s}^{-1}\text{molecule}^{-1}$. The possible exchange reactions of $\text{CD}_3\text{ScCD}_2\text{CD}_3^+$ with CH_3CH_3 were also not observed. Labeled *n*-pentane was used since we did not possess labeled ethane. We estimate that for the reaction of $\text{CD}_3\text{ScCD}_2\text{CD}_3^+$ with ethane the total bimolecular rate constant is less than $1 \times 10^{-12} \text{ cm}^3\text{s}^{-1}\text{molecule}^{-1}$.

Reaction of $\text{CH}_3\text{ScCH}_2\text{CH}_3^+$ with Propane. Reactions 28 and 29 were observed



with labeled propane (see Figure 6a), but reactions in which the methyl group instead of the ethyl group was exchanged were not observed. For the reaction of $\text{CH}_3\text{ScCH}_2\text{CH}_3^+$ with labeled propane the total bimolecular rate constant $k = 0.87 \times 10^{-10} \text{ cm}^3\text{s}^{-1}\text{molecule}^{-1}$ and the reaction efficiency $k/k_{\text{ADO}} = 0.08$.¹³

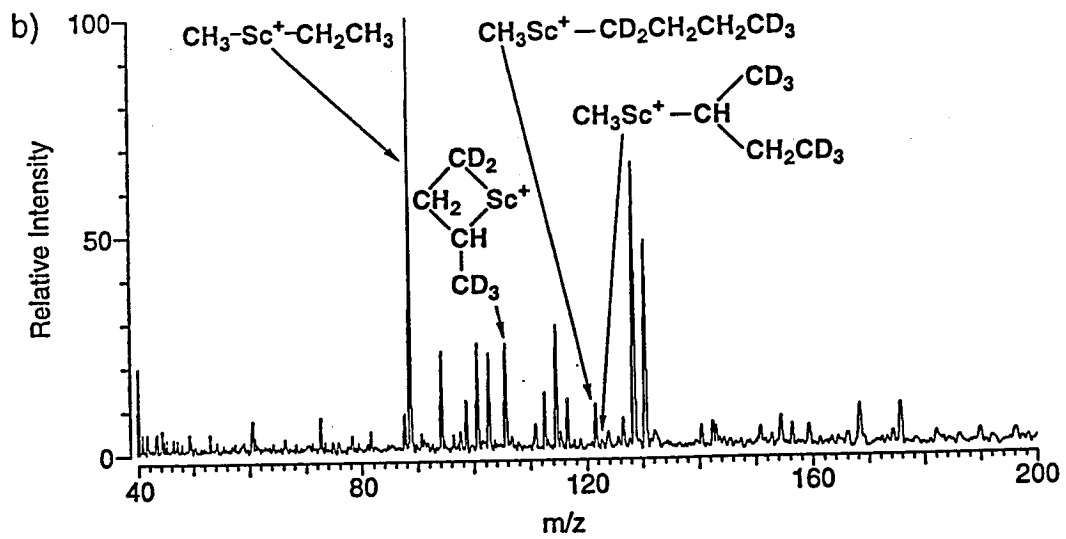
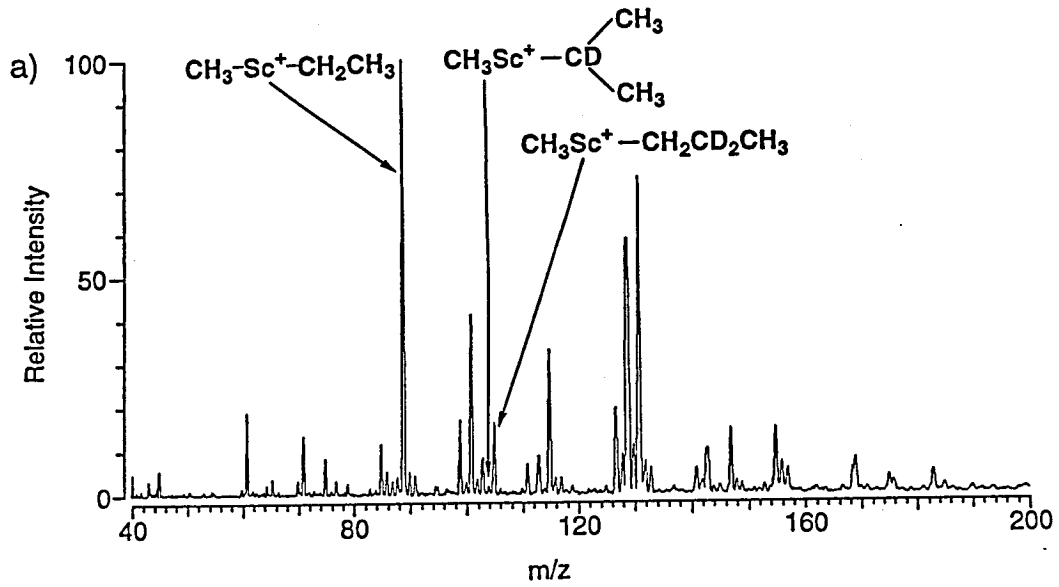
Reaction of $\text{CH}_3\text{ScCH}_2\text{CH}_3^+$ with *n*-Butane. Reactions 30-32 were observed



with labeled *n*-butane (see Figure 6b). Methyl exchange reactions were not seen. It is postulated that reaction 32 occurs when the vibrationally excited product of reaction 30 or 31 has enough energy for a second intramolecular metathesis reaction, resulting in the metallacycle product. It should be noted that the labeling of the hydrocarbon products shown in reaction 32 assumes that the initial metathesis occurs as shown in reaction 30.

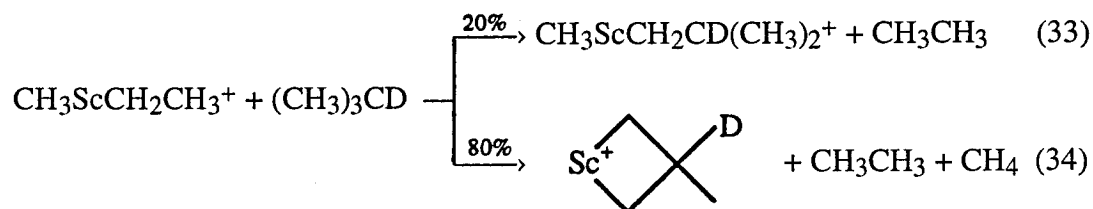
Figure 6a. Products of the reaction of $\text{CH}_3\text{ScCH}_2\text{CH}_3^+$ with [2,2-D₂]-propane. Spectrum was taken 250 ms after the isolation of $\text{CH}_3\text{ScCH}_2\text{CH}_3^+$. The main peaks above m/z 125 correspond to ScR_2^+ , R = alkyl. The peak at m/z 61 corresponds to ScO^+ . The peaks at m/z 71, 75 and 85 correspond to ScC_2H_2^+ , $\text{Sc}(\text{CH}_3)_2^+$ and $\text{CH}_3\text{ScCCH}^+$, respectively.

Figure 6b. Products of the reaction of $\text{CH}_3\text{ScCH}_2\text{CH}_3^+$ with [1,1,1,4,4,4-D₆]-*n*-butane. Spectrum was taken 250 ms after the isolation of $\text{CH}_3\text{ScCH}_2\text{CH}_3^+$. The main peaks above m/z 125 correspond to ScR_2^+ , R = alkyl. The peaks at m/z 61 and 73 correspond to ScO^+ and ScC_2H_4^+ , respectively.



However, since reaction 31 is also observed as a minor reaction pathway, hydrocarbon products with the opposite labeling are also present but in significantly smaller quantities. For the reaction of $\text{CH}_3\text{ScCH}_2\text{CH}_3^+$ with labeled *n*-butane the total bimolecular rate constant $k = 0.98 \times 10^{-10} \text{ cm}^3\text{s}^{-1}\text{molecule}^{-1}$ and the reaction efficiency $k/k_{\text{ADO}} = 0.09$.¹³

Reaction of $\text{CH}_3\text{ScCH}_2\text{CH}_3^+$ with Isobutane. Reactions 33 and 34 were observed



with labeled isobutane (see Figure 6c). No reactivity is observed at the tertiary site of isobutane. Reaction 34 occurs when the vibrationally excited product of reaction 33 has enough energy for a second intramolecular metathesis reaction to yield the metallacycle product. For the reaction of $\text{CH}_3\text{ScCH}_2\text{CH}_3^+$ with labeled isobutane the total bimolecular rate constant $k = 1.7 \times 10^{-10} \text{ cm}^3\text{s}^{-1}\text{molecule}^{-1}$ and the reaction efficiency $k/k_{\text{ADO}} = 0.15$.¹³

Discussion

Reaction of $\text{CH}_3\text{ScCH}_2\text{CH}_3^+$ with Small Alkanes. *Overview.* Table 1 summarizes the observed reactivity of $\text{CH}_3\text{ScCH}_2\text{CH}_3^+$ with the small alkanes examined in this study. Only the initial reaction observed with each alkane is noted in this summary of our results. With propane, *n*-butane, isobutane and *n*-pentane σ -bond metathesis reactions occur where an ethyl group of $\text{CH}_3\text{ScCH}_2\text{CH}_3^+$ is replaced by either a *n*-propyl, *n*-butyl, isobutyl or *n*-pentyl group. Reaction efficiencies range from approximately 0.1 for propane to 0.55 for *n*-pentane. Methyl group replacement was observed only for the reaction of $\text{CH}_3\text{ScCH}_2\text{CH}_3^+$ with *n*-pentane, and even in this case methyl group replacement was only responsible for 10% of the reactivity (Table 1). In the reaction with *n*-butane, isobutane and *n*-pentane the *n*-butyl, isobutyl and *n*-pentyl

Figure 6c. Products of the reaction of $\text{CH}_3\text{ScCH}_2\text{CH}_3^+$ with [2-D]-isobutane. Spectrum was taken 250 ms after the isolation of $\text{CH}_3\text{ScCH}_2\text{CH}_3^+$. The main peaks above m/z 125 correspond to ScR_2^+ , R = alkyl. The peak at m/z 61 corresponds to ScO^+ . The peaks at m/z 71 and 75 correspond to ScC_2H_2^+ and $\text{Sc}(\text{CH}_3)_2^+$, respectively.

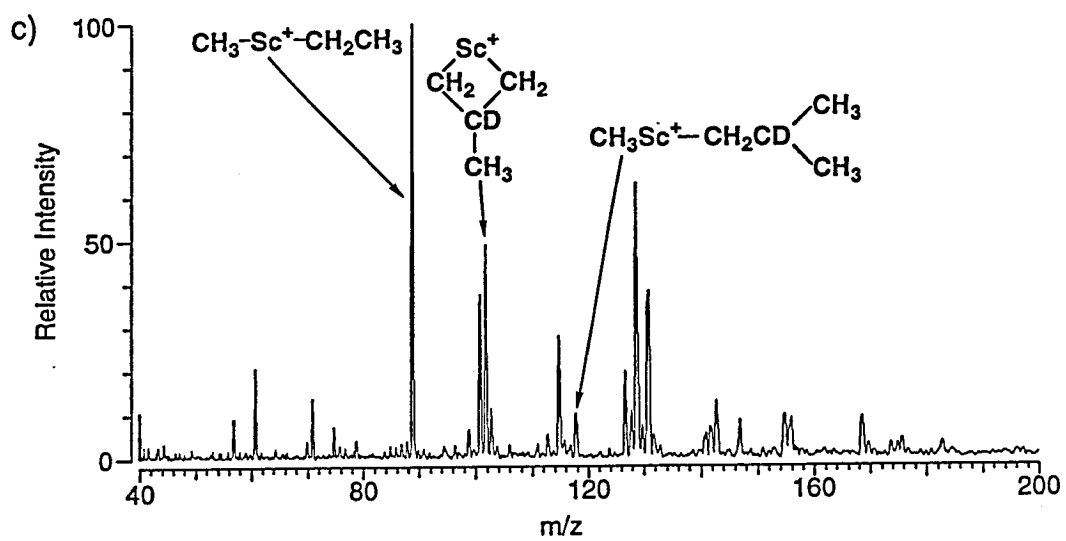


Table 1. Summary of the Observed Reactivity of $\text{CH}_3\text{ScCH}_2\text{CH}_3^+$ with the Small Alkanes Examined in this Study.^a

Process	Total Rates ($\text{cm}^3 \text{ molecule}^{-1} \text{ s}^{-1}$)	Reaction Efficiency k/k_{coll}
methane \longrightarrow no reaction	$< 10^{-12}$	< 0.001
ethane \longrightarrow no reaction	$< 10^{-12}$	< 0.001
propane \longrightarrow $\text{CH}_3\text{-Sc}^+(\text{CH}_2)_2\text{CH}_3 + \text{C}_2\text{H}_6$	9×10^{-11}	0.09
$\text{CH}_3\text{-Sc}^+\text{-CH}_2\text{CH}_3 +$ n-butane \longrightarrow $\text{CH}_3\text{-Sc}^+(\text{CH}_2)_3\text{CH}_3 + \text{C}_2\text{H}_6$	1×10^{-10}	0.10
isobutane \longrightarrow $\text{CH}_3\text{-Sc}^+\text{-CH}_2\text{CH}(\text{CH}_3)_2 + \text{C}_2\text{H}_6$	2×10^{-10}	0.20
n-pentane $\begin{array}{l} \xrightarrow{90\%} \text{CH}_3\text{-Sc}^+(\text{CH}_2)_4\text{CH}_3 + \text{C}_2\text{H}_6 \\ \xrightarrow{10\%} \text{CH}_3\text{CH}_2\text{-Sc}^+(\text{CH}_2)_4\text{CH}_3 + \text{CH}_4 \end{array}$	6×10^{-10}	0.60

^a Only the initial reaction observed with each alkane is noted in the table.

groups undergo a second intramolecular σ -bond metathesis reaction (reactions 14, 16, 32 and 34) to form four-membered metallacycles. Similar reactivity was seen for the reaction of $\text{Sc}(\text{CD}_3)_2^+$ with *n*-butane and isobutane.¹ These metathesis reactions could proceed via an oxidative addition/reductive elimination pathway or via a four-center intermediate (see Scheme I). Again, since Sc^+ only has two valence electrons with which to form strong σ bonds,³ we favor a four-center mechanism for these metathesis reactions.

Since the labeled hydrocarbons contained deuterium, it was possible that kinetic isotope effects would be present. Thus we examined the reaction of $\text{CD}_3\text{ScCD}_2\text{CD}_3^+$ with $[\text{D}_{12}]$ -*n*-pentane so that we could observe any possible kinetic isotope effects. The total bimolecular rate constants measured with *n*-pentane and $[\text{D}_{12}]$ -*n*-pentane were practically identical ($k_{\text{H}}/k_{\text{D}} = 0.98$). The product distributions observed with *n*-pentane and $[\text{D}_{12}]$ -*n*-pentane were also indistinguishable. Thus we conclude that isotope effects are unimportant in this system, even though the reaction is not occurring at the collision limit. This result is not surprising, since $\text{Sc}(\text{CD}_3)_2^+$ also exhibited no isotope effects in its reactions with small alkanes.¹

When $\text{CH}_3\text{ScCH}_2\text{CH}_3^+$ was reacted with *n*-pentane we expected the major product to be $\text{CH}_3\text{ScC}_5\text{H}_{11}^+$. However, it was possible that this product could actually be $\text{CH}_3\text{CH}_2\text{ScC}_4\text{H}_9^+$, which has the same mass as $\text{CH}_3\text{ScC}_5\text{H}_{11}^+$. To discount this possibility, we performed experiments in which $\text{CH}_3\text{ScCH}_2\text{CH}_3^+$ or $\text{CD}_3\text{ScCD}_2\text{CD}_3^+$ were reacted with *n*-pentane/ $[\text{D}_{12}]$ -*n*-pentane mixtures. Regardless of whether $\text{CH}_3\text{ScCH}_2\text{CH}_3^+$ or $\text{CD}_3\text{ScCD}_2\text{CD}_3^+$ was the reactant ion, only mass peaks corresponding to $\text{CH}_3\text{ScC}_5\text{D}_{11}^+$ or $\text{CD}_3\text{ScC}_5\text{H}_{11}^+$ were seen. No peaks corresponding to $\text{CH}_3\text{CH}_2\text{ScC}_4\text{D}_9^+$ or $\text{CD}_3\text{CD}_2\text{ScC}_4\text{H}_9^+$ were observed (Figure 5). In addition to showing that $\text{CH}_3\text{ScC}_5\text{H}_{11}^+$ is the major product of the reaction of $\text{CH}_3\text{ScCH}_2\text{CH}_3^+$ with *n*-pentane, these results also provide evidence that the ion product of reaction 3 is $\text{CH}_3\text{ScCH}_2\text{CH}_3^+$ and not an isomer such as the $\text{Sc}(\text{C}_3\text{H}_8)^+$ adduct.

Group Specificity. Group specificity was observed in the reactions of $\text{CH}_3\text{ScCH}_2\text{CH}_3^+$ with propane, *n*-butane, isobutane and *n*-pentane. For propane, *n*-butane and isobutane the initial metathesis reactions (reactions 28-31 and 33) exhibit *only* ethyl exchange. No methyl exchange is seen in the initial metathesis reactions. For *n*-pentane the initial metathesis process (reactions 8 and 11) exhibits mostly ethyl exchange. 10% or less of the initial metathesis process is due to methyl exchange for *n*-pentane. From these observations it is apparent that ethyl exchange is *much* more favorable than methyl exchange with every alkane we examined.

To explain these observations, we first note that Perry and Goddard⁴ have performed theoretical calculations which predict that the $\text{Sc}^+\text{-CH}_3$ bond is about 5 kcal mol⁻¹ stronger than the $\text{Sc}^+\text{-CH}_2\text{CH}_3$ bond. Thus, even though the H-CH_3 bond is about 4 kcal mol⁻¹ stronger than the $\text{H-CH}_2\text{CH}_3$ bond,¹⁴ overall it is still energetically more favorable (by 1 kcal mol⁻¹) to exchange an ethyl group than a methyl group (see Table 2). A larger difference probably characterizes the activation energies for the competitive processes, however, since in the transition state the weaker metal carbon bond is probably being ruptured prior to formation of the stronger C-H bond in the products. This is illustrated in Figure 7 for propane. In addition, ethane has a stronger electrostatic interaction than methane with Sc^+ due to its larger polarizability. Thus losing ethane rather than methane should give rise to a deeper potential energy well in the exit channel. This may also lower the energy of the transition state for this process, as shown in Figure 7. These effects conspire to make the loss of ethane more favorable than the loss of methane.

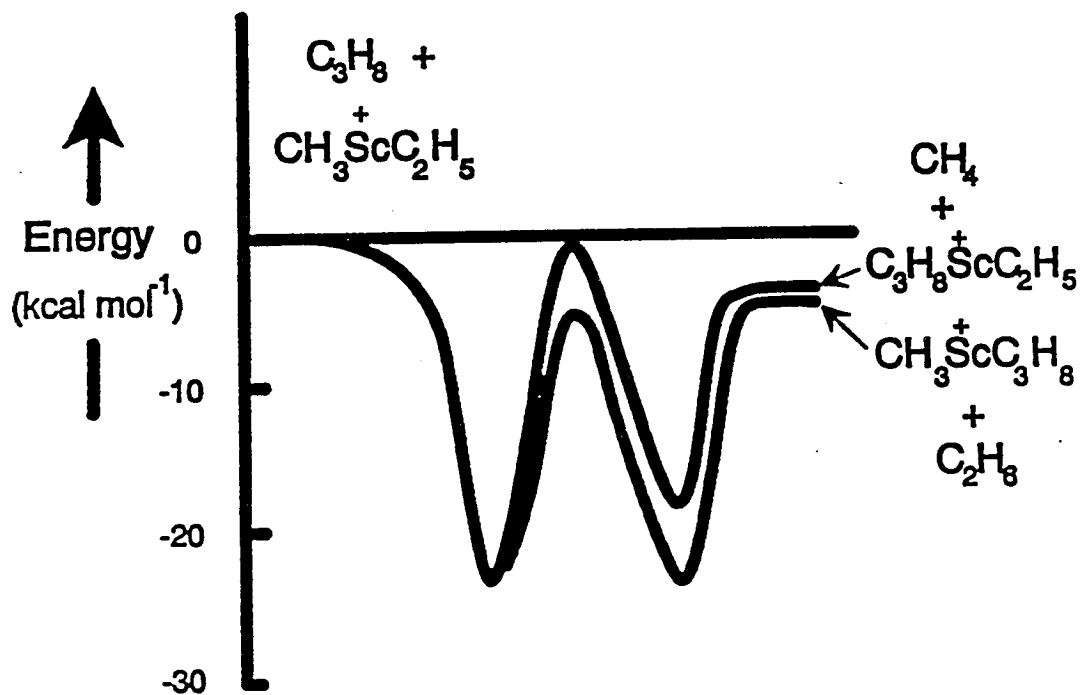
In the case of propane, *n*-butane and isobutane it appears that the electrostatic potential wells are deep enough to lower the energy of the transition state for loss of ethane below the energy of the reactants but not deep enough to lower the energy of the transition state for methane loss below the energy of the reactants. Thus there is a net barrier to the loss of methane, but no barrier to the loss of ethane. This is why no methyl

Table 2. Predicted Reaction Enthalpy^{a,b} for the σ -Bond Metathesis Reaction $\text{Sc}^+-\text{R} + \text{R}'-\text{H} \rightarrow \text{Sc}^+-\text{R}' + \text{R}-\text{H}$.

R	R' = CH ₃	C ₂ H ₅	n-C ₃ H ₇	i-C ₃ H ₇	t-C ₄ H ₉
CH ₃	0.0	1.0	-4.2	1.9	2.2
C ₂ H ₅	-1.0	0.0	-5.2	0.9	1.2
n-C ₃ H ₇	4.2	5.2	0.0	6.1	6.4
i-C ₃ H ₇	-1.9	-0.9	-6.1	0.0	0.3
t-C ₄ H ₉	-2.2	-1.2	-6.4	-0.3	0.0

^aIn kcal mol⁻¹. ^bData from reference 4.

Figure 7. Schematic of a general potential energy surface showing how the nature of the ligand being lost can affect the electrostatic potential wells present. Note that the stronger electrostatic interaction of ethane with Sc^+ and the fact that the $\text{Sc}^+\text{-CH}_2\text{CH}_3$ bond energy is about 5 kcal mol^{-1} less than the $\text{Sc}^+\text{-CH}_3$ bond energy lowers the potential energy curve for the formation of ethane below the curve for the formation of methane. Both effects conspire to make loss of the ethyl group much more favorable than loss of the methyl group.



exchange is observed for the reaction of $\text{CH}_3\text{ScCH}_2\text{CH}_3^+$ with propane and the isomeric butanes. On the other hand, *n*-pentane has a higher polarizability¹⁵ than either propane¹⁶ or the isomeric butanes.¹⁷ Thus the initial electrostatic potential energy well formed with *n*-pentane is deeper than with propane or the isomeric butanes. This lowers the energy of the transition state for methane loss enough that it is below the energy of the reactants when *n*-pentane is the neutral reactant. However, the energy of the transition state for ethane loss is still lower than that for methane loss, so that ethane loss is still the major process observed. These observations support the prediction of Perry and Goddard⁴ that the $\text{Sc}^+\text{-CH}_2\text{CH}_3$ bond is weaker than the $\text{Sc}^+\text{-CH}_3$ bond.

Site Specificity. In addition to group specificity, site specificity was also observed for the reactions of $\text{CH}_3\text{ScCH}_2\text{CH}_3^+$ with propane, *n*-butane and isobutane (see Figure 6). For propane and *n*-butane the initial metathesis reactions (reactions 28-31) show a marked preference for attack at primary rather than secondary C-H bonds. For isobutane the initial metathesis reaction (reaction 33) occurs only at primary C-H bonds. No attack is seen at the tertiary site.

These results are identical to those observed with $\text{Sc}(\text{CD}_3)_2^+$,¹ and these results are again counterintuitive considering that secondary and tertiary C-H bonds are weaker than primary C-H bonds.¹⁴ However, Perry and Goddard's⁴ recent theoretical study of $\text{Sc}^+\text{-C}$ bond strengths in $\text{Sc}\text{-alkyl}^+$ species has found that the differences in bond strengths of $\text{Sc}^+\text{-R}$ for the series $\text{R} = \text{CH}_3, \text{C}_2\text{H}_5, i\text{-C}_3\text{H}_7$ and $t\text{-C}_4\text{H}_9$ match closely the differences in bond strengths for H-R . This would suggest that the exchange reaction $\text{Sc}^+\text{-R} + \text{R}'\text{-H} \rightarrow \text{Sc}^+\text{-R}' + \text{R-H}$ should be thermoneutral for this series, but alkyl groups larger than ethyl are able to bend around and interact with the Sc^+ center. This additional interaction or "solvation" with an alkyl group can further stabilize the Sc^+ center. For example, the *n*-propyl substituent further stabilizes the Sc^+ center by about 3 kcal mol⁻¹ with this additional "solvation."⁴ This stabilization, which should be present in the transition state for the reactions as well, explains the observed preference

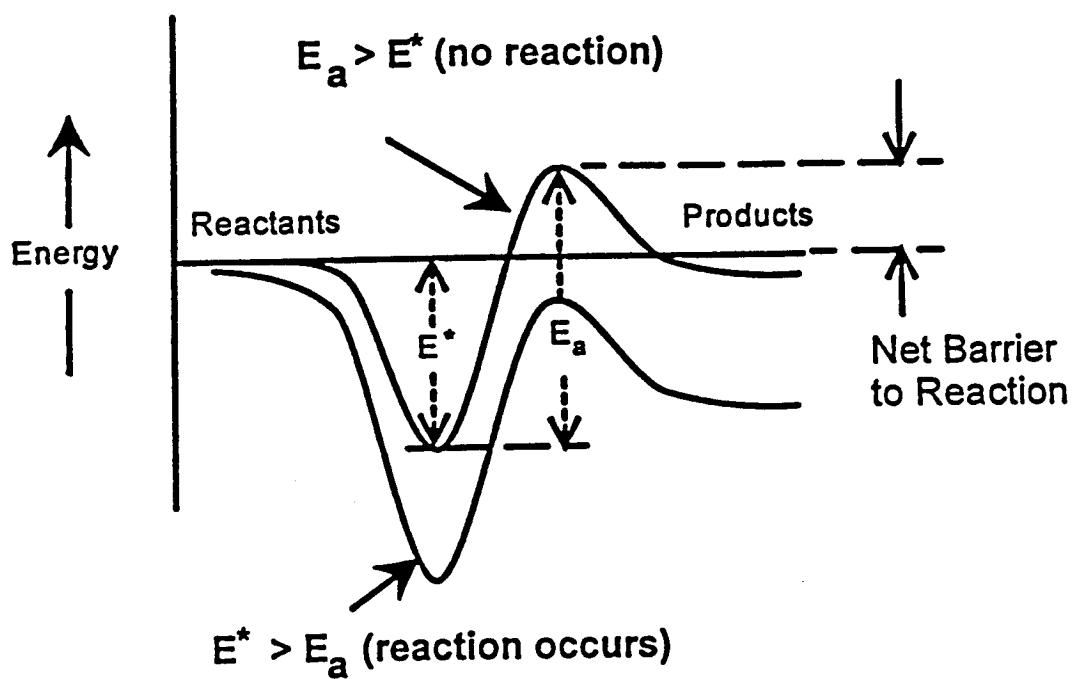
exhibited by $\text{CH}_3\text{ScCH}_2\text{CH}_3^+$ for reaction at primary sites with the larger alkanes in this study.

Reaction at primary C-H bonds may also be favored by the structure of the most stable Sc^+ -alkyl adduct. Perry et al. have found that the Co^+ -propane adduct is more stable when it exhibits η^4 coordination to the two primary carbons than when it exhibits η^2 coordination to the secondary carbon.¹⁸ $\text{CH}_3\text{ScCH}_2\text{CH}_3^+$ may show similar behavior when it forms an adduct with propane.

Our results in this system contrast with results obtained by Weinberg and Sun,¹⁹ who found that in the case of propane reacting with a Pt surface attack at secondary C-H bonds is preferred over attack at primary C-H bonds. However, reactions of iridium complexes in solution,⁶ Co^+ with propane in the gas phase⁵ and $\text{Sc}(\text{CD}_3)_2^+$ with small alkanes in the gas phase¹ have shown a preference for attack at primary C-H bonds.

Overall Reaction Efficiencies. The largest rate constant we observed was for the reaction of $\text{CH}_3\text{ScCH}_2\text{CH}_3^+$ with *n*-pentane. The rate constant for reaction with pentane was about 3.8 times larger than that for reaction with isobutane, while the rate constant for reaction with isobutane was about 1.7 times larger than that for reaction with *n*-butane and about 2.0 times larger than that for reaction with propane. Ethane and methane are not observed to react at all with $\text{CH}_3\text{ScCH}_2\text{CH}_3^+$. This trend is analogous to the trend seen with $\text{Sc}(\text{CD}_3)_2^+$.¹ The increase in reaction efficiency seen as the alkane reacting with $\text{CH}_3\text{ScCH}_2\text{CH}_3^+$ increases in size can be accounted for by the deeper potential wells which result from the increased polarizabilities of the larger alkanes. This makes it easier to overcome the intrinsic barrier to σ -bond metathesis (Figure 8). These results are reminiscent of the reactions of Co^+ with hydrocarbons, where larger hydrocarbons deepen the electrostatic potential well for the Co^+ -alkane adduct, more strongly binding the alkane to Co^+ and providing more energy for chemical activation.^{5,18}

Figure 8. Schematic of a general potential energy surface showing how the initial electrostatic potential well can affect the height of a barrier relative to the energy of the reactants. Deepening the initial electrostatic well can lower the barrier to reaction below the energy of the reactants. The upper curve would be appropriate for the reaction of $\text{CH}_3\text{ScCH}_2\text{CH}_3^+$ with methane or ethane. The lower curve would be appropriate for the reaction of $\text{CH}_3\text{ScCH}_2\text{CH}_3^+$ with propane, the isomeric butanes or *n*-pentane.



Furthermore, the kinetic efficiencies observed for $\text{CH}_3\text{ScCH}_2\text{CH}_3^+$ reacting with propane, *n*-butane and isobutane are lower than for $\text{Sc}(\text{CD}_3)_2^+$ reacting with the same alkanes.¹ This observation suggests that, compared to the energy of the reactants, the energy of the transition state for the reaction of $\text{CH}_3\text{ScCH}_2\text{CH}_3^+$ with propane, *n*-butane or isobutane is higher than the energy of the transition state for the reaction of $\text{Sc}(\text{CD}_3)_2^+$ with the same alkane. This effect could be due to extra steric interactions introduced by the larger ethyl group or a possible trans effect⁸ of the methyl and ethyl groups upon each other's bond strength with Sc^+ . Similar synergistic effects in two-ligand gas-phase metal-ion complexes have been previously observed.⁷ The group specificity observed in the reactions of $\text{CH}_3\text{ScCH}_2\text{CH}_3^+$ with propane, *n*-butane, isobutane and *n*-pentane is another example of how the replacement of one methyl group with an ethyl group synergistically affects the reactivity of the remaining methyl group compared to the reactivity observed for methyl groups in $\text{Sc}(\text{CD}_3)_2^+$.

The observation that ethane and methane do not react with $\text{CH}_3\text{ScCH}_2\text{CH}_3^+$ appears to be in accordance with the theoretical prediction of Perry and Goddard⁴ that the degenerate metathesis reaction of methane with $\text{Sc}(\text{CH}_3)_2^+$ has a net barrier of about 12 kcal mol⁻¹. Table 2 shows the theoretical values calculated by Perry and Goddard for several metathesis reactions involving small alkanes. Even though methyl and ethyl exchange reactions with both $\text{CH}_3\text{ScCH}_2\text{CH}_3^+$ and $\text{Sc}(\text{CD}_3)_2^+$ are calculated to be approximately thermoneutral, $\text{CH}_3\text{ScCH}_2\text{CH}_3^+$ does not react with either methane or ethane, and $\text{Sc}(\text{CD}_3)_2^+$ does not react with methane,¹ providing experimental support for the presence of an overall barrier to these reactions. In these cases, the energy of the transition state is apparently higher than the energy of the reactants (upper curve of Figure 8). However, both $\text{CH}_3\text{ScCH}_2\text{CH}_3^+$ and $\text{Sc}(\text{CD}_3)_2^+$ react with alkanes larger than ethane. In these cases the energy of the transition state is below the energy of the reactants so that no net barrier to reaction exists, as shown by the lower curve in Figure

8. Our observation that both $\text{CH}_3\text{ScCH}_2\text{CH}_3^+$ and $\text{Sc}(\text{CD}_3)_2^+$ react with alkanes larger than ethane is in accordance with the prediction of Steigerwald and Goddard.²

Reaction of Sc^+ and *n*-Pentane and Reaction of Subsequent Product Ions with *n*-Pentane. The reaction of Sc^+ with *n*-pentane produced a complex mixture of products. At long times many high mass $\text{R}'\text{ScR}^+$ products, where R and R' are alkyl groups, were observed. In order to determine which ions were the precursors of these species, various product ions of the reaction of Sc^+ with *n*-pentane were isolated and allowed to react in turn with *n*-pentane. $\text{CH}_3\text{ScCH}_2\text{CH}_3^+$ reacted with *n*-pentane to produce mostly $\text{CH}_3\text{ScC}_5\text{H}_{11}^+$, $\text{CH}_3\text{CH}_2\text{ScC}_5\text{H}_{11}^+$, **I**, **II** and small amounts of $\text{R}'\text{ScR}^+$ products of higher mass which result from subsequent reactions of the main product ions. $\text{CH}_3\text{ScC}_5\text{H}_{11}^+$ also reacted with *n*-pentane to produce mostly $\text{R}'\text{ScR}^+$ where R and R' are larger than ethyl. What is of interest here is that $\text{CH}_3\text{ScCH}_2\text{CH}_3^+$ reacted with *n*-pentane via a σ -bond metathesis involving only C-H bond activation, as was seen previously for the reaction of $\text{Sc}(\text{CD}_3)_2^+$ with small alkanes.¹ The reaction of $\text{CH}_3\text{ScCH}_2\text{CH}_3^+$ with alkanes smaller than *n*-pentane, as observed in this study, also involved only C-H bond activation. But the fact that $\text{CH}_3\text{ScC}_5\text{H}_{11}^+$ can produce $\text{R}'\text{ScR}^+$ where either R or R' is not a pentyl group and the fact that **II** can be formed from $\text{CH}_3\text{ScC}_5\text{H}_{11}^+$ seems to suggest that some intermolecular and intramolecular C-C bond activation is occurring.

Observation of the reaction of $\text{CH}_3\text{ScC}_5\text{H}_{11}^+$ with *n*-pentane also provided us with direct evidence that intramolecular σ -bond metathesis does occur. **I** and **II** were both observed to form from isolated $\text{CH}_3\text{ScC}_5\text{H}_{11}^+$. These products could only be observed if intramolecular σ -bond metathesis were occurring. This supports our postulate that excited CH_3ScR^+ ions, where R = *n*-butyl, isobutyl or pentyl, can perform a second intramolecular σ -bond metathesis reaction to form metallacyclic products.

Acknowledgments

We wish to thank J. K. Perry and Professor W. A. Goddard III for their theoretical work on this system.⁴ This work was supported by the National Science Foundation under grant CHE-9108318 and by a grant from AMOCO.

References

- ¹Crellin, K. C.; Geribaldi, S.; Beauchamp, J. L. *Organometallics* **1994**, *13*, 3733.
- ²Steigerwald, M. L.; Goddard, W. A. III *J. Am. Chem. Soc.* **1984**, *106*, 308.
- ³(a) Tolbert, M. A.; Beauchamp, J. L. *J. Am. Chem. Soc.* **1984**, *106*, 8117. (b) Beauchamp, J. L.; van Koppen, P. A. M. *Energetics of Organometallic Species*, J. A. M. Simoes, Ed., 1992, Kluwer Academic Publishers, The Netherlands.
- ⁴Perry, J. K.; Goddard, W. A. III *J. Am. Chem. Soc.* **1994**, *116*, 5013.
- ⁵van Koppen, P. A. M.; Brodbelt-Lustig, J.; Bowers, M. T.; Dearden, D. V.; Beauchamp, J. L.; Fisher, E. R.; Armentrout, P. B. *J. Am. Chem. Soc.* **1991**, *113*, 2359.
- ⁶(a) Wax, M. J.; Stryker, J. M.; Buchanan, J. M.; Kovac, C. A.; Bergman, R. G. *J. Am. Chem. Soc.* **1984**, *106*, 1121. (b) Buchanan, J. M.; Stryker, J. M.; Bergman, R. G. *J. Am. Chem. Soc.* **1986**, *108*, 1537.
- ⁷Kappes, M. M.; Jones, R. W.; Staley, R. H. *J. Am. Chem. Soc.* **1982**, *104*, 888.
- ⁸(a) Huheey, J. E. *Inorganic Chemistry*, 3rd ed., 1983, Harper and Row, New York, Chapter 11. (b) Hartley, F. R. *Chem. Soc. Rev.* **1973**, *2*, 163. (c) Appleton, T. G.; Clark, H. C.; Manzer, L. E. *Coord. Chem. Rev.* **1973**, *10*, 335.
- ⁹(a) Marshall, A. G. *Acc. Chem. Res.* **1985**, *18*, 316. (b) Comisarow, M. B. *Anal. Chim. Acta.* **1985**, *178*, 1.
- ¹⁰(a) Azzaro, M.; Breton, S.; Decouzon, M.; Geribaldi, S. *Int. J. Mass Spectrom. Ion Proc.* **1993**, *128*, 1. (b) Cody, R. B.; Burnier, R. C.; Reents, W. D., Jr.; Carlin, T. J.; McCrery, D. A.; Lengel, R. K.; Freiser, B. S. *Int. J. Mass Spectrom. Ion Phys.* **1980**, *33*, 37.
- ¹¹Anders, L. R.; Beauchamp, J. L.; Dunbar, R. C.; Baldeschwieler, J. D. *J. Chem. Phys.* **1966**, *45*, 1062.
- ¹²Comisarow, M. B.; Marshall, A. G. *Chem. Phys. Lett.* **1974**, *26*, 489.
- ¹³Collision rates are calculated using average dipole orientation (ADO) theory: Su, T.; Bowers, M. T. *Int. J. Mass Spectrom. Ion Phys.* **1973**, *12*, 347.
- ¹⁴McMillan, D. F.; Golden, D. M. *Ann. Rev. Phys. Chem.* **1982**, *33*, 493.
- ¹⁵For *n*-pentane $\alpha = 9.99 \text{ \AA}^3$: Maryott, A. A.; Buckley, F. *U. S. National Bureau of Standards Circular No. 537*, 1953.
- ¹⁶For propane $\alpha = 6.29 \text{ \AA}^3$: Maryott, A. A.; Buckley, F. *U. S. National Bureau of Standards Circular No. 537*, 1953.

¹⁷For *n*-butane $\alpha = 8.20 \text{ \AA}^3$: Maryott, A. A.; Buckley, F. *U. S. National Bureau of Standards Circular No. 537*, 1953.

¹⁸Perry, J. K.; Ohanessian, G.; Goddard, W. A. III *J. Phys. Chem.* **1993**, *97*, 5238.

¹⁹Weinberg, W. H.; Sun, Y. *Science* **1991**, *253*, 542.

Chapter 4

σ -BOND METATHESIS REACTIONS OF $\text{Sc}(\text{CH}_3)_2^+$ WITH SECONDARY C-H BONDS: REACTIVITY WITH CYCLOHEXANE AND CYCLOPENTANE

Kevin C. Crellin and J. L. Beauchamp

Arthur Amos Noyes Laboratory of Chemical Physics, California Institute of Technology, Pasadena, CA 91125

S. Geribaldi and M. Decouzon

Laboratoire de Chimie Physique Organique, Groupe FT-ICR, Université de Nice-Sophia Antipolis, Faculté des Sciences, Parc Valrose, 06108 Nice Cedex 2, France

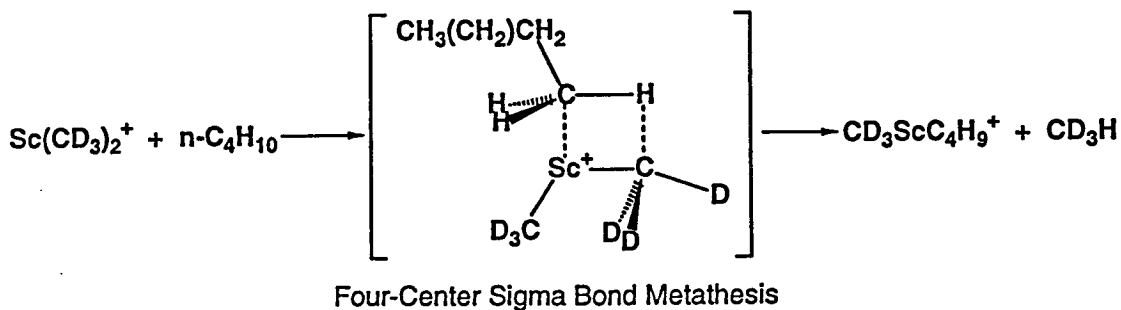
Published as an article in *Organometallics*, 1996, 15, 5368-5373.

Abstract

Fourier transform ion cyclotron resonance mass spectrometry has been used to examine the σ -bond metathesis reactions of $\text{Sc}(\text{CH}_3)_2^+$ with the secondary C-H bonds of cyclohexane and cyclopentane. Methane elimination, accompanied by further dehydrogenation, is the initial and dominant reaction observed. These processes are facile at room temperature and involve little or no activation energy. Measured total bimolecular rate constants for the reaction of $\text{Sc}(\text{CH}_3)_2^+$ with cyclohexane and cyclopentane are 6.2×10^{-10} and $5.1 \times 10^{-10} \text{ cm}^3 \text{ s}^{-1} \text{ molecule}^{-1}$, respectively. The total bimolecular rate constant for the reaction of $\text{Sc}(\text{CD}_3)_2^+$ with cyclohexane is measured to be $6.6 \times 10^{-10} \text{ cm}^3 \text{ s}^{-1} \text{ molecule}^{-1}$. In accordance with earlier theoretical predictions these metathesis reactions appear to proceed via an allowed four-center mechanism similar to that of a $2\sigma + 2\sigma$ cycloaddition. The observed gas-phase reactivity is also compared to the liquid-phase reactivity of similar complexes and the implications are discussed.

Introduction

Previous studies have observed σ -bond metathesis reactions for a variety of transition metal systems¹⁻⁴, including scandium.⁵ Exceptional reactivity has also been observed between $\text{Sc}(\text{CD}_3)_2^+$ and small alkanes in our laboratory.⁶ In these gas-phase reactions a four-center mechanism was invoked for metathesis reactions occurring at the metal center (see Scheme I), in accord with the prediction of Steigerwald and Goddard



Scheme I

that certain organometallic species containing an extremely acidic (in the Lewis sense) metal center should exhibit this kind of reactivity.⁷ These metathesis reactions exhibited a high degree of site selectivity, with activation of the primary C-H bonds of a hydrocarbon being strongly favored relative to activation of the secondary and tertiary C-H bonds.⁶ Similar positional reactivity has been observed in other studies.^{4,5a,8,9}

Recent theoretical results suggest a thermodynamic explanation¹⁰ of the preference for reaction at primary C-H bonds in the gas phase.^{6,9} However, in the liquid phase the preference for reaction at primary C-H bonds has been attributed to steric effects.^{5a} For example, in the liquid phase cyclohexane does not react with $\text{Cp}^*_2\text{ScCH}_3$,¹¹ but use of ^{13}C H_4 shows that $\text{Cp}^*_2\text{ScCH}_3$ will undergo methyl exchange.^{5a} Though it would appear that reaction with cyclohexane is sterically hindered, it is possible that the observed reactivity could be controlled by other factors.

To examine this possibility, we have investigated the reaction of $\text{Sc}(\text{CH}_3)_2^+$ with simple compounds which do not possess primary C-H bonds, specifically cyclohexane and cyclopentane. Although $\text{Sc}(\text{CH}_3)_2^+$ is charged while $\text{Cp}^*_2\text{ScCH}_3$ is not, both are formally $d^0\text{Sc}(\text{III})$ complexes and both undergo σ -bond metathesis,^{5a,6} as would be expected of electron deficient systems.⁷ In fact, Steigerwald and Goddard⁷ performed their calculations on the neutral Cl_2ScH system, but their results apply equally well to cationic scandium systems. In addition, even though $\text{Sc}(\text{CH}_3)_2^+$ may be more electrophilic than $\text{Cp}^*_2\text{ScCH}_3$, theoretical calculations by Bauschlicher and Langhoff find that the $\text{Sc}-\text{CH}_3$ and Sc^+-CH_3 bond energies differ by only 4 kcal mol⁻¹ and that the $\text{Sc}-\text{H}$ and Sc^+-H bond energies differ by only 5 kcal mol⁻¹ (in both cases, the neutral has the lower bond energy).¹² So it does not appear to be unreasonable to compare the reactivity of $\text{Sc}(\text{CH}_3)_2^+$ and $\text{Cp}^*_2\text{ScCH}_3$ with cyclohexane. Compared with $\text{Cp}^*_2\text{ScCH}_3$, there is little steric crowding around the metal center in $\text{Sc}(\text{CH}_3)_2^+$. Thus, if $\text{Sc}(\text{CH}_3)_2^+$ reacts with cyclohexane and cyclopentane, this would support the suggestion that steric factors are the main reason $\text{Cp}^*_2\text{ScCH}_3$ (and similar compounds)

does not react with secondary C-H bonds. If $\text{Sc}(\text{CH}_3)_2^+$ is not reactive with cyclohexane and cyclopentane, this would suggest that other (perhaps electronic or thermodynamic) factors control the reactivity toward secondary C-H bonds in both the gas and liquid phase.

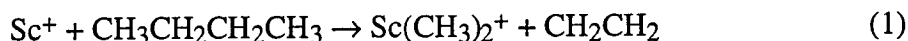
We should also note that when a straight chain alkane reacts with $\text{Sc}(\text{CD}_3)_2^+$, competitive intramolecular reactivity occurs between the primary and secondary C-H bonds. Though we have observed that primary C-H bonds are more reactive than secondary C-H bonds toward $\text{Sc}(\text{CD}_3)_2^+$,⁶ such observations only tell us about their *relative* reactivity toward $\text{Sc}(\text{CD}_3)_2^+$. Secondary C-H bonds might be rather nonreactive toward $\text{Sc}(\text{CH}_3)_2^+$ and provide little or no intramolecular competition with primary C-H bonds. Alternatively, secondary C-H bonds might be quite reactive toward $\text{Sc}(\text{CH}_3)_2^+$, but the more reactive primary C-H bonds still win the intramolecular competition for reaction with $\text{Sc}(\text{CH}_3)_2^+$. However, since cycloalkanes have *only* secondary C-H bonds, there are no primary bonds present to compete with the secondary bonds. Thus the reactivity we observe between $\text{Sc}(\text{CH}_3)_2^+$ and cycloalkanes should shed light on the *absolute* reactivity of secondary C-H bonds, without intramolecular competition from primary C-H bonds.

Experimental

Reactions were investigated with Fourier transform ion cyclotron resonance (FT-ICR) mass spectrometry, of which a number of reviews are available.¹³ In the Caltech instrument, a 1-in. cubic trapping cell is located between the poles of a Varian 15-in. electromagnet maintained at 1.0 T. Pressures were measured with a Schultz-Phelps ion gauge calibrated against an MKS 390 HA-00001SP05 capacitance manometer. The instrument at the University of Nice-Sophia Antipolis has the same specifications, except that pressures are measured with a Bayard-Alpert (BA) ionization gauge (Alcatel BN 111). The operation of the BA gauge has been described previously.¹⁴ Uncertainties in the absolute pressure limit rate constants to an accuracy of $\pm 20\%$.

Cyclohexane and cyclopentane were obtained commercially from Aldrich and purified by freeze-pump-thaw cycling.

Sc⁺ ions were produced by laser ablation of a scandium metal target with a N₂ laser at 337.1 nm. The reactant ion was generated by reaction 1¹⁵ and unwanted ions



were ejected from the cell using double resonance techniques¹⁶ and/or frequency sweep excitation.¹⁷ Cyclohexane and cyclopentane were then added along with *n*-butane and reactions due to the additional alkane were observed. In order to further elucidate reaction mechanisms and identify possible kinetic isotope effects, the reaction of isolated Sc(CD₃)₂⁺ (made via reaction 1 using [1,1,1,4,4,4-D₆]-*n*-butane) with cyclohexane was examined. Rate constants were determined in a straightforward manner, from slopes of semilog plots of the decay of reactant ion abundance versus time, with various pressures of the neutral reactants.

Collision induced dissociation (CID) experiments were also performed on the instrument in France. The CID experiments were performed in the multiple-collision regime using previously described methodologies.¹⁸ Argon at a pressure of about 9.0x10⁻⁷ torr was used as the collision gas. The collision energy was varied between 0 and 50 eV in the laboratory.

Results

Reaction with Cyclohexane. Sc(CH₃)₂⁺ can react with cyclohexane as shown in reactions 2-6 (see Figure 1a). The main process observed with cyclohexane is the

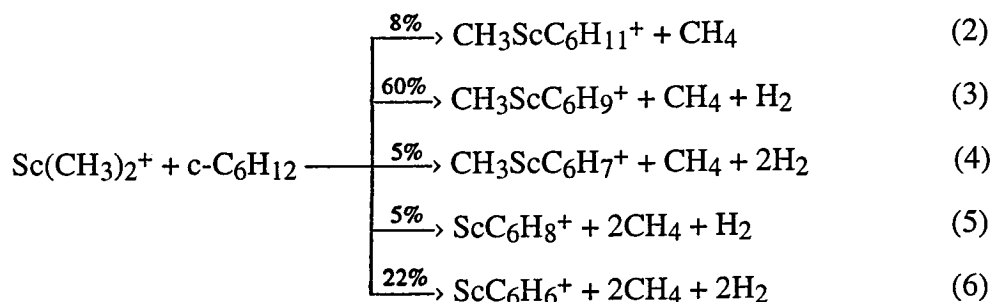
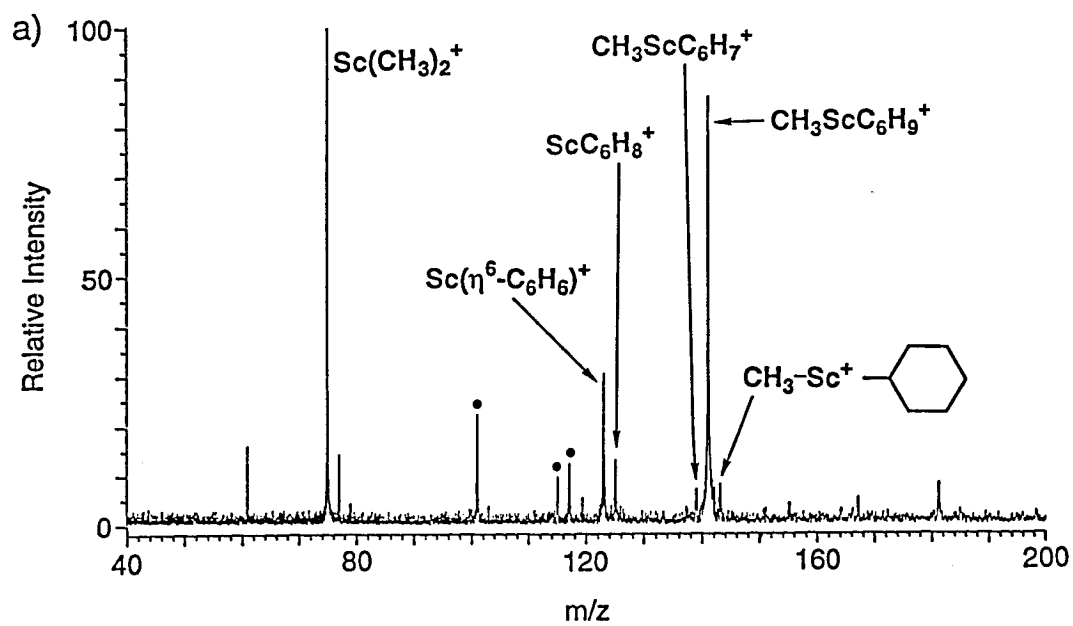
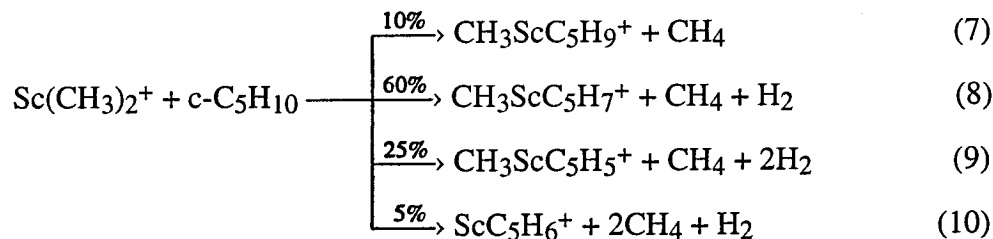


Figure 1a. Products of reaction of $\text{Sc}(\text{CH}_3)_2^+$ with cyclohexane. Spectrum was taken 600 ms after isolation of $\text{Sc}(\text{CH}_3)_2^+$. The peaks above m/z 150 correspond to ScR_2^+ , R = alkyl. Peaks at m/z 61, 77 and 79 correspond to ScO^+ , CH_3ScOH^+ and $\text{Sc}(\text{OH})_2^+$, respectively. Peaks at 101, 115 and 117 correspond to ScC_4H_8^+ , $\text{CH}_3\text{ScC}_4\text{H}_7^+$ and $\text{CH}_3\text{ScC}_4\text{H}_9^+$, respectively. These products (marked with bullets) result from reactions with the *n*-butane neutral. No products were observed above m/z 200.



metathesis reaction 2 and the accompanying dehydrogenations of reactions 3 and 4. Reaction 5 is observed when the nascent product of reaction 3 eliminates methane, while reaction 6 is seen when the nascent product of reaction 5 loses hydrogen. Reaction 6 could also be observed when the nascent product of reaction 4 eliminates methane, but it is unlikely that such a process would occur (see the discussion section). When $\text{Sc}(\text{CD}_3)_2^+$ is reacted with cyclohexane a nearly identical product distribution is seen (within experimental error). Additional metathesis reactions with a second cyclohexane molecule were not observed. To insure that the products of reaction 5 and 6 are formed from the nascent product of reaction 3, CID experiments were performed on the isolated $\text{CH}_3\text{ScC}_6\text{H}_9^+$ ion (see Figure 1b). These experiments confirmed that excitation of $\text{CH}_3\text{ScC}_6\text{H}_9^+$ leads to the formation of ScC_6H_8^+ and ScC_6H_6^+ . The CID of $\text{CH}_3\text{ScC}_6\text{H}_9^+$ also led to the formation of $\text{CH}_3\text{ScC}_6\text{H}_7^+$. For the reaction of $\text{Sc}(\text{CH}_3)_2^+$ with cyclohexane the total bimolecular rate constant $k = 6.2 \times 10^{-10} \text{ cm}^3\text{s}^{-1} \text{ molecule}^{-1}$ and the reaction efficiency $k/k_{\text{Langevin}} = 0.51$.^{19,20} For the reaction of $\text{Sc}(\text{CD}_3)_2^+$ with cyclohexane the total bimolecular rate constant $k = 6.6 \times 10^{-10} \text{ cm}^3\text{s}^{-1} \text{ molecule}^{-1}$ and the reaction efficiency $k/k_{\text{Langevin}} = 0.55$.^{19,20}

Reaction with Cyclopentane. $\text{Sc}(\text{CH}_3)_2^+$ reacts with cyclopentane as shown in reactions 7-10 (see Figure 2). The main process observed with cyclopentane is the



metathesis reaction 7 and the accompanying dehydrogenations (reactions 8 and 9). Reaction 10 is observed when the nascent product of reaction 8 eliminates methane. For the reaction of $\text{Sc}(\text{CH}_3)_2^+$ with cyclopentane the total bimolecular rate constant $k = 5.1 \times 10^{-10} \text{ cm}^3\text{s}^{-1} \text{ molecule}^{-1}$ and the reaction efficiency $k/k_{\text{Langevin}} = 0.43$.^{19,21}

Figure 1b. Spectrum of products from the CID of isolated $\text{CH}_3\text{ScC}_6\text{H}_9^+$. For this spectrum the maximum energy in the laboratory frame of reference is 48 eV, corresponding to a center-of-mass collision energy of 10.6 eV. The peaks at m/z 99 and 124 (marked with asterisks) are due to electrical noise.

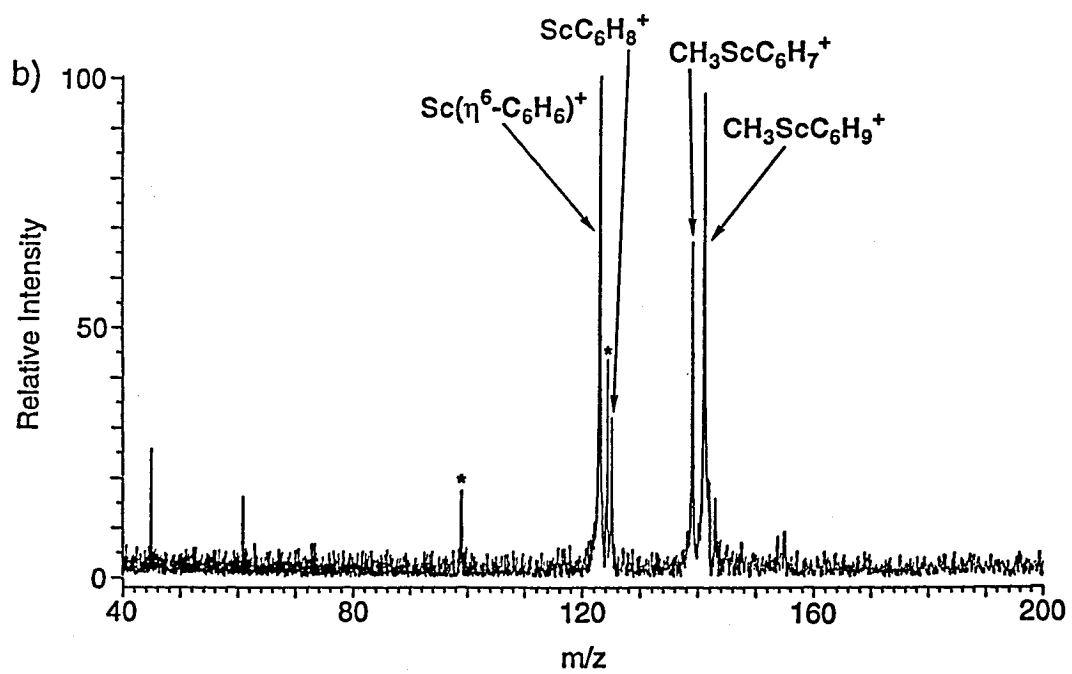
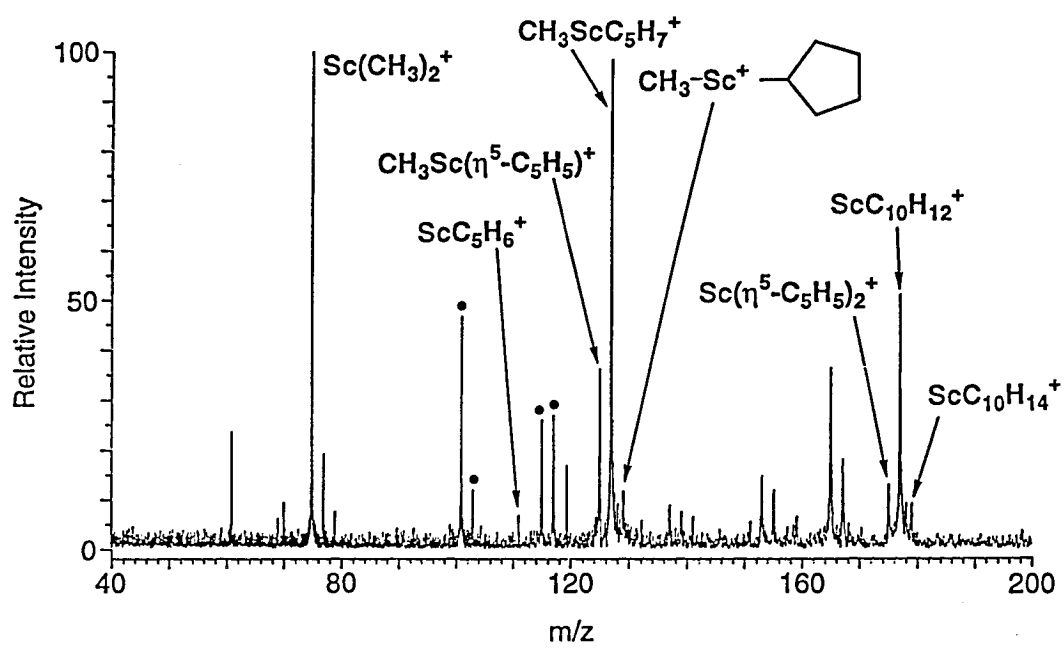
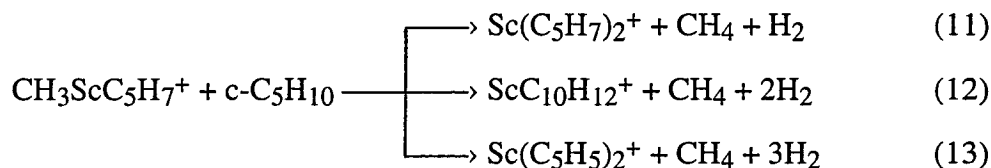


Figure 2. Products of reaction of $\text{Sc}(\text{CH}_3)_2^+$ with cyclopentane. Spectrum was taken 840 ms after isolation of $\text{Sc}(\text{CH}_3)_2^+$. The main peaks between m/z 135 and 170 correspond to ScR_2^+ , R = alkyl. Peaks at m/z 61, 77 and 79 correspond to ScO^+ , CH_3ScOH^+ and $\text{Sc}(\text{OH})_2^+$, respectively. Peaks at 101, 103, 115 and 117 correspond to ScC_4H_8^+ , $\text{ScC}_4\text{H}_{10}^+$, $\text{CH}_3\text{ScC}_4\text{H}_7^+$ and $\text{CH}_3\text{ScC}_4\text{H}_9^+$, respectively. These products (marked with bullets) result from reactions with the *n*-butane neutral.



At longer times the product of reaction 8 can subsequently undergo σ -bond metathesis and accompanying dehydrogenation with a second cyclopentane, as shown in reactions 11-13. In principle, the ionic products of reactions 7 and 9 could undergo the



same reactions, but since the $\text{CH}_3\text{ScC}_5\text{H}_7^+$ product of reaction 8 predominates, we only show its specific reactions. A rate constant was not derived for this process. Such reactivity was not observed with cyclohexane.

Discussion

Overview. In this study σ -bond metathesis reactions involving secondary C-H bonds are observed to occur with cyclohexane and cyclopentane, where a methyl group of $\text{Sc}(\text{CH}_3)_2^+$ is replaced by either a cyclohexyl or cyclopentyl group. Subsequent dehydrogenation of the metathesis product is observed with both cyclohexane and cyclopentane. With cyclohexane, a second methane is eventually eliminated leading to the formation of $\text{Sc}(\eta^6\text{-C}_6\text{H}_6)^+$. $\text{Sc}(\eta^6\text{-C}_6\text{H}_6)^+$ has also been previously observed in the reaction of Sc^+ with cyclohexane.²² In general, metathesis reactions can proceed via an oxidative addition/reductive elimination pathway or via a four-center intermediate. Since Sc^+ has only two valence electrons with which to form strong σ bonds,^{15,23} we favor a four-center mechanism for these metathesis reactions (as shown in Scheme I for the reaction of $\text{Sc}(\text{CD}_3)_2^+$ with *n*-butane). The high kinetic efficiencies observed indicate low barriers for these metathesis reactions, in accordance with the predictions of Steigerwald and Goddard.⁷

To investigate the possible presence of kinetic isotope effects, we also used [1,1,1,4,4,4- D_6]-*n*-butane to generate $\text{Sc}(\text{CD}_3)_2^+$, which we then allowed to react with cyclohexane. The total bimolecular rate constants measured with each ion differed slightly ($k_{\text{H}}/k_{\text{D}} = 0.94$), indicating that a small but measurable isotope effect exists in this

system. This is a slightly larger isotope effect than seen previously with straight chain alkanes but the deuterium labeled system has the larger rate constant, consistent with previous observations.^{6,9}

Small amounts of ScO^+ , CH_3ScOH^+ and $\text{Sc}(\text{OH})_2^+$ are observed from the reaction of $\text{Sc}(\text{CH}_3)_2^+$ with trace amounts of water in the background gas. These ions have been observed previously.^{6,9} Though the ion at m/z 61 is assigned to be ScO^+ , it could also correspond to $\text{Sc}(\text{CH}_4)^+$. However, the absence of any shift in this peak when $\text{Sc}(\text{CD}_3)_2^+$ was used confirms the assignment as ScO^+ .

The efficiencies ($k_{\text{reaction}}/k_{\text{collision}}$) for the reaction of $\text{Sc}(\text{CH}_3)_2^+$ with cyclohexane and cyclopentane differ by about 20%, with cyclohexane exhibiting the larger kinetic efficiency. The higher kinetic efficiency seen for the reaction of $\text{Sc}(\text{CH}_3)_2^+$ with cyclohexane can be accounted for by the deeper potential well which results from the larger polarizability of cyclohexane.^{20,21} This makes it easier to overcome any intrinsic barrier to σ -bond metathesis. These results are consistent with previous observations of $\text{Sc}(\text{CD}_3)_2^+$ reacting with straight chain hydrocarbons,⁶ and reminiscent of the reactions of Co^+ with hydrocarbons, where larger hydrocarbons deepen the electrostatic potential well for the Co^+ -alkane adduct. This provides greater chemical activation to the system, which facilitates overcoming the barrier to bond insertion.^{8,24}

Comparison of Gas-Phase and Liquid-Phase Reactivity. Previous gas-phase^{6,9} and liquid-phase^{5a} work involving σ -bond metathesis processes with scandium have shown a preference for reaction at primary C-H bonds. In the liquid phase, this preference has been attributed to steric effects resulting from the bulky Cp^* ligands bound to scandium. However, in the gas phase the $\text{Sc}(\text{CH}_3)_2^+$ ion exhibits the same preference.

Recent theoretical results suggest that the exchange reaction $\text{Sc}^+-\text{R} + \text{R}'-\text{H} \rightarrow \text{Sc}^+-\text{R}' + \text{R}-\text{H}$ ($\text{R} =$ small alkanes) should be approximately thermoneutral in the gas

phase.¹⁰ However, alkyl groups larger than ethyl can bend around and interact further with the Sc^+ metal center via an ion-polarization interaction. This additional interaction will further stabilize the Sc^+ metal center, but can only occur if primary C-H bonds are attacked. Thermodynamic considerations can, therefore, explain the observed preference $\text{Sc}(\text{CH}_3)_2^+$ shows for reacting with primary C-H bonds.^{6,9} Since there is no steric crowding around $\text{Sc}(\text{CH}_3)_2^+$, the thermodynamic explanation is the only way to rationalize this preference for reaction at primary C-H bonds in the gas phase.

Thus, when a straight chain alkane reacts with $\text{Sc}(\text{CH}_3)_2^+$, the primary and secondary sites intramolecularly compete with each other. This competition is usually won by the primary site. Unfortunately, this tells us nothing of the absolute reactivity of secondary C-H bonds toward σ -bond metathesis reactions. All it shows is that primary sites are more reactive. However, both cyclohexane and cyclopentane contain only secondary C-H bonds and both exhibit high kinetic efficiencies in their reactions with $\text{Sc}(\text{CH}_3)_2^+$. This shows that secondary C-H bonds are *not* thermodynamically forbidden from reacting. In fact, secondary C-H bonds are very reactive toward σ -bond metathesis, but primary C-H bonds are even more reactive. The preference to react at primary C-H bonds is simply a reflection that the intrinsic barrier to primary C-H bond activation is lower than the intrinsic barrier to secondary C-H bond activation.

What implications does this have for the liquid-phase reactivity of $\text{Cp}^*_2\text{ScCH}_3$ toward C-H bonds? Our present results show that the preference of $\text{Sc}(\text{CH}_3)_2^+$ to react with primary C-H bonds in the gas phase does not imply that secondary C-H bonds will not react when no primary C-H bonds are present. This observation supports the view that it is steric effects in the liquid phase that modify the potential energy surface so as to render $\text{Cp}^*_2\text{ScCH}_3$ unreactive toward cyclohexane.^{5a}

Reaction Energetics. The product distributions from the reaction of cyclohexane with $\text{Sc}(\text{CH}_3)_2^+$ and the CID of $\text{CH}_3\text{ScC}_6\text{H}_9^+$ exhibit an interesting and subtle feature. Very little $\text{CH}_3\text{ScC}_6\text{H}_7^+$ is seen in the direct reaction of $\text{Sc}(\text{CH}_3)_2^+$ with cyclohexane,

while a large amount is produced by CID of $\text{CH}_3\text{ScC}_6\text{H}_9^+$. However, $\text{Sc}(\eta^6\text{-C}_6\text{H}_6)^+$ and ScC_6H_8^+ are observed to form in both cases. To explore this point further, we have constructed a reaction coordinate diagram (see Figure 3) for the processes shown in reactions 2-6. Thermochemical values relevant to this work are shown in Tables 1 and 2. The necessary values were mostly obtained directly from the literature or calculated from other literature values in a straightforward manner. However, some had to be estimated as follows.

For $\text{Sc}(\eta^6\text{-C}_6\text{H}_6)^+$, Lech and Freiser²² found from bracketing experiments that the bond energy was 53 ± 5 kcal mol⁻¹. However, recent work by Meyer et al.²⁸ has determined the $\text{Ti}(\eta^6\text{-C}_6\text{H}_6)^+$ and $\text{V}(\eta^6\text{-C}_6\text{H}_6)^+$ bond energies to be 62 and 56 kcal mol⁻¹, respectively. This suggests that the $\text{Sc}(\eta^6\text{-C}_6\text{H}_6)^+$ bond energy may be slightly higher than 53 kcal mol⁻¹. Thus we estimate the $\text{Sc}(\eta^6\text{-C}_6\text{H}_6)^+$ bond energy to be approximately 60 kcal mol⁻¹.

For $\text{CH}_3\text{Sc}(\eta^3\text{-C}_6\text{H}_9)^+$ one might expect the $\text{Sc}^+(\eta^3\text{-C}_6\text{H}_9)^+$ bond energy to be intermediate between the bond energies of $\text{Sc}(\eta^4\text{-C}_6\text{H}_8)^+$ and $\text{Sc}(\eta^2\text{-C}_6\text{H}_{10})^+$. But prior work by Huang et al.^{5b} has found that $\text{CH}_3\text{Sc}(\eta^3\text{-C}_3\text{H}_5)^+$ is approximately 15 kcal mol⁻¹ more stable than $\text{Sc}^+(\text{1-butene})$. Assuming that the bond energy of $\text{Sc}^+(\text{1-butene})$ is 45 kcal mol⁻¹ (similar to the bond energy of 47 kcal mol⁻¹ for $\text{Sc}^+(\text{2-butene})$ calculated from known heats of formation²⁵) we can then calculate from known thermochemistry²⁵ that the bond energy of $\text{CH}_3\text{Sc}(\eta^3\text{-C}_6\text{H}_9)^+$ is approximately 75 kcal mol⁻¹. As this value seems a bit high, we estimate the value of the $\text{CH}_3\text{Sc}(\eta^3\text{-C}_6\text{H}_9)^+$ bond energy to be 70 kcal mol⁻¹, which is slightly larger than the $\text{Sc}(\eta^4\text{-C}_6\text{H}_8)^+$ bond energy. Furthermore, we would expect $\text{CH}_3\text{Sc}(\eta^5\text{-C}_6\text{H}_7)^+$ to exhibit parallel behavior and have a bond energy slightly larger than that for $\text{Sc}(\eta^6\text{-C}_6\text{H}_6)^+$. Therefore, we estimate the $\text{CH}_3\text{Sc}(\eta^5\text{-C}_6\text{H}_7)^+$ bond energy to be 65 kcal mol⁻¹.

Figure 3. Illustration of reaction energetics for processes resulting from interaction of cyclohexane with $\text{Sc}(\text{CH}_3)_2^+$. The relative energies are derived from the thermochemistry given in Tables 1 and 2. Some of the values have significant uncertainties (see text for discussion). Note the comparatively high energy required to reach $\text{CH}_3\text{Sc}(\eta^5\text{-C}_6\text{H}_7)^+$, which prevents the formation of $\text{CH}_3(\text{H})\text{Sc}(\eta^6\text{-C}_6\text{H}_6)^+$. Because of this, $\text{CH}_3\text{ScC}_6\text{H}_9^+$ will preferentially lose methane to form ScC_6H_8^+ .

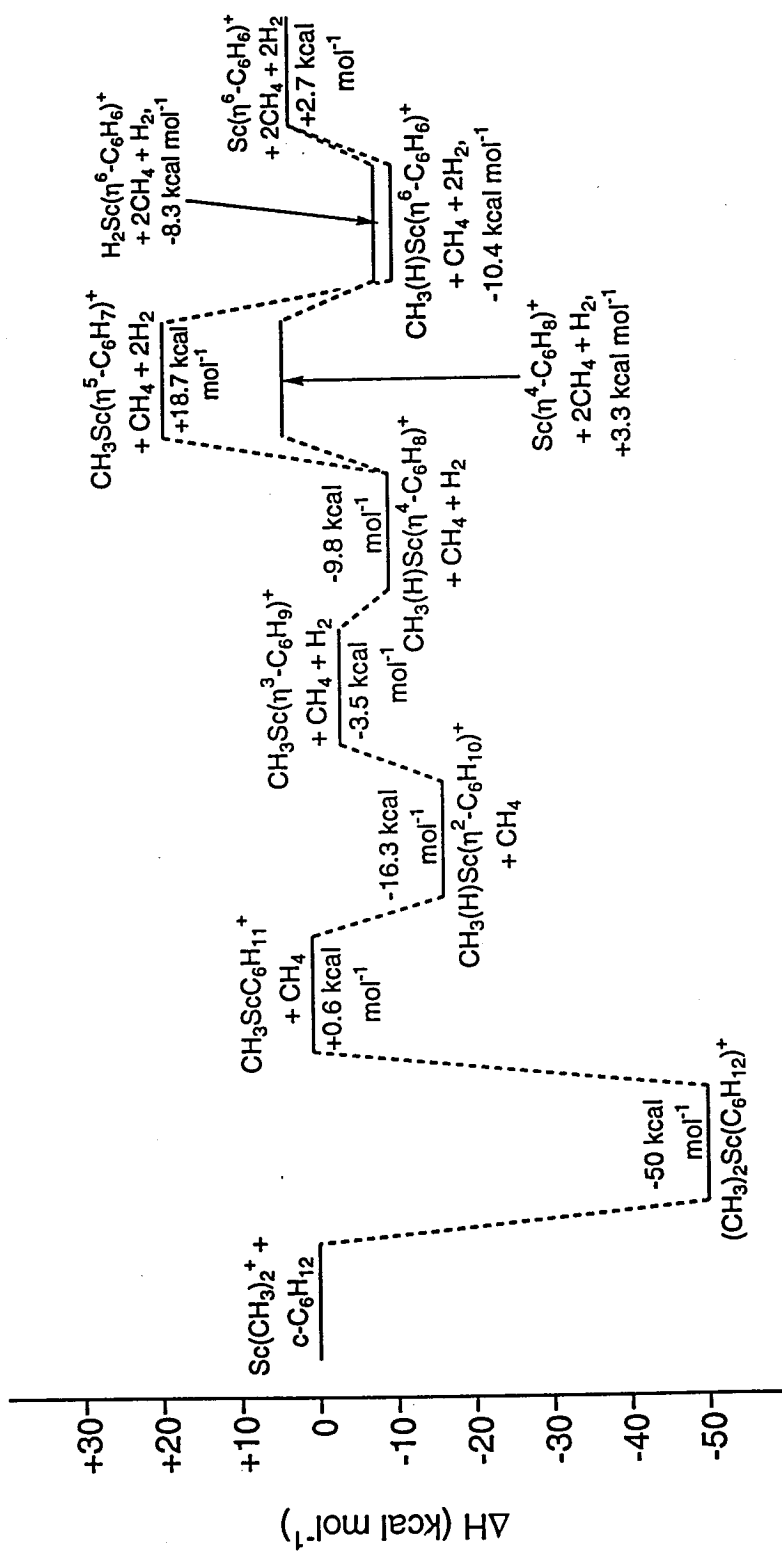


Table 1. Gas-Phase Heats of Formation at 298 K for Chemical Species Relevant to this Work.^{a,b}

Species	$\Delta H^\circ_{f,298}$ (kcal mol ⁻¹)
CH ₄	-17.8(0.1)
CH ₃	+35.1(0.2) ^c
H	+52.1(0.1)
Sc ⁺	+241(5)
ScCH ₃ ⁺	+217(6) ^d
Sc(CH ₃) ₂ ⁺	+192(7) ^e
ScH ⁺	+237(5) ^d
ScH ₂ ⁺	+230(6) ^e
c-C ₆ H ₁₂	-29.5(0.1)
c-C ₆ H ₁₁	+13.9(1) ^c
c-C ₆ H ₁₀	-1.1(0.1)
c-C ₆ H ₉	+29.8(1) ^f
c-C ₆ H ₈	+25.4(0.1)
c-C ₆ H ₇	+47(5) ^c
C ₆ H ₆	+19.8(0.1)

^aUncertainties are in parentheses. ^bUnless otherwise noted, all values come from Reference 25. ^cReference 26. ^dDerived from the equation $\Delta H^\circ_{f,298}(\text{ScX}^+) = \Delta H^\circ_{f,298}(\text{Sc}^+) + \Delta H^\circ_{f,298}(\text{X}) - D^\circ_{298}(\text{Sc}^+-\text{X})$. The appropriate bond energy is taken from Table 2. ^eDerived from the equation $\Delta H^\circ_{f,298}(\text{ScX}_2^+) = \Delta H^\circ_{f,298}(\text{ScX}^+) + \Delta H^\circ_{f,298}(\text{X}) - D^\circ_{298}(\text{XSc}^+-\text{X})$. The appropriate bond energy is taken from Table 2. ^fDerived from the measured bond energy of the allyl hydrogen to cyclohexene, using the equation $\Delta H^\circ_{f,298}(\text{c-C}_6\text{H}_9) = \Delta H^\circ_{f,298}(\text{c-C}_6\text{H}_{10}) - \Delta H^\circ_{f,298}(\text{H}) + D^\circ_{298}(\text{cyclohexenyl-allyl H})$. The appropriate bond energy is taken from Table 2.

Table 1. (Continued)

Species	$\Delta H^\circ_{f,298}$ (kcal mol ⁻¹)
CH ₃ Sc ⁺ -C ₆ H ₁₁	+180.9(8) ^g
CH ₃ Sc ⁺ -(η^3 -C ₆ H ₉)	+176.8(9) ^g
Sc ⁺ -(η^4 -C ₆ H ₈)	+201.4(8) ^d
CH ₃ Sc ⁺ -(η^5 -C ₆ H ₇)	+199(10) ^g
Sc ⁺ -(η^6 -C ₆ H ₆)	+200.8(8) ^d
(CH ₃) ₂ Sc ⁺ -(C ₆ H ₁₂)	+112.5(10) ^h
(CH ₃)(H)Sc ⁺ -(η^2 -C ₆ H ₁₀)	+164(9) ⁱ
(CH ₃)(H)Sc ⁺ -(η^4 -C ₆ H ₈)	+170.5(10) ⁱ
(CH ₃)(H)Sc ⁺ -(η^6 -C ₆ H ₆)	+169.9(10) ⁱ
H ₂ Sc ⁺ -(η^6 -C ₆ H ₆)	+189.8(9) ^h

^gDerived from the equation $\Delta H^\circ_{f,298}(\text{XSc-Y}^+) = \Delta H^\circ_{f,298}(\text{ScX}^+) + \Delta H^\circ_{f,298}(\text{Y}) - D^\circ_{298}(\text{XSc-Y}^+)$. The appropriate bond energy is taken from Table 2. ^hDerived from the equation $\Delta H^\circ_{f,298}(\text{X}_2\text{Sc-Y}^+) = \Delta H^\circ_{f,298}(\text{ScX}_2^+) + \Delta H^\circ_{f,298}(\text{Y}) - D^\circ_{298}(\text{X}_2\text{Sc-Y}^+)$. The appropriate bond energy is taken from Table 2. ⁱDerived from the equation $\Delta H^\circ_{f,298}((\text{X})(\text{Y})\text{Sc-Z}^+) = \Delta H^\circ_{f,298}(\text{ScX}^+) + \Delta H^\circ_{f,298}(\text{Y}) + \Delta H^\circ_{f,298}(\text{Z}) - D^\circ_{298}(\text{XSc-Y}^+) - D^\circ_{298}((\text{X})(\text{Y})\text{Sc-Z}^+)$. The appropriate bond energy is taken from Table 2.

Table 2. Gas-Phase Bond Energies at 298 K for Chemical Species Relevant to this Work.^a

Species	D°_{298} (kcal mol ⁻¹)
c-C ₆ H ₁₁ -H	95.5(1) ^b
c-C ₆ H ₉ -allyl H	83(1) ^c
c-C ₆ H ₇ -allyl H	73(5) ^b
c-C ₅ H ₉ -H	94.5(1) ^b
HSc ⁺ -H	59(4) ^d
Sc ⁺ -H	56(2) ^d
CH ₃ Sc ⁺ -CH ₃	60(5) ^d
Sc ⁺ -CH ₃	59(3) ^d
Sc ⁺ -C ₅ H ₉	50(5) ^e
Sc ⁺ -(η^6 -C ₆ H ₆)	60(7) ^f
Sc ⁺ -(η^5 -C ₆ H ₇)	65(7) ^g
Sc ⁺ -(η^4 -C ₆ H ₈)	65(7) ^h
Sc ⁺ -(η^3 -C ₆ H ₉)	70(7) ⁱ
Sc ⁺ -(η^2 -C ₆ H ₁₀)	45(5) ^j
Sc ⁺ -C ₆ H ₁₁	50(5) ^e
Sc ⁺ -C ₆ H ₁₂	50(7) ^k

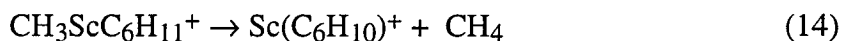
^aUncertainties are in parentheses. ^bReference 26. ^cEstimated assuming a resonance stabilization energy of approximately 12 kcal mol⁻¹ for an allyl hydrogen (Reference 26). ^dReference 27. ^eEstimated from Perry and Goddard's (Reference 10) theoretical bond energy of 36.9 kcal mol⁻¹ for a secondary carbon bonded to Sc⁺. We have included a correction of approximately 15 kcal mol⁻¹, since Perry and Goddard's calculated Sc-CH₃ bond energy is 15 kcal mol⁻¹ lower than the experimentally determined value (Reference 27). ^fReference 22 and 28. See discussion in text. ^gSee

Table 2. (Continued)

discussion in text. ^hEstimated utilizing the facts that butadiene will displace benzene from $\text{Sc}(\eta^6\text{-C}_6\text{H}_6)^+$ in the gas phase and that CID of $\text{Sc}(\eta^4\text{-C}_4\text{H}_6)(\eta^6\text{-C}_6\text{H}_6)^+$ leads predominantly to the loss of benzene (Reference 22). ⁱReference 5b. See discussion in text. ^jEstimated to be similar to the bond energy of 47 kcal mol⁻¹ for $\text{Sc}(\text{-2-butene})^+$. The bond energy of $\text{Sc}(\text{-2-butene})^+$ is calculated using values for the heats of formation from reference 25. ^kEstimated utilizing reference 24 and 29. See discussion in text.

Experimental work by Kemper et al.,²⁹ Hill et al.³⁰ and Armentrout and co-workers,³¹ in conjunction with theoretical work by Perry et al.²⁴ has demonstrated that the complexation energies between transition metal cations and alkanes are significantly larger than one might have anticipated. For example, Kemper et al. found that the $\text{Co}^+(\text{C}_2\text{H}_6)_2$ molecular complex has a total binding energy of about 55 kcal mol^{-1} .²⁹ Cyclohexane is more polarizable than ethane, but due to its ring shape cyclohexane can only interact through three of its hydrogen atoms, so we might expect the binding energy of Sc^+ and cyclohexane to be similar to the binding energy of two ethanes to Co^+ . Thus we estimate a bond energy of 50 kcal mol^{-1} for $(\text{CH}_3)_2\text{Sc}^+-\text{C}_6\text{H}_{12}$.

The reaction coordinate diagram shown in Figure 3 assumes a stepwise sequential reaction mechanism for the eventual dehydrogenation of cyclohexane to benzene. The initial step is adduct formation with cyclohexane, leading to the σ -bond metathesis of reaction 2. The next step could then be one of two paths: dehydrogenation of the cyclohexyl ring (reaction 3), or a second intramolecular metathesis reaction (reaction 14). As shown in Figure 3, the dehydrogenation of the cyclohexyl ring is



achieved by moving through an $\eta^2 \pi$ -complex (via a β -hydride transfer) with the subsequent elimination of H_2 . Since no $\text{Sc}(\text{C}_6\text{H}_{10})^+$ is observed, we conclude that reaction 14 does not occur.

This mechanistic pattern continues in a stepwise sequence. After the initial σ -bond metathesis, β -hydride transfer leads to an intermediate species, which then eliminates either H_2 or methane until the final product $\text{Sc}(\eta^6\text{-C}_6\text{H}_6)^+$ is reached. From Figure 3, we see that most species involved in reactions 2-6 are below or just slightly above the energy of the reactants. However, $\text{CH}_3\text{Sc}(\eta^5\text{-C}_6\text{H}_7)^+$ is seen to be energetically quite unfavorable when compared with the reactants. Thus very little $\text{CH}_3(\text{H})\text{Sc}(\eta^6\text{-C}_6\text{H}_6)^+$ (which can only be reached from $\text{CH}_3\text{Sc}(\eta^5\text{-C}_6\text{H}_7)^+$) will form without any external activation, and $\text{CH}_3\text{ScC}_6\text{H}_9^+$ will preferentially eliminate methane

(instead of H₂) to form ScC₆H₈⁺. Furthermore, we see that the product of reaction 6 must then arise from dehydrogenation of ScC₆H₈⁺, since almost no CH₃ScC₆H₇⁺ is produced. On the other hand, if enough excitation energy is supplied through processes such as CID, then it will be possible to form significant amounts of CH₃ScC₆H₇⁺. Such behavior was in fact observed.

Comparison of the Behavior of Cyclohexane and Cyclopentane. After the initial metathesis reactions, an interesting difference between the reactivity of CH₃ScC₆H₉⁺ and CH₃ScC₅H₇⁺ is observed. With CH₃ScC₆H₉⁺, only subsequent dehydrogenation leading eventually to the formation of Sc(η^6 -C₆H₆)⁺ is seen. In contrast to the reactivity of CH₃ScC₆H₉⁺, CH₃ScC₅H₇⁺ will undergo a second metathesis reaction with a second cyclopentane molecule (eliminating the remaining methyl group) and subsequently dehydrogenate to form the observed products, including Sc(η^5 -C₅H₅)₂⁺ (i.e., scandocenium). We should note that scandocenium has been observed previously as a product of the reaction of Sc⁺ with cyclopentene,²² but in our system it is generated from a ligated Sc⁺ metal center and a saturated hydrocarbon. Apparently, the dehydrogenation of CH₃ScC₆H₉⁺ is more facile than the dehydrogenation of CH₃ScC₅H₇⁺. Subsequent collisions of CH₃ScC₆H₉⁺ with cyclohexane may lead to dehydrogenation rather than a second σ -bond metathesis reaction.

Acknowledgments

This work was supported by the National Science Foundation under grant CHE-9108318 and by a grant from AMOCO. We also wish to acknowledge the Beckman Foundation and Institute for continuing support of the FT-ICR research facility.

References

- ¹Bryndza, H. E.; Fong, L. K.; Paciello, R. A.; Tam, W.; Bercaw, J. E. *J. Am. Chem. Soc.* **1987**, *109*, 1444.
- ²Uppal, J. S.; Douglas, D. E.; Staley, R. H. *J. Am. Chem. Soc.* **1981**, *103*, 508.
- ³Christ, C. S.; Eyler, J. R.; Richardson, D. E. *J. Am. Chem. Soc.* **1988**, *110*, 4038.
- ⁴(a) Wax, M. J.; Stryker, J. M.; Buchanan, J. M.; Kovac, C. A.; Bergman, R. G. *J. Am. Chem. Soc.* **1984**, *106*, 1121. (b) Buchanan, J. M.; Stryker, J. M.; Bergman, R. G. *J. Am. Chem. Soc.* **1986**, *108*, 1537.
- ⁵(a) Thompson, M. E.; Baxter, S. M.; Bulls, A. R.; Burger, B. J.; Nolan, M. C.; Santarsiero, B. D.; Schaefer, W. P.; Bercaw, J. E. *J. Am. Chem. Soc.* **1987**, *109*, 203. (b) Huang, Y.; Hill, Y. D.; Sodupe, M.; Bauschlicher, C. W., Jr.; Freiser, B. S. *J. Am. Chem. Soc.* **1992**, *114*, 9106.
- ⁶Crellin, K. C.; Geribaldi, S.; Beauchamp, J. L. *Organometallics* **1994**, *13*, 3733.
- ⁷Steigerwald, M. L.; Goddard, W. A. III *J. Am. Chem. Soc.* **1984**, *106*, 308.
- ⁸van Koppen, P. A. M.; Brodbelt-Lustig, J.; Bowers, M. T.; Dearden, D. V.; Beauchamp, J. L.; Fisher, E. R.; Armentrout, P. B. *J. Am. Chem. Soc.* **1991**, *113*, 2359.
- ⁹Crellin, K. C.; Geribaldi, S.; Widmer, M.; Beauchamp, J. L. *Organometallics* **1995**, *14*, 4366.
- ¹⁰Perry, J. K.; Goddard, W. A. III *J. Am. Chem. Soc.* **1994**, *116*, 5013.
- ¹¹Throughout this chapter Cp* = (η^5 -C₅(CH₃)₅).
- ¹²Bauschlicher, C. W., Jr.; Langhoff, S. R. *Int. Rev. Phys. Chem.* **1990**, *9*, 149.
- ¹³(a) Marshall, A. G. *Acc. Chem. Res.* **1985**, *18*, 316. (b) Comisarow, M. B. *Anal. Chim. Acta.* **1985**, *178*, 1.
- ¹⁴Azzaro, M.; Breton, S.; Decouzon, M.; Geribaldi, S. *Int. J. Mass Spectrom. Ion Proc.* **1993**, *128*, 1.
- ¹⁵Tolbert, M. A.; Beauchamp, J. L. *J. Am. Chem. Soc.* **1984**, *106*, 8117.
- ¹⁶Anders, L. R.; Beauchamp, J. L.; Dunbar, R. C.; Baldeschwieler, J. D. *J. Chem. Phys.* **1966**, *45*, 1062.
- ¹⁷Comisarow, M. B.; Marshall, A. G. *Chem. Phys. Lett.* **1974**, *26*, 489.
- ¹⁸(a) Freiser, B. S. *Anal. Chim. Acta.* **1985**, *178*, 137. (b) Grosshans, P. B.; Marshall, A. G. *Int. J. Mass Spectrom. Ion Proc.* **1990**, *100*, 347.

¹⁹Collision rates are calculated using Langevin theory: Su, T.; Bowers, M. T. *Gas Phase Ion Chemistry*, Vol. 1, M. T. Bowers, Ed., 1979, Academic Press, New York.

²⁰For cyclohexane, the polarizability $\alpha = 10.87 \text{ \AA}^3$: Stuart, H. A. *Landolt-Börnstein Zahlenwerte und Funktionen*, Vol. 1, Part 3, A. Eucken and K. H. Hellwege, Eds., 1951, Springer-Verlag, Berlin.

²¹For cyclopentane, the polarizability $\alpha = 9.15 \text{ \AA}^3$: Applequist, J.; Carl, J. R.; Fung, K.-K. *J. Am. Chem. Soc.* **1972**, *94*, 2952.

²²Lech, L. M.; Freiser, B. S. *Organometallics* **1988**, *7*, 1948.

²³Beauchamp, J. L.; van Koppen, P. A. M. *Energetics of Organometallic Species*, J. A. M. Simoes, Ed., 1992, Kluwer Academic Publishers, The Netherlands.

²⁴Perry, J. K.; Ohanessian, G.; Goddard, W. A. III *J. Phys. Chem.* **1993**, *97*, 5238.

²⁵Lias, S. G.; Bartmess, J. E.; Liebman, J. F.; Holmes, J. L.; Levin, R. D.; Mallard, W. G. *J. Phys. Chem. Ref. Data* **1988**, *17*, Suppl. 1.

²⁶McMillen, D. F.; Golden, D. M. *Ann. Rev. Phys. Chem.* **1982**, *33*, 493.

²⁷Armentrout, P. B.; Georgiadis, R. *Polyhedron* **1988**, *7*, 1573.

²⁸Meyer, F.; Khan, F. A.; Armentrout, P. B. *J. Am. Chem. Soc.* **1995**, *117*, 9740.

²⁹Kemper, P. R.; Bushnell, J.; van Koppen, P.; Bowers, M. T. *J. Phys. Chem.* **1993**, *97*, 1810.

³⁰Hill, Y. D.; Freiser, B. S.; Bauschlicher, C. W. *J. Am. Chem. Soc.* **1991**, *113*, 1507.

³¹(a) Schultz, R. H.; Armentrout, P. B. *J. Am. Chem. Soc.* **1991**, *113*, 729. (b) Schultz, R. H.; Armentrout, P. B. *J. Phys. Chem.* **1992**, *96*, 1662.

Chapter 5

σ -BOND METATHESIS REACTIONS OF $\text{Sc}(\text{OCD}_3)_2^+$ WITH WATER, ETHANOL, AND 1-PROPANOL: MEASUREMENTS OF EQUILIBRIUM CONSTANTS, RELATIVE BOND STRENGTHS AND ABSOLUTE BOND STRENGTHS

Kevin C. Crellin and J. L. Beauchamp

Arthur Amos Noyes Laboratory of Chemical Physics, California Institute of Technology, Pasadena, CA 91125

W. A. Goddard, III

Materials and Process Simulations Center, Beckman Institute, 139-74, California Institute of Technology, Pasadena, CA 91125

S. Geribaldi and M. Decouzon

Laboratoire de Chimie Physique Organique, Groupe FT-ICR, Université de Nice-Sophia Antipolis, Faculté des Sciences, Parc Valrose, 06108 Nice Cedex 2, France

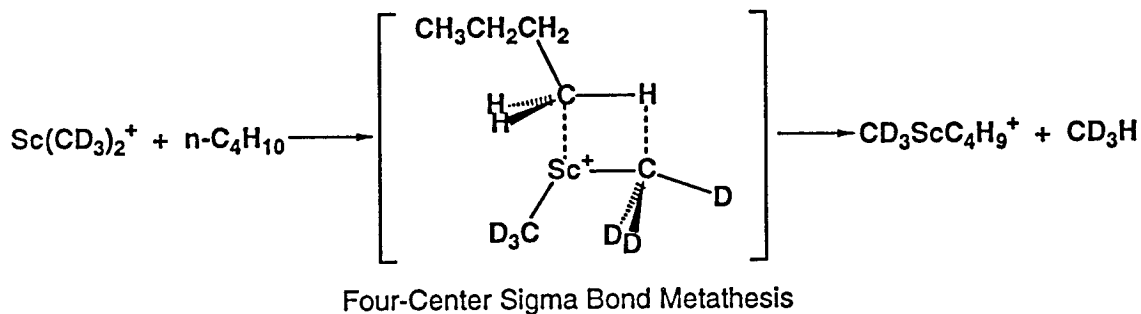
Submitted for publication as an article in the *Journal of the American Chemical Society*.

Abstract

Fourier transform ion cyclotron resonance mass spectrometry has been used to examine the reactions of $\text{Sc}(\text{OCD}_3)_2^+$ with water, ethanol and 1-propanol. σ -bond metathesis resulting in the elimination of CD_3OH is the initial reaction observed, with further solvation of the metal center and subsequent elimination of hydrogen occurring as additional reaction channels. These processes are facile at room temperature and involve little or no activation energy. Measured equilibrium constants for the reaction $\text{Sc}(\text{OCD}_3)_2^+ + \text{ROH} \rightleftharpoons \text{CD}_3\text{OScOR}^+ + \text{CD}_3\text{OH}$ with $\text{R} = \text{H}$, ethyl, and *n*-propyl are 0.013 ± 0.004 , 0.5 ± 0.15 and 0.7 ± 0.2 , respectively. For the reaction $\text{ROScOCD}_3^+ + \text{ROH} \rightleftharpoons \text{Sc}(\text{OR})_2^+ + \text{CD}_3\text{OH}$ with $\text{R} = \text{H}$ and ethyl the measured equilibrium constants are 0.013 ± 0.004 and 0.3 ± 0.1 , respectively. ΔS is estimated for these processes using theoretical calculations and statistical thermodynamics, and in conjunction with the measured equilibrium constants we have evaluated ΔH for these reactions and the relative and absolute bond strengths of the Sc^+-OR bonds, $\text{R} = \text{H}$, methyl, ethyl and *n*-propyl. The relative bond strengths, $D^\circ_{298}(\text{CD}_3\text{OSc}^+-\text{OR}) - D^\circ_{298}(\text{CD}_3\text{OSc}^+-\text{OCD}_3)$, for $\text{R} = \text{H}$, methyl, ethyl and *n*-propyl are $+11.9 \pm 0.5$, 0 , -0.1 ± 0.5 and -1.4 ± 0.5 kcal mol⁻¹, respectively. The absolute bond strengths for $\text{HOSc}^+-\text{OCD}_3$, $\text{CD}_3\text{OSc}^+-\text{OCD}_3$, $\text{CD}_3\text{OSc}^+-\text{OC}_2\text{H}_5$, $\text{CD}_3\text{OSc}^+-\text{OCH}_2\text{CH}_2\text{CH}_3$ and $\text{H}_5\text{C}_2\text{OSc}^+-\text{OC}_2\text{H}_5$ are 115.0 ± 2.0 , 115.0 ± 2.0 , 114.9 ± 2.0 , 113.6 ± 2.0 and 114.7 ± 2.0 kcal mol⁻¹, respectively. Theoretical calculations with an LAV3P* ECP basis set at the level of localized second-order Møller-Plesset perturbation theory were performed to evaluate ΔS and ΔG for the specific equilibria $\text{Sc}(\text{OH})_2^+ + \text{CD}_3\text{OH} \rightleftharpoons \text{CD}_3\text{OScOH} + \text{H}_2\text{O}$, $\text{CD}_3\text{OScOH} + \text{CD}_3\text{OH} \rightleftharpoons \text{Sc}(\text{OCD}_3)_2^+ + \text{H}_2\text{O}$, and $\text{Sc}(\text{OCD}_3)_2^+ + \text{C}_2\text{H}_5\text{OH} \rightleftharpoons \text{CD}_3\text{OScOC}_2\text{H}_5^+ + \text{CD}_3\text{OH}$. The theoretically determined ΔG values agree reasonably well with the experimentally determined ΔG values. In accordance with earlier theoretical predictions, these metathesis reactions are consistent with an allowed four-center mechanism similar to that of a $2\sigma + 2\sigma$ cycloaddition.

Introduction

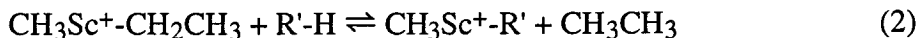
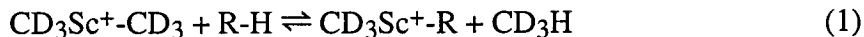
σ -bond metathesis has been observed in a variety of transition metal systems,¹⁻⁶ including scandium-containing systems.^{7,8} A mechanism involving a four-center transition state is generally invoked for these metathesis reactions (as shown in Scheme I for the reaction of $\text{Sc}(\text{CD}_3)_2^+$ with *n*-butane), in accord with the prediction of



Scheme I

Steigerwald and Goddard⁹ that certain organometallic species containing an extremely acidic (in the Lewis sense) metal center should exhibit this kind of reactivity. These σ -bond metathesis processes have proven to be extremely useful in investigating the ligand exchange behavior of the organometallic complexes studied. For example, Bryndza et al.¹ have used equilibrium data from σ -bond metathesis reactions to determine the relative metal-ligand σ bond strengths for several series of transition metal complexes in solution.

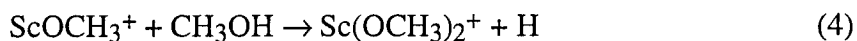
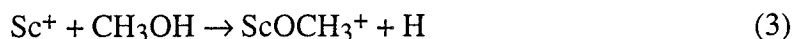
Part of the motivation for our previous studies of the σ -bond metathesis reactions of $\text{Sc}(\text{CD}_3)_2^+$ and $\text{CH}_3\text{ScCH}_2\text{CH}_3^+$ with small alkanes in the gas phase⁸ was the hope that equilibrium for reactions 1 and 2 (R = ethyl, propyl, *n*-butyl or isobutyl; R' = propyl,



n-butyl or isobutyl) would be observed. When $\text{CD}_3\text{Sc}^+-\text{R}$ or $\text{CH}_3\text{Sc}^+-\text{R}'$ was isolated, no reactivity with methane or ethane, respectively, was observed. The chemical activation provided by the interaction of methane and ethane with $\text{CD}_3\text{Sc}^+-\text{R}$ or $\text{CH}_3\text{Sc}^+-\text{R}'$,

respectively, is apparently insufficient to overcome the intrinsic barrier to σ -bond metathesis.⁸ With larger hydrocarbons the reaction sequences were too complex to facilitate observation of equilibria, and the reaction exothermicities were likely too large to quantify the equilibria with room temperature Fourier transform ion cyclotron resonance mass spectral measurements.

Although exchange equilibria via σ -bond metathesis were not quantified with alkyl substituents, we reasoned that it might still be possible to observe such reactivity with other classes of ligands. In particular, work by Azzaro et al.¹⁰ has shown that $\text{Sc}(\text{OCH}_3)_2^+$ can be generated by reactions 3 and 4. One can surmise that $\text{Sc}(\text{OCH}_3)_2^+$



might undergo exchange reactions with other alcohols analogous to the reactions seen between $\text{Sc}(\text{CH}_3)_2^+$ and small alkanes. In this paper we extend our previous work with scandium alkyl systems to scandium alkoxide systems and present evidence for the observation of ligand exchange equilibria via σ -bond metathesis between $\text{Sc}(\text{OCH}_3)_2^+$ and ROH (R = H, ethyl, or *n*-propyl) or ROScOCH_3^+ and ROH (R = H or ethyl). We use the measured equilibrium constants to evaluate the relative and absolute bond strengths of these various alkoxide ligands to Sc^+ .

Experimental

Reactions were investigated with Fourier transform ion cyclotron resonance (FT-ICR) mass spectrometry, of which a number of reviews are available.¹¹ Only details relevant to these experiments are outlined here. In the Caltech instrument, a 1-in. cubic trapping cell is located between the poles of a Varian 15-in. electromagnet maintained at 1.0 T. Data collection is accomplished with an IonSpec Omega 386 FT-ICR data system and associated electronics. Neutral gases are introduced into the cell by separate leak valves, and their pressures are measured with a Schultz-Phelps ion gauge calibrated against an MKS 390 HA-00001SP05 capacitance manometer. The instrument at the

University of Nice-Sophia Antipolis has the same specifications, except that data collection is accomplished with a Bruker data system and associated electronics and pressures are measured with a Bayard-Alpert (BA) ionization gauge (Alcatel BN 111). The operation of the BA gauge has been described previously.¹⁰ Uncertainties in absolute pressures are estimated to be $\pm 20\%$. CD_3OH was obtained commercially from Merck, Sharp and Dohme, while ethanol and 1-propanol were obtained from Aldrich. All alcohols used were purified by freeze-pump-thaw cycling.

Sc^+ ions were produced by laser ablation of a scandium metal target with a N_2 laser at 337.1 nm.^{8,10} The reactant ion $\text{Sc}(\text{OCD}_3)_2^+$ was generated by reaction of Sc^+ with CD_3OH as shown in reactions 3 and 4, and unwanted ions were ejected from the cell using double resonance techniques¹² and/or frequency sweep excitation.¹³ Water, ethanol or 1-propanol was then added along with the labeled methanol and the resulting metathesis reactions were observed. By isolating the resultant $\text{CD}_3\text{OScOR}^+$ ($\text{R} = \text{H}$, or ethyl) that formed, we were also able to observe a second metathesis reaction. The CD_3OH pressures used in these experiments were in the range $(0.3-1.5)\times 10^{-7}$ Torr, while the pressure of the additional alcohols were typically in the range $(0.1-2.0)\times 10^{-7}$ Torr. The H_2O pressures used were in the range $(1.5-2.5)\times 10^{-7}$ Torr. Time plots of the relative abundance of ions versus time were recorded for all reactions. Equilibrium was deemed to have been achieved when the relative ion abundances (with respect to each other) of the two ions of interest ceased to vary with time. For the general process $\text{A}^+ + \text{B} \rightarrow \text{C}^+ + \text{D}$ the equilibrium constant is derived from equation 5, where I_{A^+} and I_{C^+} are the

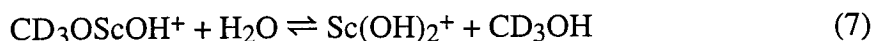
$$K = \frac{(I_{\text{C}^+})(P_{\text{D}})}{(I_{\text{A}^+})(P_{\text{B}})} \quad (5)$$

relative intensities of A^+ and C^+ and P_{B} and P_{D} are the partial pressures of B and D. The reported equilibrium constants are averages of several different sets of experimental data taken at different pressures of the neutral gases. Rate constants were calculated from appropriate semilog plots of reactant ion abundance versus time. Errors in the rate

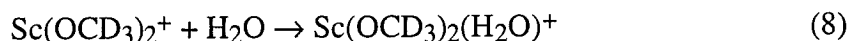
constants are estimated to be $\pm 20\%$ due to uncertainties in the determination of absolute pressure. All experiments were performed at ambient temperature.

Results

Reaction of $\text{Sc}(\text{OCD}_3)_2^+$ with Water. The processes of interest to us are the metathesis reactions 6 and 7. However, in addition to these metathesis processes, several



solvation processes (reactions 8-10) are also observed. Higher mass clusters were not



seen. Equilibrium was established for reactions 6 and 7. In some experiments $\text{Sc}(\text{OCD}_3)_2^+$ was isolated (see Figure 1a) and allowed to react with water. A typical mass spectrum of the products is shown in Figure 1b. In Figure 2 we present a time plot of the relative abundance of $\text{Sc}(\text{OCD}_3)_2^+$ and $\text{CD}_3\text{OScOH}^+$ versus time. For $\text{Sc}(\text{OCD}_3)_2^+$ we found that the rate constants for solvation with water and CD_3OH , k_8 and k_9 , are 1.7×10^{-11} and $6.2 \times 10^{-11} \text{ cm}^3\text{s}^{-1}\text{molecule}^{-1}$, respectively. For reaction 6 we find that the equilibrium constant K is 0.013. With this value of K we can calculate that the forward and reverse rate constants of reaction 6, k_6 and k_{-6} , are 2.9×10^{-11} and $2.0 \times 10^{-9} \text{ cm}^3\text{s}^{-1}\text{molecule}^{-1}$, respectively.

By monitoring the reaction of isolated $\text{CD}_3\text{OScOH}^+$ (see Figure 3a) with water (a typical mass spectrum of the products is shown in Figure 3b), we were able to derive time plots of the relative abundance of $\text{CD}_3\text{OScOH}^+$ and $\text{Sc}(\text{OH})_2^+$ (see Figure 4). For $\text{CD}_3\text{OScOH}^+$ we find that the rate constant of metathesis with CD_3OH , k_{-6} , is $1.7 \times 10^{-9} \text{ cm}^3\text{s}^{-1}\text{molecule}^{-1}$, in good agreement with the value derived from the reaction of $\text{Sc}(\text{OCD}_3)_2^+$ with water. For reaction 7 we find that the equilibrium constant K is 0.013.

Figure 1. Reaction of $\text{Sc}(\text{OCD}_3)_2^+$ with a $\text{H}_2\text{O}/\text{CD}_3\text{OH}$ mixture. The pressures of CD_3OH and H_2O were 0.41×10^{-7} Torr and 1.12×10^{-7} Torr, respectively: a) Isolation of $\text{Sc}(\text{OCD}_3)_2^+$ at $t = 0$ ms. b) Products of the reaction of $\text{Sc}(\text{OCD}_3)_2^+$ with the $\text{H}_2\text{O}/\text{CD}_3\text{OH}$ mixture. Spectrum was taken 700 ms after isolation of $\text{Sc}(\text{OCD}_3)_2^+$.

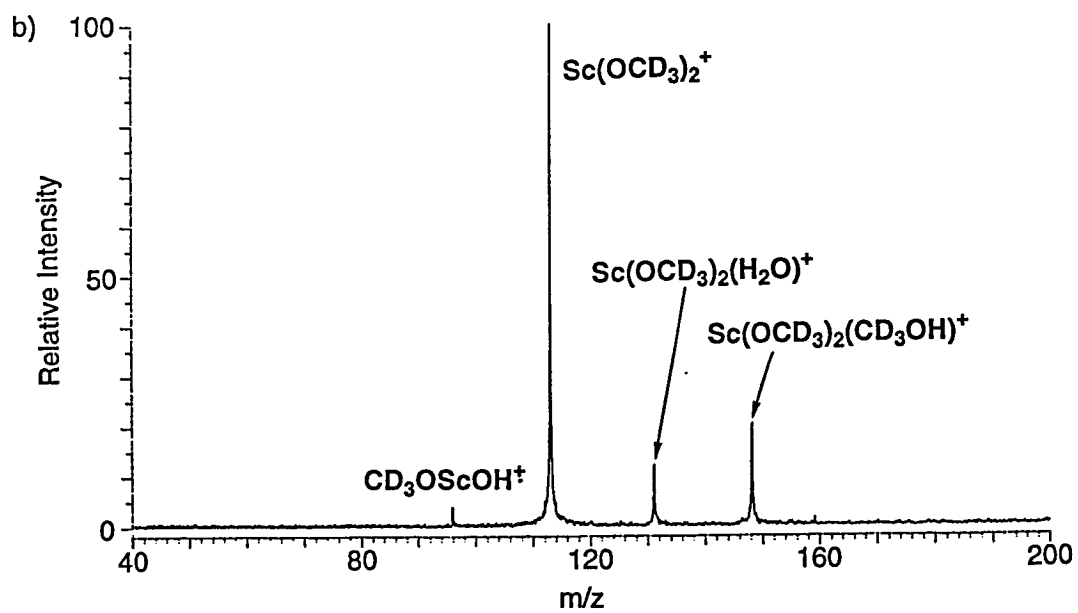
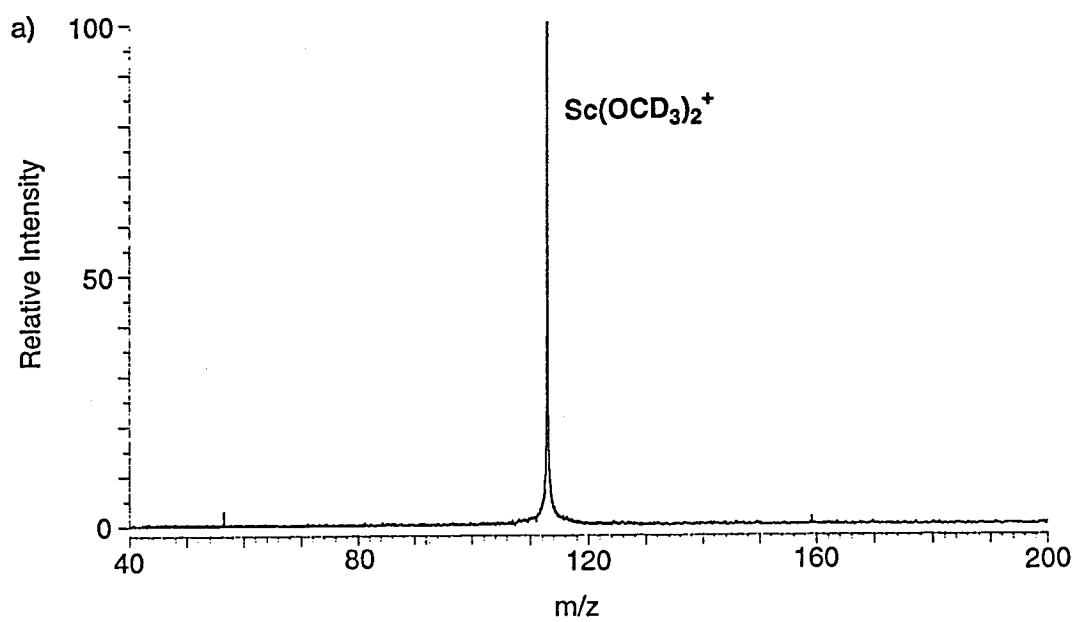


Figure 2. Time plot of the relative abundance of $\text{Sc}(\text{OCD}_3)_2^+$ and $\text{CD}_3\text{OScOH}^+$ versus time. During this time plot the pressures of CD_3OH and H_2O were 0.47×10^{-7} Torr and 1.43×10^{-7} Torr, respectively. For this specific time plot we find that $K = 0.014$.

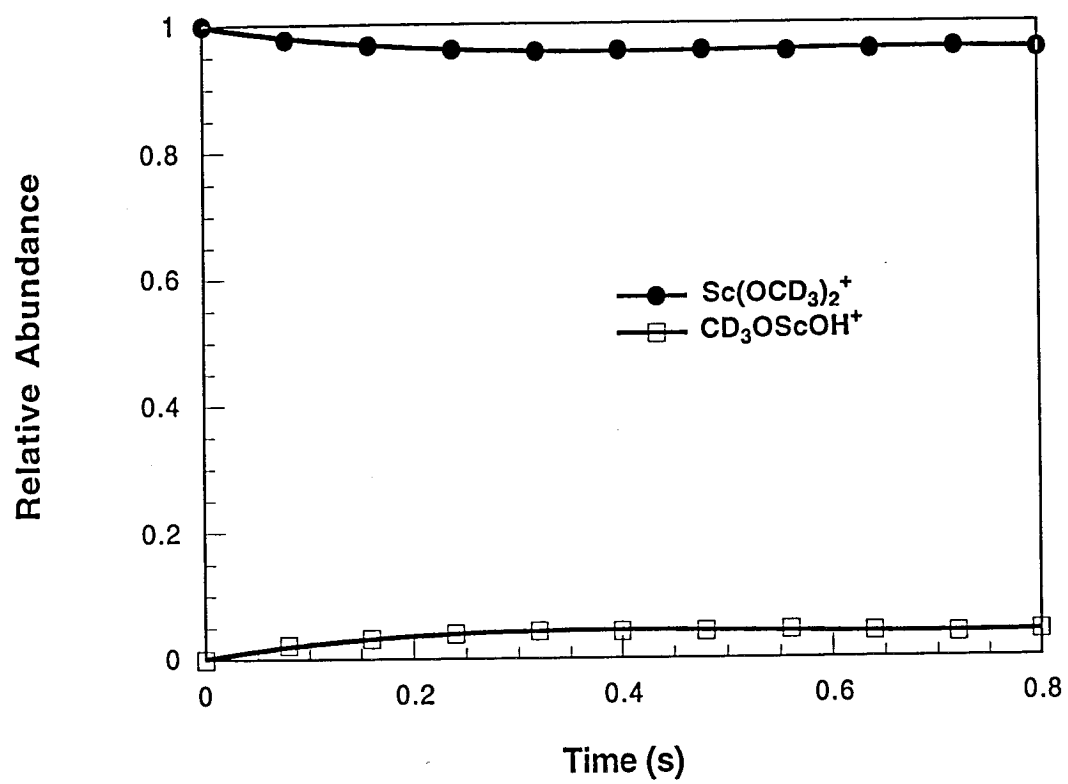


Figure 3. Reaction of $\text{CD}_3\text{OScOH}^+$ with a $\text{H}_2\text{O}/\text{CD}_3\text{OH}$ mixture. The pressures of CD_3OH and H_2O were 0.45×10^{-7} Torr and 1.43×10^{-7} Torr, respectively: a) Isolation of $\text{CD}_3\text{OScOH}^+$ at $t = 0$ ms. b) Products of the reaction of $\text{CD}_3\text{OScOH}^+$ with the $\text{H}_2\text{O}/\text{CD}_3\text{OH}$ mixture. Spectrum was taken 450 ms after isolation of $\text{CD}_3\text{OScOH}^+$.

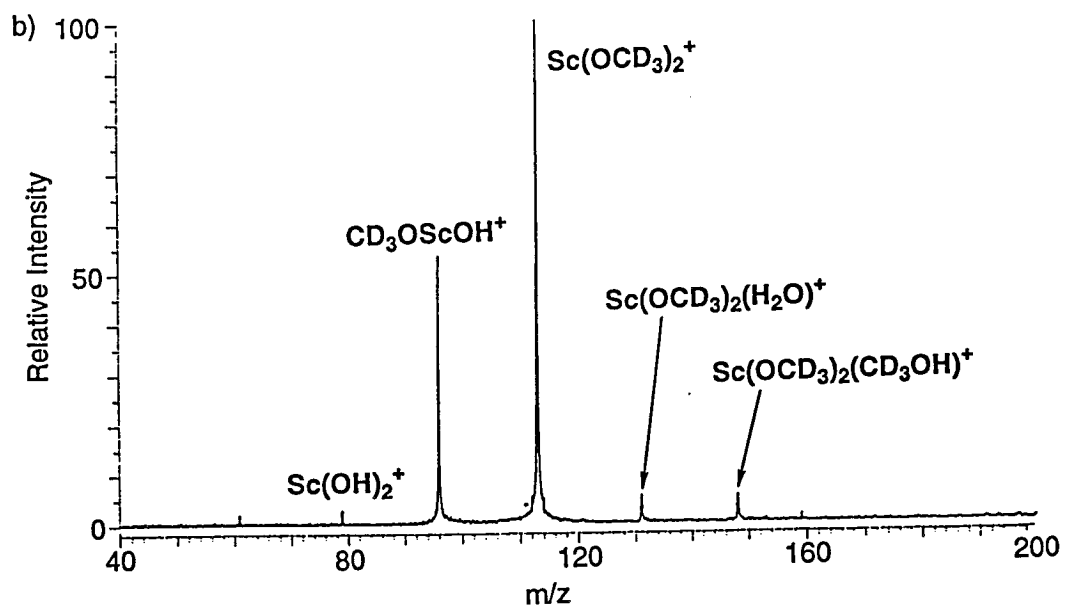
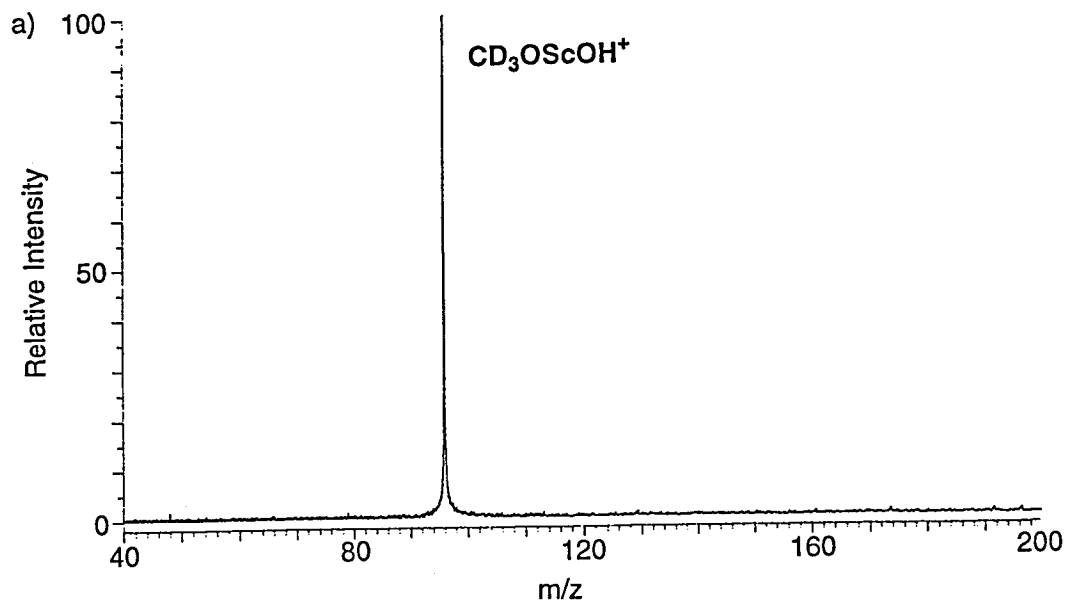
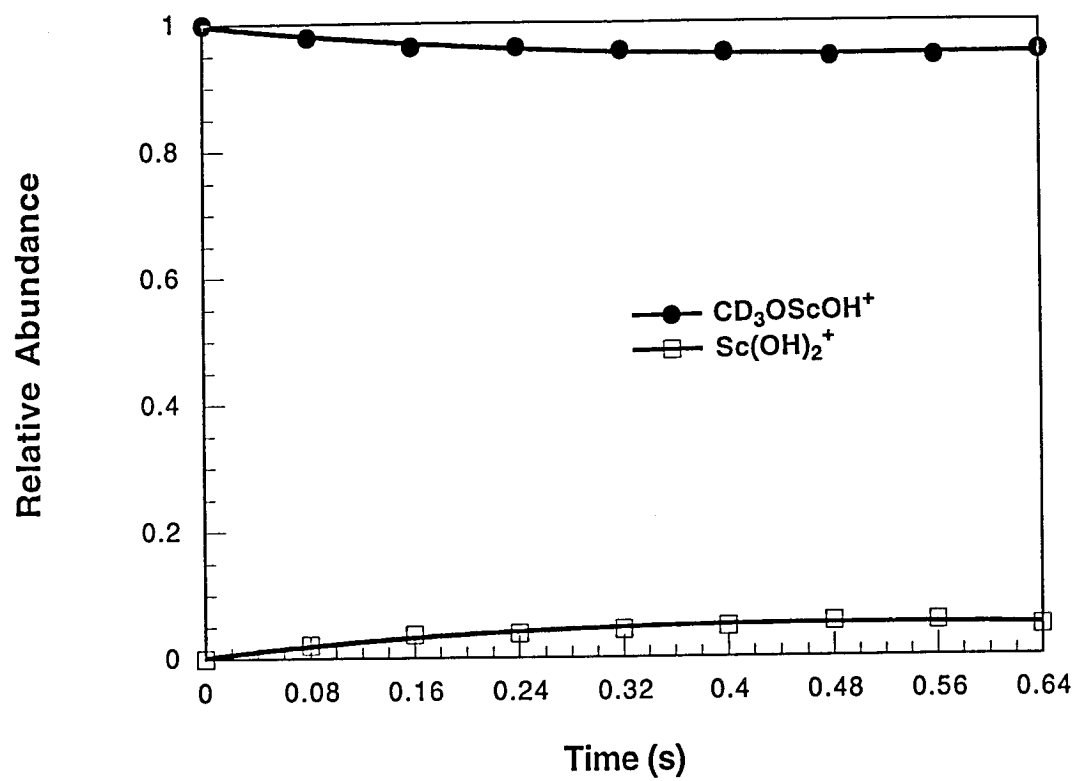


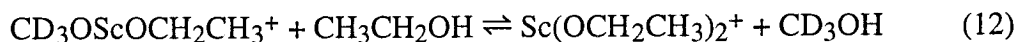
Figure 4. Time plot of the relative abundance of $\text{CD}_3\text{OScOH}^+$ and $\text{Sc}(\text{OH})_2^+$ versus time. During this time plot the pressures of CD_3OH and H_2O were 0.45×10^{-7} Torr and 1.43×10^{-7} Torr, respectively. For this specific time plot we find that $K = 0.013$.



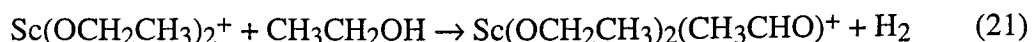
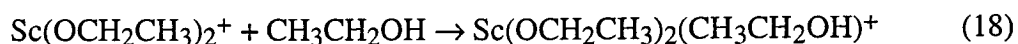
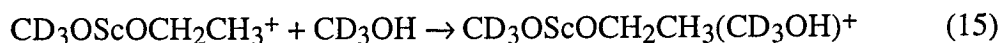
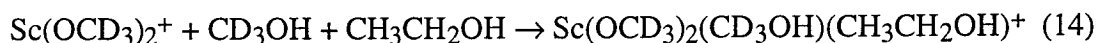
With this value of K we can calculate that the forward and reverse rate constants of reaction 7, k_7 and k_{-7} , are 3.3×10^{-11} and $2.3 \times 10^{-9} \text{ cm}^3 \text{ s}^{-1} \text{ molecule}^{-1}$, respectively.

Reaction 6 reaches equilibrium quickly and the half-life to reach equilibrium is 0.22 s, while the half-life for the solvation of $\text{Sc}(\text{OCD}_3)_2^+$ with methanol is 8.5 s. This suggests that the equilibrium constant derived was not affected by the solvation of $\text{Sc}(\text{OCD}_3)_2^+$. For $\text{CD}_3\text{OScOH}^+$ the rate constant of metathesis with CD_3OH , k_{-6} , is only slightly smaller than the reverse rate constant, k_{-7} , of reaction 7, and the half-life for reaction 7 to reach equilibrium is 0.19 s, while the half-life for metathesis with CD_3OH is 0.18 s. However, reaction 7 usually reached equilibrium while the relative intensity of $\text{CD}_3\text{OScOH}^+$ was greater than 80%. Thus, although it is possible that the observed equilibrium constant was adversely affected by the metathesis reaction of $\text{CD}_3\text{OScOH}^+$ with CD_3OH , we believe that the observed equilibrium constant for reaction 7 is near its true value.

Reaction of $\text{Sc}(\text{OCD}_3)_2^+$ with Ethanol. The processes of interest to us are the metathesis reactions 11 and 12. In addition to these metathesis processes several



solvation (reactions 9 and 13-18) and elimination (reactions 19-21) processes are also



observed. We did not attempt to observe higher mass clusters. No HD loss is seen, indicating that the elimination of hydrogen from complexed methanol does not occur. Such clustering has been observed previously between $\text{Sc}(\text{OCH}_3)_2^+$ and CH_3OH .¹⁰ Equilibrium was established for reactions 11 and 12. In some experiments $\text{Sc}(\text{OCD}_3)_2^+$ was isolated (see Figure 5a) and allowed to react with ethanol. A typical mass spectrum of the products is shown in Figure 5b. In Figure 6 we show a time plot of the relative abundance of $\text{Sc}(\text{OCD}_3)_2^+$ and $\text{CD}_3\text{OScOCH}_2\text{CH}_3^+$ versus time. For $\text{Sc}(\text{OCD}_3)_2^+$ we found that the rate constants of solvation with CD_3OH and $\text{CH}_3\text{CH}_2\text{OH}$, k_9 and k_{13} , are 6.1×10^{-11} and $7.7 \times 10^{-10} \text{ cm}^3\text{s}^{-1}\text{molecule}^{-1}$, respectively. The value of k_9 derived here is in excellent agreement with the value derived when $\text{Sc}(\text{OCD}_3)_2^+$ is reacted with $\text{CD}_3\text{OH}/\text{water}$ mixtures. For reaction 11 we find that the equilibrium constant K is 0.5. With this value of K we can calculate that the forward and reverse rate constants of reaction 11, k_{11} and k_{-11} , are 4.6×10^{-10} and $9.3 \times 10^{-10} \text{ cm}^3\text{s}^{-1}\text{molecule}^{-1}$, respectively.

By monitoring the reaction of the isolated $\text{CD}_3\text{OScOCH}_2\text{CH}_3^+$ (see Figure 7a) with ethanol (a typical mass spectrum of the products is shown in Figure 7b), we were also able to derive time plots of the relative abundance of $\text{CD}_3\text{OScOCH}_2\text{CH}_3^+$ and $\text{Sc}(\text{OCH}_2\text{CH}_3)_2^+$ (see Figure 8). For $\text{CD}_3\text{OScOCH}_2\text{CH}_3^+$ we find that the rate constants of solvation with CD_3OH and $\text{CH}_3\text{CH}_2\text{OH}$, k_{15} and k_{16} , are 5.4×10^{-10} and $4.1 \times 10^{-10} \text{ cm}^3\text{s}^{-1}\text{molecule}^{-1}$, respectively. For $\text{CD}_3\text{OScOCH}_2\text{CH}_3^+$ we find that the rate constant of metathesis with CD_3OH , k_{-11} , is $7.2 \times 10^{-10} \text{ cm}^3\text{s}^{-1}\text{molecule}^{-1}$, in reasonable agreement with the value derived from the reaction of $\text{Sc}(\text{OCD}_3)_2^+$ with ethanol. For reaction 12 we find that the equilibrium constant K is 0.3. With this value of K we can calculate that the forward and reverse rate constants of reaction 12, k_{12} and k_{-12} , are 2.3×10^{-11} and $7.5 \times 10^{-10} \text{ cm}^3\text{s}^{-1}\text{molecule}^{-1}$, respectively.

For reaction 11, equilibrium is usually reached while relative intensity of $\text{Sc}(\text{OCD}_3)_2^+$ is greater than 80%. Furthermore, the half-life to reach equilibrium is 0.12 s, while the half-life for the solvation of $\text{Sc}(\text{OCD}_3)_2^+$ with ethanol is 0.39 s. This

Figure 5. Reaction of $\text{Sc}(\text{OCD}_3)_2^+$ with a $\text{CD}_3\text{OH}/\text{CH}_3\text{CH}_2\text{OH}$ mixture. The pressures of CD_3OH and $\text{CH}_3\text{CH}_2\text{OH}$ were 1.16×10^{-7} Torr and 0.71×10^{-7} Torr, respectively: a) Isolation of $\text{Sc}(\text{OCD}_3)_2^+$ at $t = 0$ ms. b) Products of the reaction of $\text{Sc}(\text{OCD}_3)_2^+$ with the $\text{CD}_3\text{OH}/\text{CH}_3\text{CH}_2\text{OH}$ mixture. Spectrum was taken 400 ms after isolation of $\text{Sc}(\text{OCD}_3)_2^+$. CH_3CH_2 is abbreviated as Et in this figure. The peaks at m/z 148 and m/z 196 correspond to $\text{Sc}(\text{OCD}_3)_2(\text{CD}_3\text{OH})^+$ and $\text{Sc}(\text{OCD}_3)_2(\text{CD}_3\text{OH})(\text{CH}_3\text{CH}_2\text{OH})^+$, respectively. We should note that $\text{CD}_3\text{OScOCH}_2\text{CH}_3(\text{CH}_3\text{CH}_2\text{OH})^+$ and $\text{Sc}(\text{OCD}_3)_2(\text{CH}_3\text{CH}_2\text{OH})^+$ could also be $\text{Sc}(\text{OCH}_2\text{CH}_3)_2(\text{CD}_3\text{OH})^+$ and $\text{CD}_3\text{OScOCH}_2\text{CH}_3(\text{CD}_3\text{OH})^+$, respectively. However, since the reactant ion is $\text{Sc}(\text{OCD}_3)_2^+$, it is likely that the two former structures are the dominant forms present.

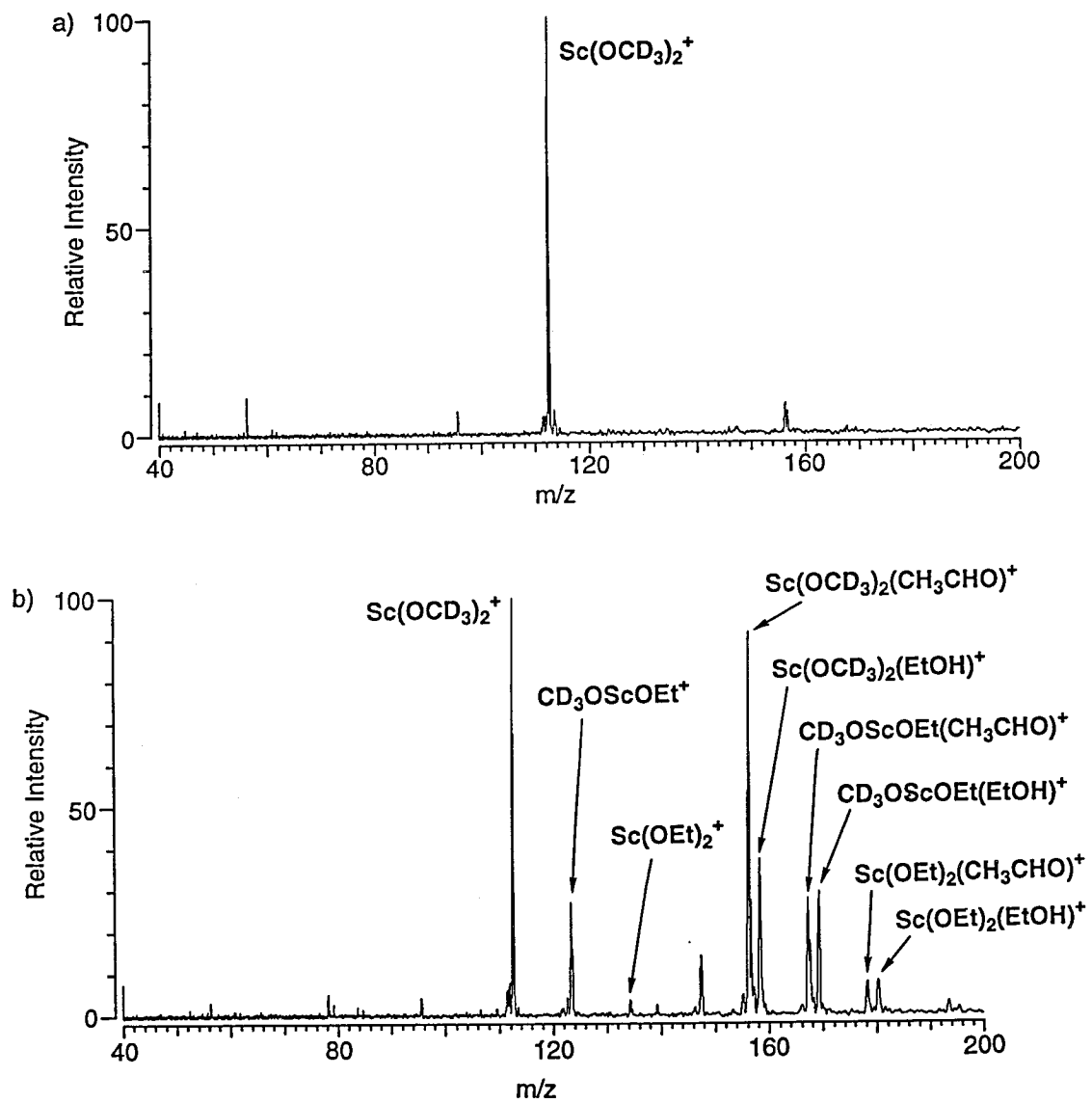


Figure 6. Time plot of the relative abundance of $\text{Sc}(\text{OCD}_3)_2^+$ and $\text{CD}_3\text{OScOCH}_2\text{CH}_3^+$ versus time. CH_3CH_2 is abbreviated as Et in this figure. During this time plot the pressures of CD_3OH and $\text{CH}_3\text{CH}_2\text{OH}$ were 1.16×10^{-7} Torr and 0.71×10^{-7} Torr, respectively. For this specific time plot we find that $K = 0.46$.

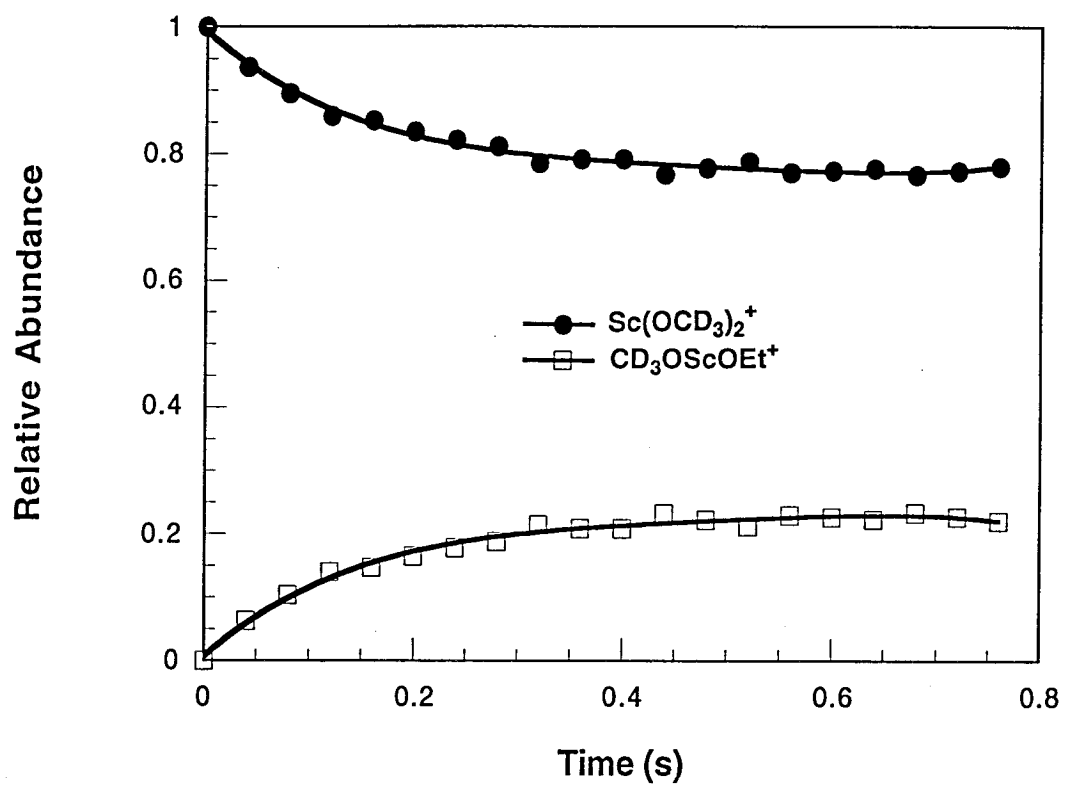


Figure 7. Reaction of $\text{CD}_3\text{OScOCH}_2\text{CH}_3^+$ with a $\text{CD}_3\text{OH}/\text{CH}_3\text{CH}_2\text{OH}$ mixture. The pressures of CD_3OH and $\text{CH}_3\text{CH}_2\text{OH}$ were 0.69×10^{-7} Torr and 0.75×10^{-7} Torr, respectively. CH_3CH_2 is abbreviated as Et in this figure: a) Isolation of $\text{CD}_3\text{OScOCH}_2\text{CH}_3^+$ at $t = 0$ ms. b) Products of the reaction of $\text{CD}_3\text{OScOCH}_2\text{CH}_3^+$ with the $\text{CD}_3\text{OH}/\text{CH}_3\text{CH}_2\text{OH}$ mixture. Spectrum was taken 540 ms after isolation of $\text{CD}_3\text{OScOCH}_2\text{CH}_3^+$. We should note that $\text{CD}_3\text{OScOCH}_2\text{CH}_3(\text{CD}_3\text{OH})^+$ and $\text{CD}_3\text{OScOCH}_2\text{CH}_3(\text{CH}_3\text{CH}_2\text{OH})^+$ could also be $\text{Sc}(\text{OCD}_3)_2(\text{CH}_3\text{CH}_2\text{OH})^+$ and $\text{Sc}(\text{OCH}_2\text{CH}_3)_2(\text{CD}_3\text{OH})^+$, respectively. However, since the reactant ion is $\text{CD}_3\text{OScOCH}_2\text{CH}_3^+$, it is likely that the two former structures are the dominant forms present.

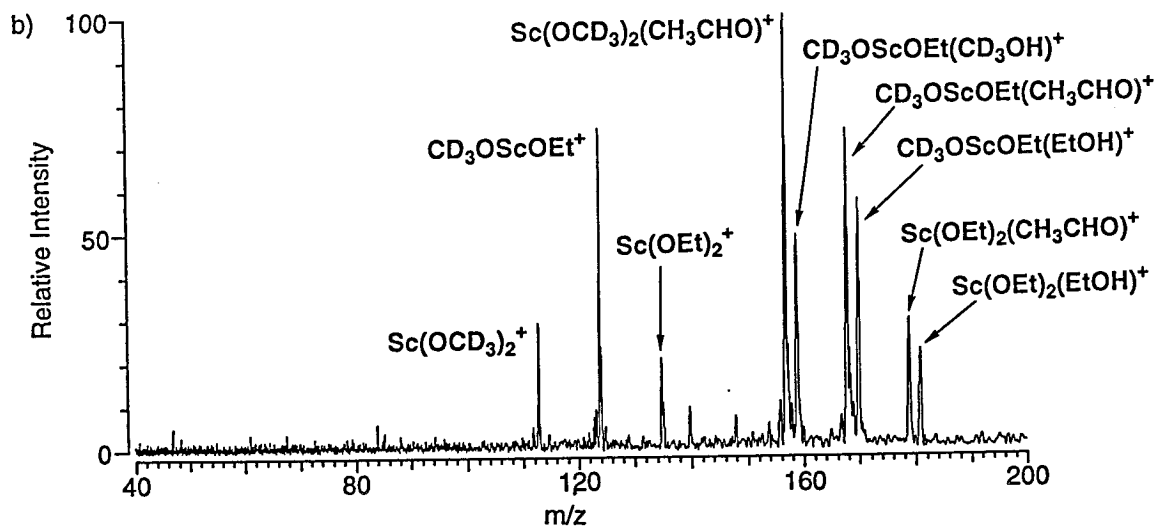
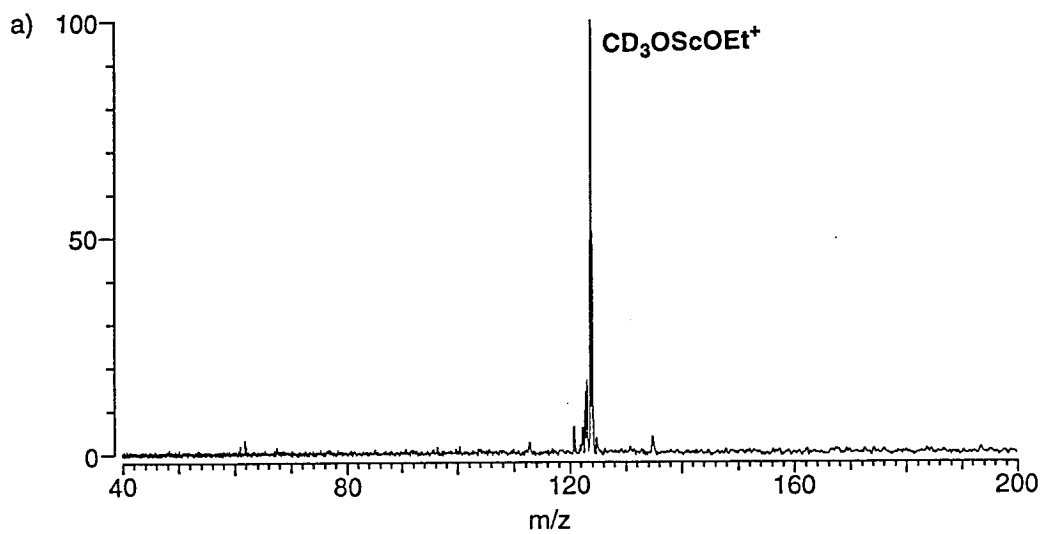
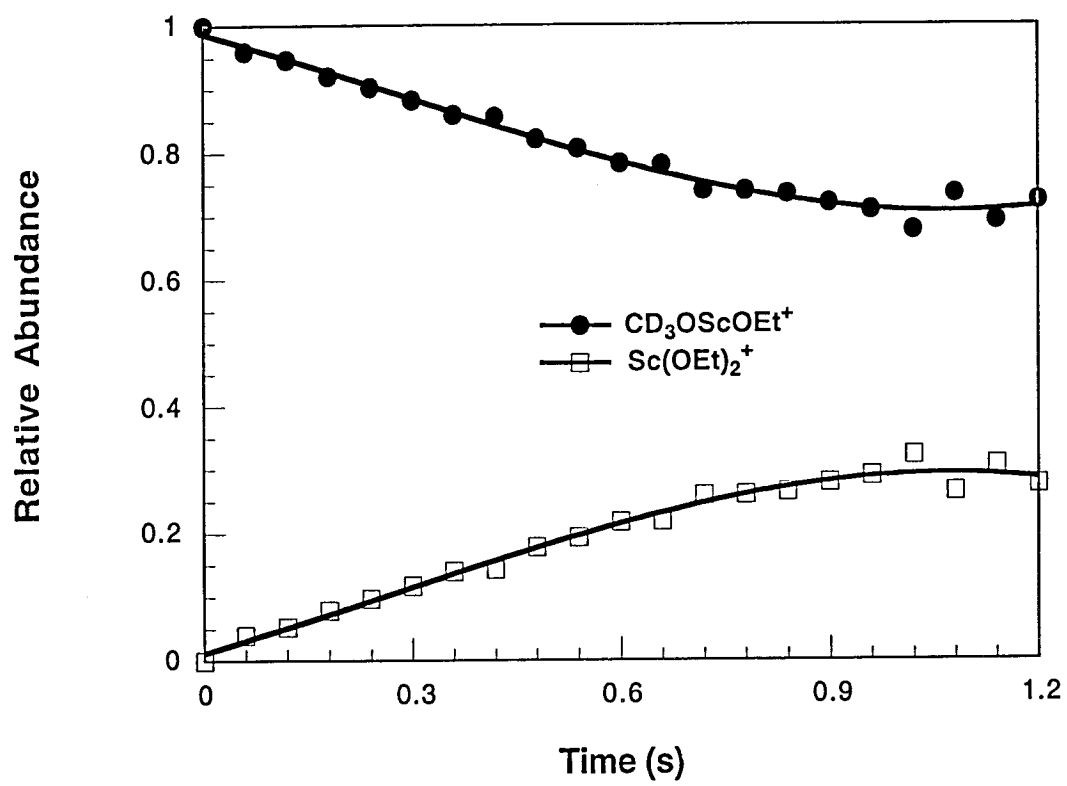
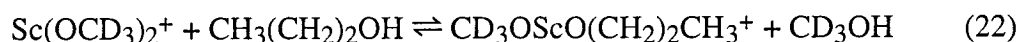


Figure 8. Time plot of the relative abundance of $\text{CD}_3\text{OScOCH}_2\text{CH}_3^+$ and $\text{Sc}(\text{OCH}_2\text{CH}_3)_2^+$ versus time. CH_3CH_2 is abbreviated as Et in this figure. During this time plot the pressures of CD_3OH and $\text{CH}_3\text{CH}_2\text{OH}$ were 0.69×10^{-7} Torr and 0.75×10^{-7} Torr, respectively. For this specific time plot we find that $K = 0.38$.

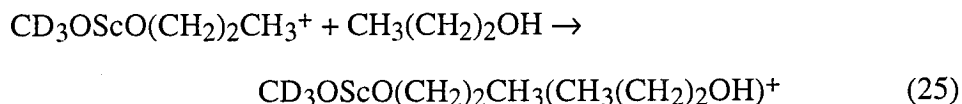
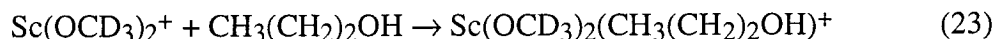


suggests that the observed equilibrium constant is not affected by the solvation of $\text{Sc}(\text{OCD}_3)_2^+$. For $\text{CD}_3\text{OScOCH}_2\text{CH}_3^+$, the rate constants for solvation with CD_3OH and $\text{CH}_3\text{CH}_2\text{OH}$, k_{15} and k_{16} , are comparable to the reverse rate constant of reaction 12. However, even though the half-life to reach equilibrium is 0.31 s while the half-life for the solvation of $\text{CD}_3\text{OScOCH}_2\text{CH}_3^+$ with methanol is 0.58 s, equilibrium was generally not reached until the relative intensity of $\text{CD}_3\text{OScOCH}_2\text{CH}_3^+$ had fallen below 50%. Thus it is possible that the observed equilibrium constant for reaction 12 was adversely affected by the competing solvation processes.

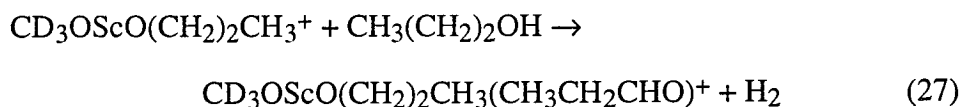
Reaction of $\text{Sc}(\text{OCD}_3)_2^+$ with 1-Propanol. The main process of interest to us is the metathesis reaction 22. Unfortunately, we were unable to reproducibly measure an



equilibrium constant for the reaction of $\text{CD}_3\text{OScO}(\text{CH}_2)_2\text{CH}_3^+$ with $\text{CH}_3(\text{CH}_2)_2\text{OH}$. Again, in addition to reaction 22 several solvation (reactions 9 and 23-25) and



elimination (reactions 26 and 27) processes are also observed. We did not attempt to



observe higher mass clusters. Equilibrium was established for reaction 22. $\text{Sc}(\text{OCD}_3)_2^+$ was isolated as shown in Figure 9a and allowed to react with 1-propanol. A typical mass spectrum of the products is shown in Figure 9b and a time plot of the relative abundance of $\text{Sc}(\text{OCD}_3)_2^+$ and $\text{CD}_3\text{OScO}(\text{CH}_2)_2\text{CH}_3^+$ versus time is presented in Figure 10. We found that the rate constants of solvation with CD_3OH and $\text{CH}_3(\text{CH}_2)_2\text{OH}$, k_9 and k_{23} , are 6.3×10^{-11} and $1.3 \times 10^{-9} \text{ cm}^3\text{s}^{-1}\text{molecule}^{-1}$, respectively. Again, the value of k_9

Figure 9. Reaction of $\text{Sc}(\text{OCD}_3)_2^+$ with a $\text{CD}_3\text{OH}/\text{CH}_3(\text{CH}_2)_2\text{OH}$ mixture. The pressures of CD_3OH and $\text{CH}_3(\text{CH}_2)_2\text{OH}$ were 0.58×10^{-7} Torr and 0.14×10^{-7} Torr, respectively: a) Isolation of $\text{Sc}(\text{OCD}_3)_2^+$ at $t = 0$ ms. b) Products of the reaction of $\text{Sc}(\text{OCD}_3)_2^+$ with $\text{CH}_3(\text{CH}_2)_2\text{OH}$. Spectrum was taken 1200 ms after isolation of $\text{Sc}(\text{OCD}_3)_2^+$. $\text{CH}_3(\text{CH}_2)_2$ is abbreviated as Pr in this figure. We should note that $\text{Sc}(\text{OCD}_3)_2(\text{CH}_3(\text{CH}_2)_2\text{OH})^+$ and $\text{CD}_3\text{OScO}(\text{CH}_2)_2\text{CH}_3(\text{CH}_3(\text{CH}_2)_2\text{OH})^+$ could also be $\text{CD}_3\text{OScO}(\text{CH}_2)_2\text{CH}_3(\text{CD}_3\text{OH})^+$ and $\text{Sc}(\text{O}(\text{CH}_2)_2\text{CH}_3)_2(\text{CD}_3\text{OH})^+$, respectively. However, since the reactant ion is $\text{Sc}(\text{OCD}_3)_2^+$, it is likely that the two former structures are the dominant forms present.

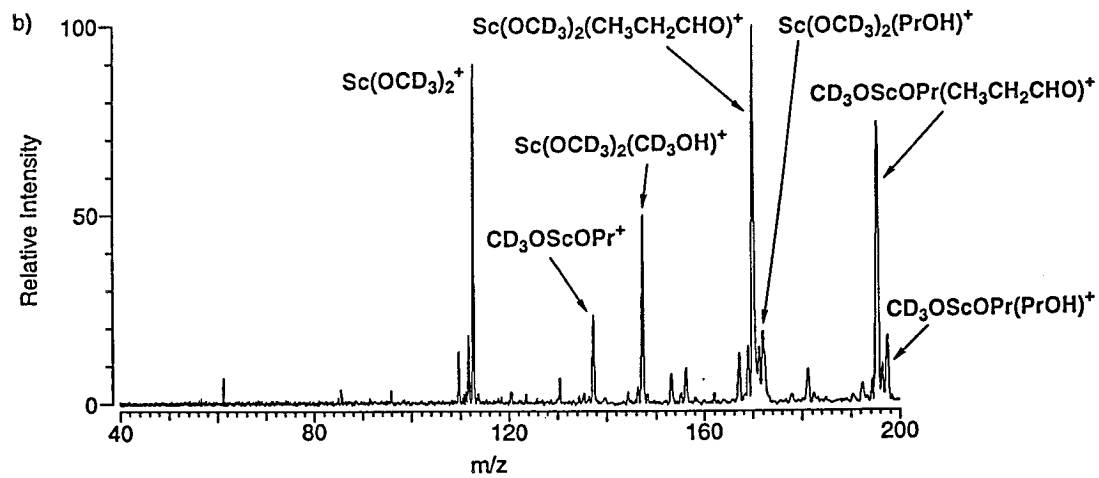
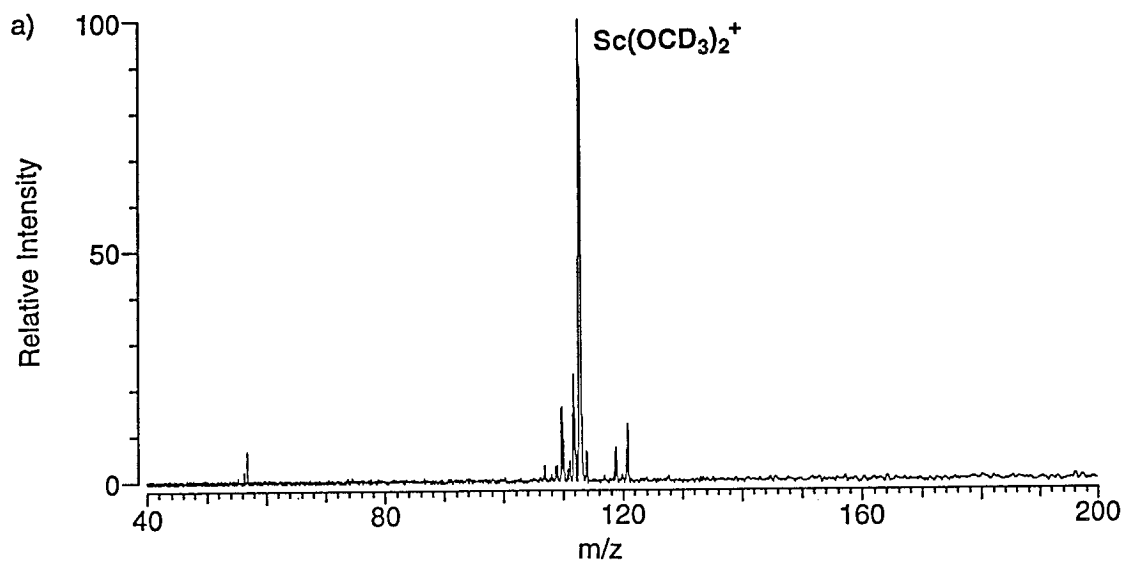
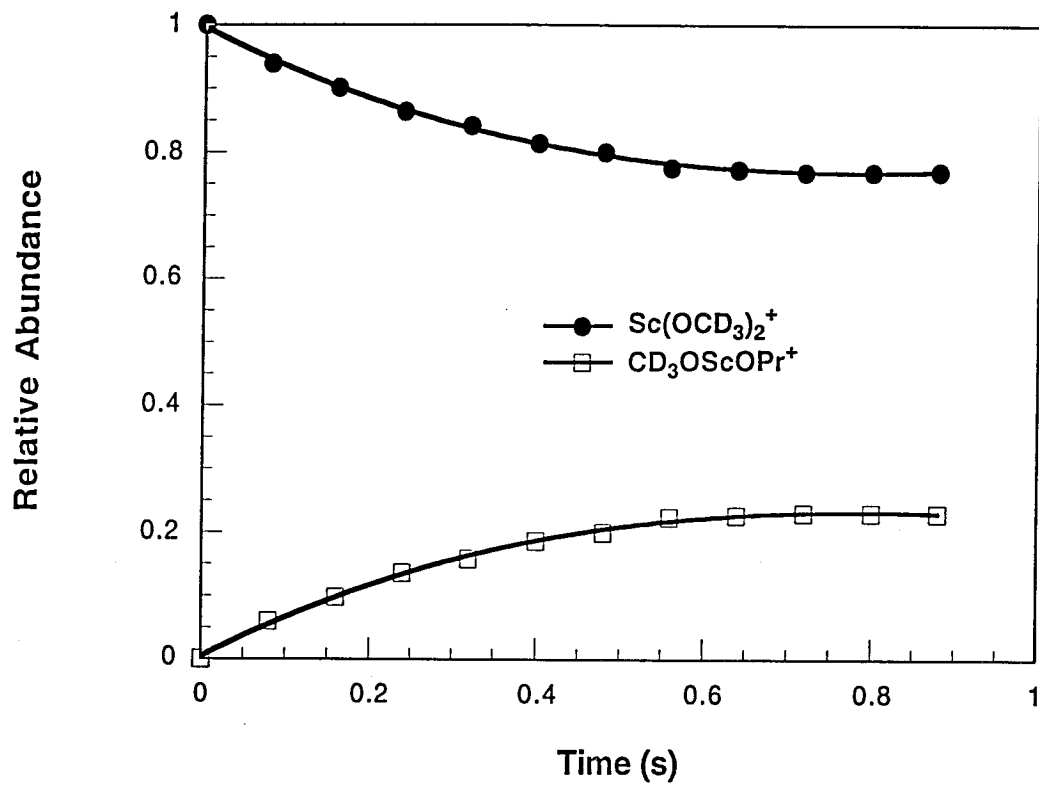


Figure 10. Time plot of the relative abundance of $\text{Sc}(\text{OCD}_3)_2^+$ and $\text{CD}_3\text{OScO}(\text{CH}_2)_2\text{CH}_3^+$ versus time. $\text{CH}_3(\text{CH}_2)$ is abbreviated as Pr in this figure. During this time plot the pressures of CD_3OH and $\text{CH}_3(\text{CH}_2)\text{OH}$ were 0.58×10^{-7} Torr and 0.23×10^{-7} Torr, respectively. For this specific time plot we find that $K = 0.75$.



derived here is in excellent agreement with the value derived when $\text{Sc}(\text{OCD}_3)_2^+$ is reacted with $\text{CD}_3\text{OH}/\text{water}$ mixtures. For reaction 22 we find that the equilibrium constant K is 0.7. With this value of K we can calculate that the forward and reverse rate constants of reaction 22, k_{22} and k_{-22} , are 8.2×10^{-10} and $1.2 \times 10^{-9} \text{ cm}^3\text{s}^{-1}\text{molecule}^{-1}$, respectively. For reaction 22 the half-life to reach equilibrium is 0.27 s, while the half-life for the solvation of $\text{Sc}(\text{OCD}_3)_2^+$ with 1-propanol is 1.2 s. Furthermore, the relative intensity of $\text{Sc}(\text{OCD}_3)_2^+$ is usually greater than 90% when equilibrium is reached. This suggests that the equilibrium constant derived was not affected by the solvation of $\text{Sc}(\text{OCD}_3)_2^+$. Table 1 presents a summary of the metathesis equilibria we observed.

Ab Initio Calculations

Equilibrium measurements will provide us with ΔG for a reaction, but we cannot calculate ΔH without knowing ΔS . In order to estimate ΔS for these reactions and compare the theoretical values of ΔG to our experimental measurements, we performed ab initio calculations to theoretically evaluate ΔS and ΔH for the metathesis reactions shown in reactions 28-30 (identical to the reverse of reaction 7, the reverse of reaction 6,



and reaction 11, respectively, except that the methoxide ligands contain H instead of D).

The PS-GVB system of programs¹⁴ was used for all the calculations performed. A 6-31G* basis set was used for C, H and O, while for Sc^+ we used an effective core potential (ECP) to replace all but the valence and outer core 3s/3p electrons.¹⁵ Initial geometry optimizations were performed at the Hartree-Fock (HF) level for $\text{Sc}(\text{OH})_2^+$, $\text{CH}_3\text{OScOH}^+$, $\text{Sc}(\text{OCH}_3)_2^+$, $\text{CH}_3\text{OScOCH}_2\text{CH}_3^+$, H_2O , CH_3OH and $\text{CH}_3\text{CH}_2\text{OH}$. These structures were then further optimized at the localized second-order Møller-Plesset (LMP2) perturbation level of theory. Harmonic vibrational frequencies were also

Table 1. Summary of Observed Ligand Exchange Equilibria Established Via σ -Bond Metathesis.^a

Process	K	ΔG (kcal mol ⁻¹)	ΔH (kcal mol ⁻¹) ^b
$\text{Sc}(\text{OH})_2^+ + \text{CD}_3\text{OH} \rightleftharpoons$			
$\text{CD}_3\text{OScOH}^+ + \text{H}_2\text{O}$	77(27)	-2.6(0.2)	-2.9(0.6) ^c
$\text{CD}_3\text{OScOH}^+ + \text{CD}_3\text{OH} \rightleftharpoons$			
$\text{Sc}(\text{OCD}_3)_2^+ + \text{H}_2\text{O}$	77(27)	-2.6(0.2)	-2.9(0.6) ^c
$\text{Sc}(\text{OCD}_3)_2^+ + \text{CH}_3\text{CH}_2\text{OH} \rightleftharpoons$			
$\text{CD}_3\text{OScOCH}_2\text{CH}_3^+ + \text{CD}_3\text{OH}$	0.5(0.15)	+0.4(0.1)	+0.1(0.6) ^c
$\text{CD}_3\text{OScOCH}_2\text{CH}_3^+ + \text{CH}_3\text{CH}_2\text{OH} \rightleftharpoons$			
$\text{Sc}(\text{OCH}_2\text{CH}_3)_2^+ + \text{CD}_3\text{OH}$	0.3(0.1)	+0.7(0.2)	+0.3(0.6) ^d
$\text{Sc}(\text{OCD}_3)_2^+ + \text{CH}_3(\text{CH}_2)_2\text{OH} \rightleftharpoons$			
$\text{CD}_3\text{OScO}(\text{CH}_2)_2\text{CH}_3^+ + \text{CD}_3\text{OH}$	0.7(0.2)	+0.2(0.1)	+0.6(0.6) ^e

^aUncertainties are in parentheses. ^bAll values calculated assuming ambient $T = 298$ K.

^cCalculated using theoretical LMP2 value of ΔS (see Table 3). ^dCalculated assuming $\Delta S = -R\ln 2 = -1.38$ cal mol⁻¹K⁻¹ (ΔS estimated with equation 33). ^eCalculated assuming $\Delta S = R\ln 2 = 1.38$ cal mol⁻¹K⁻¹ (ΔS estimated with equation 33).

calculated for each of these species at the LMP2 level to obtain zero-point energies and absolute entropies at 298 K.

Several different conformations were calculated for $\text{Sc}(\text{OH})_2^+$, $\text{CH}_3\text{OScOH}^+$, $\text{Sc}(\text{OCH}_3)_2^+$ and $\text{CH}_3\text{OScOCH}_2\text{CH}_3^+$. Figure 11 shows the LMP2-optimized lowest energy geometry for these species.¹⁶ Table 2 presents the total energy, zero-point energy and absolute entropy calculated for $\text{Sc}(\text{OH})_2^+$, $\text{CH}_3\text{OScOH}^+$, $\text{Sc}(\text{OCH}_3)_2^+$, $\text{CH}_3\text{OScOCH}_2\text{CH}_3^+$, H_2O , CH_3OH and $\text{CH}_3\text{CH}_2\text{OH}$ at the LMP2 level of theory. Since the LMP2 level of theory is size-consistent, ΔH can be calculated as the difference of the electronic energies of the products and electronic energies of the reactants (with zero-point energies taken into account). The calculated ΔH_{298} , ΔS_{298} and ΔG_{298} for reactions 28-30 are given in Table 3.

In order to estimate the accuracy of these calculations, we have compared, where possible, the calculated values of $H_{298} - H_0$ and \bar{S}_{298} with the experimentally known values (see Table 2). For H_2O , CH_3OH and $\text{CH}_3\text{CH}_2\text{OH}$ the calculated values of $H_{298} - H_0$ agree very well with the experimental values, although the agreement worsens for the larger species. The calculated values of \bar{S}_{298} for H_2O , CH_3OH and $\text{CH}_3\text{CH}_2\text{OH}$ are also in good agreement with the experimental values, though again the agreement worsens as the size of the species increases. It appears that the LMP2 level of theory systematically underestimates the values of both $H_{298} - H_0$ and \bar{S}_{298} , with the error increasing as the size of the species increases. For ethanol the calculated \bar{S}_{298} is in error by about 3 cal mol⁻¹K⁻¹, so we estimate that our calculated \bar{S}_{298} values could be low by as much as 5-7 cal mol⁻¹K⁻¹ for $\text{CH}_3\text{OScOCH}_2\text{CH}_3^+$, the largest species for which we performed calculations. The error in our calculated ΔS_{298} values for reactions 28-30 should be less than this, but because the systematic error increases with size, we estimate that uncertainty in our calculated ΔS_{298} values could be as large as ± 2 cal mol⁻¹K⁻¹. We also compared our calculated values of ΔG_{298} for reactions 28-30 with the experimental values derived for reactions 6, 7 and 11 (see Table 3). In each case the calculated value

Figure 11. LMP2-optimized lowest energy geometry for (a) $\text{Sc}(\text{OH})_2^+$, (b) $\text{CH}_3\text{OScOH}^+$, (c) $\text{Sc}(\text{OCH}_3)_2^+$ and (d) $\text{CH}_3\text{OScOCH}_2\text{CH}_3^+$. All were calculated using the LAV3P* ECP basis set with no symmetry constraints. The optimized $\text{CH}_3\text{OScOH}^+$ and $\text{Sc}(\text{OCH}_3)_2^+$ geometries deviated slightly from C_s and C_{2v} symmetry, respectively. Structural parameters for each of these species are shown in Tables 4A-7A in the appendix to this chapter.

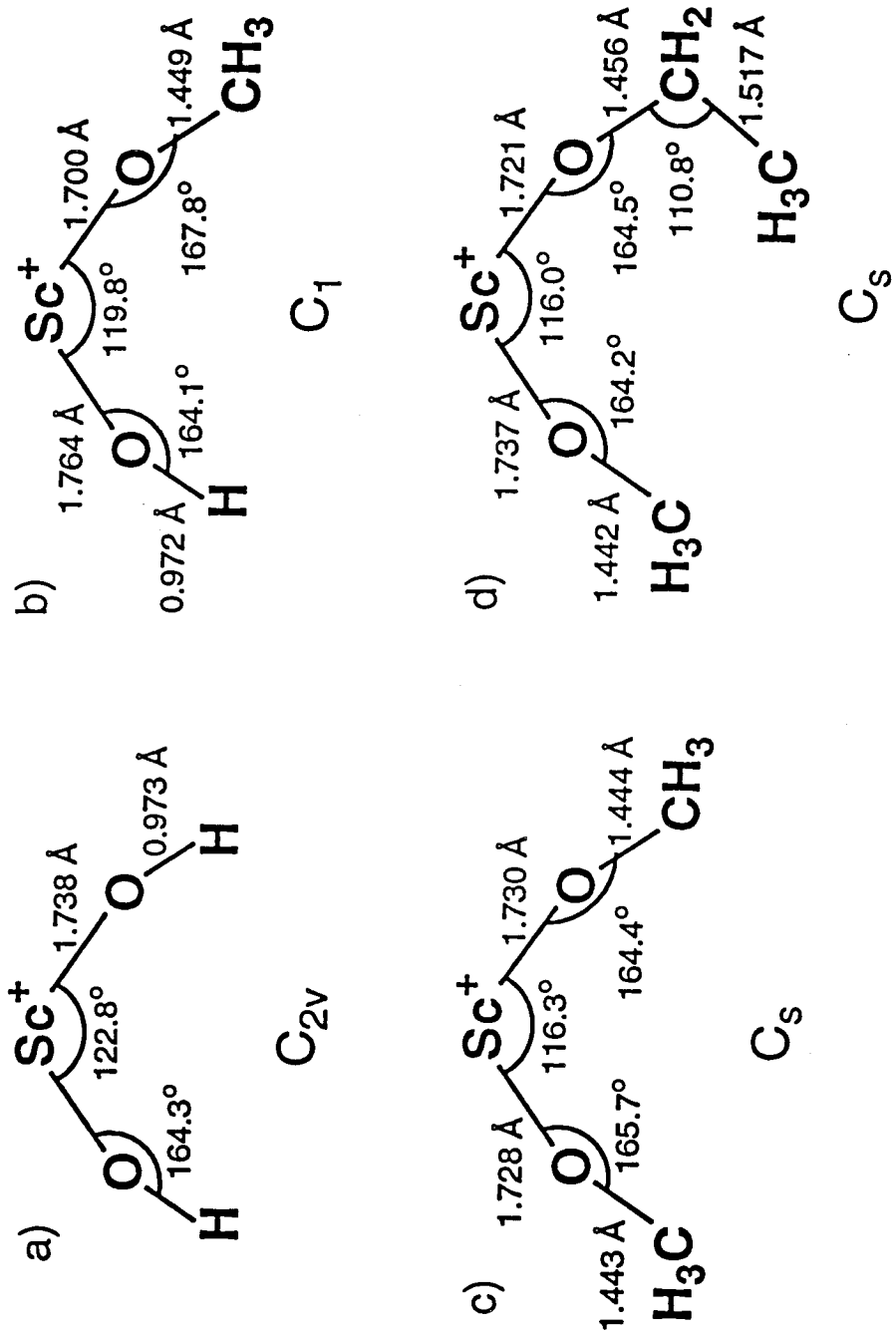


Table 2. Calculated Total Energies, Zero-Point Energies (ZPE), 0 K to 298 K Enthalpy Corrections ($H_{298} - H_0$) and Absolute Entropies.

Species	Total Energy (Hartree)	ZPE (kcal mol ⁻¹)	$H_{298} - H_0$ (kcal mol ⁻¹)	\bar{S}_{298} (cal mol ⁻¹ K ⁻¹)
H ₂ O	-76.19902	13.45	2.37 ^a	45.14 ^b
CH ₃ OH	-115.35021	33.00	2.65 ^c	56.71 ^d
CH ₃ CH ₂ OH	-154.52122	51.51	3.23 ^e	64.10 ^f
Sc(OH) ₂ ⁺	-152.77798	15.55	3.55	67.18
CH ₃ OScOH ⁺	-191.93894	34.53	4.65	77.68
Sc(OCH ₃) ₂ ⁺	-231.09899	52.98	5.92	88.11
CH ₃ OScOCH ₂ CH ₃ ⁺	-270.26630	71.24	6.29	94.60

^aExperimental value is 2.37 kcal mol⁻¹ (reference 17). ^bExperimental value is 45.10 cal mol⁻¹K⁻¹ (reference 17). ^cExperimental value is 2.73 kcal mol⁻¹ (reference 17). ^dExperimental value is 57.29 cal mol⁻¹K⁻¹ (reference 17). ^eExperimental value is 3.39 kcal mol⁻¹ (reference 17). ^fExperimental value is 67.54 cal mol⁻¹K⁻¹ (reference 17).

Table 3. Calculated ΔH_{298} , ΔS_{298} and ΔG_{298} for Reactions 28-30.

Reaction	ΔH_{298} (kcal mol ⁻¹)	ΔG_{298} (kcal mol ⁻¹)	ΔS_{298} (cal mol ⁻¹ K ⁻¹)
<hr/>			
Sc(OH) ₂ ⁺ + CH ₃ OH ⇌			
CH ₃ OScOH ⁺ + H ₂ O	-5.89	-5.57 ^a	-1.07 ^b
CH ₃ OScOH ⁺ + CH ₃ OH ⇌			
Sc(OCH ₃) ₂ ⁺ + H ₂ O	-5.66	-5.32 ^c	-1.14 ^d
Sc(OCH ₃) ₂ ⁺ + CH ₃ CH ₂ OH ⇌			
CH ₃ OScOCH ₂ CH ₃ ⁺ + CH ₃ OH	+3.26	+3.53 ^e	-0.90 ^f

^aExperimental value is -2.6 kcal mol⁻¹. ^bEquation 33 predicts that $\Delta S_{298} = R \ln 1 = 0$ cal mol⁻¹K⁻¹. ^cExperimental value is -2.6 kcal mol⁻¹. ^dEquation 33 predicts that $\Delta S_{298} = -R \ln 4 = -2.75$ cal mol⁻¹K⁻¹. ^eExperimental value is +0.4 kcal mol⁻¹. ^fEquation 33 predicts that $\Delta S_{298} = R \ln 2 = 1.38$ cal mol⁻¹K⁻¹.

differs from the experimental value by about 3 kcal mol⁻¹. The errors do not appear to be systematic, so the uncertainty in our calculated ΔG_{298} values are estimated to be at least ± 3 kcal mol⁻¹.

Discussion

Overview. In this study we were able to observe σ -bond metathesis reactions of $\text{Sc}(\text{OCD}_3)_2^+$ with water, ethanol and 1-propanol. This reactivity is analogous to the reactions of $\text{Sc}(\text{CD}_3)_2^+$ and $\text{CH}_3\text{ScCH}_2\text{CH}_3^+$ with small alkanes.⁸ However, with $\text{Sc}(\text{OCD}_3)_2^+$ and water, ethanol or 1-propanol, we succeeded in establishing ligand exchange equilibria via σ -bond metathesis (reactions 6, 7, 11, 12 and 22) and measured the equilibrium constants (see Table 1) for these processes. These metathesis reactions could proceed via an oxidative addition/reductive elimination pathway or via a four-center intermediate. Since Sc^+ has only two valence electrons with which to form strong σ bonds,^{18,19} we favor a four-center mechanism for these metathesis reactions⁹ (as shown in Scheme I for the reaction of $\text{Sc}(\text{CD}_3)_2^+$ with *n*-butane).

All the alcohols used in these experiments were unlabeled except for methanol, which was deuterated at the methyl positions (CD_3OH). CD_3OH was used to allow us to distinguish between $\text{Sc}(\text{OCH}_3)_2^+$ and $\text{HOscOCH}_2\text{CH}_3^+$, which would otherwise have identical masses. Since the observed σ -bond metathesis reactions occur at the oxygen atom in alcohols, the labeling in CD_3OH should not give rise to kinetic isotope effects. The labeling has a small secondary isotope effect on the O-H bond strength in CD_3OH (see Table 4), and we presume that the secondary isotope effect on the $\text{Sc}^+\text{-OCD}_3$ bond strength in $\text{CD}_3\text{OScOR}^+$ would be similar.

Calculation of Bond Energies. As Bryndza et al.¹ have shown, equilibrium data from σ -bond metathesis reactions can be used to determine the relative metal-ligand bond strengths for a series of complexes. To illustrate, consider the general σ -bond metathesis process shown in reaction 31, where R = H or alkyl. Equation 32 relates *K* to



Table 4. Gas-Phase Bond Energies at 298 K for Chemical Species Relevant to this Work.

Species	D°_{298} (kcal mol ⁻¹) ^{a,b}
HO-H	119(1)
CH ₃ O-H	104.4(1)
CD ₃ O-H	104.2(1) ^c
CH ₃ CH ₂ O-H	104.2(1)
CH ₃ CH ₂ CH ₂ O-H	103.4(1)
Sc ⁺ -OH	120.4(2.1) ^d , 118.8 ^e
HOSc ⁺ -OH	126.9(2.1) ^f
HSc ⁺ -H	59(4) ^g
HSc ⁺ -D	60(4) ^h
Sc ⁺ -O=CD ₂	39(5) ⁱ
Sc ⁺ -O=CHCH ₃	43(5) ⁱ
Sc ⁺ -(CD ₃ OH)	30(5) ⁱ
Sc ⁺ -(CH ₃ CH ₂ OH)	35(5) ⁱ

^aUncertainties are in parentheses. ^bUnless otherwise noted, all values come from reference 20. ^dCalculated from values in reference 21. ^dReference 22. The value here has been corrected by 1.2 kcal mol⁻¹ to convert it from D°_0 to D°_{298} . ^eTheoretical value, reference 23. The value here has been corrected by 1.2 kcal mol⁻¹ to convert it from D°_0 to D°_{298} . ^fTheoretical value (corrected by 1.2 kcal mol⁻¹ to convert it from D°_0 to D°_{298}) is 125.3 kcal mol⁻¹ (reference 23). Since theoretical value for Sc⁺-OH bond energy was underestimated by 1.6 kcal mol⁻¹, we have adjusted the theoretical bond energy for HOSc⁺-OH upward by the same amount. ^gReference 24. ^hThis value has been corrected by 1 kcal mol⁻¹ to account for the change in D°_{298} upon substituting D for H. ⁱSee discussion in text.

$$\Delta H = -RT \ln K + T \Delta S \quad (32)$$

ΔH . Since our study was conducted at a single temperature, we are unable to experimentally measure ΔS . Theoretical calculations were used to estimate ΔS_{298} for reactions 28-30 (see Table 3), but the large size of $\text{Sc}(\text{OCH}_2\text{CH}_3)_2^+$ and $\text{CD}_3\text{OScOCH}_2\text{CH}_2\text{CH}_3^+$ made it impractical to perform ab initio calculations on them. However, vibrational contributions to ΔS are likely to be small for the metathesis reaction 31, and the main rotational contribution to ΔS will arise from symmetry numbers. Therefore, we can estimate ΔS for reactions 12 and 22 using equation 33. The

$$\Delta S \approx R \ln \left[\frac{\prod_i \sigma_{i,\text{reactants}}}{\prod_i \sigma_{i,\text{products}}} \right] \quad (33)$$

values of ΔS_{298} for reactions 28-30 predicted using equation 33 are also given in Table 3. Comparison with the LMP2 values of ΔS_{298} indicate that for metathesis processes such as reaction 31 the entropies calculated from equation 33 are accurate to within ± 2.5 cal mol⁻¹K⁻¹. Since the error in our LMP2 values for ΔS_{298} are estimated to be ± 2 cal mol⁻¹K⁻¹, our estimates of ΔS for reactions 12 and 22 calculated from equation 33 appear to be reasonably accurate.²⁵

Once ΔH for reaction 31 is known, we can then calculate the *relative* bond strength between $\text{CD}_3\text{OSc}^+-\text{OCD}_3$ and $\text{CD}_3\text{OSc}^+-\text{OR}$ with equation 34. If one

$$D^\circ(\text{CD}_3\text{OSc}^+-\text{OR}) - D^\circ(\text{CD}_3\text{OSc}^+-\text{OCD}_3) = D^\circ(\text{RO-H}) - D^\circ(\text{CD}_3\text{O-H}) - \Delta H \quad (34)$$

$\text{R}'\text{OSc}^+-\text{OR}$ bond strength is known from other experimental methods, then we can use appropriate equilibrium measurements to determine the *absolute* bond strengths of other Sc^+ -alkoxide bonds. In fact, values for the Sc^+-OH and HOSc^+-OH bond energies are known (see Table 4). Therefore, using the method just outlined, we have determined the bond strengths for Sc^+-OR bonds where R = methyl, ethyl and *n*-propyl. Bond strengths relevant to this work are given in Table 4, and the derived relative and absolute Sc^+-OR bond strengths are presented in Tables 5 and 6, respectively.

Table 5. Gas-Phase Bond Energies of Sc⁺-Alkoxide Bonds Relative to Sc⁺-OCD₃.^a

Species (CD ₃ OSc ⁺ -OR)	$D^{\circ}_{298}(\text{CD}_3\text{OSc}^+-\text{OR}) - D^{\circ}_{298}(\text{CD}_3\text{OSc}^+-\text{OCD}_3)^{\text{b}}$ (kcal mol ⁻¹)
CD ₃ OSc ⁺ -OH	+11.9 ^c
CD ₃ OSc ⁺ -OCD ₃	0.0
CD ₃ OSc ⁺ -OCH ₂ CH ₃	-0.1
CD ₃ OSc ⁺ -OCH ₂ CH ₂ CH ₃	-1.4

^aThe uncertainty in these values is estimated to be ± 0.5 kcal mol⁻¹. ^bCalculated from equation 34. ^cCalculated assuming $D^{\circ}_{298}(\text{CD}_3\text{OSc}^+-\text{OH}) = D^{\circ}_{298}(\text{HOSc}^+-\text{OH})$.

Table 6. Gas-Phase Sc⁺-Oxygen Bond Energies at 298 K.^a

Species	D°_{298} (kcal mol ⁻¹)
HOSc ⁺ -OH	126.9(2.1) ^b
HOSc ⁺ -OCD ₃	115.0
CD ₃ OSc ⁺ -OCD ₃	115.0
CD ₃ OSc ⁺ -OCH ₂ CH ₃	114.9
CD ₃ OSc ⁺ -OCH ₂ CH ₂ CH ₃	113.6
CH ₃ CH ₂ OSc ⁺ -OCH ₂ CH ₃	114.7

^aUnless otherwise noted, the uncertainty in these values is estimated to be ± 2 kcal mol⁻¹.

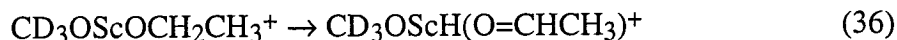
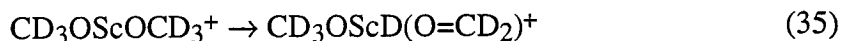
^bSee Table 4. The uncertainty in this number is given in parentheses.

We should note that our experimental results are consistent with recent calculations by Bauschlicher and Partridge.²³ They find that the $\text{HOSc}^+\text{-OH}$ bond is 8.8 ± 0.5 kcal mol⁻¹ stronger than the $\text{HOSc}^+\text{-OCH}_3$ bond. They also note that the difference is likely underestimated by 1-2 kcal mol⁻¹, which implies that the $\text{HOSc}^+\text{-OH}$ bond is actually about 10.5 kcal mol⁻¹ stronger than the $\text{HOSc}^+\text{-OCH}_3$ bond. In conjunction with their calculated bond strength for $\text{HOSc}^+\text{-OH}$ of 126.9 kcal mol⁻¹, they calculate the $\text{HOSc}^+\text{-OCH}_3$ bond strength to be 116.4 ± 0.5 kcal mol⁻¹. This value is in good agreement with our experimental value of 115.0 ± 2.0 kcal mol⁻¹ for the $\text{HOSc}^+\text{-OCD}_3$ bond strength, and provides additional evidence that subsequent solvation and elimination processes did not have a large effect on the measured equilibrium constants.

Examination of the bond energies in Tables 4 and 6 show that the trends in the $\text{Sc}^+\text{-OR}$ and H-OR bond energies for $\text{R} = \text{H}$, methyl, ethyl and *n*-propyl mirror each other closely. Similar behavior is seen when comparing $\text{Sc}^+\text{-R}$ and H-R ($\text{R} = \text{alkyl}$) bond strengths.²⁶ Furthermore, since the trends in the $\text{Sc}^+\text{-OR}$ and H-OR bond strengths correlate closely, we should be able use H-OR ($\text{R} = \text{alkyl}$ group larger than *n*-propyl) bond strengths to predict the corresponding $\text{Sc}^+\text{-OR}$ bond strengths. Although the predictive value of such an approach has been previously demonstrated for liquid-phase ruthenium and platinum systems,^{1,27} this work provides additional evidence that this kind of correlation is generally valid with a wide range of organometallic compounds.

Elimination Processes and Reaction Energetics. Although the main focus of this paper is not concerned with the elimination of H_2 from solvated $\text{Sc}^+\text{-alkoxide}$ species (reactions 19-21, 26 and 27), we will make a few comments about these observed processes here. First, we note that in all these reactions no HD loss is observed. This indicates that the methoxide ligand does not participate in reactions 19 and 20. However, solvated $\text{Sc}^+\text{-alkoxide}$ species containing either ethanol or the ethoxide ligand appear to readily dehydrogenate. Thus it could be imagined that $\text{CD}_3\text{OScOCH}_2\text{CH}_3^+$ might isomerize to $\text{CD}_3\text{OScH(O=CHCH}_3)^+$.

To examine these points further, we have estimated the enthalpy of reactions 35 and 36. Relevant thermochemical values are shown in Tables 4, 6 and 7. Most of the



necessary values were obtained from the literature. However, we used the values from this work for the $\text{Sc}^+\text{-OCD}_3$ and $\text{Sc}^+\text{-OCH}_2\text{CH}_3$ bond energies, and since the $\text{Sc}^+\text{-O=CD}_2$ and $\text{Sc}^+\text{-O=CHCH}_3$ bond energies are not known, we estimated them as follows. Magnera et al. found the $\text{Sc}^+\text{-OH}_2$ bond strength to be $31.4 \text{ kcal mol}^{-1}$,³⁰ while Bauschlicher and Langhoff calculate a value of $34.5 \text{ kcal mol}^{-1}$.³¹ This suggests that adducts between Sc^+ and oxygen-containing species have comparatively low bond energies. Further, in previous work by Halle et al.,³² the $\text{Co}^+\text{-O=CH}_2$ and $\text{Co}^+\text{-O=CHCH}_3$ bond energies were estimated to be 43 kcal mol^{-1} and 47 kcal mol^{-1} , respectively. Since Bauschlicher and Langhoff calculated that the $\text{Co}^+\text{-OH}_2$ bond strength is about 4 kcal mol^{-1} higher than the $\text{Sc}^+\text{-OH}_2$ bond strength,³¹ we estimate the $\text{Sc}^+\text{-O=CD}_2$ and $\text{Sc}^+\text{-O=CHCH}_3$ bond energies to be 39 kcal mol^{-1} and 43 kcal mol^{-1} , respectively. With these thermochemical values, we can calculate that for reaction 35 $\Delta H = +40.5 \text{ kcal mol}^{-1}$, while for reaction 36 $\Delta H = +28.6 \text{ kcal mol}^{-1}$. Thus it appears quite unlikely that any $\text{CD}_3\text{OScD(O=CD}_2\text{)}^+$ or $\text{CD}_3\text{OScH(O=CHCH}_3\text{)}^+$ is being generated in our experiments. However, our data clearly show that once $\text{Sc(OCD}_3\text{)}_2^+$ is solvated with ethanol or $\text{CD}_3\text{OScOCH}_2\text{CH}_3^+$ is solvated with either methanol or ethanol, elimination of H_2 does occur. How is this apparently unfavorable elimination facilitated?

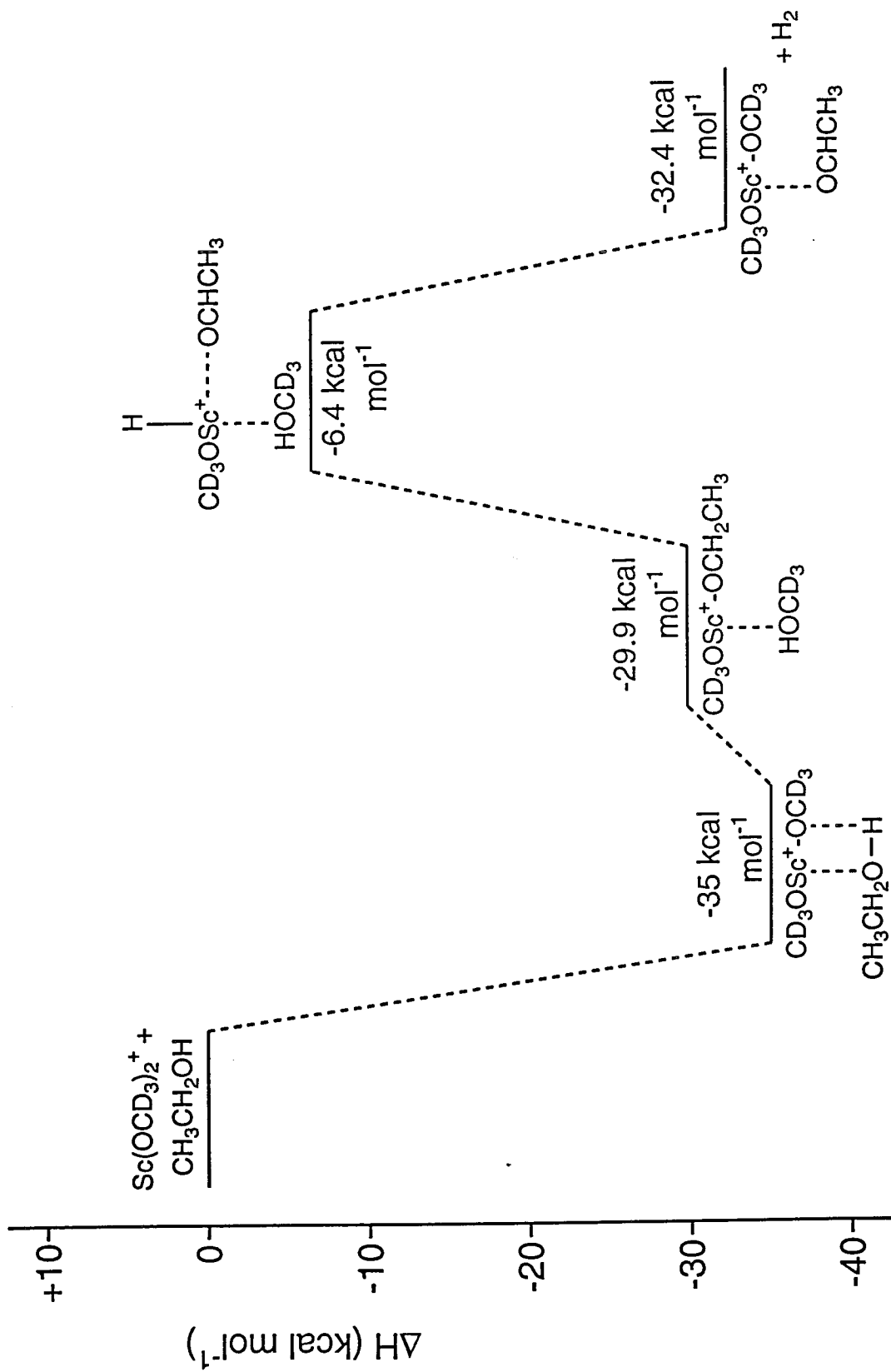
Apparently the presence of solvating alcohols makes the subsequent elimination of H_2 possible. To illustrate this conclusion, we have constructed the reaction coordinate diagram in Figure 12. We used the thermochemical values from Tables 4, 6 and 7 to evaluate the enthalpy changes of the various steps in this diagram. We were unable to locate bond energies for $\text{Sc}^+\text{-(CD}_3\text{OH)}$ or $\text{Sc}^+\text{-(CH}_3\text{CH}_2\text{OH)}$, but we estimate

Table 7. Gas-Phase Heats of Formation at 298 K for Chemical Species Relevant to this Work.

Species	$\Delta H_{f,298}^{\circ}$ (kcal mol ⁻¹) ^{a,b}
H	52.1(0.1)
D	53.0(0.1)
OCD ₃	1.0(1) ^c
OCH ₂ CH ₃	-4.1(0.1) ^d
O=CD ₂	-27.5(1) ^e
O=CHCH ₃	-39.6(0.1)

^aUncertainties are in parentheses. ^bUnless otherwise noted, all values come from reference 28. ^cCalculated from values in reference 21. ^dReference 20. ^eReference 29.

Figure 12. Illustration of reaction energetics for processes resulting from the interaction of $\text{CH}_3\text{CH}_2\text{OH}$ with $\text{Sc}(\text{OCD}_3)_2^+$. The relative energies are derived from the thermochemistry given in Tables 4, 6 and 7. Some of the values have significant uncertainties (see text for discussion). Note the lack of a barrier to H_2 elimination.



that their bond energies will be similar to the $\text{Sc}^+\text{-OH}_2$ bond energy, with the $\text{Sc}^+\text{-(CH}_3\text{CH}_2\text{OH)}$ bond energy being slightly larger due to the higher polarizability of ethanol.

The initial step in the elimination of H_2 from $\text{Sc}(\text{OCD}_3)_2(\text{CH}_3\text{CH}_2\text{OH})^+$ is solvation, which has an associated enthalpy change of $-35 \text{ kcal mol}^{-1}$. The next two steps (metathesis and a β -hydride transfer) only require $28.6 \text{ kcal mol}^{-1}$ (the same as the enthalpy change for reaction 36), so there is no overall barrier to the loss of H_2 . The initial solvation provides the chemical activation needed to overcome the intrinsic barrier to β -hydride transfer. On the other hand, HD elimination from $\text{Sc}(\text{OCD}_3)_2(\text{CD}_3\text{OH})^+$ is not seen because the intrinsic barrier to β -hydride transfer is much larger ($40.5 \text{ kcal mol}^{-1}$, the enthalpy change for reaction 35). Apparently the initial solvation with CD_3OH cannot provide the chemical activation necessary to overcome the larger barrier.

Comparison of Theoretical Results with Experimental Observations. One interesting feature in our theoretically determined lowest energy geometries for $\text{Sc}(\text{OH})_2^+$, $\text{CD}_3\text{OScOH}^+$, $\text{Sc}(\text{OCD}_3)_2^+$ and $\text{CD}_3\text{OScOCH}_2\text{CH}_3^+$ is the large $\text{Sc}^+\text{-O-C}$ bond angles ($\approx 165^\circ$, see Figure 6) that are found. Bauschlicher and Partridge obtained similar results from their optimization of the $\text{Sc}(\text{OH})_2^+$ geometry.²⁴ These large $\text{Sc}^+\text{-O-C}$ bond angles suggest that strong dative interactions between Sc^+ and each oxygen atom are occurring in all these ions. The calculated $\text{O-Sc}^+\text{-O}$ bond angles of $116^\circ\text{-}122^\circ$ in these ions (see Figure 6) are also indicative of significant dative interactions. We should note that such dative bonding has been observed previously with $\text{Sc}^+\text{-OH}$. Tilson and Harrison found that in the ground state $\text{Sc}^+\text{-OH}$ has a linear geometry and a triple bond between Sc^+ and OH .³³ Also, previous work by Clemmer et al.²² determined that $D^0_0(\text{Sc}^+\text{-OH}) = 119 \text{ kcal mol}^{-1}$, which is much greater than the $\text{Sc}^+\text{-CH}_3$ bond energy of 59 kcal mol^{-1} .²⁴ This enhanced bond strength for $\text{Sc}^+\text{-OH}$ was attributed to the ability of the OH group to donate its two lone pairs of electrons to Sc^+ in a dative interaction.

However, atomic charges calculated from Mulliken populations indicate that Sc carries a net charge of about +1.8 in $\text{Sc}(\text{OH})_2^+$, $\text{CD}_3\text{OScOH}^+$, $\text{Sc}(\text{OCD}_3)_2^+$ and $\text{CD}_3\text{OScOCH}_2\text{CH}_3^+$ (varying from 1.84 in $\text{Sc}(\text{OH})_2^+$ to 1.76 in $\text{CD}_3\text{OScOCH}_2\text{CH}_3^+$, with the net charge decreasing as larger alkoxide groups are added). This indicates a significant electrostatic contribution to the bonding. Thus our present results indicate that both ionic and dative interactions contribute significantly to the bonding between Sc^+ and each oxygen atom in diligated species. It also appears that both ligands can participate equally in dative interactions.

Acknowledgments

This work was supported by the National Science Foundation under Grant CHE-9108318, by a grant from AMOCO, and by the Office of Naval Research. We also wish to thank the Beckman Foundation and Institute for continuing support of the FT-ICR research facility and the Beckman Institute Materials and Process Simulations Center (supported by DOE-BCTR and the National Science Foundation under Grant CHE-9522179) for supporting our theoretical calculations. Francesco Faglioni and Jason K. Perry gave especially helpful advice concerning the theoretical calculations in this work.

References

- ¹Bryndza, H. E.; Fong, L. K.; Paciello, R. A.; Tam, W.; Bercaw, J. E. *J. Am. Chem. Soc.* **1987**, *109*, 1444.
- ²Uppal, J. S.; Douglas, D. E.; Staley, R. H. *J. Am. Chem. Soc.* **1981**, *103*, 508.
- ³Christ, C. S.; Eyler, J. R.; Richardson, D. E. *J. Am. Chem. Soc.* **1988**, *110*, 4038.
- ⁴(a) Wax, M. J.; Stryker, J. M.; Buchanan, J. M.; Kovac, C. A.; Bergman, R. G. *J. Am. Chem. Soc.* **1984**, *106*, 1121. (b) Buchanan, J. M.; Stryker, J. M.; Bergman, R. G. *J. Am. Chem. Soc.* **1986**, *108*, 1537.
- ⁵Jeske, G.; Lauke, H.; Mauermann, H.; Schumann, H.; Marks, T. J. *J. Am. Chem. Soc.* **1985**, *107*, 8111.
- ⁶Watson, P. L. *J. Am. Chem. Soc.* **1983**, *105*, 6491.
- ⁷(a) Thompson, M. E.; Baxter, S. M.; Bulls, A. R.; Burger, B. J.; Nolan, M. C.; Santarsiero, B. D.; Schaefer, W. P.; Bercaw, J. E. *J. Am. Chem. Soc.* **1987**, *109*, 203. (b) Huang, Y.; Hill, Y. D.; Sodupe, M.; Bauschlicher, C. W., Jr.; Freiser, B. S. *J. Am. Chem. Soc.* **1992**, *114*, 9106.
- ⁸(a) Crellin, K. C.; Beauchamp, J. L.; Geribaldi, S.; Decouzon, M. *Organometallics* **1996**, *15*, 5368. (b) Crellin, K. C.; Geribaldi, S.; Widmer, M.; Beauchamp, J. L. *Organometallics* **1995**, *14*, 4366. (c) Crellin, K. C.; Geribaldi, S.; Beauchamp, J. L. *Organometallics* **1994**, *13*, 3733.
- ⁹Steigerwald, M. L.; Goddard, W. A. III *J. Am. Chem. Soc.* **1984**, *106*, 308.
- ¹⁰Azzaro, M.; Breton, S.; Decouzon, M.; Geribaldi, S. *Int. J. Mass Spectrom. Ion Proc.* **1993**, *128*, 1.
- ¹¹(a) Marshall, A. G. *Acc. Chem. Res.* **1985**, *18*, 316. (b) Comisarow, M. B. *Anal. Chim. Acta* **1985**, *178*, 1.
- ¹²Anders, L. R.; Beauchamp, J. L.; Dunbar, R. C.; Baldeschwieler, J. D. *J. Chem. Phys.* **1966**, *45*, 1062.
- ¹³Comisarow, M. B.; Marshall, A. G. *Chem. Phys. Lett.* **1974**, *26*, 489.
- ¹⁴Ringnalda, M. N.; Langlois, J.-M.; Greeley, B. H.; Murphy, R. B.; Russo, T. V.; Cortis, C.; Muller, R. P.; Marten, B.; Donnelly, R. B., Jr.; Mainz, D. T.; Wright, J. R.; Pollard, W. T.; Cao, Y.; Won, Y.; Miller, G. H.; Goddard, W. A. III, Friesner, R. A. *PS-GVB*, v.2.2, Schrödinger, Inc., 1995.
- ¹⁵Specifically, we used the LAV3P* ECP basis set: (a) Hay, P. J.; Wadt, W. R. *J. Chem. Phys.* **1985**, *82*, 270. (b) Hay, P. J.; Wadt, W. R. *J. Chem. Phys.* **1985**, *82*, 284.

¹⁶The structural parameters for these species are presented in the appendix at the end of this chapter.

¹⁷Wagman, D. D.; Evans, W. H.; Parker, V. B.; Halow, I.; Baily, S. M.; Schumm, R. H. *Selected Values of Chemical Thermodynamic Properties*, National Bureau of Standards Technical Note 270-3, 1968, United States Government Printing Office, Washington, D.C.

¹⁸Tolbert, M. A.; Beauchamp, J. L. *J. Am. Chem. Soc.* **1984**, *106*, 8117.

¹⁹Beauchamp, J. L.; van Koppen, P. A. M. *Energetics of Organometallic Species*, J. A. M. Simoes, Ed., 1992, Kluwer Academic Publishers, The Netherlands.

²⁰McMillen, D. F.; Golden, D. M. *Ann. Rev. Phys. Chem.* **1982**, *33*, 493.

²¹Barlow, S. E.; Dang, T. T.; Bierbaum, V. M. *J. Am. Chem. Soc.* **1990**, *112*, 6832.

²²Clemmer, D. E.; Aristov, N.; Armentrout, P. B. *J. Phys. Chem.* **1993**, *97*, 544.

²³Bauschlicher, C. W., Jr.; Partridge, H., personal communication.

²⁴Armentrout, P. B.; Georgiadis, R. *Polyhedron*, **1988**, *7*, 1573.

²⁵The quality of our calculations can also be gauged by comparing the theoretically calculated values of ΔG_{298} with our experimental values. For reactions 28-30, the calculated value of ΔG_{298} for each reaction was within 3.1 kcal mol⁻¹ of the experimental value. Furthermore, the calculated values of ΔG_{298} for reactions 28 and 29 were within 0.3 kcal mol⁻¹ of each other, in excellent agreement with our experimental results. Thus the LMP2 level of theory appears to perform reasonably well at calculating the thermodynamic values associated with these metathesis reactions.

²⁶Perry, J. K.; Goddard, W. A., III *J. Am. Chem. Soc.* **1994**, *116*, 5013.

²⁷Bryndza, H. E.; Tam, W. *Chem. Rev.* **1988**, *88*, 1163.

²⁸Lias, S. G.; Bartmess, J. E.; Liebman, J. F.; Holmes, J. L.; Levin, R. D.; Mallard, W. G. *J. Phys. Chem. Ref. Data* **1988**, *17*, Suppl. 1.

²⁹Frenkel, M.; Marsh, K. N.; Wilhoit, R. C.; Kabo, G. J.; Roganov, G. N. *Thermodynamics of Organic Compounds in the Gas Phase*, Vol. I, 1994, Thermodynamics Research Center, College Station, Texas.

³⁰Magnera, T. F.; David, D. E.; Michl, J. *J. Am. Chem. Soc.* **1989**, *111*, 4100.

³¹Bauschlicher, C. W., Jr.; Langhoff, S. R. *Int. Rev. Phys. Chem.* **1990**, *9*, 149.

³²Halle, L. F.; Crowe, W. E.; Armentrout, P. B.; Beauchamp, J. L. *Organometallics* **1984**, *3*, 1694.

³³Tilson, J. L.; Harrison, J. F. *J. Chem. Phys.* **1985**, *83*, 166.

Appendix

The structural parameters obtained from the geometry optimizations of the lowest energy conformations of H₂O, CH₃OH, CH₃CH₂OH, Sc(OH)₂⁺, CH₃OScOH⁺, Sc(OCH₃)₂⁺ and CH₃OScOCH₂CH₃⁺ are given in the following Tables 1A-7A, respectively.

Table 1A. LMP2-Optimized Bond Distances (\AA) and Angles (deg) for the Lowest Energy Conformation of H_2O .

Bond Length	
O1-H2	0.9690
O1-H3	0.9690
Bond Angle	
H2-O1-H3	103.91

Table 2A. LMP2-Optimized Bond Distances (Å) and Angles (deg) for the Lowest Energy Conformation of CH₃OH.

Bond Length	
C1-O2	1.4285
C1-H3	1.0897
C1-H4	1.0967
C1-H5	1.0967
O2-H6	0.9704
Bond Angle	
C1-O2-H6	107.10
O2-C1-H3	106.32
O2-C1-H4	112.24
O2-C1-H5	112.24
H3-C1-H5	108.55
H4-C1-H5	108.80
Torsional Angle	
H3-C1-O2-H6	180.00
H4-C1-O2-H6	61.45
H5-C1-O2-H6	-61.46

Table 3A. LMP2-Optimized Bond Distances (Å) and Angles (deg) for the Lowest Energy Conformation of CH₃CH₂OH.

Bond Length	
C1-C2	1.5167
C1-O3	1.4344
C1-H4	1.0989
C1-H5	1.0989
C2-H6	1.0936
C2-H7	1.0921
C2-H8	1.0921
O3-H9	0.9716
Bond Angle	
C1-C2-H6	110.55
C1-C2-H7	110.13
C1-C2-H8	110.13
C1-O3-H9	107.38
C2-C1-O3	107.38
C2-C1-H4	110.11
C2-C1-H5	110.12
O3-C1-H4	110.81
O3-C1-H5	110.81
H4-C1-H5	107.64
H6-C2-H7	108.75
H6-C2-H8	108.75
H7-C2-H8	108.49

Table 3A. (Continued)

Torsional Angle

C2-C1-O3-H9	180.00
O3-C1-C2-H6	180.00
O3-C1-C2-H7	-59.81
O3-C1-C2-H8	59.79
H4-C1-C2-H6	-59.28
H4-C1-C2-H7	60.92
H4-C1-C2-H8	-179.48
H4-C1-C2-H9	59.71
H5-C1-C2-H6	59.26
H5-C1-C2-H7	179.46
H5-C1-C2-H8	-60.93
H5-C1-C2-H9	-59.71

Table 4A. LMP2-Optimized Bond Distances (Å) and Angles (deg) for the Lowest Energy Conformation of Sc(OH)₂⁺.

Bond Length	
Sc1-O2	1.7376
Sc1-O3	1.7376
O2-H4	0.9735
O3-C5	0.9735
Bond Angle	
Sc1-O2-H4	164.26
Sc1-O3-H5	164.26
O2-Sc1-O3	122.78
Torsional Angle	
O2-Sc1-O3-H5	0.00
O3-Sc1-O2-H4	0.00

Table 5A. LMP2-Optimized Bond Distances (Å) and Angles (deg) for the Lowest Energy Conformation of CH₃OscOH⁺.

Bond Length	
Sc1-O2	1.7640
Sc1-O3	1.7000
O2-H5	0.9716
O3-C4	1.4492
C4-H6	1.0894
C4-H7	1.0889
C4-H8	1.0895
Bond Angle	
Sc1-O2-H5	169.28
Sc1-O3-C4	167.98
O2-Sc1-O3	121.12
O2-C4-H6	109.09
O3-C4-H7	108.62
O3-C4-H8	108.62
H6-C4-H7	106.77
H6-C4-H8	106.77
H7-C4-H8	109.39
Torsional Angle	
Sc1-O3-C4-H6	-3.95
Sc1-O3-C4-H7	116.25
Sc1-O3-C4-H8	-124.08

Table 5A. (Continued)

Torsional Angle

O2-Sc1-O3-C4	0.82
O3-Sc1-O2-H5	0.76

Table 6A. LMP2-Optimized Bond Distances (Å) and Angles (deg) for the Lowest Energy Conformation of $\text{Sc}(\text{OCH}_3)_2^+$.

Bond Length	
Sc1-O2	1.7296
Sc1-O3	1.7284
O2-C4	1.4436
O3-C5	1.4432
C4-H6	1.0903
C4-H7	1.0900
C4-H8	1.0898
C5-H9	1.0903
C5-H10	1.0899
C5-H11	1.0899
Bond Angle	
Sc1-O2-C4	164.36
Sc1-O3-C5	165.70
O2-Sc1-O3	116.30
O2-C4-H6	109.01
O2-C4-H7	108.44
O2-C4-H8	108.41
O3-C5-H9	108.99
O3-C5-H10	108.56
O3-C5-H11	108.42
H6-C4-H7	110.34
H6-C4-H8	110.38

Table 6A. (Continued)

Bond Angle	
H7-C4-H8	110.20
H9-C5-H10	110.36
H9-C5-H11	110.38
H10-C5-H11	110.19
Torsional Angle	
Sc1-O2-C4-H6	-9.10
Sc1-O2-C4-H7	111.06
Sc1-O2-C4-H8	-129.30
Sc1-O3-C5-H9	3.75
Sc1-O3-C5-H10	-116.42
Sc1-O3-C5-H11	123.93
O2-Sc1-O3-C5	-0.63
O3-Sc1-O2-C4	1.33

Table 7A. LMP2-Optimized Bond Distances (Å) and Angles (deg) for the Lowest Energy Conformation of $\text{CH}_3\text{OScOCH}_2\text{CH}_3^+$.

Bond Length	
Sc1-O2	1.7367
Sc1-O3	1.7210
O2-C4	1.4423
O3-C5	1.4555
C4-H7	1.0905
C4-H8	1.0901
C4-H9	1.0901
C5-C6	1.5169
C5-H10	1.0921
C5-H11	1.0921
C6-H12	1.0935
C6-H13	1.0928
C6-H14	1.0928
Bond Angle	
Sc1-O2-C4	164.21
Sc1-O3-C5	164.50
O2-Sc1-O3	116.04
O2-C4-H7	109.02
O2-C4-H8	108.50
O2-C4-H9	108.50
O3-C5-C6	110.79
O3-C5-H10	106.51

Table 7A. (Continued)

Bond Angle	
O3-C5-H11	106.51
C5-C6-H12	109.33
C5-C6-H13	110.92
C5-C6-H14	110.92
C6-C5-H10	111.92
C6-C5-H11	111.92
H7-C4-H8	110.33
H7-C4-H9	110.33
H8-C4-H9	110.12
H10-C5-H11	108.91
H12-C6-H13	108.15
H12-C6-H14	108.15
H13-C6-H14	109.28
Torsional Angle	
Sc1-O2-C4-H7	0.32
Sc1-O2-C4-H8	-119.86
Sc1-O2-C4-H9	120.50
Sc1-O3-C5-C6	0.14
Sc1-O3-C5-H10	122.08
Sc1-O3-C5-H11	-121.80
O2-Sc1-O3-C5	-0.16
O3-Sc1-O2-C4	-0.34
O3-C5-C6-H12	-180.00

Table 7A. (Continued)

Torsional Angle

O3-C5-C6-H13	60.82
O3-C5-C6-H14	-60.81
H10-C5-C6-H12	61.30
H10-C5-C6-H13	-57.89
H10-C5-C6-H14	-179.52
H11-C5-C6-H12	-61.28
H11-C5-C6-H13	179.54
H11-C5-C6-H14	57.90

Chapter 6

REACTION OF CHLORIDE IONS WITH CHLORINE NITRATE AND ITS IMPLICATIONS FOR STRATOSPHERIC CHEMISTRY

Kevin C. Crellin, Bernd-Michael Haas and Mitchio Okumura

Contribution No. 2922, Arthur Amos Noyes Laboratory of Chemical Physics,
California Institute of Technology, Pasadena, CA 91125

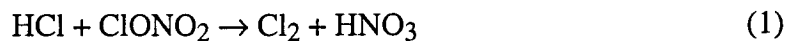
Adapted from an article in the *Journal of Physical Chemistry*, **1994**, *98*, 6740-6745.

Abstract

We present experimental evidence for the rapid gas-phase reaction of Cl^- with ClONO_2 to form Cl_2 and NO_3^- . The reaction was studied using Fourier transform ion cyclotron resonance mass spectrometry, and a reaction rate constant of $(9.2 \pm 3.0) \times 10^{-10} \text{ cm}^3 \text{ s}^{-1} \text{ molecule}^{-1}$ at 298 K was determined. This value is $\approx 80\%$ of the rate constant estimated from ion-dipole collision theory. The reaction enthalpy remains exothermic with the inclusion of ion hydration enthalpies, indicating that the reaction could proceed in condensed-phase water. These considerations suggest that chloride ions may react directly with ClONO_2 on water ice films and type II polar stratospheric cloud particles. From the rapidity of the reaction, we also infer that gas-phase chloride ion cannot serve as a sink for negative charge or active chlorine in the stratosphere.

Introduction

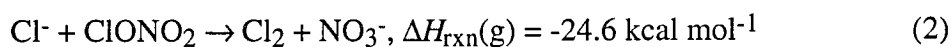
Heterogeneous reactions on aerosols are now held to be responsible for the high degree of activation of chlorine in the polar stratosphere during winter and early spring.¹⁻³ Relatively inert reservoir species such as HCl and ClONO_2 decompose readily on the surfaces of polar stratospheric cloud (PSC) particles. These aerosols are believed to be composed of nitric acid hydrates (type I) or water ice (type II). While laboratory studies have found that a number of reactions occur on model PSC films,⁴⁻¹⁴ Webster et al.¹⁵ conclude from recent field measurements of HCl and ClO concentrations in the stratosphere that reaction 1 is critical in determining the winter and



spring chlorine budget within the polar vortex. The homogeneous rate of reaction 1 has not been detectable ($k < 10^{-19} \text{ cm}^3 \text{ s}^{-1}$), but laboratory studies^{4-10,14} indicate that this reaction has a high probability on water ice and water-rich nitric acid trihydrate (NAT). Tabazadeh and Turco¹⁶ have attempted to construct a physicochemical model for this and other heterogeneous reactions occurring on PSC surfaces, but their models can be improved by a sound understanding of the reaction mechanisms.

Although the form of HCl on PSCs has not been established, laboratory studies on films suggest that the HCl is dissociatively ionized. This has led Molina and co-workers^{4,14,17,18} to propose an ionic mechanism in which the chloride ion Cl^- reacts by fast ion-ion recombination with Cl^+ from dissociatively ionized molecules such as Cl^+HO^- or Cl^+NO_3^- . Burley and Johnston¹⁹ have also hypothesized that ionic mechanisms involving concerted nucleophilic displacement are important, especially for reactions in sulfuric acid aerosols. Okumura and co-workers have investigated gas-phase ion-molecule and cluster ion reactions in order to provide insights into possible ionic mechanisms of heterogeneous reactions at the molecular level. In an earlier paper,²⁰ Nelson and Okumura demonstrated that the reactions of ClONO_2 with protonated water clusters produced protonated nitric acid, in the form $\text{NO}_2^+(\text{H}_2\text{O})_n$, which led them to suggest that the reaction $\text{ClONO}_2 + \text{H}_2\text{O}$ would proceed by proton catalysis.

The proposed existence of solvated Cl^- on PSC particles^{17,18} raises the question of whether chlorine nitrate reacts directly with the chloride anion. As a first step, we have examined (in the gas phase) reaction 2, which from known heats of formation is exothermic.^{21,22} The gas-phase rate of reaction 2 has not been measured. Cl^- undergoes



analogous exothermic reactions with HNO_3 and N_2O_5 . All three are driven in part by the high electron affinity²¹ of NO_3 . Davidson et al.²³ have found in ion flow tube experiments that the latter two reactions proceed with near Langevin rates, raising the possibility that reaction 2 is also fast.

The reactivity of Cl^- in the gas phase would also raise doubts about the proposal by Wong et al.²⁴ to alleviate the threat to stratospheric ozone by removing the accumulation of chlorine in the stratosphere from anthropogenic sources. They propose to temporarily charge the atmosphere with sufficient electron density to trap active chlorine as chloride ion. Their proposal rests on the assumption that the resulting

chloride ion is chemically inert; however, if Cl^- reacts with an abundant ($> 10^9 \text{ cm}^{-3}$) neutral species such as ClONO_2 , such a scheme may not be feasible.

In this paper, we present experimental measurements of the reaction rate of Cl^- with ClONO_2 in the gas phase using a Fourier transform ion cyclotron resonance (FT-ICR) mass spectrometer. We find that the chloride ion reacts rapidly with chlorine nitrate. We discuss the implications of our results for the proposed ozone mitigation scheme, and then present thermodynamic considerations which suggest that this reaction could proceed in the condensed phases of water.

Experimental

FT-ICR mass spectrometry is a well-established technique, and its experimental aspects have been discussed in the literature.^{25,26} Only details relevant to this experiment are presented here. A 1-in. cubic trapping cell is located between the poles of a Varian 15-in. electromagnet maintained at a field of 1.0 T. Data were collected with an IonSpec Omega/386 FT-ICR data system and associated electronics. Neutral gases ClONO_2 and CCl_4 were introduced into the cell from ultrahigh-vacuum (UHV) inlet lines by separate leak valves, and their pressures were measured with a Schultz-Phelps ion gauge calibrated against an MKS 390 HA-00001SP05 capacitance manometer. Uncertainties in the absolute pressure limited the accuracy of rate constants to $\pm 20\%$. ClONO_2 was synthesized from the reaction of Cl_2O and N_2O_5 and then purified.²⁷ Purity was confirmed by UV absorption spectroscopy of a sample of ClONO_2 in a gas cell.

Two chlorine nitrate gas handling systems were used. In the first experiments, ClONO_2 was introduced through a standard UHV stainless steel inlet line and high-precision leak valve (sapphire/OFHC-copper seal). Because stainless steel surfaces can catalyze ClONO_2 decomposition,²⁸ the inlet lines and vacuum chamber were treated prior to introduction of ClONO_2 . Halocarbon vacuum grease was used on joints in the inlet system, and the entire system was extensively baked to remove H_2O . Passivation

of the inlet line with ClONO₂ for 2-3 days was essential to minimize decomposition of chlorine nitrate in the inlet line. During experiments, ClONO₂ was kept in a glass sample bulb held at a temperature of -45 °C by an acetonitrile/dry ice bath to maintain a ClONO₂ pressure of approximately 20 Torr in the inlet line.

To confirm the results obtained using the stainless steel inlet system and to exclude the possibility of competing reactions with decay products, we repeated the experiments introducing ClONO₂ through a glass (Pyrex) inlet line with Teflon valves. The drawbacks of this inlet system were coarser control of gas flow by the Teflon leak valve and slightly poorer vacuum seals compared to the UHV seals of the stainless steel line. To compensate for the higher flow rates through the Teflon valve, the stagnation pressure of ClONO₂ was kept at approximately 1 Torr by cooling the sample to -80 °C in an acetone/dry ice bath.

We used the positive ion mass spectrum as a diagnostic to assess the purity of the ClONO₂ sample in the ICR cell. Spectra were taken 80 ms following a 20 ms pulse of 70 eV electrons (at an emission current of 0.3 μA). Primary ions formed by electron impact ionization underwent 1-2 collisions prior to recording the mass spectrum. We used the Cl₂⁺ signal as a measure of the quality of ClONO₂ in the ICR cell, because Cl₂⁺ is produced only by ionization of the neutral Cl₂ decomposition product and not from fragmentation of ionized ClONO₂. In the absence of passivation of the stainless steel line, the mass spectrum consisted almost entirely of Cl₂⁺; after passivation, the Cl₂⁺ signal was reduced by 3 orders of magnitude and accounted for less than 5% of the total ion signal. No decomposition was observed using the glass line.

Reactant chloride ions were formed by electron attachment to background gas. Chlorine nitrate did not prove to be an efficient source of Cl⁻ under any negative ionization conditions. Instead, we chose to generate Cl⁻ from CCl₄. This precursor is ideally suited as a chloride ion source because it has a large cross section for dissociative

attachment to form Cl^- and CCl_3 as products.^{29,30} CCl_3 is inert toward ClONO_2 . CCl_4 also serves to scavenge electrons after the electron beam pulse.³¹

CCl_4 was added to the ICR cell through a separate leak valve and Cl^- reactant ions were formed by electron bombardment of CCl_4 at a partial pressure of approximately 3.0×10^{-7} Torr with an electron energy of 1.7 eV. The Cl^- ions were then selectively isolated (see Figure 1, upper panel) and trapped in the ICR cell by ejecting the unwanted ions NO_2^- and NO_3^- . After ejecting ions of other m/z (defining $t = 0$ ms), we followed the reaction of the Cl^- ions with background neutral ClONO_2 at partial pressures in the range of $(1-4) \times 10^{-7}$ Torr. All experiments were performed at room temperature (298 K). Mass spectra were then recorded in time intervals of 50 ms to monitor the disappearance of Cl^- and the appearance of NO_3^- . Positive ion spectra of ClONO_2 were taken after approximately 2 hours to assess the extent of decomposition that had occurred by observing the amount of the decomposition product Cl_2^+ present. These spectra indicated that, although the stainless steel line had been thoroughly passivated, up to 25% of the ClONO_2 had decomposed in the inlet line during a run of experiments. When ClONO_2 was introduced through the glass inlet line, no sign of decomposition was evident in the mass spectra.

Results

Reaction 2 was the only observed reaction of Cl^- with ClONO_2 (see Figure 1). The most likely interference would have come from products of chlorine nitrate decomposition: NO , NO_2 and Cl_2 . Bakeout of the UHV-sealed chamber and inlet line minimized H_2O contamination, so the products HOCl and HNO_3 from ClONO_2 hydrolysis were absent. All of the expected contaminants have electron affinities below that of Cl and therefore could neither react with Cl^- nor produce NO_3^- .

Figure 1 displays mass spectra taken at $t = 0$ ms and $t = 200$ ms and illustrates how the reaction proceeds in time. Figure 2 shows a semilog plot of the decay

Figure 1. (upper) Isolation of Cl^- at 75 ms after the 1.7 eV electron beam pulse corresponding to $t = 0$ ms, the time at which all other ions have been ejected. (lower) At $t = 200$ ms, NO_3^- products from $\text{Cl}^- + \text{ClONO}_2 \rightarrow \text{Cl}_2 + \text{NO}_3^-$ have been formed. The pressure of ClONO_2 was 2.28×10^{-7} Torr and the pressure of CCl_4 was approximately 3×10^{-7} Torr.

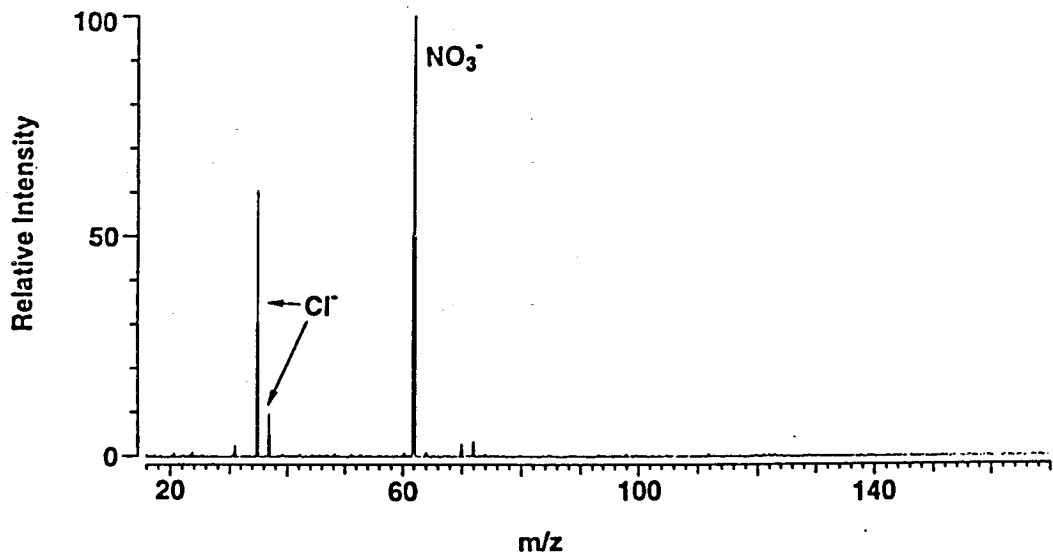
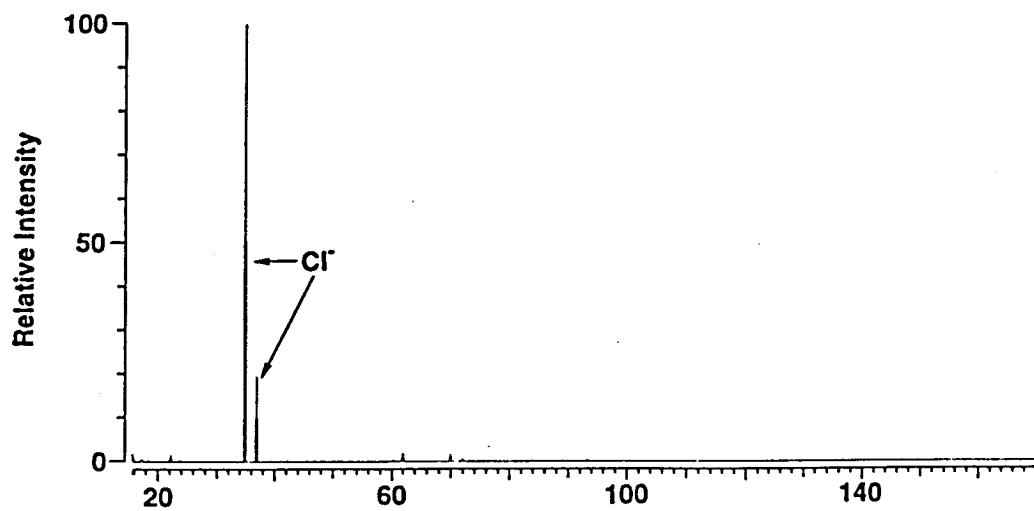
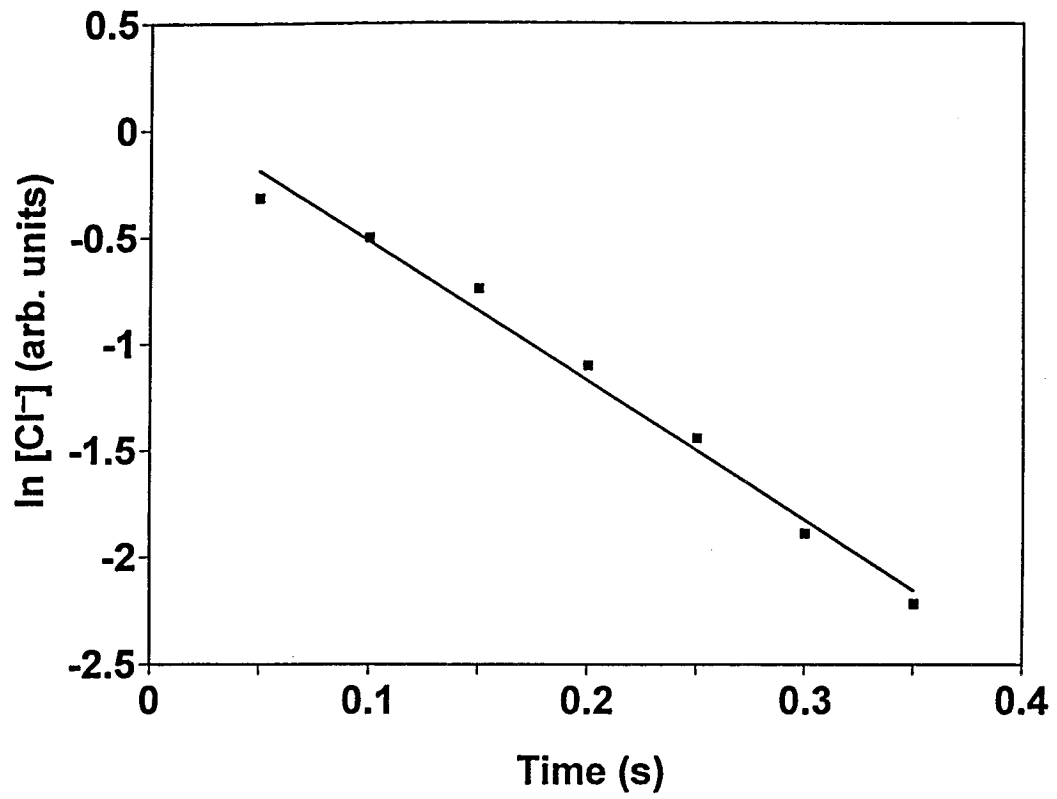


Figure 2. Observed decay of the Cl^- abundance with time for a single run. The line is a fit to the data. Conditions were the same as in Figure 1.



of the Cl^- relative abundance versus time for a single experiment. Rate constants for reaction 2 were determined from the decay of Cl^- abundance versus time by integrating the pseudo-first-order rate equation $d[\text{Cl}^-]/dt = -k[\text{ClONO}_2][\text{Cl}^-]$ with $[\text{ClONO}_2]$ held constant. $[\text{Cl}^-]$ was calculated as the sum of both Cl^- isotopes. Five experiments were performed with the stainless steel inlet line and four with the glass inlet line.

The rate constant obtained with the stainless steel inlet system, assuming that 25% of the ClONO_2 decomposed in the inlet line during each set of runs, was $(7.4 \pm 3.0) \times 10^{-10} \text{ cm}^3 \text{ s}^{-1} \text{ molecule}^{-1}$, where the error bar (1σ) includes the uncertainty in the extent of chlorine nitrate decomposition that had occurred during a given run and the accuracy of the absolute pressure measurements. The rate constant obtained when ClONO_2 was introduced through the glass inlet system was $(11.3 \pm 3.7) \times 10^{-10} \text{ cm}^3 \text{ s}^{-1} \text{ molecule}^{-1}$. The results from the set of runs done with the glass system are somewhat higher, suggesting that we did not account for all the decomposition of ClONO_2 in the stainless steel inlet line; however, the two results are still comparable. We calculated an average rate constant for reaction 2 of $(9.2 \pm 3.0) \times 10^{-10} \text{ cm}^3 \text{ s}^{-1} \text{ molecule}^{-1}$; the two results are within the error bars of their average. We can compare the observed k to a theoretical prediction for the collision rate based on the average dipole orientation (ADO) theory.³² From the experimental ClONO_2 dipole moment of 0.77 D,³³ and the theoretically calculated ClONO_2 polarizability of 4.54 Å,³⁴ we calculate that the ion-dipole collision rate constant $k_{\text{ADO}} = 1.16 \times 10^{-10} \text{ cm}^3 \text{ s}^{-1} \text{ molecule}^{-1}$. The reaction efficiency $k/k_{\text{ADO}} = 0.79$.

Discussion

We have found that chloride ions react with chlorine nitrate in the gas phase at near ion-dipole collision rates. Thus there is little or no activation barrier for this reaction. Previous ab initio calculations by Kuwata and Okumura have indicated that there is no energetic barrier for the approach of a Cl^- ion toward the chlorine atom in ClONO_2 . In fact, they find a minimum along the reaction coordinate pathway

corresponding to the ion-molecule complex $\text{Cl}_2 \cdot \text{NO}_3^-$, and calculated a binding enthalpy of $\Delta H_{298} = 5.9 \text{ kcal mol}^{-1}$ for this complex relative to $\text{Cl}_2 + \text{NO}_3^-$.³⁴ The ab initio structure of the complex³⁴ is shown in Figure 3. The reaction pathway (including the ion-molecule complex) is shown in Figure 4 (upper curve) and is similar to that of other exothermic ion-molecule reactions.

Our results have immediate implications for the ozone mitigation scheme proposed by Wong et al.²⁴ The large rate constant we have observed at room temperature suggests that Cl^- will react with the ClONO_2 present in the stratosphere. While we do not know the temperature dependence of the rate constant for the reaction, exothermic ion-molecule reactions with small barriers and bound transition complexes typically have either zero or negative temperature dependences. We therefore expect the reaction rate constant to be similar at stratospheric temperatures. For a ClONO_2 mixing ratio of 2 ppb at 100 Torr in the stratosphere, the lifetime of Cl^- will be on the order of seconds to minutes. The chlorine nitrate densities in the stratosphere are sufficiently high to assure that there is an excess of ClONO_2 relative to Cl^- , even at charge densities as high as 10^9 cm^{-3} . Furthermore, reaction 2 has the deleterious effect of not only destroying Cl^- but also activating the comparatively inert Cl reservoir species ClONO_2 to form the photoactive Cl_2 molecule and sequestering the negative charge in the inert NO_3^- ion, thus potentially contributing to stratospheric ozone depletion. In addition, we find that low-energy electron attachment directly to chlorine nitrate does not lead to production of Cl^- . On the basis of the present results, we conclude that the chloride ion will not be a stable sink of negative charge or atomic chlorine in the stratosphere.

We should note that Wong et al.³⁵ have recently demonstrated a charged-induced recovery of ozone in a chamber experiment, which they attribute to formation of inert Cl^- . However, the applicability of their results to the atmosphere remains in doubt, because the experiment does not include trace constituents such as ClONO_2 and HNO_3 at relative concentrations of $[\text{X}]/[\text{O}_3] \approx 10^{-3}$ similar to the lower stratosphere. The rate

Figure 3. Ab initio structure of the $\text{Cl}_2\cdot\text{NO}_3^-$ complex calculated by Kuwata and Okumura (reference 34). The binding enthalpy ΔH_{298} of this complex is $5.9 \text{ kcal mol}^{-1}$. Note that Cl_1 is the attacking Cl^- ion.

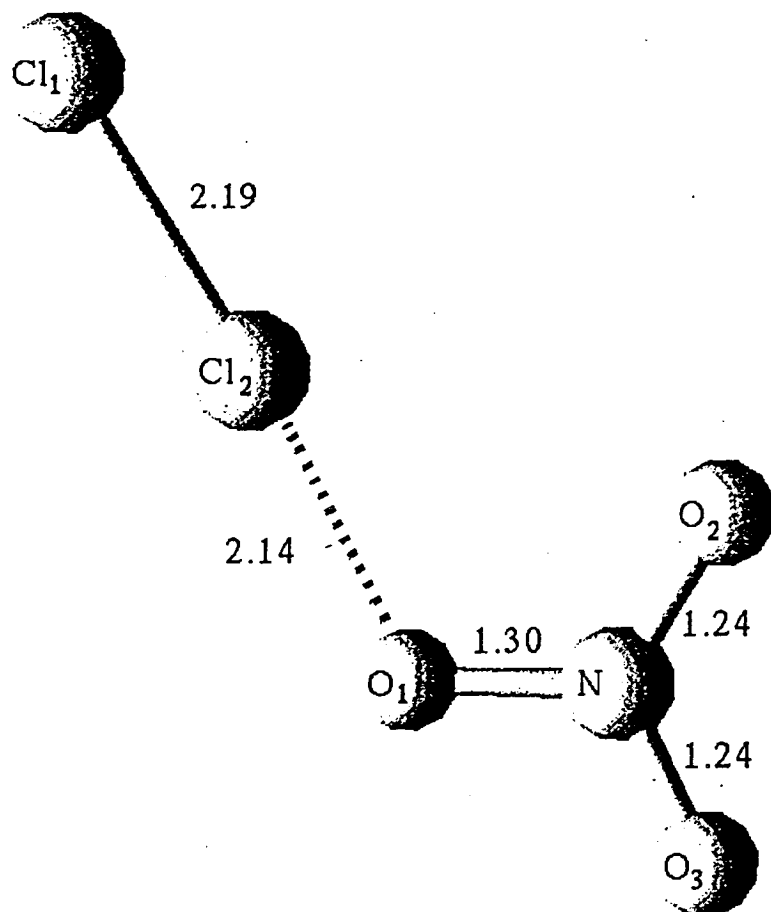
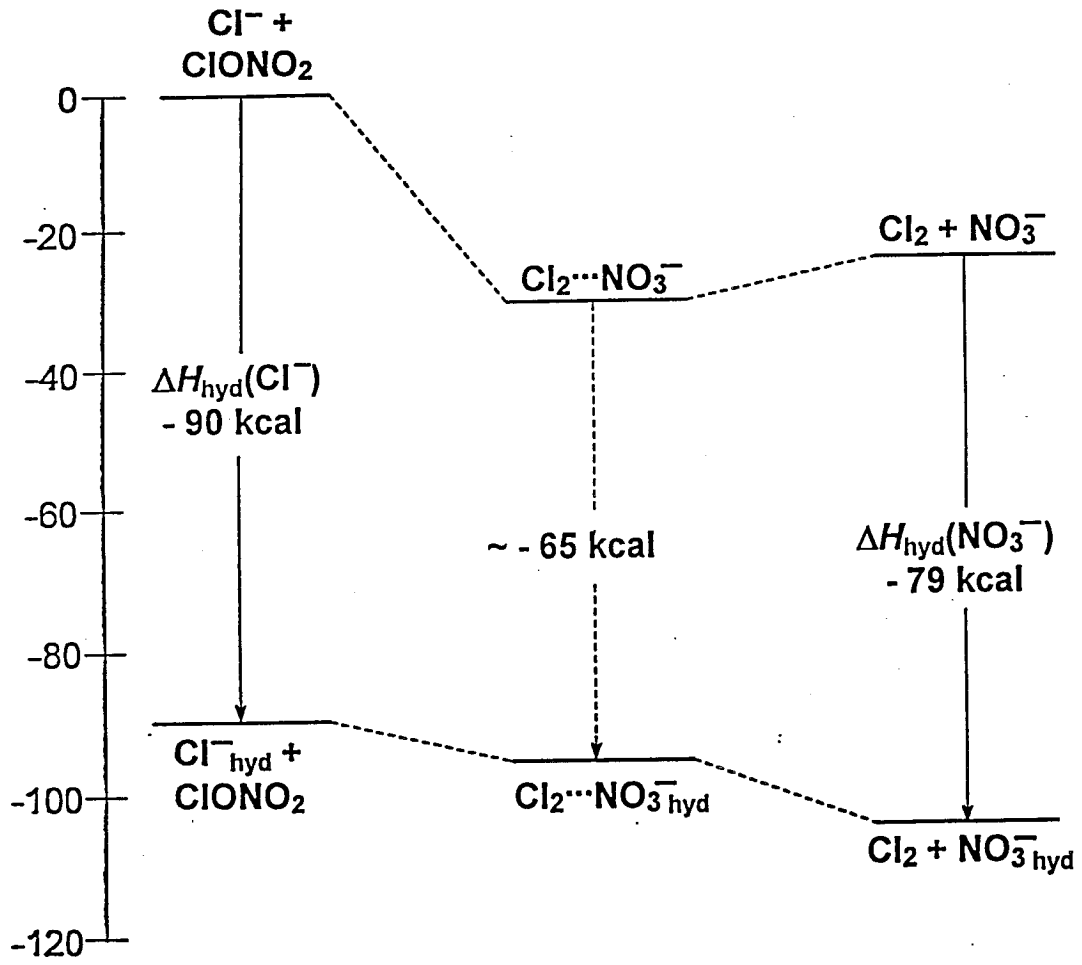


Figure 4. Reaction coordinate diagram for $\text{Cl}^- + \text{ClONO}_2 \rightarrow \text{Cl}_2 + \text{NO}_3^-$. The upper curve is based on the gas-phase enthalpies. The lower curve includes corrections for ion solvation enthalpies. The ionic hydration enthalpy of the $\text{Cl}_2\cdot\text{NO}_3^-$ intermediate is obtained by estimating the hydration of Kuwata and Okumura's ab initio charge distribution calculated for $\text{Cl}_2\cdot\text{NO}_3^-$ (reference 34). Details of the hydration calculation are given in the text.



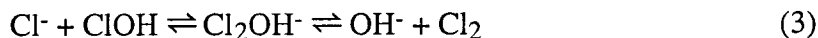
constants measured in this work and by Davidson et al.²³ indicate that such trace species can rapidly and completely convert the chloride ions back to radical forms, even at the charge densities and time scales used in the chamber experiment.

The reaction of Cl^- with ClONO_2 in the gas phase raises the possibility that such a reaction could also occur on a PSC surface. Such a reaction is consistent with the hypothesis that HCl is dissociatively ionized in stratospheric particles. Our results support the speculation of Molina and co-workers^{4,14,17,18} that the chloride ion is involved in the reactions HCl with ClONO_2 and HOCl on PSCs. However, there does not appear to be a need to invoke explicit ionization of the partner,¹⁸ e.g., Cl^+NO_3^- or Cl^+OH^- . Chu et al.¹⁰ have also recently questioned whether such ionization of the partner occurs, but the expression Cl^+NO_3^- could still be considered formally correct in that it describes the partial charges on neutral chlorine nitrate calculated by Kuwata and Okumura.³⁴ A direct ionic reaction is especially plausible if the PSC surfaces have a quasi-liquid structure that would allow solvent reorganization as proposed by Molina et al.^{4,18} In the following paragraphs we examine the effects of going from the gas phase to the condensed phase of water.

The reaction enthalpy is modified to first order by the heats of hydration ΔH_{hyd} of the ions. From the literature,³⁶ we find that $\Delta H_{\text{hyd}}(\text{Cl}^-) = -90 \text{ kcal mol}^{-1}$, somewhat higher than $\Delta H_{\text{hyd}}(\text{NO}_3^-) = -79 \text{ kcal mol}^{-1}$. With these corrections, we find $\Delta H_{\text{rxn}}(\text{hyd}) \approx -14 \text{ kcal mol}^{-1}$ (see Figure 4), where we use the notation "(hyd)" to refer to ion hydration. Thus the reaction remains significantly exothermic. A second-order correction to ΔH_{rxn} requires the solvation energetics for the neutral species. The solvation energetics of neutral chlorine nitrate is not known, but if we assume a crude estimate for the hydration enthalpy of ClONO_2 of approximately $-15 \text{ kcal mol}^{-1}$ (roughly 3-4 hydrogen bonds),¹⁶ then with $\Delta H_{\text{hyd}}(\text{Cl}_2) = -6.5 \text{ kcal mol}^{-1}$ for Cl_2 aqueous hydration,³⁷ we find that the heat of reaction would still be exothermic by approximately 5 kcal mol^{-1} .

The rate of reaction in the condensed phase will depend on how solvation affects the transition region of the reaction. As is well-known in S_N2 reactions,³⁸⁻⁴⁰ the charge becomes delocalized and the transition region is less stable relative to the reactants and products in polar solvents, especially protic solvents. These effects destabilize ion-molecule complexes and increase transition-state energies, thus slowing reaction rates.

Although the $Cl^- + ClONO_2$ system is quite polar, and the ion-molecule complex $Cl_2 \cdot NO_3^-$ may remain a stable intermediate in aqueous or solid H_2O . Kuwata and Okumura's previously calculated binding enthalpy of Cl_2 to the nitrate anion is 6 kcal mol⁻¹,³⁴ which is somewhat less than that of H_2O to NO_3^- (14.6 kcal mol⁻¹).⁴¹ An analogous complex, Cl_2OH^- , has been proposed by Eigen and Kustin⁴² as an intermediate in the aqueous hydrolysis of Cl_2 as shown in reaction 3. This reaction has



been proposed based on experimental evidence from aqueous-phase studies.

We can roughly estimate the ionic part of the hydration enthalpy of the intermediate complexes by considering the hydration of $Cl^{\delta-1} \cdots Cl \cdots NO_3^{-\delta}$. The contribution of each partially charged moiety to the total ionic hydration enthalpy can be estimated by scaling the experimental hydration enthalpies of Cl^- and NO_3^- using weighting factors obtained from the Born model of ion solvation.^{36,43} The Born equation states that the electrostatic energy of interaction between a charged sphere and a continuous dielectric medium is given by equation 4, where ϵ is the dielectric constant

$$W_{\text{Born}} = \frac{(ze)^2 \left(1 - \frac{1}{\epsilon}\right)}{8\pi\epsilon_0 r} \quad (4)$$

of the medium, ze is the charge of the sphere and r is the radius. The model thus predicts that the solvation energy simply scales as the square of the charge if we assume that the radius r does not change. With these assumptions, we can estimate the solvation enthalpy of the $Cl_2 \cdot NO_3^-$ complex by using the interpolation of equation 5, with $z(X_i)$

$$\Delta H_{\text{hyd}}(\text{Cl}_2 \bullet \text{NO}_3^-) = \Delta H_{\text{hyd}}(\text{Cl}^-) \left[\frac{z(\text{Cl}_1)}{z^0(\text{Cl}_1)} \right]^2 + \frac{1}{3} \Delta H_{\text{hyd}}(\text{NO}_3^-) \sum_i \left[\frac{z(\text{O}_i)}{z^0(\text{O}_i)} \right]^2 \quad (5)$$

denoting the calculated partial charges residing on the atom X_i of the $\text{Cl}_2 \bullet \text{NO}_3^-$ complex, and $z^0(X_i)$ the calculated charge on atom X_i of the separated ions Cl^- and NO_3^- . Kuwata and Okumura find that $z^0(\text{Cl}_1) = -1$, $z^0(\text{O}_i) = -0.55$, $z(\text{Cl}_1) = -0.29$, $z(\text{O}_1) = -0.49$, $z(\text{O}_2) = -0.45$ and $z(\text{O}_3) = -0.47$. The charge on the center N atom is not included in the summation for NO_3^- because Kuwata and Okumura found it does not change in going from NO_3^- to $\text{Cl}_2 \bullet \text{NO}_3^-$.³⁴

We obtain an estimate for $\Delta H_{\text{hyd}}(\text{Cl}_2 \bullet \text{NO}_3^-)$ of $-65 \text{ kcal mol}^{-1}$. The hydrated complex thus has an enthalpy 7 kcal mol^{-1} below the reactants, as shown in Figure 4 (lower curve). Unfortunately, there is no identifiable "neutral" moiety, so we cannot readily estimate the total (ion + neutral) hydration enthalpy of the complex. By comparison, equation 5 predicts that the activation barrier for the reaction $\text{Cl}^- + \text{CH}_3\text{Cl}$ is 48 kcal mol^{-1} , far greater than a solution-phase value of 28 kcal mol^{-1} predicted in a recent simulation.⁴⁴ The z^2 dependence thus probably overestimates the effects of solvent destabilization. Even this simple model then predicts that $\text{Cl}_2 \bullet \text{NO}_3^-$ may be a stable complex in condensed-phase H_2O .

From the solvation energetics we conclude that the reaction $\text{Cl}^- + \text{ClONO}_2$ could be energetically favored in condensed-phase H_2O . While we cannot estimate the height of the activation barrier in solution or on ice, the above considerations suggest that the transition state may be stabilized more in reaction 2 than in simple symmetric $\text{S}_{\text{N}}2$ reactions such as $\text{Cl}^- + \text{CH}_3\text{Cl}$. Furthermore, since solvent H_2O molecules likely already form hydrogen bonds with the polar nitrate group of neutral ClONO_2 , only small changes in the solvent microstructure are necessary to stabilize NO_3^- as charge is transferred. The free energy of activation may therefore be low enough for the reaction to proceed on time scales relevant to the stratosphere.

Our demonstration that Cl^- and ClONO_2 react rapidly in the gas phase is a first step toward an understanding of the molecular mechanism for the heterogeneous reaction 1. We have presented qualitative arguments which suggest that the direct reaction of Cl^- with ClONO_2 is thus a plausible mechanism for the reaction observed to take place on model PSC films, $\text{HCl} + \text{ClONO}_2 \rightarrow \text{Cl}_2 + \text{HNO}_3$. Other mechanisms are possible, e.g., solvent-assisted reactions of neutral HCl or dissociative ionization of ClONO_2 to $\text{ClO}^- + \text{NO}_2^+$. However, the proposed mechanism is consistent with the high Cl^- concentration observed in laboratory films exposed to HCl and with our understanding of the effects of solvation on $\text{S}_{\text{N}}2$ reactions.

A number of issues must be clarified before we can establish that this ionic pathway does in fact occur on ice and PSC surfaces. We must understand not only solvation energetics but also the molecular structure of PSC surfaces (crystalline, amorphous or quasi-liquid), entropic barriers on ice, reactant diffusion and dissociative ionization of HCl or ClONO_2 . Direct reaction of Cl^- will also be in competition with ClONO_2 hydrolysis followed by the reaction $\text{HOCl} + \text{HCl}$. Ultimately, studies of such questions should provide a detailed molecular picture of heterogeneous reactions occurring on or near the surfaces of PSC particles.

Acknowledgments

We wish to acknowledge the support of a National Science Foundation Presidential Young Investigator Award CHE-8957243, an NSF Graduate Fellowship for K. C. C. and a Deutsche Forschungsgemeinschaft Fellowship for B. M. H. We are grateful to J. L. Beauchamp for use of the ICR instrument, supported by NSF under Grant CHE-9108318, and for helpful advice. We thank A. Tabazadeh and M. T. Leu for providing preprints of their work.

References

- ¹Solomon, S.; Garcia, R. R.; Rowland, F. S.; Wuebbles, D. J. *Nature* **1986**, *321*, 755.
- ²Toon, O. B.; Turco, R. P. *Sci. Am.* **1991**, *264*, 68.
- ³Brune, W. H.; Anderson, J. G.; Toohey, D. W.; Fahey, D. W. *Science* **1991**, *252*, 1260.
- ⁴Molina, M. J.; Tso, T. L.; Molina, L. T.; Wang, F. C. W. *Science* **1987**, *238*, 1253.
- ⁵Tolbert, M. A.; Rossi, M. J.; Malhotra, R.; Golden, D. M. *Science* **1987**, *238*, 1258.
- ⁶Leu, M. T. *Geophys. Res. Lett.* **1988**, *15*, 17.
- ⁷Leu, M. T.; Moore, S. B.; Keyser, L. F. *J. Phys. Chem.* **1991**, *95*, 7763.
- ⁸Hanson, D. R.; Ravishankara, A. R. *J. Geophys. Res.* **1991**, *96*, 5081.
- ⁹Hanson, D. R.; Ravishankara, A. R. *J. Phys. Chem.* **1992**, *96*, 2682.
- ¹⁰Chu, L. T.; Leu, M. T.; Keyser, L. F. *J. Phys. Chem.* **1993**, *97*, 12798.
- ¹¹Tolbert, M. A.; Rossi, M. J.; Golden, D. M. *Science* **1988**, *240*, 1018.
- ¹²Tolbert, M. A.; Rossi, M. J.; Golden, D. M. *Geophys. Res. Lett.* **1988**, *15*, 847.
- ¹³Leu, M. T. *Geophys. Res. Lett.* **1988**, *15*, 851.
- ¹⁴Abbatt, J. P.; Molina, M. J. *J. Phys. Chem.* **1992**, *96*, 7674.
- ¹⁵Webster, C. R.; May R. D.; Toohey D. W.; Avallone, L. M.; Anderson J. G.; Newman, P.; Lait, L.; Schoeberl, M. R.; Elkins, J. W.; Chan, K. R. *Science* **1993**, *261*, 1130.
- ¹⁶Tabazadeh, A.; Turco, R. P. *J. Geophys. Res.* **1993**, *98*, 12727.
- ¹⁷Abbatt, J. P.; Beyer, K. D.; Fucaloro, A. F.; McMahon, J. R.; Woolridge, P. J.; Zhang, R.; Molina, M. J. *J. Geophys. Res.* **1992**, *97*, 15819.
- ¹⁸Molina, M. J. CHEMRAWN VII: *The Chemistry of the Atmosphere: Its Impact on Global Change*, J. G. Calvert, Ed., 1994, CRC Press, Inc., Boca Raton, Florida.
- ¹⁹Burley, J. D.; Johnston, H. S. *Geophys. Res. Lett.* **1992**, *19*, 1359.
- ²⁰Nelson, C. M.; Okumura, M. *J. Phys. Chem.* **1992**, *96*, 6112.

²¹Lias, S. G.; Bartmess, J. E.; Liebman, J. F.; Holmes, J. L.; Levin, R. D.; Mallard, W. G. *J. Phys. Chem. Ref. Data* **1988**, *17*, Suppl. 1.

²²DeMore, W. B.; Sander, S. P.; Golden, D. M. Hampson, R. F.; Kurylo, M. J.; Howard, C. J. Ravishankara, A. R.; Kolb, C. E.; Molina, M. J. *Chemical Kinetics and Photochemical Data for Use in Stratospheric Modeling*, Publication 92-20, Jet Propulsion Laboratory, Pasadena, CA, 1992.

²³Davidson, J. A.; Viggiano, A. A.; Howard, C. J.; Dotan, I., Fehsenfeld, F. C.; Albritton, D. L.; Ferguson, E. E. *J. Chem. Phys.* **1978**, *68*, 2085.

²⁴Wong, A. Y.; Steinhauer, J.; Close, R.; Fukuchi, T.; Milikh, G. M.; *Comments Plasma Phys. Contolled Fusion* **1989**, *12*, 223.

²⁵Marshall, A. G. *Acc. Chem. Res.* **1985**, *18*, 316.

²⁶Comisarow, M. B. *Anal. Chim. Acta.* **1985**, *178*, 1.

²⁷Schmeisser, M. *Inorg. Synth.* **1967**, *9*, 127.

²⁸Schack, C. J. *Inorg. Chem.* **1967**, *6*, 1938.

²⁹Brion, C. E.; Thomas, G. E. *Int. J. Mass Spectrom. Ion Phys.* **1968**, *1*, 25.

³⁰Christophorou, L. G.; Stockdale, J. A. D. *J. Phys. Chem.* **1968**, *48*, 1956.

³¹Ridge, D. P.; Beauchamp, J. L. *J. Chem. Phys.* **1969**, *51*, 470.

³²Su, T.; Bowers, M. T. *Int. J. Mass Spectrom. Ion Phys.* **1973**, *12*, 3471.

³³Suenram, R. D.; Johnson, D. R. *J. Mol. Spectrosc.* **1977**, *65*, 239.

³⁴Kuwata, K. T.; Okumura, M., manuscript in preparation. Also see: Haas, B.-M.; Crellin, K. C.; Kuwata, K. T.; Okumura, M. *J. Phys. Chem.* **1994**, *98*, 6740.

³⁵Wong, A. Y.; Sensharma, D. K.; Tang, A. W.; Suchanek, R. G.; Ho, D. *Phys. Rev. Lett.* **1994**, *72*, 3124.

³⁶Marcus, Y. *Ion Solvation*, 1985, John Wiley and Sons, Chichester. Other values of $\Delta H_{\text{hyd}}(\text{Cl}^-)$ exist; we use the values here for consistency between Cl^- and NO_3^- .

³⁷Wartenberg, H. v.; Werth, H. Z. *Phys. Chem. (Munich)* **1930**, *151*, 109.

³⁸See for example: (a) Dougherty, R. C.; Dalton J.; Roberts, J. D.; *Org. Mass Spectrom.* **1974**, *8*, 77. (b) Olmstead, W. M.; Brauman, J. I. *J. Am. Chem. Soc.* **1977**, *99*, 4219. (c) Kebarle, P.; Dillow, G. W.; Hirao, K.; Chowdhury, S. J. *J. Chem. Soc., Faraday Discuss.* **1988**, *85*, 23.

³⁹Lowry, T. H.; Richardson, K. S. *Mechanism and Theory in Organic Chemistry*, 1987, Harper & Row, New York.

⁴⁰Parker, A. J. *Chem. Rev.* **1969**, *69*, 1.

⁴¹Keesee, R. G. Castleman, A. W. *J. Phys. Chem. Ref. Data* **1986**, *15*, 1011.

⁴²Eigen, M.; Kustin, K. *J. Am. Chem. Soc.* **1962**, *84*, 1355.

⁴³Born, M. *Z. Phys.* **1920**, *21*, 45.

⁴⁴Chandrasekhar, J.; Smith, S. F.; Jorgensen W. L. *J. Am. Chem. Soc.* **1985**, *107*, 154.

Chapter 7

CHEMICAL IONIZATION OF TNT AND RDX WITH TRIMETHYLSILYL CATION

Kevin C. Crellin, M. Widmer and J. L. Beauchamp

Contribution No. 9166, Arthur Amos Noyes Laboratory of Chemical Physics,
California Institute of Technology, Pasadena, CA 91125

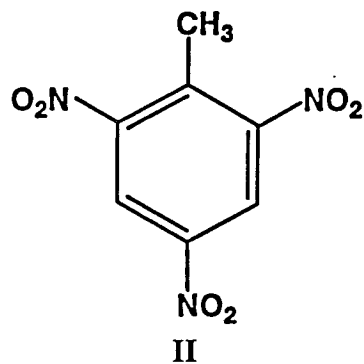
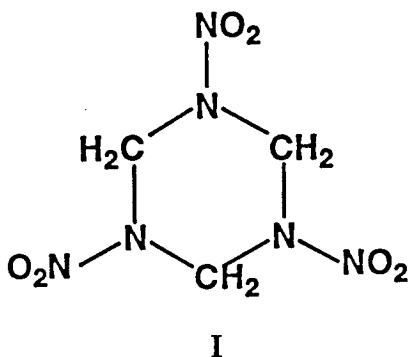
Published as an article in *Analytical Chemistry*, **1997**, *69*, 1092-1101.

Abstract

Fourier transform ion cyclotron resonance mass spectrometry has been used to examine the reactions of $\text{Si}(\text{CH}_3)_3^+$ with nitrobenzene, TNT and RDX. With nitrobenzene the only reaction observed is adduct formation which generates the $\text{C}_6\text{H}_5\text{NO}_2\text{Si}(\text{CH}_3)_3^+$ ion. The bimolecular rate constant for the reaction of $\text{Si}(\text{CH}_3)_3^+$ with nitrobenzene is measured to be $1.8 \times 10^{-9} \text{ cm}^3\text{s}^{-1}\text{molecule}^{-1}$. With TNT fragmentation and adduct formation were observed. The bimolecular rate constant for the reaction of $\text{Si}(\text{CH}_3)_3^+$ with TNT is measured to be $0.85 \times 10^{-9} \text{ cm}^3\text{s}^{-1}\text{molecule}^{-1}$. With RDX the dominant reaction observed is adduct formation, but some fragmentation is seen as a minor reaction pathway. The bimolecular rate constant for the reaction of $\text{Si}(\text{CH}_3)_3^+$ with RDX is estimated to be similar to that observed with TNT (approximately $0.7 \times 10^{-9} \text{ cm}^3\text{s}^{-1}\text{molecule}^{-1}$). Collision induced dissociation experiments performed on both the TNT- $\text{Si}(\text{CH}_3)_3^+$ and the RDX- $\text{Si}(\text{CH}_3)_3^+$ adducts using off-resonance collisional activation show the same fragmentation pattern that is observed during adduct formation. This fragmentation pattern appears to be a "fingerprint" for both adducts. These reactions appear to be driven by the high affinity of Si for oxygen and the attraction of the $\text{Si}(\text{CH}_3)_3^+$ ion to the formal negative charge of oxygen in a nitro group. A reaction coordinate diagram for reactions of RDX with $\text{Si}(\text{CH}_3)_3^+$ is derived (from known thermochemistry and ab initio calculations on the reactive intermediates) and its implications discussed. Reactions of this type could be useful as a detection scheme for common explosives.

Introduction

The threat of terrorism against increasingly diverse targets has focused much attention on developing methods to detect the explosives commonly used by terrorists.¹⁻³ One of the most common explosives used is 1,3,5-trinitro-1,3,5-triazacyclohexane (structure I), which is commonly called RDX and is the major explosive ingredient used in the plastic explosive C-4. 2,4,6-trinitrotoluene (abbreviated TNT and shown in structure II) is another explosive often used by terrorists. One class



of methods being investigated for use in detection of explosives such as RDX and TNT is mass spectrometry. It would be convenient to be able to detect these explosives with mass spectrometry, but two problems must be overcome. One problem is the low vapor pressures of most explosives.^{1,4} This problem can be overcome by heating the sample, which facilitates the vaporization of the explosive.

The second and greater problem is the complex chemistry exhibited by these explosives. Because of the high electron affinity of the NO₂ group,⁵ many attempts have been made to form negative ions of these explosives for detection by mass spectrometry. Electron attachment⁶ and negative chemical ionization⁷⁻⁹ have been tried, but mostly fragmentation is observed, making the interpretation of spectra difficult. Laser desorption/ion mobility mass spectrometry¹⁰ has shown promise with detection of the anions of explosives, but a large amount of fragmentation is still seen with RDX and HMX (1,3,5,7-tetranitro-1,3,5,7-tetrazacyclooctane).

Detection in positive ion modes has also been tried. Laser ionization/time of flight mass spectrometry has been used to detect NO^+ from explosives.¹¹ However, any compound with an NO_x group could produce the same signal, leaving this technique open to defeat by interferences. Much effort has been put into attempts to detect explosives by using chemical ionization mass spectrometry.^{7,12-20} Some of the reagents tried in past studies include hydrogen,¹⁴ water,¹⁵ methane,¹⁷⁻¹⁹ isobutane^{16,17,20} and ammonia.¹⁸ Unfortunately, the working conditions and gas used greatly affect the fragmentation spectra observed.¹³ Furthermore, fragmentation often dominates the spectra in these previous studies, which greatly complicates the interpretation of the observed spectra. It should also be noted that explosives are not particularly basic, and thus detection with the chemical ionization agents tried previously might be masked by the presence of trace species of higher proton affinity.

The two terminal oxygens of the nitro group in explosives possess a sizable partial negative charge due to the electronegativity of oxygen. Thus the terminal oxygens are expected to be susceptible to attack by Lewis acids. In addition, oxygen has a high affinity for Si. The $(\text{CH}_3)_3\text{Si-OH}$ bond energy, D°_{298} , is $128 \text{ kcal mol}^{-1}$,²¹ whereas the $(\text{CH}_3)_3\text{Si-CH}_3$, $(\text{CH}_3)_3\text{Si-NHCH}_3$ and $(\text{CH}_3)_3\text{Si-H}$ bond energies are $89.4 \text{ kcal mol}^{-1}$, $100 \text{ kcal mol}^{-1}$, and $90.3 \text{ kcal mol}^{-1}$, respectively.²¹ Previous studies have shown that $\text{Si}(\text{CH}_3)_3^+$, the trimethylsilyl cation, will readily form adducts with oxygen-containing compounds.²²⁻²⁴ Therefore we surmised that an ion such as $\text{Si}(\text{CH}_3)_3^+$ should form strongly bound complexes with molecules containing NO_2 groups. Most common explosives contain nitro groups, so $\text{Si}(\text{CH}_3)_3^+$ should selectively react with these and analogous compounds. Furthermore, since $\text{Si}(\text{CH}_3)_3^+$ interacts strongly with oxygen, it should not be labile like a proton. Rather, $\text{Si}(\text{CH}_3)_3^+$ should remain where it initially attaches. The purpose of this work is to test our hypothesis that $\text{Si}(\text{CH}_3)_3^+$ forms stable adducts with compounds containing nitro groups and evaluate its possible use as an alternative chemical ionization reagent for the detection of explosives. We will

present evidence showing that such reactivity is observed and provides a basis for the mass spectrometric detection of explosive compounds such as TNT and RDX.

Experimental

Overview. Fourier transform ion cyclotron resonance (FT-ICR) mass spectrometry is a well-established technique and its experimental aspects have been discussed previously in the literature.²⁵ Only details relevant to this experiment are presented here. A 1-in. cubic trapping cell is located between the poles of a Varian 15-in. electromagnet maintained at a field of 2.0 T. Data were collected with an IonSpec Omega/386 FT-ICR data system and associated electronics. Tetramethylsilane (TMS), $\text{Si}(\text{CH}_3)_4$, and nitrobenzene were introduced into the cell from vacuum inlet lines by separate leak valves, and their pressures were measured with a Schultz-Phelps (SP) ion gauge calibrated against an MKS 390 HA-00001SP05 capacitance manometer. Uncertainties in the absolute pressure limited rate constants to an accuracy of $\pm 20\%$. Both TMS (99.9% pure) and nitrobenzene (99% pure) were obtained commercially from Aldrich and purified by freeze-pump-thaw cycling. TNT was obtained from Thermedics and RDX was obtained commercially from Radian Corporation. The TNT was obtained as a solid, and the RDX in a solution with a 1:1 v/v mixture of acetonitrile and methanol. The concentration of RDX in the solution was 1 mg/ml.

Trimethylsilyl cation was generated by electron impact of TMS at a partial pressure of about $(9-10) \times 10^{-8}$ Torr. We found that a nominal electron energy of 22 eV was the most favorable energy for the formation of $\text{Si}(\text{CH}_3)_3^+$ ions. We then introduced nitrobenzene to the cell at pressures in the range of $(2-3) \times 10^{-7}$ Torr, and $\text{Si}(\text{CH}_3)_3^+$ was isolated by ejecting unwanted ions from the cell using frequency sweep excitation.²⁶ Subsequent reactions of nitrobenzene with $\text{Si}(\text{CH}_3)_3^+$ were then observed. Rate constants were determined in a straightforward manner, from slopes of semilog plots of the decay of reactant ion abundance versus time and the pressure of the neutral reactant. The reported rate constants are averages of several different sets of experimental data

taken at different pressures of the neutral gases. The temperature was assumed to be 298 K for all data sets.

The Probe Inlet/Internal Source Apparatus. RDX and TNT were introduced to the ICR cell with a newly designed probe assembly (Figure 1). When the probe is not inserted, a gate valve is present to close off the main chamber from the probe inlet vacuum line. Vacuum is maintained by a mechanically-backed diffusion pump. A liquid nitrogen (LN₂) trap is also used with the diffusion pump to prevent pump oil from diffusing throughout the vacuum system. Pressures as low as 1×10^{-8} Torr can be obtained in the probe inlet line, but experiments are run with background pressures as high as 5×10^{-8} Torr. When the gate valve between the probe inlet line and main vacuum chamber is opened, the probe can be inserted next to the ICR cell.

Figure 2 shows the design of the heated probe tip. The sample is placed in a 1.5 mm O.D. glass capillary tube and inserted into a copper holder. This holder is resistively heated and the temperature of the tip is measured with an Omega #HHM57A digital multimeter thermometer using a standard alumel-chromel thermocouple. With this implementation, non-volatile solids can be introduced to vacuum and heated to induce vaporization.

Solid TNT was inserted into a 1.5 mm O.D. glass capillary tube. The sample tube was then inserted into the probe tip and the probe tip was introduced to the vacuum chamber. No heating was required to generate TNT vapor, but with heating we were able to produce enough vapor to calibrate the SP ion gauge against the capacitance manometer. For the reaction with $\text{Si}(\text{CH}_3)_3^+$, the partial pressures of TNT present in the cell were in the range $(1-2) \times 10^{-7}$ Torr. The RDX solution was injected into a 1.5 mm O.D. glass capillary tube and the solvent evaporated. Generation of RDX vapor from the solid required heating the sample tube to approximately 100 °C, which is below 175 °C, the decomposition temperature of RDX.^{4a} We were unable to produce enough RDX vapor to calibrate the SP ion gauge against the capacitance manometer. Thus we were

Figure 1. Schematic of the complete probe inlet/internal source apparatus.

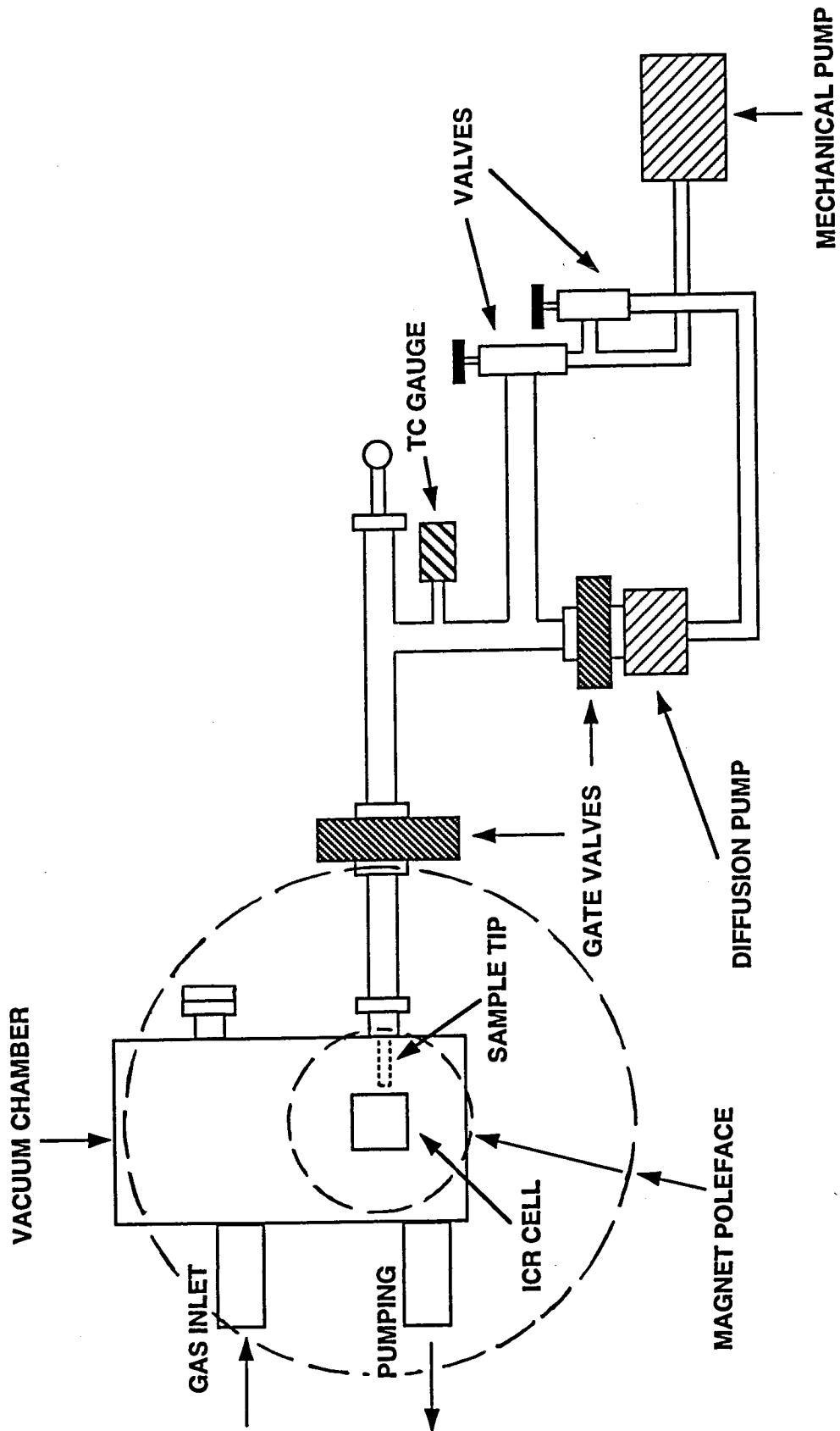
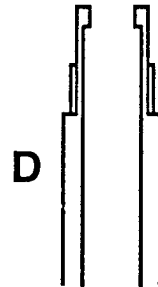
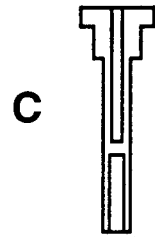
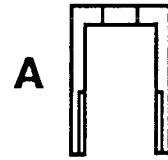


Figure 2. Schematic of the assembly of the heated probe tip. Drawing A shows a cross section of the cap to the probe tip, which screws on the top of the probe assembly. Component C is the resistively heated copper holder which houses the glass capillary tube. Drawing D shows a cross section of the end of the metal probe, which is approximately 1 m long, hollow and open to atmosphere. The probe is hollow to allow us to insert the heating wires and the thermocouple. B is a Viton o-ring which is placed between the copper holder and the metal probe. By tightly screwing on the cap of the probe tip the o-ring is squeezed between the holder and the probe, sealing off the inside of the probe (which is at atmosphere) from vacuum. Drawing E shows how the components are put together for use.



unable to directly measure the absolute pressure of RDX present in the cell. However, if we assume that the sensitivity of the SP gauge to RDX is similar to the gauge's sensitivity to TNT and nitrobenzene, then we can estimate that the partial pressures of RDX present in the cell were in the range $(2-4) \times 10^{-7}$ Torr.

With both TNT and RDX, TMS was already present in the cell at pressures of about 1×10^{-7} Torr, and after isolation of the $\text{Si}(\text{CH}_3)_3^+$ ion subsequent reactions of TNT and RDX with $\text{Si}(\text{CH}_3)_3^+$ were then observed. Rate constants were calculated using the pressure of TNT and the estimated pressures of RDX. The temperature is assumed to be 100 °C for the RDX experiments. For the TNT experiments we assume the cell is at the ambient temperature.

Collision Induced Dissociation (CID) Experiments. CID experiments were performed on the TNT- $\text{Si}(\text{CH}_3)_3^+$ and RDX- $\text{Si}(\text{CH}_3)_3^+$ adducts to characterize the fragmentation patterns observed and determine if unique fragments are produced that could act as a "fingerprint" for either explosive. We used sustained off-resonance irradiation (SORI)²⁷ to achieve the CID of both adducts. The collision energy for TNT was varied between 0 and 12 eV, while for RDX the energy was varied between 0 and 7 eV in the laboratory frame of reference. The TMS gas and TNT or RDX vapor present in the cell served as the collision gas.

Results

Reaction of $\text{Si}(\text{CH}_3)_3^+$ with Nitrobenzene. Reaction 1 was the only process



observed when $\text{Si}(\text{CH}_3)_3^+$ reacted with nitrobenzene (see Figure 3). Figure 4 shows a typical semilog plot of the decay of the $\text{Si}(\text{CH}_3)_3^+$ relative abundance for a single experiment. For the reaction of $\text{Si}(\text{CH}_3)_3^+$ with nitrobenzene the total bimolecular rate constant $k = 1.8 \times 10^{-9} \text{ cm}^3\text{s}^{-1}\text{molecule}^{-1}$ and the reaction efficiency $k/k_{\text{ADO}} = 0.68$.²⁸⁻³⁰

Figure 3a. Isolation of the $\text{Si}(\text{CH}_3)_3^+$ ion at $t = 0$ ms.

Figure 3b. Spectrum of the products of the reaction of $\text{Si}(\text{CH}_3)_3^+$ with nitrobenzene at $t = 150$ ms. The pressure of nitrobenzene in the cell is 2.2×10^{-7} Torr.

Figure 3c. Spectrum of the products of the reaction of $\text{Si}(\text{CH}_3)_3^+$ with nitrobenzene at $t = 400$ ms.

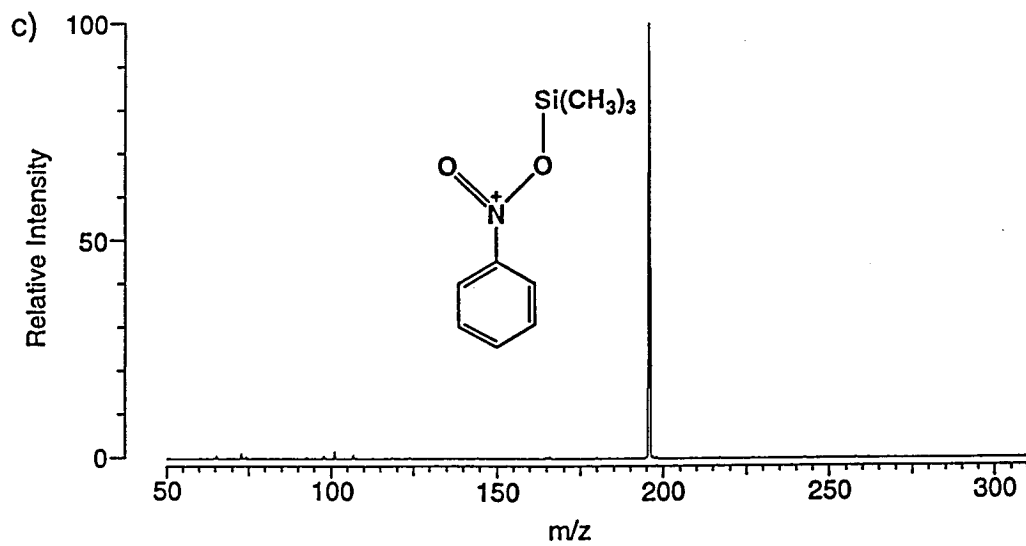
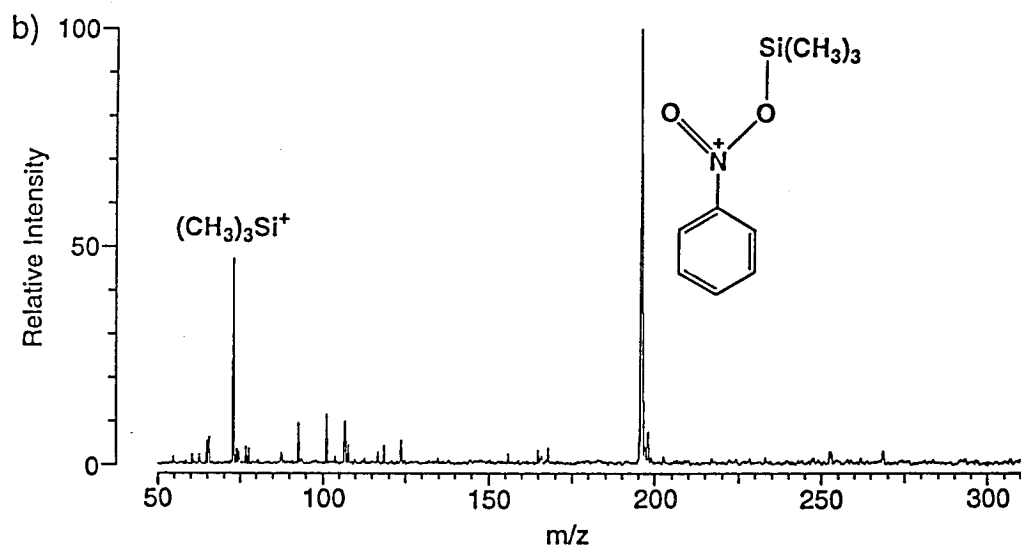
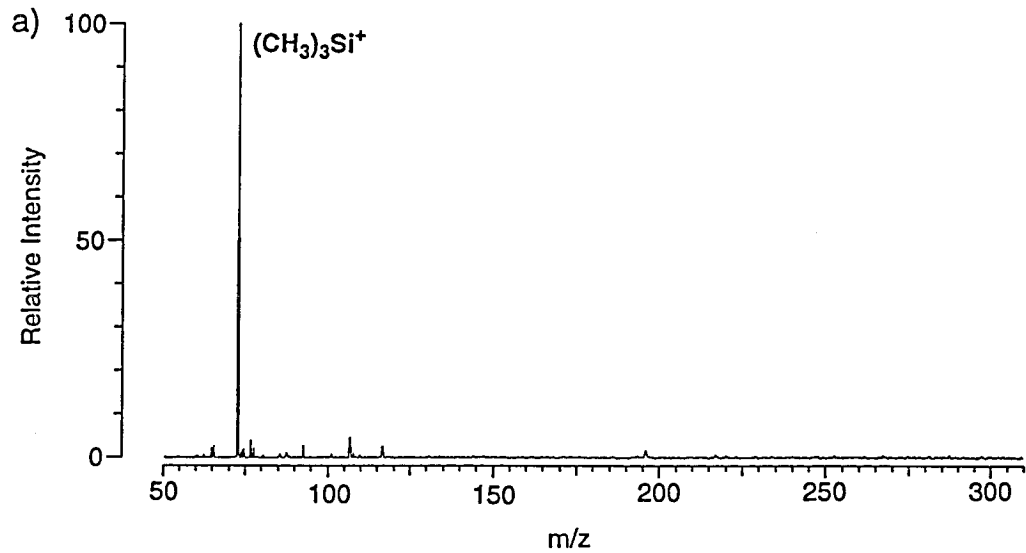
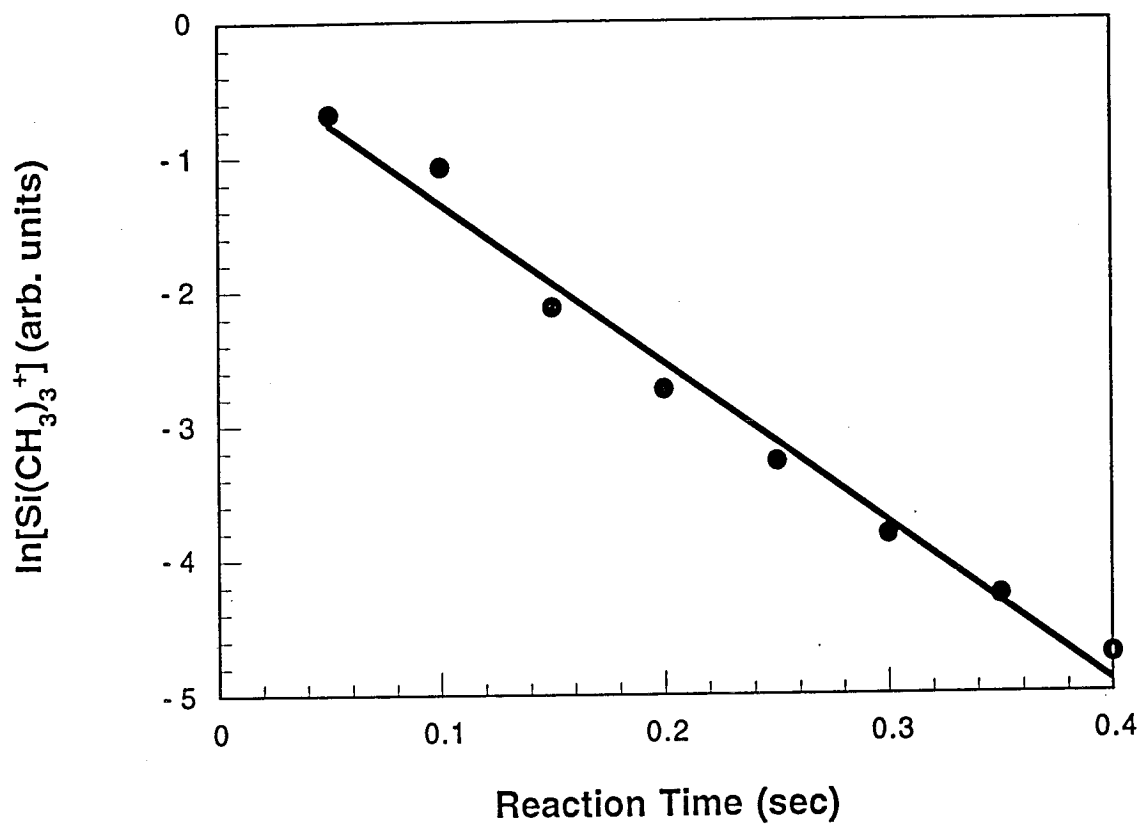
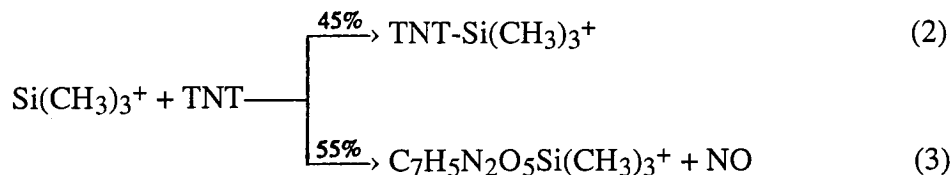


Figure 4. A semilog plot of the decay of the $\text{Si}(\text{CH}_3)_3^+$ abundance with time for a single experimental run with nitrobenzene. The line is a fit to the data.



Reaction of $\text{Si}(\text{CH}_3)_3^+$ with TNT. Reactions 2 and 3 were observed when



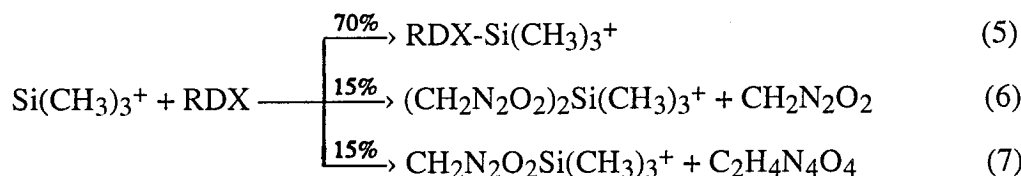
$\text{Si}(\text{CH}_3)_3^+$ reacted with TNT (see Figure 5). For the reaction of $\text{Si}(\text{CH}_3)_3^+$ with TNT the total bimolecular rate constant $k = 0.85 \times 10^{-9} \text{ cm}^3\text{s}^{-1}\text{molecule}^{-1}$ and the reaction efficiency $k/k_{\text{ADO}} = 0.53$.^{28,31}

CID of the $\text{TNT-Si}(\text{CH}_3)_3^+$ Adduct. Reaction 4 was the only reaction observed



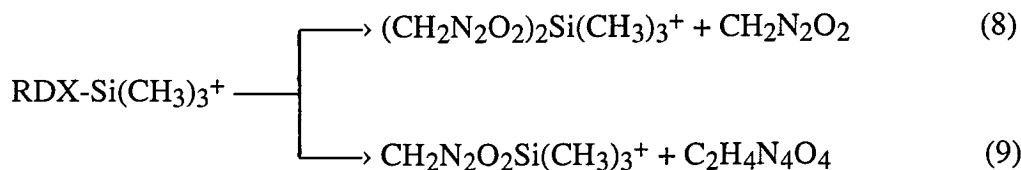
when the $\text{TNT-Si}(\text{CH}_3)_3^+$ adduct underwent CID (see Figure 6). The fragment observed from CID of the $\text{TNT-Si}(\text{CH}_3)_3^+$ adduct is the same as the fragment seen as a product of the reaction of TNT with $\text{Si}(\text{CH}_3)_3^+$. This fragment appears to be characteristic of the $\text{TNT-Si}(\text{CH}_3)_3^+$ adduct.

Reaction of $\text{Si}(\text{CH}_3)_3^+$ with RDX. Reactions 5-7 were observed when $\text{Si}(\text{CH}_3)_3^+$



reacted with RDX (see Figure 7). The product distribution given corresponds to reaction times greater than 500 ms. For the reaction of $\text{Si}(\text{CH}_3)_3^+$ with RDX the total bimolecular rate constant k is estimated to be $0.7 \times 10^{-9} \text{ cm}^3\text{s}^{-1}\text{molecule}^{-1}$ at 100°C . We estimate that the reaction efficiency $k/k_{\text{ADO}} = 0.2$.^{28,32}

CID of the $\text{RDX-Si}(\text{CH}_3)_3^+$ Adduct. Reactions 8 and 9 were observed when the



$\text{RDX-Si}(\text{CH}_3)_3^+$ adduct underwent CID (see Figure 8). The fragments observed from CID of the $\text{RDX-Si}(\text{CH}_3)_3^+$ adduct are the same as the fragments seen as minor products

Figure 5a. Isolation of the $\text{Si}(\text{CH}_3)_3^+$ ion at $t = 0$ ms.

Figure 5b. Spectrum of the products of the reaction of $\text{Si}(\text{CH}_3)_3^+$ with TNT at $t = 400$ ms. The pressure of TNT in the cell is 1.2×10^{-7} Torr.

Figure 5c. Spectrum of the products of the reaction of $\text{Si}(\text{CH}_3)_3^+$ with TNT at $t = 1000$ ms.

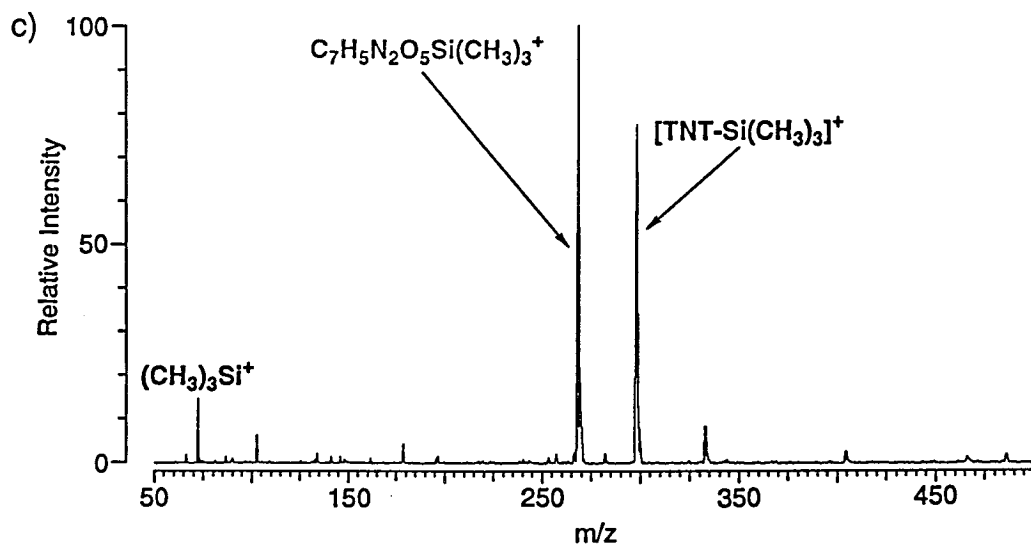
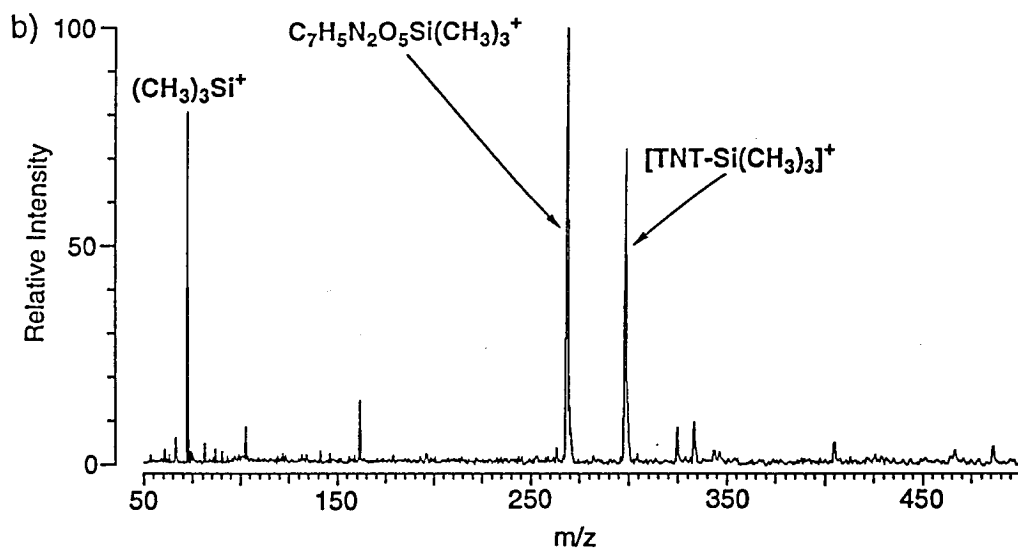
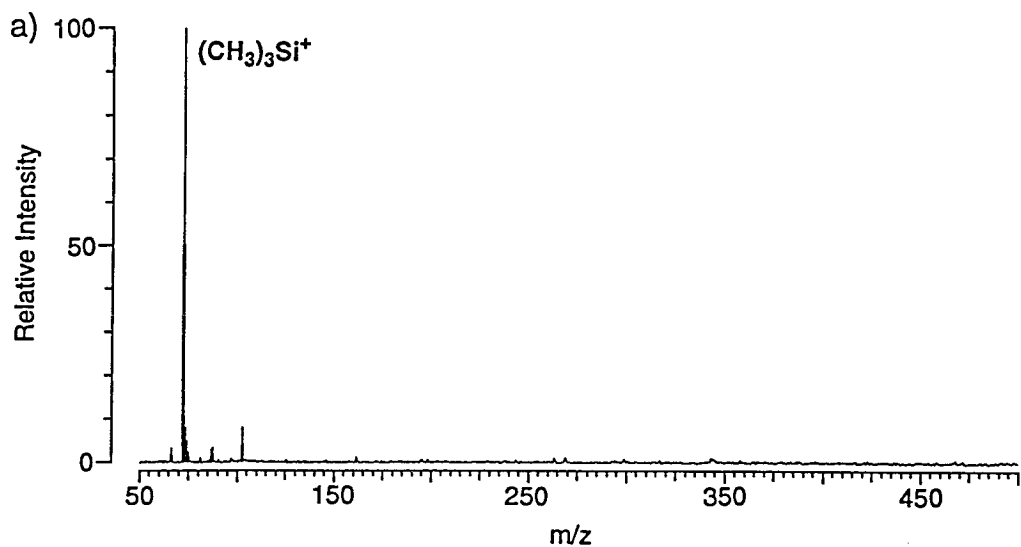


Figure 6a. Isolation of the TNT-Si(CH₃)₃⁺ adduct at $t = 0$ ms, after the Si(CH₃)₃⁺ has had 1000 ms to form the adduct.

Figure 6b. CID spectrum of the TNT-Si(CH₃)₃⁺ adduct. The collision gas is a mixture of TNT and TMS in a 1:1 ratio. Ions were excited at a frequency approximately 2000 Hz below the resonant frequency of the ion (approximately 6 m/z higher) for 500 ms. The average collision energy was 3.7 eV for the TNT-Si(CH₃)₃⁺ adduct in the center-of-mass frame of reference.

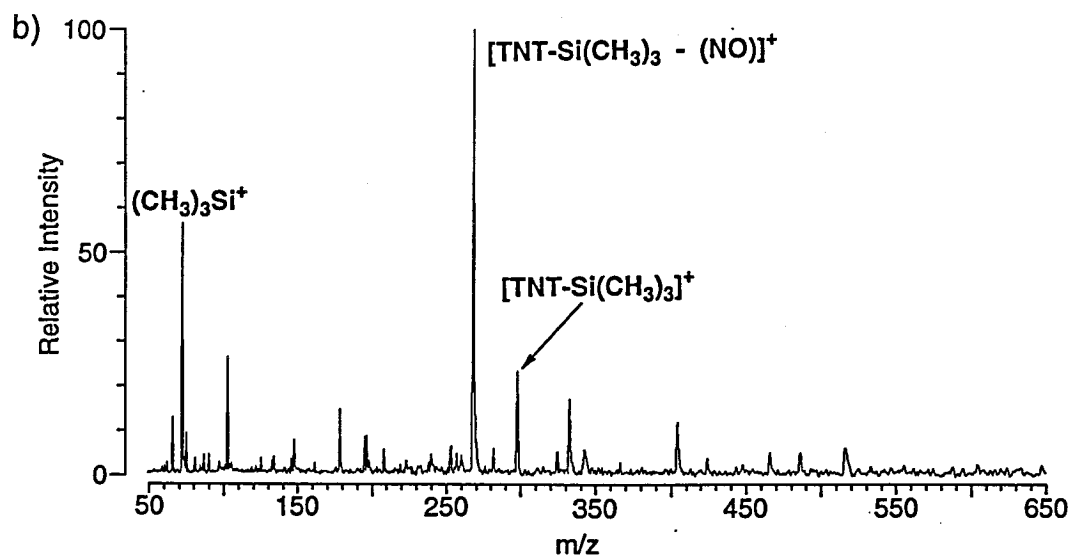
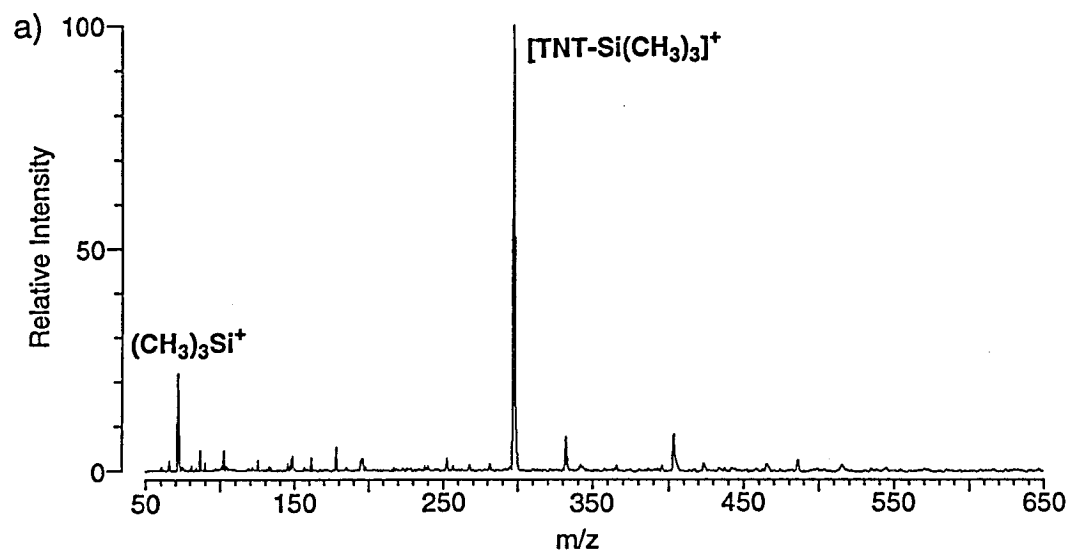


Figure 7a. Isolation of the $\text{Si}(\text{CH}_3)_3^+$ ion at $t = 0$ ms.

Figure 7b. Spectrum of the products of the reaction of $\text{Si}(\text{CH}_3)_3^+$ with RDX at $t = 300$ ms. The estimated pressure of RDX in the cell is $(2-3) \times 10^{-7}$ Torr. The RDX sample has been heated to approximately 100 °C. The peak at m/z 279 is attributed to the loss of atomic oxygen from a small amount of the RDX- $\text{Si}(\text{CH}_3)_3^+$ adduct.

Figure 7c. Spectrum of the products of the reaction of $\text{Si}(\text{CH}_3)_3^+$ with RDX at $t = 1000$ ms. The peak at m/z 279 is attributed to the loss of atomic oxygen from a small amount of the RDX- $\text{Si}(\text{CH}_3)_3^+$ adduct.

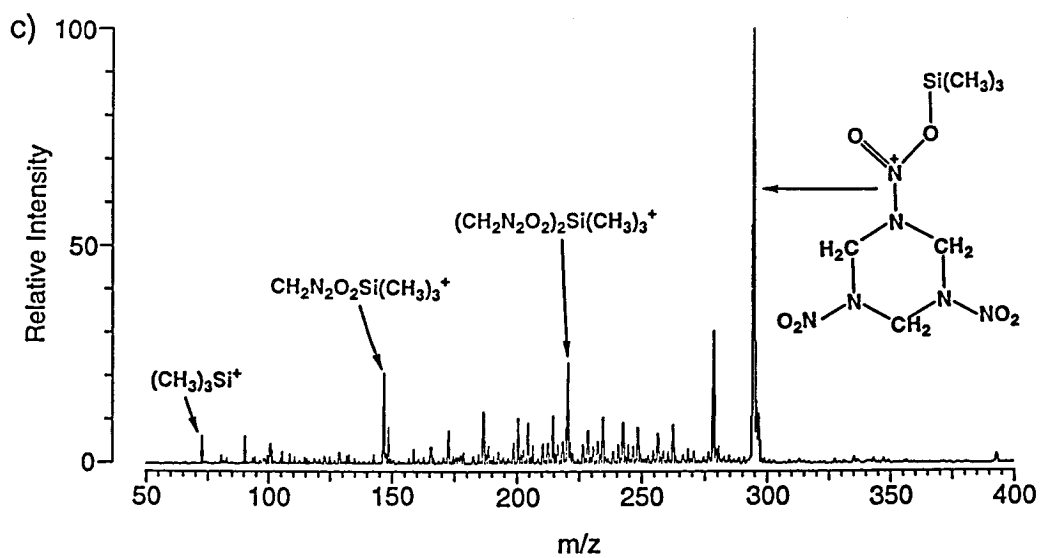
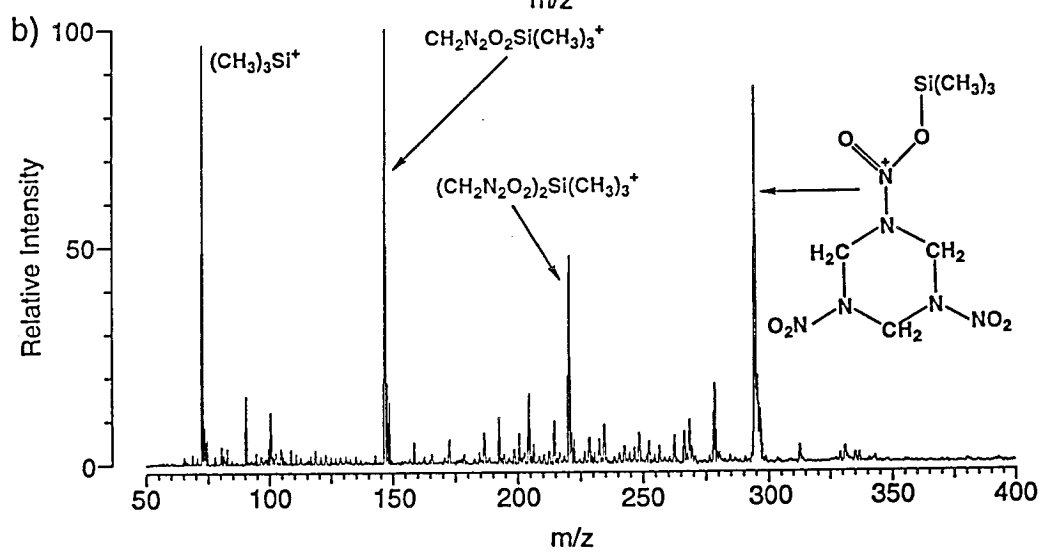
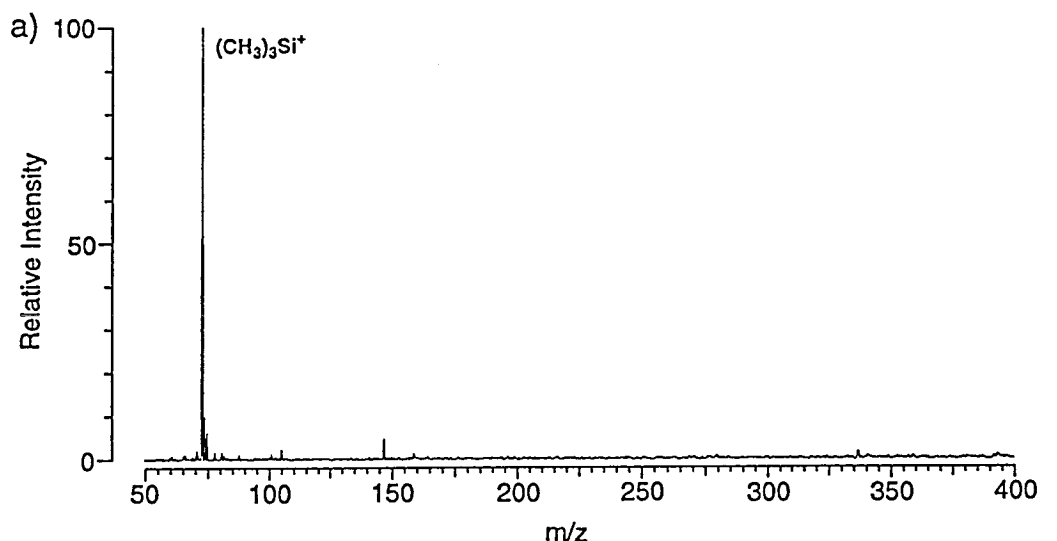
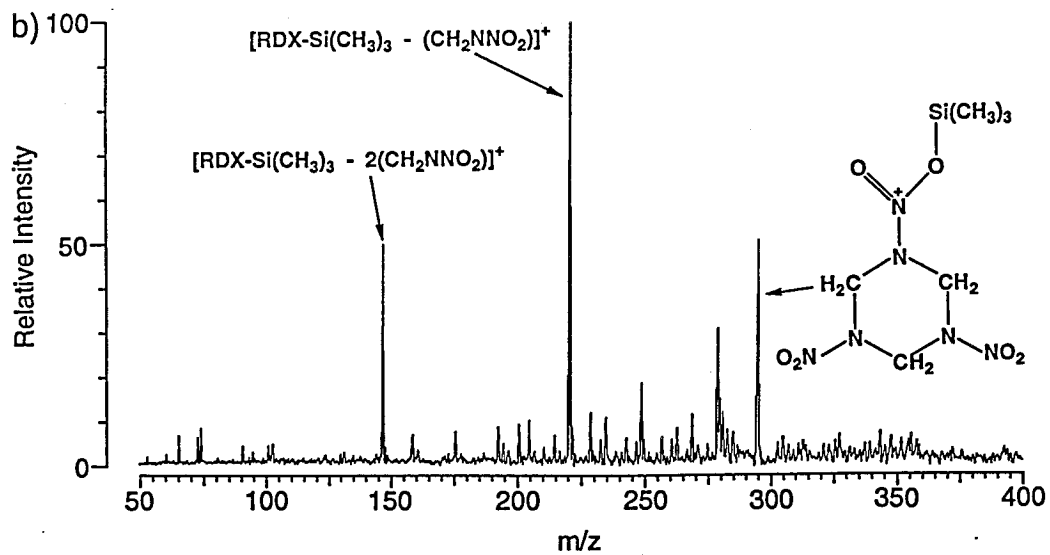
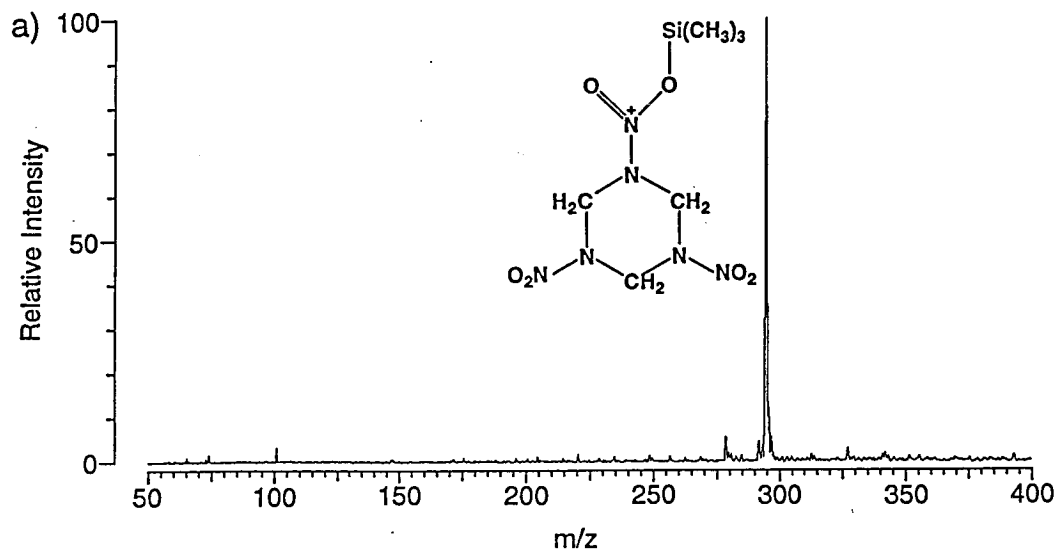


Figure 8a. Isolation of the RDX-Si(CH₃)₃⁺ adduct at $t = 0$ ms, after the Si(CH₃)₃⁺ has had 1000 ms to form the adduct.

Figure 8b. CID spectrum of the RDX-Si(CH₃)₃⁺ adduct. The collision gas is mixture of RDX and TMS in a 3:1 ratio. Ions were excited at a frequency approximately 1400 Hz below the resonant frequency of the ion (approximately 4 m/z higher) for 125 ms. The average collision energy was 1.3 eV for the RDX-Si(CH₃)₃⁺ adduct in the center-of-mass frame of reference. The peak at m/z 279 is attributed to the loss of atomic oxygen from a small amount of the RDX-Si(CH₃)₃⁺ adduct.



of the reaction of RDX with $\text{Si}(\text{CH}_3)_3^+$. These fragments appear to be characteristic of the $\text{RDX-Si}(\text{CH}_3)_3^+$ adduct. We should note that the product distribution is dependent on the average collision energy. At an average collision energy of 0.6 eV (in the center-of-mass frame of reference), very little of the product of reaction 9 is seen. However, as the collision energy is increased, the relative amount of $\text{CH}_2\text{N}_2\text{O}_2\text{Si}(\text{CH}_3)_3^+$ that is formed also increases.

Semi-Empirical and Ab Initio Calculations

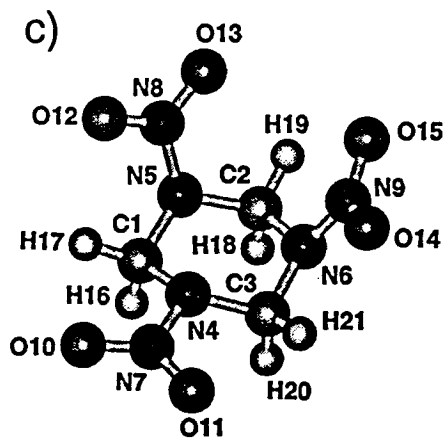
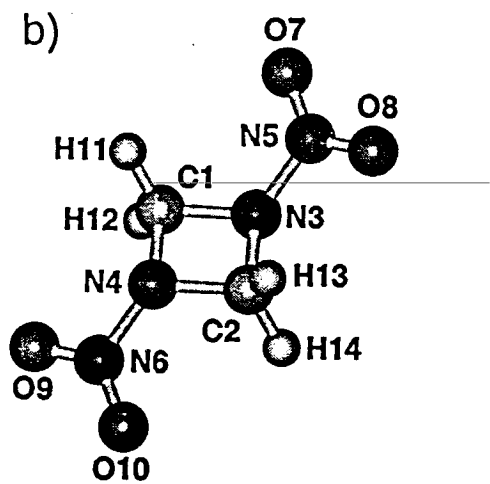
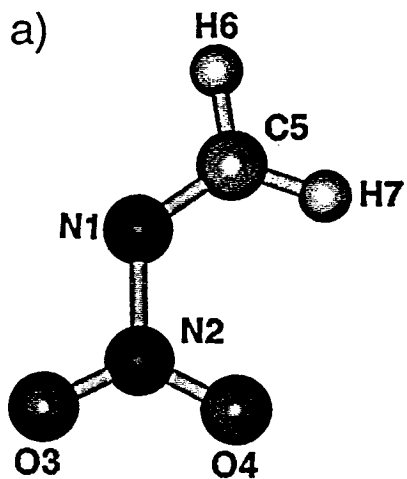
Overview. From the structure of RDX one can see that it is made up of three monomer units in a ring. The products we have seen in reactions 6-9 show that under the conditions present in the ICR cell, fragmentation involves the loss of one or two $\text{CH}_2\text{N}_2\text{O}_2$ units, leaving behind a dimer or monomer adduct. To assist us in the elucidation of the energetics of RDX, its fragments, and the adducts of RDX and its fragments with $\text{Si}(\text{CH}_3)_3^+$, we used semi-empirical and ab initio calculations to study these various species. Semi-empirical calculations on the adduct species were performed with HyperChem,³³ while PS-GVB³⁴ and the Gaussian 92 suite of programs³⁵ were used to perform ab initio calculations on RDX and its fragments.

RDX and Neutral Fragments. Initial geometry optimizations were performed using PS-GVB to identify the lowest energy isomers of the various species. These optimizations were done at the Hartree-Fock (HF) level with a 6-31G** basis set. Single-point calculations at the localized second-order Møller-Plesset (LMP2) level with a 6-31G** basis set were then performed on all of the HF-optimized structures to confirm the HF energies and obtain better estimates of the relative energies of RDX and its fragments. The dipole moment and polarizability of the lowest energy RDX conformation was also calculated at the HF level to provide the estimates used in the results section for calculation of reaction efficiencies. Gaussian 92 was then used to calculate the harmonic vibrational frequencies for the lowest energy monomer, dimer

and trimer structures to obtain zero-point energies. The frequency calculations were done at the HF level with a 6-31G** basis set.

Several different geometries were calculated for RDX and its dimer and monomer fragments. Figure 9 shows the HF-optimized lowest energy geometries of RDX and its dimer and monomer fragments.³⁶ For RDX the lowest energy conformation is a chair form with two nitro groups in an axial position and the remaining nitro group equatorially oriented. The lowest energy dimer fragment of RDX is composed of a planar four-membered ring with the nitro groups oriented in a trans fashion with respect to the plane of the ring. The CH₂NNO₂ unit was found to have a planar geometry in its lowest energy conformation. Although a previous study³⁷ found that the lowest energy geometry for RDX had a chair conformation with all nitro groups axial (they found the chair form with two axial nitro groups was 0.6 kcal mol⁻¹ higher in energy), the highest level of calculation Coffin et al. utilized was HF with a 4-21G basis set. Gas-phase electron diffraction studies have found that RDX has a chair conformation with all nitro groups axial,³⁸ in contrast to our calculations. However, we found that in our calculations the energy of the chair form of RDX with all nitro groups axial was only 0.64 kcal mol⁻¹ higher than the chair form with two nitro groups axial. This is the virtually the same energy difference found by Coffin et al.,³⁷ but our energy ordering for these two forms are reversed. Furthermore, we find that the energies of chair RDX with one axial nitro group and no axial nitro groups are 1.2 and 6.5 kcal mol⁻¹ higher, respectively, than our calculated lowest energy form. Coffin et al. calculated that the energies of chair RDX with one axial nitro group and no axial nitro groups are 1.7 and 7.2 kcal mol⁻¹ higher, respectively, than their calculated lowest energy form. Thus our calculations appear to agree fairly well with those of Coffin et al., except for the ordering of the two lowest energy conformers.

Figure 9. HF-optimized geometries of the lowest energy conformations of (a) CH_2NNO_2 , (b) $(\text{CH}_2\text{NNO}_2)_2$, and (c) RDX. Optimizations performed with a 6-31G** basis set. Structural parameters for each of these species are shown in Tables 1A-3A in the appendix to this chapter.



From the calculated LMP2 relative energies of RDX and its dimer and monomer fragments, we can theoretically evaluate ΔH for reactions 10-12. Since the LMP2 level



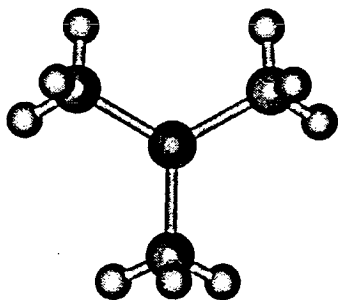
of theory is size-consistent, ΔH can be rigorously calculated as the difference of the electronic energies of the products and the electronic energies of the reactants. When zero-point energies are taken into account and 0 K enthalpies are corrected to 298 K enthalpies, we find that $\Delta H_{10} = +37.6 \text{ kcal mol}^{-1}$, $\Delta H_{11} = +30.5 \text{ kcal mol}^{-1}$ and $\Delta H_{12} = +7.1 \text{ kcal mol}^{-1}$. The dipole moment and polarizability of RDX were calculated to be 6.5 D and 12.3 \AA^3 , respectively, at the HF level of theory. Our calculated dipole moment agrees well with previously calculated dipole moments.³⁹

In addition to the previously described ab initio calculations on RDX and its fragments, we also performed semi-empirical calculations at the PM3 level⁴⁰ with HyperChem on RDX and its fragments (to complement the calculations described in the next section). These calculations predict that $\Delta H_{f,298}^\circ(\text{RDX,g}) = +42.0 \text{ kcal mol}^{-1}$, $\Delta H_{f,298}^\circ(\text{dimer,g}) = +33.2 \text{ kcal mol}^{-1}$ and $\Delta H_{f,298}^\circ(\text{monomer,g}) = +27.4 \text{ kcal mol}^{-1}$. The values for ΔH_{10} , ΔH_{11} and ΔH_{12} calculated from these semi-empirical heats of formation are 40.2, 18.6 and 21.6 kcal mol⁻¹, respectively. The poor agreement between the ab initio and semi-empirical enthalpies of reactions 11 and 12 is probably a reflection of the inaccurate prediction of $\Delta H_{f,298}^\circ(\text{dimer,g})$ by the PM3 method.⁴¹

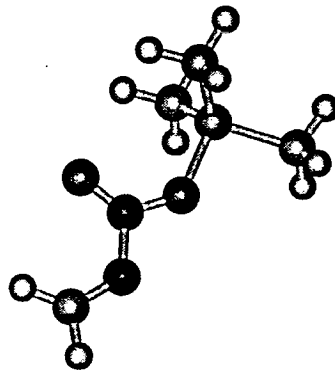
RDX-Si(CH₃)₃⁺ and Cationic Fragments. Geometry optimizations were performed using HyperChem to determine the lowest energy conformations of RDX-Si(CH₃)₃⁺, its cationic fragments, and Si(CH₃)₃⁺. The optimizations were done at the PM3 level of calculation. Figure 10 shows the PM3-optimized geometries of RDX-Si(CH₃)₃⁺, its dimer and monomer fragment adducts, and Si(CH₃)₃⁺.³⁶ For the RDX-Si(CH₃)₃⁺ adduct, the lowest energy form had all three nitro groups in an axial position.

Figure 10. PM3-optimized geometries of the lowest energy conformations of the (a) $\text{Si}(\text{CH}_3)_3^+$ ion and the (b) $\text{CH}_2\text{NNO}_2\text{-Si}(\text{CH}_3)_3^+$, (c) $(\text{CH}_2\text{NNO}_2)_2\text{-Si}(\text{CH}_3)_3^+$, and (d) $\text{RDX-Si}(\text{CH}_3)_3^+$ adducts. Structural parameters for each of these species are shown in Tables 4A-7A in the appendix to this chapter.

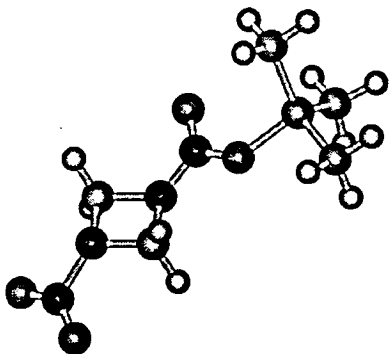
a)



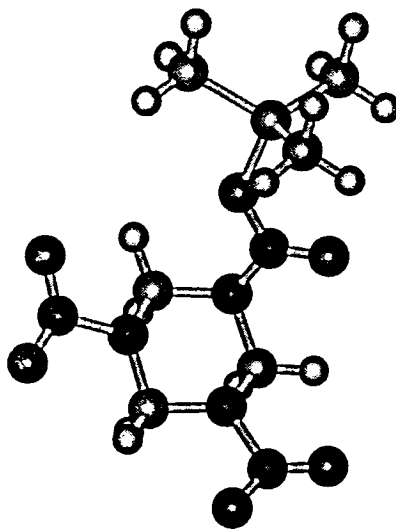
b)



c)



d)



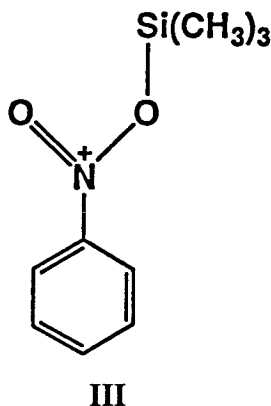
The lowest energy dimer adduct had a planar four-membered ring with the nitro groups oriented in a trans fashion with respect to the plane of the ring, and the monomer adduct was found to have a planar geometry. The $\text{Si}(\text{CH}_3)_3^+$ ion had a trigonal planar geometry.

These calculations predict that $\Delta H_{\text{f},298}^\circ(\text{RDX-Si}(\text{CH}_3)_3^+, \text{g}) = +149.1 \text{ kcal mol}^{-1}$, $\Delta H_{\text{f},298}^\circ(\text{dimer-Si}(\text{CH}_3)_3^+, \text{g}) = +142.7 \text{ kcal mol}^{-1}$, $\Delta H_{\text{f},298}^\circ(\text{monomer-Si}(\text{CH}_3)_3^+, \text{g}) = +134.0 \text{ kcal mol}^{-1}$ and $\Delta H_{\text{f},298}^\circ(\text{Si}(\text{CH}_3)_3^+, \text{g}) = +141.3 \text{ kcal mol}^{-1}$. These heats of formation, in conjunction with the semi-empirical heats of formation of RDX and its fragments from the previous section, allow us to determine D_{298}° of the silicon-oxygen bonds in $\text{RDX-Si}(\text{CH}_3)_3^+$ and its dimer and monomer adducts to be 34.2, 31.8 and 34.7 kcal mol^{-1} , respectively.⁴³ These bond energies are in good agreement with the average $\text{Si}^+\text{-O}$ single bond energy of approximately 40 kcal mol^{-1} experimentally observed in other studies.^{23,44} Still, it appears that the PM3 method has underestimated the silicon-oxygen bond energies by approximately 5 kcal mol^{-1} . The larger 8 kcal mol^{-1} underestimate of the silicon-oxygen bond strength in the dimer adduct is probably the result of the inaccurate predictions at the PM3 level of $\Delta H_{\text{f},298}^\circ(\text{dimer-Si}(\text{CH}_3)_3^+, \text{g})$ and $\Delta H_{\text{f},298}^\circ(\text{dimer}, \text{g})$.

Discussion

Formation of $\text{Si}(\text{CH}_3)_3^+$ Adducts with Nitrobenzene, TNT and RDX. In order to test our hypothesis that $\text{Si}(\text{CH}_3)_3^+$ will react with compounds containing nitro groups we first observed the reaction between $\text{Si}(\text{CH}_3)_3^+$ and nitrobenzene. Only reaction 1 was observed to occur, as shown in Figure 3. Although this reaction has been reported previously,²³ no supporting data was shown and no kinetic analysis performed. This process is fast and efficient at room temperature and fragmentation of the adduct was not seen. We postulate that the adduct exists as structure **III**, for the following reasons. First, Si has a higher affinity for oxygen than for carbon, nitrogen or hydrogen. In addition, the oxygen atoms of a nitro group possess large partial negative charges.

Therefore the oxygens of a nitro group should exhibit nucleophilic behavior and strongly interact with the $\text{Si}(\text{CH}_3)_3^+$ ion. Such adduct formation with oxygen containing



compounds has previously been observed.²²⁻²⁴ Finally, in order for $\text{Si}(\text{CH}_3)_3^+$ to bond to a carbon, nitrogen or hydrogen atom in nitrobenzene, a bond somewhere in the molecule must first be broken. Thus it is likely that energetic barriers prevent $\text{Si}(\text{CH}_3)_3^+$ from attacking carbon, nitrogen or hydrogen in nitrobenzene. But the oxygen atoms on the nitro group have unshared electron pairs that $\text{Si}(\text{CH}_3)_3^+$ can attack without breaking bonds already present, so there should be little or no barrier to bond formation at an oxygen atom. From the preceding discussion we conclude that **III** is the only reasonable structure for the $\text{C}_6\text{H}_5\text{NO}_2\text{Si}(\text{CH}_3)_3^+$ adduct.

Since $\text{Si}(\text{CH}_3)_3^+$ readily reacted with nitrobenzene as hypothesized, we next observed the reactions of TNT and RDX with $\text{Si}(\text{CH}_3)_3^+$ in order to investigate if $\text{Si}(\text{CH}_3)_3^+$ would be a suitable chemical ionization reagent for use in the detection and identification of explosives by mass spectrometry. Reactions 2 and 3 were observed with TNT, and typical results are shown in Figure 5. Much fragmentation is observed, but a significant amount of the TNT- $\text{Si}(\text{CH}_3)_3^+$ adduct is seen. As with nitrobenzene, the reaction of TNT with $\text{Si}(\text{CH}_3)_3^+$ occurs quickly and efficiently. When RDX was reacted with $\text{Si}(\text{CH}_3)_3^+$, reactions 5-7 were observed, as shown in Figure 7. A small amount of fragmentation is observed, but the major product is the RDX- $\text{Si}(\text{CH}_3)_3^+$ adduct. We were unfortunately unable to directly measure the RDX pressure in the cell,

but the reaction of $\text{Si}(\text{CH}_3)_3^+$ with RDX occurs on a similar time scale as the reaction of TNT with $\text{Si}(\text{CH}_3)_3^+$. This indicates that the reaction of RDX with $\text{Si}(\text{CH}_3)_3^+$ is also fast and efficient. Rough estimates of the pressure of RDX in the cell allowed us to estimate the rate constant and efficiency of the reaction of RDX with $\text{Si}(\text{CH}_3)_3^+$, and the estimated rate constant is about the same as the rate constant for TNT reacting with $\text{Si}(\text{CH}_3)_3^+$.

Fragmentation Processes of TNT- $\text{Si}(\text{CH}_3)_3^+$ and RDX- $\text{Si}(\text{CH}_3)_3^+$. The formation of both the TNT- $\text{Si}(\text{CH}_3)_3^+$ and the RDX- $\text{Si}(\text{CH}_3)_3^+$ adducts were accompanied by fragmentation. Loss of NO from the TNT- $\text{Si}(\text{CH}_3)_3^+$ adduct was observed, while for the RDX- $\text{Si}(\text{CH}_3)_3^+$ adduct, comparison of the chemical formulae in reactions 5-7 with structure I show that these fragments are formed by the loss of either one or two of the CH_2NNO_2 units which constitute the RDX molecule. To further investigate the observed fragmentation patterns, SORI-CID was performed on the TNT- $\text{Si}(\text{CH}_3)_3^+$ and RDX- $\text{Si}(\text{CH}_3)_3^+$ adducts. As Figures 6 and 8 show, we observe the same fragmentation pattern with CID as we saw during adduct formation for both TNT- $\text{Si}(\text{CH}_3)_3^+$ and RDX- $\text{Si}(\text{CH}_3)_3^+$. This suggests that the fragmentation seen during adduct formation is not a result of $\text{Si}(\text{CH}_3)_3^+$ reacting with the gaseous fragments from the thermal decomposition of TNT or RDX. Rather, $\text{Si}(\text{CH}_3)_3^+$ initially forms an adduct with TNT or RDX, which then unimolecularly decomposes to yield the characteristic fragments of each adduct. Apparently each adduct has enough excess vibrational energy from the explosive molecule and $\text{Si}(\text{CH}_3)_3^+$ for dissociation to be observed, even without excitation by CID. Since this characteristic fragmentation can be observed during adduct formation or induced by CID of each adduct, it seems that this reactivity can be used as a "fingerprint" for the detection and identification of TNT and RDX vapor. The large amount of TNT- $\text{Si}(\text{CH}_3)_3^+$ or RDX- $\text{Si}(\text{CH}_3)_3^+$ adduct observed, in conjunction with the simple, uniform fragmentation pattern of the parent adduct,

produces an easily recognizable signature for the TNT or RDX molecule and facilitates the interpretation of the mass spectrum.

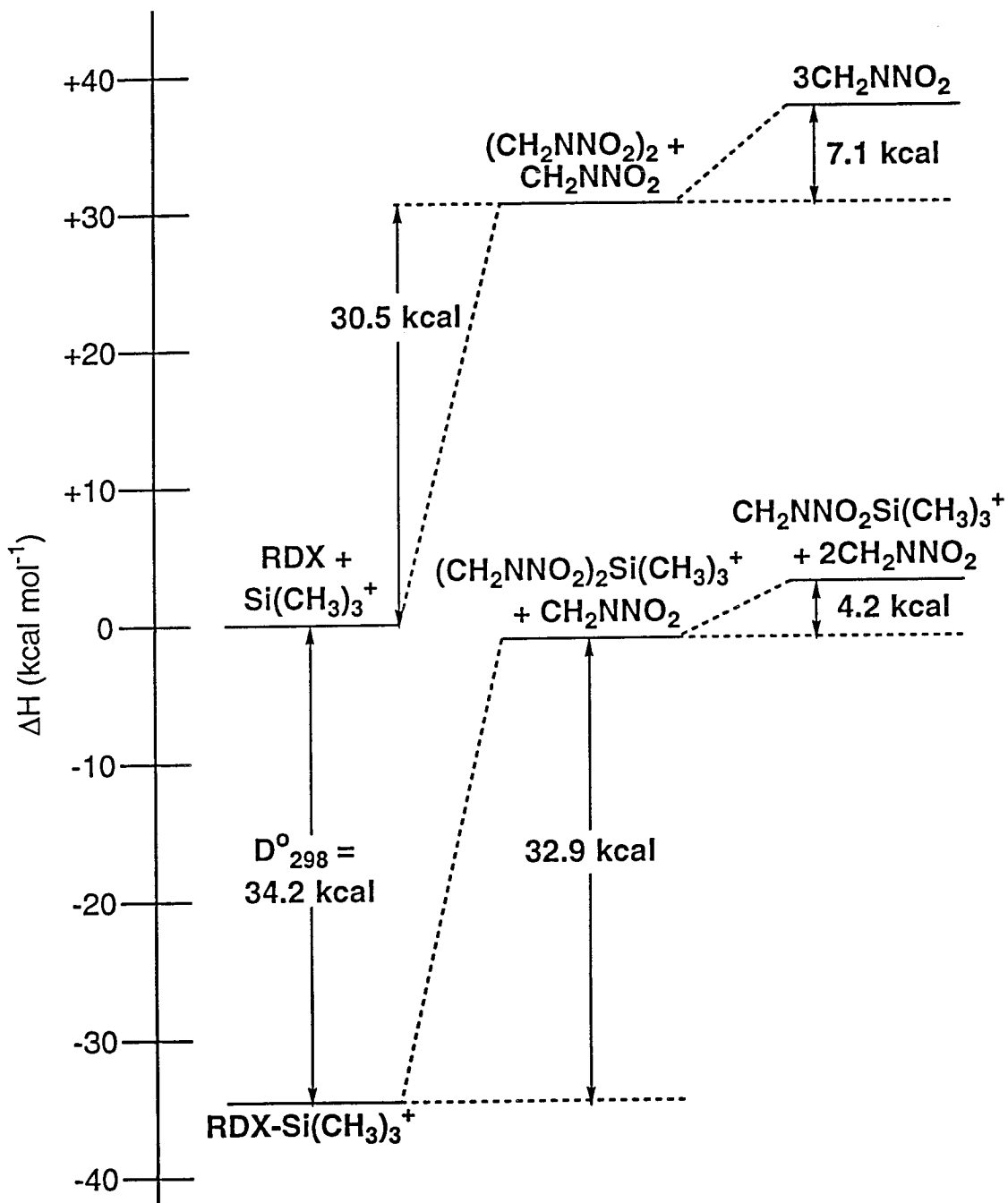
Implications of Observed Fragmentation Patterns. The observed fragmentation also provides us with information about the low energy dissociation pathways of TNT and RDX, where the $\text{Si}(\text{CH}_3)_3^+$ ion acts as a charged label which facilitates the detection of products. These products of the low energy dissociation pathways can suggest mechanisms for the initial steps involved in the decomposition of these explosives. For TNT, loss of NO was the only fragmentation process observed. Loss of NO has been previously observed,^{6,7,9} and the present results suggest that this is the lowest energy decomposition pathway for gas-phase TNT.

With RDX, the only fragmentation we saw corresponded to the loss of CH_2NNO_2 units from the adduct, suggesting that C-N bond cleavage in RDX is the lowest energy decomposition pathway in the gas phase. The CH_2NNO_2 fragment has been observed in many previous studies,^{13-15,17-19,45,46} both as the protonated and unprotonated fragment or as an adduct with other chemical ionization reagents. In particular, Zitrin observed large amounts of $(\text{CH}_2\text{NNO}_2)\text{H}^+$ and $(\text{CH}_2\text{NNO}_2)_2\text{H}^+$ from the chemical ionization of RDX with methane.¹³ However, Zhao et al. have performed infrared multiphoton dissociation (IRMPD) studies of RDX to determine the gas-phase decomposition pathway,⁴⁷ and they observed both N-N bond cleavage with loss of an NO_2 group from RDX and C-N bond cleavage to form CH_2NNO_2 fragments, with a branching ratio of 2:1 for C-N bond cleavage versus N-N bond cleavage. They did not see the formation of $(\text{CH}_2\text{NNO}_2)_2$ fragments, which led them to propose that the ring cleavage is a concerted process where the three C-N bond cleavages occur simultaneously. In contrast to this, we observe the formation of both $\text{CH}_2\text{NNO}_2\text{Si}(\text{CH}_3)_3^+$ and $(\text{CH}_2\text{NNO}_2)_2\text{Si}(\text{CH}_3)_3^+$ adducts, indicating that the C-N bond cleavages need not be simultaneous. Also, we saw no evidence for N-N bond cleavage in our CID experiments. It is possible that the IRMPD experiments imparted enough

energy to the molecules to induce fragmentation by additional, higher energy pathways, whereas in our CID experiments only the lowest energy decomposition pathway was accessed. This interpretation is supported by the work of Sewell and Thompson,⁴⁸ who investigated the unimolecular decomposition of RDX with classical trajectory calculations. They calculated the height of the barrier to C-N bond dissociation and found it to be about 10 kcal mol⁻¹ less than the barrier to N-N bond dissociation. With their derived potential energy surfaces they found that they could reproduce the experimental results of Zhao et al.⁴⁷ in their calculations.

We can explore this further by constructing reaction coordinate diagrams for the decomposition of RDX in the gas phase, both with and without bonding to the Si(CH₃)₃⁺ ion. These diagrams are shown in Figure 11. The reaction coordinate is shown for the case where RDX and its fragments are not bound to Si(CH₃)₃⁺ (the upper curve) and the case where Si(CH₃)₃⁺ has formed an adduct with RDX and its fragments (the lower curve). Adduct formation lowers the enthalpy of each of the species by the D°_{298} of each species with Si(CH₃)₃⁺. The enthalpy differences shown in Figure 11 are derived from the relative energies of the various species that we have theoretically calculated. Some of these values can also be calculated from other known and estimated heats of formation and act as a check on our calculated values. From $\Delta H^{\circ}_{f,298}(\text{RDX},\text{s})$ ⁴⁹ and $\Delta H_{\text{sub}}(\text{RDX})$,⁵⁰ we find that $\Delta H^{\circ}_{f,298}(\text{RDX},\text{g}) = +47.0 \text{ kcal mol}^{-1}$.⁴⁸ The heat of formation of gaseous CH₂NNO₂ has also been estimated: Shaw and Walker report $\Delta H^{\circ}_{f,298}(\text{CH}_2\text{NNO}_2,\text{g}) = 23.8 \text{ kcal mol}^{-1}$,⁵¹ while Melius and Binkley report $\Delta H^{\circ}_{f,298}(\text{CH}_2\text{NNO}_2,\text{g}) = 33.6 \text{ kcal mol}^{-1}$.⁵² However, both Zhao et al.⁴⁷ and Sewell and Thompson⁴⁸ have noted that $\Delta H^{\circ}_{f,298}(\text{CH}_2\text{NNO}_2,\text{g}) = 33.6 \text{ kcal mol}^{-1}$ seems unreasonably high. From these values the enthalpy of reaction 10 can be calculated to be anywhere from 24.4 kcal mol⁻¹ to 53.8 kcal mol⁻¹. The average of these two values, 39.1 kcal mol⁻¹, is close to our ab initio value for ΔH_{10} of 37.6 kcal mol⁻¹. Thus our

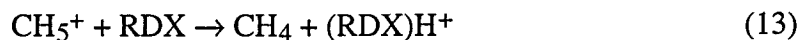
Figure 11. Reaction coordinate diagrams for the decomposition of RDX. The lower curve shows the decomposition pathway observed in this study for the RDX-Si(CH₃)₃⁺ adduct. The upper curve shows the decomposition pathway for RDX when not bound to the Si(CH₃)₃⁺ ion (the Si(CH₃)₃⁺ ion is only shown explicitly in the first entry of the upper curve). Adduct formation lowers the enthalpy of each species by the D°_{298} of each species with Si(CH₃)₃⁺. Notice that the overall energy required to go from RDX to three CH₂NNO₂ units is 37.6 kcal mol⁻¹, close to the value of 38.3 kcal mol⁻¹ calculated by Sewell and Thompson (see reference 48) for the barrier to concerted decomposition of RDX.



calculated ab initio enthalpies for reactions 10-12 appear to be as accurate as the currently known thermochemistry.

If we compare the endothermicity of reaction 10 to the estimated N-N bond energy in RDX of $47.8 \text{ kcal mol}^{-1}$,⁵² we see that it is approximately 10 kcal mol^{-1} more favorable to cleave C-N bonds and form CH_2NNO_2 fragments than to cleave N-N bonds and lose NO_2 from RDX. This is true regardless of whether we start with RDX or with the $\text{RDX-Si}(\text{CH}_3)_3^+$ adduct. Sewell and Thompson⁴⁸ have calculated that the barrier to decomposition by reaction 10, assuming that all 3 C-N bonds cleave simultaneously, is $38.3 \text{ kcal mol}^{-1}$, which is lower than the energy required to cleave a N-N bond in RDX (and close to our calculated enthalpy for reaction 10 of $37.6 \text{ kcal mol}^{-1}$). Our results indicate that the C-N bonds need not cleave simultaneously, so it is not even necessary to complete reaction 10 in one step; the required $37.6 \text{ kcal mol}^{-1}$ need not be accumulated at once, but can be provided sequentially in smaller amounts. Thus under CID conditions we would expect to see exactly the kind of sequential fragmentation we actually observed. These considerations suggest that loss of CH_2NNO_2 fragments is the lowest energy decomposition pathway, in agreement with our CID results, and that the N-N bond cleavage seen by Zhao et al.⁴⁷ with IRMPD occurred when enough energy was imparted to the RDX molecules to access higher energy decomposition pathways.

The thermochemistry presented in Figure 11 also agrees with Zitrin's observations¹³ of the chemical ionization of RDX with methane. The proton affinity of methane is $131.6 \text{ kcal mol}^{-1}$,⁴² and if we assume that RDX has a proton affinity similar to nitrobenzene's ($193.4 \text{ kcal mol}^{-1}$),⁴² we calculate that the proton transfer in reaction 13 is exothermic by about 60 kcal mol^{-1} . Our thermochemical calculations suggest that



60 kcal mol^{-1} should easily provide the chemical activation required to form the $(\text{CH}_2\text{NNO}_2)\text{H}^+$ and $(\text{CH}_2\text{NNO}_2)_2\text{H}^+$ fragment ions, and such behavior was in fact observed.¹³

We should mention that Figure 11 does not show the possible $\text{CH}_2\text{NNO}_2\text{Si}(\text{CH}_3)_3^+ + (\text{CH}_2\text{NNO}_2)_2$ fragmentation products, even though these fragments are more stable than the $(\text{CH}_2\text{NNO}_2)_2\text{Si}(\text{CH}_3)_3^+ + \text{CH}_2\text{NNO}_2$ fragments by 2.9 kcal mol⁻¹ (the difference between the silicon-oxygen bond strengths in $\text{CH}_2\text{NNO}_2\text{Si}(\text{CH}_3)_3^+$ and $(\text{CH}_2\text{NNO}_2)_2\text{Si}(\text{CH}_3)_3^+$ at the PM3 level). This would imply that the $\text{CH}_2\text{NNO}_2\text{Si}(\text{CH}_3)_3^+$ produced should be accompanied by $(\text{CH}_2\text{NNO}_2)_2$ rather than $2\text{CH}_2\text{NNO}_2$. However, CID of the RDX-Si(CH₃)₃⁺ adduct produced more $(\text{CH}_2\text{NNO}_2)_2\text{Si}(\text{CH}_3)_3^+$ than $\text{CH}_2\text{NNO}_2\text{Si}(\text{CH}_3)_3^+$ for average collision energies as high as 2.5 eV in the center-of-mass frame of reference. Furthermore the relative amount of $\text{CH}_2\text{NNO}_2\text{Si}(\text{CH}_3)_3^+$ formed increased as the collision energy was increased. If the formation of $\text{CH}_2\text{NNO}_2\text{Si}(\text{CH}_3)_3^+$ was accompanied by $(\text{CH}_2\text{NNO}_2)_2$ as expected, we should have seen more $\text{CH}_2\text{NNO}_2\text{Si}(\text{CH}_3)_3^+$ than $(\text{CH}_2\text{NNO}_2)_2\text{Si}(\text{CH}_3)_3^+$ at any collision energy and the relative amount of $\text{CH}_2\text{NNO}_2\text{Si}(\text{CH}_3)_3^+$ formed should have decreased as the collision energy was increased. Therefore it seems that the production of $\text{CH}_2\text{NNO}_2\text{Si}(\text{CH}_3)_3^+$ is accompanied by $2\text{CH}_2\text{NNO}_2$, as shown in Figure 11. But it is hard to rationalize why the apparently more favorable production of $\text{CH}_2\text{NNO}_2\text{Si}(\text{CH}_3)_3^+$ accompanied by $(\text{CH}_2\text{NNO}_2)_2$ is not seen. The probable explanation for this behavior is that the silicon-oxygen bond strength for $(\text{CH}_2\text{NNO}_2)_2\text{Si}(\text{CH}_3)_3^+$ calculated at the PM3 level is too low. If the actual silicon-oxygen bond strength for $(\text{CH}_2\text{NNO}_2)_2\text{Si}(\text{CH}_3)_3^+$ is 2 or 3 kcal mol⁻¹ higher than the silicon-oxygen bond strength in $\text{CH}_2\text{NNO}_2\text{Si}(\text{CH}_3)_3^+$, then we would expect the CID behavior that we actually observed, where the production of $\text{CH}_2\text{NNO}_2\text{Si}(\text{CH}_3)_3^+$ is accompanied by both $(\text{CH}_2\text{NNO}_2)_2$ and $2\text{CH}_2\text{NNO}_2$.

Comparison of Gas-Phase and Condensed-Phase Fragmentation Pathways for RDX. It is also of interest to compare the decomposition pathway we observe to those seen in condensed-phase RDX. Work by Behrens and Bulusu using simultaneous thermogravimetric modulated beam mass spectrometry has shown that the

decomposition of RDX in the condensed phase is usually initiated by the cleavage of the N-N bond and loss of NO_2 . Furthermore, although later formation of N_2O and CH_2O is attributed to the decomposition of CH_2NNO_2 fragments, only 10% or less of the reactivity follows that pathway.^{53,54} Botcher and Wight^{55,56} have also observed the decomposition of RDX using transient thin film laser pyrolysis, which has the advantage of being able to detect the initial products of thermal decomposition under realistic combustion conditions. They found that N-N bond cleavage is the dominant initial step in the solid-phase decomposition of RDX, but subsequent decomposition takes place at least partly in the gas phase. However, both groups⁵³⁻⁵⁶ note that though the decomposition pathways observed in the condensed phase differ drastically from those observed in the gas phase, the experimental conditions are drastically different as well. Thus, even though our observed decomposition pathways differ from those observed in condensed-phase studies, this is not unexpected. We should also note that though the decomposition pathways we observed may not be the initial step in the decomposition of condensed-phase RDX, both Behrens et al.^{53,54} and Botcher et al.^{55,56} concluded that many subsequent steps in the decomposition occur in the gas phase, and our present results indicate that loss of CH_2NNO_2 fragments from RDX is the lowest energy decomposition pathway for RDX under such conditions.

Conclusions

We have used FT-ICR mass spectrometry to investigate the reactivity of trimethylsilyl cations with compounds containing nitro groups. Our hypothesis that $\text{Si}(\text{CH}_3)_3^+$ ions will form adducts by bonding to an oxygen atom of the nitro group has been demonstrated to be correct. These reactions are shown to be fast and efficient. Examination of the reactions of TNT and RDX with $\text{Si}(\text{CH}_3)_3^+$ indicate that the $\text{Si}(\text{CH}_3)_3^+$ ion may prove to be a useful chemical ionization reagent for the detection and identification of TNT, RDX and other explosive molecules which contain nitro groups. CID experiments on the isolated $\text{RDX-Si}(\text{CH}_3)_3^+$ adduct have identified the lowest

energy decomposition pathway for this adduct in the gas phase, and these results are consistent with previous gas-phase findings.^{13-15,17-19,45-48} The gas-phase decomposition pathway we observe is different from those seen in the decomposition of condensed-phase RDX, but this is expected since the experimental conditions are drastically different in each case.

We should note that although this work was performed using FT-ICR mass spectrometry, these methods could be applied with other kinds of mass spectrometers as well. In particular, portable ion trap mass spectrometers could be used to detect explosives via chemical ionization with the trimethylsilyl cation. McLuckey and co-workers have already shown that atmospheric sampling glow discharge ionization can be successfully coupled with an ion trap mass spectrometer and have investigated the application of this coupled methodology to the detection of explosives.⁵⁷ Their methodology could possibly be modified to allow for the formation and use of trimethylsilyl cations as a chemical ionization reagent in the glow discharge source. It should also be possible to interface a chromatographic method with an ion trap mass spectrometer. Chromatography would be used to remove interferences while the ion trap detects the products from the chemical ionization of any explosives present with trimethylsilyl cation.

Acknowledgments

We wish to acknowledge the Federal Aviation Administration for support of this work under grant 93-G-060, and the Beckman Foundation and Institute for continuing support of the FT-ICR research facility. We also wish to acknowledge Professor William A. Goddard, III, and the Beckman Institute Materials and Process Simulations Center for supporting our theoretical calculations. Francesco Faglioni gave especially helpful advice concerning the theoretical calculations in this work.

References

- ¹Fainberg, A. *Science* **1992**, 255, 1531.
- ²U. S. Congress, Office of Technology Assessment, *Technology Against Terrorism: The Federal Effort, OTA ISC-481*, Government Printing Office, Washington, DC, July, 1991.
- ³U. S. Congress, Office of Technology Assessment, *Technology Against Terrorism: Structuring Security, OTA ISC-511*, Government Printing Office, Washington, DC, January, 1992.
- ⁴(a) Dionne, B.C; Rounbehler, D. P.; Achter, E. K.; Hobbs, J. R.; Fine, D. H. *Journal of Energetic Materials* **1986**, 4, 447. (b) Dobratz, B. M.; Crawford, P. C. *LLNL Explosives Handbook, Properties of Chemical Explosives and Explosives Simulants* LLNL Report-UCRL-52997 Change 2, January, 1985.
- ⁵The electron affinity of NO₂ is 2.273 eV: Ervin, K. M.; Ho. J.; Lineberger, W. *C. J. Phys. Chem.* **1988**, 92, 5405.
- ⁶Boumsellek, S.; Alajajian, S. H.; Chutjian, A. *J. Am. Soc. Mass Spectrom.* **1992**, 3, 243.
- ⁷Yinon, J.; Fraise, D.; Dagley, I. *J. Org. Mass Spectrom.* **1991**, 26, 867.
- ⁸Yinon, J.; Boettger, H. G. *Int. J. Mass Spectrom. Ion Phys.* **1972**, 10, 161.
- ⁹Yinon, J. *J. Forensic Sci.* **1980**, 25, 401.
- ¹⁰Huang, S. D.; Kolaitis, L.; Lubman, D. M. *Applied Spectroscopy* **1987**, 8, 1371.
- ¹¹Marshall, A.; Clark, A.; Ledingham, K. W. D.; Sander, J.; Singhal, R. P.; Kosmidis, C.; Deas, R. M. *Rapid Comm. Mass Spectrom.* **1994**, 8, 521.
- ¹²Burrows, E. P. *Org. Mass Spectrom.* **1994**, 29, 315.
- ¹³Zitrin, S. *Org. Mass Spectrom.* **1982**, 17, 74.
- ¹⁴Gillis, R. G.; Lacey, M. J.; Shannon, J. S. *Org. Mass Spectrom.* **1974**, 9, 359.
- ¹⁵Yinon, J. *Biomed. Mass Spectrom.* **1974**, 1, 393.
- ¹⁶Saferstein, R.; Chao, J. M.; Manura, J. J. *J. Assoc. Off. Anal. Chem.* **1975**, 58, 734.
- ¹⁷Zitrin, S.; Yinon, J. *Advances in Mass Spectrometry in Biochemistry and Medicine*, Vol. 1, A. Frigerio and N. Castagnoli, Eds., 1976, Spectrum Publications, New York.

¹⁸Vouros, P.; Petersen, B. A.; Colwell, L.; Karger, B. L.; Harris, H. *Anal. Chem.* **1977**, *49*, 1039.

¹⁹Pate, C. T.; Mach, M. H. *Int. J. Mass Spectrom. Ion Phys.* **1978**, *26*, 267.

²⁰Yinon, J. *Org. Mass Spectrom.* **1980**, *15*, 637.

²¹McMillan, D. F.; Golden, D. M. *Ann. Rev. Phys. Chem.* **1982**, *33*, 493.

²²Orlando, R.; Munson, B. *Anal. Chem.* **1986**, *58*, 2788.

²³Clemens, D.; Munson, B. *Anal. Chem.* **1985**, *57*, 2022.

²⁴Stillwell, R. N.; Carroll, D. I.; Nowlin, J. G.; Horning, E. C. *Anal. Chem.* **1983**, *55*, 1313, and references contained therein.

²⁵(a) Marshall, A. G. *Acc. Chem. Res.* **1985**, *18*, 316. (b) Comisarow, M. B. *Anal. Chim. Acta* **1985**, *178*, 1.

²⁶Comisarow, M. B.; Marshall, A. G. *Chem. Phys. Lett.* **1974**, *26*, 489.

²⁷(a) Gauthier, J. W.; Trautman, T. R.; Jacobson, D. B. *Anal. Chim. Acta* **1991**, *246*, 211. (b) Marzluff, E. M.; Campbell, S.; Rodgers, M. T.; Beauchamp, J. L. *J. Am. Chem. Soc.* **1994**, *116*, 7787.

²⁸The collision rate is calculated using average dipole orientation (ADO) theory: Su, T.; Bowers, M. T. *Int. J. Mass Spectrom. Ion Phys.* **1973**, *12*, 347.

²⁹For nitrobenzene we use $\alpha = 13.8 \text{ \AA}^3$, which is an average of two values: (a) Maryott, A. A.; Buckley, F. *U. S. National Bureau of Standards Circular No. 537* 1953. (b) Stuart, H. A. *Landolt-Börnstein Zahlenwerte und Funktionen*, Vol. 1, Part 3, A. Eucken and K. H. Hellwege, Eds., 1951, Springer-Verlag, Berlin.

³⁰For nitrobenzene we use $\mu = 4.22 \text{ D}$: Nelson, R. D.; Lide, D. R.; Maryott, A. *A. Selected Values of Electric Dipole Moments for Molecules in the Gas Phase*, Natl. Stand. Ref. Data Ser. — Natl. Bur. Stands. 10, 1967.

³¹The dipole moment and polarizability of TNT were calculated at the Hartree-Fock level with a 6-31** basis set to be 1.8 D and 15.6 \AA^3 , respectively. The geometry optimization, dipole moment and polarizability calculations were performed with PS-GVB (see reference 38).

³²The dipole moment and polarizability of RDX were theoretically calculated to be 6.5 D and 12.3 \AA^3 , respectively. Details of the calculation are given in the Semi-Empirical and Ab Initio Calculations section of this paper.

³³*HyperChem™ Computational Chemistry Software Package, Version 4.0*, Hypercube Inc., 1994.

³⁴Rignalda, M. N.; Langlois, J.-M.; Greeley, B. H.; Murphy, R. B.; Russo, T. V.; Cortis, C.; Muller, R. P.; Marten, B.; Donnelly, R. E., Jr.; Mainz, D. T.; Wright, J. R.; Pollard, W. T.; Cao, Y.; Won, Y.; Miller, G. H.; Goddard, W. A. III; Freisner, R. A. *PS-GVB, v2.1*, Schrödinger, Inc., 1995.

³⁵Frisch, M. J.; Trucks, G. W.; Head-Gordon, M.; Gill, P. M. W.; Wong, M. W.; Foresman, J. B.; Johnson, B. G.; Schlegel, H. B.; Robb, M. A.; Replogle, E. S.; Gomperts, R.; Andres, J. L.; Raghavachari, K.; Binkley, J. S.; Gonzales, C.; Martin, R. L.; Fox, D. J.; Defrees, D. J.; Baker, J.; Stewart, J. J. P.; Pople, J. A. *Gaussian 92, Revision D.2*, Gaussian, Inc.: Pittsburgh, PA, 1992.

³⁶The structural parameters for these species are presented in the appendix at the end of this chapter.

³⁷Coffin, J. M.; Newton, S. Q.; Ewbank, J. D.; Schäfer, L.; Van Alsenoy, C.; Siam, K. *J. Mol. Struct.* **1991**, *251*, 219.

³⁸Shishkov, I. F.; Vilkov, L. V.; Kolonits, M.; Rozsondai, B. *Struct. Chem.* **1991**, *2*, 57.

³⁹Habibollahzadeh, D.; Grodzicki, M.; Seminario, J. M.; Politzer, P. *J. Phys. Chem.* **1991**, *95*, 7699.

⁴⁰(a) Stewart, J. J. P. *Method J. Comput. Chem.* **1989**, *10*, 209. (b) Stewart, J. J. P. *Method J. Comput. Chem.* **1989**, *10*, 221.

⁴¹For example, PM3 calculations predict that the heat of formation of cyclobutane is $-3.9 \text{ kcal mol}^{-1}$, compared to the experimental value of $+6.8 \text{ kcal mol}^{-1}$ (Reference 42).

⁴²Lias, S. G.; Bartmess, J. E.; Liebman, J. F.; Holmes, J. L.; Levin, R. D.; Mallard, W. G. *J. Phys. Chem. Ref. Data* **1988**, *17*, Suppl. 1.

⁴³For the process $A + B \rightarrow AB$, we can calculate the bond energy of AB with the following equation: $D^{\circ}_{298}(A-B) = \Delta H^{\circ}_{f,298}(A) + \Delta H^{\circ}_{f,298}(B) - \Delta H^{\circ}_{f,298}(A-B)$.

⁴⁴Hendewerk, M. L.; Weil, D. A.; Stone, T. L.; Ellenberger, M. R.; Farneth, W. E.; Dixon, D. A. *J. Am. Chem. Soc.* **1982**, *104*, 1794.

⁴⁵Yinon, J. *Mass Spectrom. Rev.* **1982**, *1*, 257.

⁴⁶Farber, M. *Mass Spectrom. Rev.* **1992**, *11*, 137.

⁴⁷Zhao, X.; Hints, E. J.; Lee, Y. T. *J. Chem. Phys.* **1988**, *88*, 801.

⁴⁸Sewell, T. D.; Thompson, D. L. *J. Phys. Chem.* **1991**, *95*, 6228.

⁴⁹*Thermochemical Data of Organic Compounds*, J. B. Pedley, R. D. Naylor, S. P. Kirby, Eds., 1986, Chapman and Hall, New York. They consider 15.9 kcal mol⁻¹ to be the best value for $\Delta H_f^\circ(\text{RDX},s)$ at 300 K.

⁵⁰Rosen, J. M.; Dickinson, C. *J. Chem. Eng. Data* **1969**, *14*, 120. They find that $\Delta H_{\text{sub}}(\text{RDX}) = 31.1$ kcal mol⁻¹.

⁵¹Shaw, R.; Walker, R. E. *J. Phys. Chem.* **1977**, *81*, 2572.

⁵²Melius, C. F.; Binkley, J. S. *Symp. (Int.) Combust., [Proc.]* **1986**, *21*, 1953.

⁵³Behrens, R., Jr.; Bulusu, S. *J. Phys. Chem.* **1992**, *96*, 8877.

⁵⁴Behrens, R., Jr.; Bulusu, S. *J. Phys. Chem.* **1992**, *96*, 8891.

⁵⁵Botcher, T. R.; Wight, C. A. *J. Phys. Chem.* **1993**, *97*, 9149.

⁵⁶Botcher, T. R.; Wight, C. A. *J. Phys. Chem.* **1994**, *98*, 5441.

⁵⁷(a) McLuckey, S. A.; Glish, G. L.; Asano, K. G.; Grant, B. C. *Anal. Chem.* **1988**, *60*, 2220. (b) McLuckey, S. A.; Goeringer, D. E.; Asano, K. G.; Vaidyanathan, G.; Stephenson, J. L., Jr. *Rapid Comm. Mass Spectrom.* **1996**, *10*, 287.

Appendix

The structural parameters obtained from the geometry optimizations of the lowest energy conformations of CH_2NNO_2 , $(\text{CH}_2\text{NNO}_2)_2$, RDX, $\text{Si}(\text{CH}_3)_3^+$, $\text{CH}_2\text{NNO}_2\text{-Si}(\text{CH}_3)_3^+$, $(\text{CH}_2\text{NNO}_2)_2\text{-Si}(\text{CH}_3)_3^+$ and $\text{RDX-Si}(\text{CH}_3)_3^+$ are given in the following Tables 1A-7A, respectively.

Table 1A. HF-Optimized Bond Distances (Å) and Angles (deg) for the Lowest Energy Conformation of CH₂NNO₂.

Bond Length	
N1-N2	1.4227
N1-C5	1.2549
N2-O3	1.1789
N2-O4	1.1939
C5-H6	1.0751
C5-H7	1.0757
Bond Angle	
C5-N1-N2	113.88
O3-N2-N1	113.52
O4-N2-N1	120.13
O4-N2-O3	126.34
H6-C5-N1	116.25
H7-C5-N1	123.66
H7-C5-H6	120.08
Torsional Angle	
N2-N1-C5-H6	180.00
N2-N1-C5-H7	0.00
O3-N2-N1-C5	180.00
O4-N2-N1-C5	0.00

Table 2A. HF-Optimized Bond Distances (Å) and Angles (deg) for the Lowest Energy Conformation of (CH₂NNO₂)₂.

Bond Length

C1-N3	1.4661
C1-N4	1.4663
C1-H11	1.0784
C1-H12	1.0784
C2-N3	1.4661
C2-N4	1.4663
C2-H13	1.0784
C2-H14	1.0784
N3-N5	1.3546
N4-N6	1.3547
N5-O7	1.1910
N5-O8	1.1910
N6-O9	1.1910
N6-O10	1.1910

Table 2A. (Continued)

Bond Angle		Bond Angle	
N4-C1-N3	87.34	C2-N3-C1	92.66
H11-C1-N3	114.33	N5-N3-C1	120.01
H11-C1-N4	113.81	N5-N3-C2	120.01
H12-C1-N3	113.82	C2-N4-C1	92.65
H12-C1-N4	114.32	N6-N4-C1	119.97
H12-C1-H11	111.35	N6-N4-C2	119.97
N4-C2-N3	87.34	O7-N5-N3	116.40
H13-C2-N3	114.33	O8-N5-N3	116.40
H13-C2-N4	113.81	O8-N5-O7	127.16
H14-C2-N3	113.82	O9-N6-N4	116.39
H14-C2-N4	114.32	O10-N6-N4	116.39
H14-C2-H13	111.35	O10-N6-O9	127.17

Table 2A. (Continued)

Torsional Angle		Torsional Angle	
C1-N3-C2-N4	0.02	C2-N4-C1-H11	-115.46
C1-N3-C2-H13	-114.97	C2-N4-C1-H12	115.03
C1-N3-C2-H14	115.51	C2-N4-N6-O9	34.51
C1-N3-N5-O7	147.78	C2-N4-N6-O10	-147.72
C1-N3-N5-O8	-34.47	N3-C1-N4-N6	-127.13
C1-N4-C2-N3	-0.02	N3-C2-N4-N6	127.13
C1-N4-C2-H13	115.46	N4-C1-N3-N5	-127.26
C1-N4-C2-H14	-115.03	N4-C2-N3-N5	127.26
C1-N4-N6-O9	147.72	N5-N3-C1-H11	-12.27
C1-N4-N6-O10	-34.51	N5-N3-C1-H12	117.25
C2-N3-C1-N4	-0.02	N5-N3-C2-H13	12.27
C2-N3-C1-H11	114.97	N5-N3-C2-H14	-117.25
C2-N3-C1-H12	-115.51	N6-N4-C1-H11	117.38
C2-N3-N5-O7	34.47	N6-N4-C1-H12	-12.13
C2-N3-N5-O8	-147.78	N6-N4-C2-H13	-117.38
C2-N4-C1-N3	0.02	N6-N4-C2-H14	12.13

Table 3A. HF-Optimized Bond Distances (Å) and Angles (deg) for the Lowest Energy Conformation of RDX.

Bond Length

C1-N4	1.4651
C1-N5	1.4420
C1-H16	1.0857
C1-H17	1.0691
C2-N5	1.4520
C2-N6	1.4520
C2-H18	1.0808
C2-H19	1.0702
C3-N4	1.4651
C3-N6	1.4420
C3-H20	1.0857
C3-H21	1.0691
N4-N7	1.3613
N5-N8	1.3755
N6-N9	1.3755
N7-O10	1.9194
N7-O11	1.1914
N8-O12	1.1888
N8-O13	1.1878
N9-O14	1.1888
N9-O15	1.1878

Table 3A. (Continued)

Bond Angle		Bond Angle	
N5-C1-N4	108.59	C3-N4-C1	115.31
H16-C1-N4	110.44	N7-N4-C1	115.29
H16-C1-N5	107.31	N7-N4-C3	115.29
H17-C1-N4	110.02	C2-N5-C1	115.46
H17-C1-N5	110.57	N8-N5-C1	117.43
H17-C1-H16	109.89	N8-N5-C2	117.87
N6-C2-N5	111.38	C3-N6-C2	115.46
H18-C2-N5	106.82	N9-N6-C2	117.87
H18-C2-N6	106.82	N9-N6-C3	117.43
H19-C2-N5	110.80	O10-N7-N4	117.02
H19-C2-N6	110.80	O11-N7-N4	117.02
H19-C2-H18	110.07	O11-N7-O10	125.96
N6-C3-N4	108.59	O12-N8-N5	117.13
H20-C3-N4	110.44	O13-N8-N5	116.58
H20-C3-N6	107.31	O13-N8-O12	126.20
H21-C3-N4	110.02	O14-N9-N6	117.13
H21-C3-N6	110.57	O15-N9-N6	116.58
H21-C3-H20	109.89	O15-N9-O14	126.20

Table 3A. (Continued)

Torsional Angle		Torsional Angle	
C1-N4-C3-N6	54.29	C3-N4-N7-O11	21.34
C1-N4-C3-H20	-63.12	C3-N6-C2-N5	49.82
C1-N4-C3-H21	175.43	C3-N6-C2-H18	-66.47
C1-N4-N7-O10	-21.34	C3-N6-C2-H19	173.64
C1-N4-N7-O11	159.61	C3-N6-N9-O14	15.38
C1-N5-C2-N6	-49.82	C3-N6-N9-O15	-167.88
C1-N5-C2-H18	66.47	N4-C1-N5-N8	-94.86
C1-N5-C2-H19	-173.64	N4-C3-N6-N9	94.86
C1-N5-N8-O12	-15.37	N5-C1-N4-N7	167.45
C1-N5-N8-O13	167.88	N5-C2-N6-N9	-96.17
C2-N5-C1-N4	51.28	N6-C2-N5-N8	96.17
C2-N5-C1-H16	-68.12	N6-C3-N4-N7	-167.45
C2-N5-C1-H17	172.07	N7-N4-C1-H16	-75.14
C2-N5-N8-O12	-160.69	N7-N4-C1-H17	46.32
C2-N5-N8-O13	22.57	N7-N4-C3-H20	75.14
C2-N6-C3-N4	-51.28	N7-N4-C3-H21	-46.32
C2-N6-C3-H20	68.12	N8-N5-C1-H16	145.75
C2-N6-C3-H21	-172.07	N8-N5-C1-H17	25.93
C2-N6-N9-O14	160.69	N8-N5-C2-H18	-147.54
C2-N6-N9-O15	-22.57	N8-N5-C2-H19	-27.65
C3-N4-C1-N5	-54.28	N9-N6-C2-H18	147.54
C3-N4-C1-H16	63.12	N9-N6-C2-H19	27.66
C3-N4-C1-H17	-175.42	N9-N6-C3-H20	-145.74
C3-N4-N7-O10	-159.61	N9-N6-C3-H21	-25.94

Table 4A. PM3-Optimized Bond Distances (Å) and Angles (deg) for the Lowest Energy Conformation of $\text{Si}(\text{CH}_3)_3^+$.

Bond Length

Si1-C2	1.8001
Si1-C3	1.8002
Si1-C4	1.8003
C2-H5	1.1060
C2-H6	1.0989
C2-H7	1.0995
C3-H8	1.1057
C3-H9	1.0997
C3-H10	1.0989
C4-H11	1.1060
C4-H12	1.0989
C4-H13	1.0994

Table 4A. (Continued)

Bond Angle

C2-Si1-C3	120.02
C2-Si1-C4	119.99
C3-Si1-C4	119.96
Si1-C2-H5	110.11
Si1-C2-H6	113.61
Si1-C2-H7	113.41
H5-C2-H6	106.05
H5-C2-H7	105.91
H6-C2-H7	107.21
Si1-C3-H8	110.15
Si1-C3-H9	113.37
Si1-C3-H10	113.62
H8-C3-H9	105.90
H8-C3-H10	106.08
H9-C3-H10	107.19
Si1-C4-H11	110.21
Si1-C4-H12	113.58
Si1-C4-H13	113.37
H11-C4-H12	106.03
H11-C4-H13	105.90
H12-C4-H13	107.21

Table 5A. PM3-Optimized Bond Distances (Å) and Angles (deg) for the Lowest Energy Conformation of CH₂NNO₂-Si(CH₃)₃⁺.

Bond Length

C1-H2	1.0924
C1-H3	1.0947
C1-N4	1.2970
N4-N5	1.4198
N5-O6	1.2670
N5-O7	1.1932
O6-Si8	1.7820
Si8-C9	1.8597
Si8-C10	1.8602
Si8-C11	1.8602
C9-H12	1.0990
C9-H13	1.0953
C9-H14	1.0953
C10-H15	1.0998
C10-H16	1.0954
C10-H17	1.0950
C11-H18	1.0997
C11-H19	1.0953
C11-H20	1.0950

Table 5A. (Continued)

Bond Angle		Bond Angle	
H2-C1-H3	118.50	Si8-C9-H14	112.60
H2-C1-N4	114.33	H12-C9-H13	107.29
H3-C1-N4	127.17	H12-C9-H14	107.29
C1-N4-N5	125.95	H13-C9-H14	107.60
N4-N5-O6	112.47	Si8-C10-H15	109.05
N4-N5-O7	125.03	Si8-C10-H16	112.80
O6-N5-O7	122.50	Si8-C10-H17	113.24
N5-O6-Si8	132.34	H15-C10-H16	106.71
O6-Si8-C9	97.58	H15-C10-H17	106.79
O6-Si8-C10	107.30	H16-C10-H17	107.88
O6-Si8-C11	107.30	Si8-C11-H18	109.05
C9-Si8-C10	114.40	Si8-C11-H19	112.80
C9-Si8-C11	114.40	Si8-C11-H20	113.23
C10-Si8-C11	114.00	H18-C11-H19	106.72
Si8-C9-H12	109.20	H18-C11-H20	106.79
Si8-C9-H13	112.60	H19-C11-H20	107.88

Table 6A. PM3-Optimized Bond Distances (Å) and Angles (deg) for the Lowest Energy Conformation of $(\text{CH}_2\text{NNO}_2)_2\text{-Si}(\text{CH}_3)_3^+$.

Bond Length

C1-N2	1.5314
C1-N4	1.4961
C1-H5	1.1083
C1-H6	1.1080
N2-C3	1.5299
N2-N9	1.3617
C3-N4	1.4957
C3-H7	1.1083
C3-H8	1.1075
N4-N10	1.5760
N9-O13	1.1946
N9-O14	1.2898
N10-O11	1.1903
N10-O12	1.1908
O14-Si15	1.7792
Si15-C16	1.8639
Si15-C17	1.8604
Si15-C18	1.8609
C16-H19	1.0988
C16-H20	1.0950
C16-H21	1.0947
C17-H22	1.0995
C17-H23	1.0952

Table 6A. (Continued)

Bond Length			
	C17-H24	1.0951	
	C18-H25	1.0993	
	C18-H26	1.0951	
	C18-H27	1.0950	
Bond Angle		Bond Angle	
C1-N2-C3	92.94	O14-Si15-C16	97.01
N2-C1-N4	85.60	O14-Si15-C17	107.96
C1-N4-C3	95.78	C16-Si15-C17	114.11
N2-C3-N4	85.67	O14-Si15-C18	107.96
N2-C1-H5	113.08	C16-Si15-C18	114.09
N4-C1-H5	117.68	C17-Si15-C18	114.11
N2-C1-H6	115.75	Si15-C16-H19	109.15
N4-C1-H6	113.47	Si15-C16-H20	112.65
H5-C1-H6	109.69	H19-C16-H20	107.18
N2-C3-H7	112.97	Si15-C16-H21	112.47
N4-C3-H7	117.63	H19-C16-H21	107.38
N2-C3-H8	115.83	H20-C16-H21	107.75
N4-C3-H8	113.42	Si15-C17-H22	109.15
H7-C3-H8	109.75	Si15-C17-H23	112.70
C1-N2-N9	126.98	H22-C17-H23	106.81
C3-N2-N9	128.03	Si15-C17-H24	113.08
C1-N4-N10	122.50	H22-C17-H24	106.87
C3-N4-N10	122.29	H23-C17-H24	107.89

Table 6A. (Continued)

Bond Angle		Bond Angle	
N4-N10-O11	113.40	Si15-C18-H25	109.10
N4-N10-O12	113.19	Si15-C18-H26	113.01
O11-N10-O12	133.40	H25-C18-H26	106.89
N2-N9-O13	122.71	Si15-C18-H27	112.85
N2-N9-O14	114.68	H25-C18-H27	106.80
O13-N9-O14	122.53	H26-C18-H27	107.84
N9-O14-Si15	130.26		

Table 7A. PM3-Optimized Bond Distances (Å) and Angles (deg) for the Lowest Energy Conformation of RDX-Si(CH₃)₃⁺.

Bond Length

C1-N2	1.5237
C1-N6	1.4775
C1-H7	1.1125
C1-H8	1.1127
N2-C3	1.5191
N2-N13	1.3941
C3-N4	1.4806
C3-H9	1.1127
C3-H10	1.1122
N4-C5	1.4956
N4-N14	1.5754
C5-N6	1.4526
C5-H11	1.1135
C5-H12	1.1107
N6-N15	1.5922
N13-O16	1.1941
N13-O17	1.2897
N14-O18	1.1945
N14-O19	1.1898
N15-O20	1.1888
N15-O21	1.1914
O17-Si22	1.7788
Si22-C23	1.8645

Table 7A. (Continued)

Bond Length			
	Si22-C24		1.8628
	Si22-C25		1.8618
	C23-H26		1.0986
	C23-H27		1.0948
	C23-H28		1.0951
	C24-H29		1.0991
	C24-H30		1.0950
	C24-H31		1.0948
	C25-H32		1.0991
	C25-H33		1.0950
	C25-H34		1.0950
Bond Angle		Bond Angle	
C1-N2-C3	111.06	N4-N14-O19	115.04
N2-C3-N4	106.48	O18-N14-O19	131.66
C3-N4-C5	113.07	N6-N15-O20	114.31
N2-C1-N6	106.20	N6-N15-O21	113.25
C1-N6-C5	113.10	O20-N15-O21	132.42
N4-C5-N6	104.28	N13-O17-Si22	129.86
N2-C1-H7	105.19	O17-Si22-C23	97.10
N6-C1-H7	113.34	O17-Si22-C24	108.13
N2-C1-H8	111.83	C23-Si22-C24	113.98
N6-C1-H8	112.36	O17-Si22-C25	107.86
H7-C1-H8	107.75	C23-Si22-C25	114.14

Table 7A. (Continued)

Bond Angle		Bond Angle	
N2-C3-H9	105.07	C24-Si22-C25	113.91
N4-C3-H9	113.09	Si22-C23-H26	109.14
N2-C3-H10	111.97	Si22-C23-H27	112.53
N4-C3-H10	112.32	H26-C23-H27	107.36
H9-C3-H10	107.73	Si22-C23-H28	112.54
N4-C5-H11	111.50	H26-C23-H28	107.31
N6-C5-H11	111.58	H27-C23-H28	107.69
N4-C5-H12	110.45	Si22-C24-H29	109.18
N6-C5-H12	110.61	Si22-C24-H30	112.71
H11-C5-H12	108.41	H29-C24-H30	106.88
C1-N2-N13	118.62	Si22-C24-H31	112.98
C3-N2-N13	120.46	H29-C24-H31	106.89
C3-N4-N14	119.27	H30-C24-H31	107.87
C5-N4-N14	119.81	Si22-C25-H32	109.15
C1-N6-N15	119.73	Si22-C25-H33	113.03
C5-N6-N15	119.85	H32-C25-H33	106.89
N2-N13-O16	122.94	Si22-C25-H34	112.68
N2-N13-O17	116.55	H32-C25-H34	106.90
O16-N13-O17	120.27	H33-C25-H34	107.85
N4-N14-O18	113.27		

Chapter 8

CHEMICAL IONIZATION OF THE NITRATE ESTER EXPLOSIVES EGDN AND PETN BY TRIMETHYLSILYL CATION AND COMPARISON OF THE REACTIVITY OF NITRATE ESTER AND NITRO EXPLOSIVES TOWARD TRIMETHYLSILYL CATION

Kevin C. Crellin, Nathan Dalleska and J. L. Beauchamp

Arthur Amos Noyes Laboratory of Chemical Physics, California Institute of
Technology, Pasadena, CA 91125

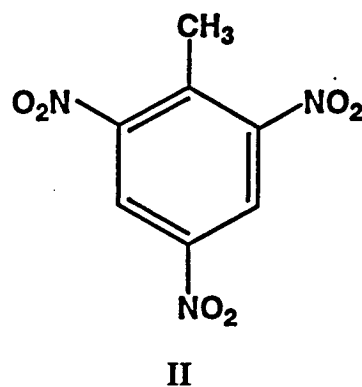
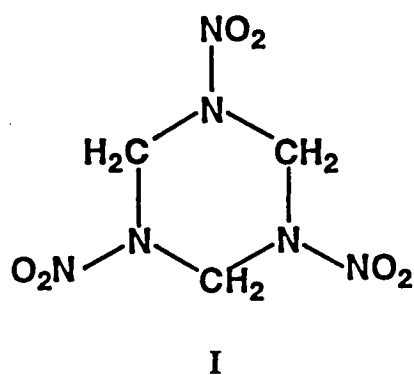
Submitted for publication as an article in the *International Journal of Mass Spectrometry and Ion Processes*.

Abstract

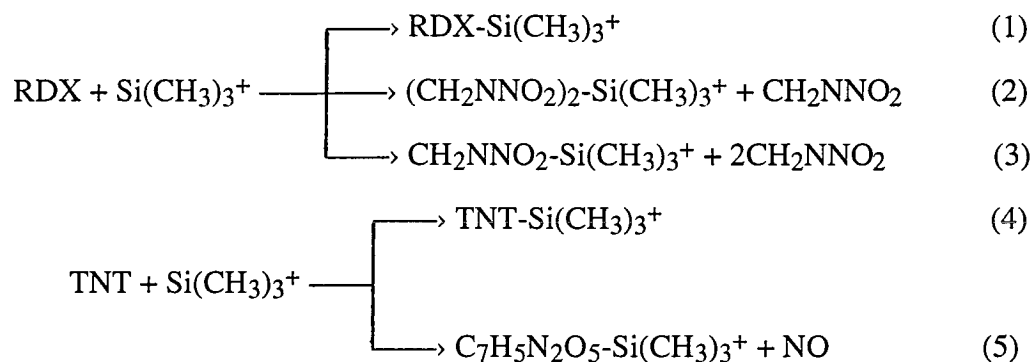
Fourier transform ion cyclotron resonance mass spectrometry has been used to examine the reactions of $\text{Si}(\text{CH}_3)_3^+$ with EGDN and PETN. The reactions of $\text{Si}(\text{CH}_3)_3^+$ with PETN and EGDN were also examined in a magnetic sector mass spectrometer. No adduct formation was observed with either EGDN or PETN in the Fourier transform ion cyclotron resonance mass spectrometer, but characteristic fragment ions are seen. Both EGDN and PETN form adducts with $\text{Si}(\text{CH}_3)_3^+$ in the sector mass spectrometer. The bimolecular rate constant for the reaction of $\text{Si}(\text{CH}_3)_3^+$ with EGDN is measured to be $0.91 \times 10^{-10} \text{ cm}^3 \text{ s}^{-1} \text{ molecule}^{-1}$, and the bimolecular rate constant for the reaction of $\text{Si}(\text{CH}_3)_3^+$ with PETN is estimated to be $8 \times 10^{-10} \text{ cm}^3 \text{ s}^{-1} \text{ molecule}^{-1}$. Collision induced dissociation experiments were performed on the major fragment ion products to characterize the observed fragmentation patterns. The fragment ions observed in both cases are characteristic of each explosive and could be useful in the analytical detection and identification of EGDN and especially PETN. Reaction coordinate diagrams for the reactions of EGDN and PETN with $\text{Si}(\text{CH}_3)_3^+$ are derived (from known thermochemistry and semi-empirical calculations on the involved species). The reactivity of nitro and nitrate ester explosives with $\text{Si}(\text{CH}_3)_3^+$ is compared and reasons for their different chemical behavior are discussed.

Introduction

In previous work,¹ we have found that both 1,3,5-trinitro-1,3,5-triazacyclohexane (RDX, **I**) and 2,4,6-trinitrotoluene (TNT, **II**) react efficiently with $\text{Si}(\text{CH}_3)_3^+$ to form

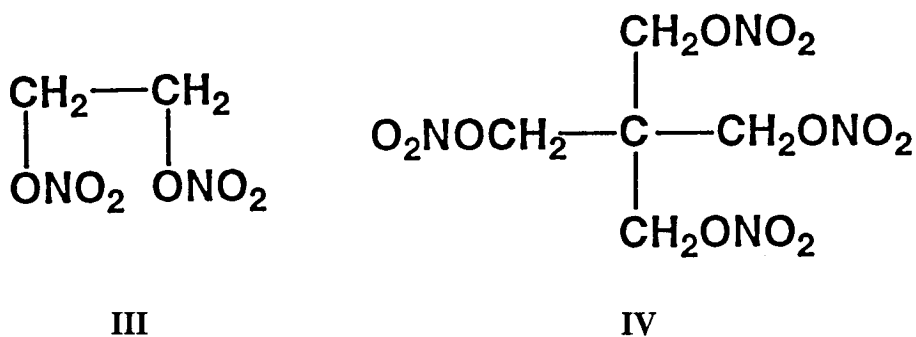


strongly bound adducts, as indicated in reactions 1 and 4. Fragmentation of these adducts was also observed (reactions 2, 3 and 5), and collision induced dissociation



(CID) of the stable adducts produced the same fragmentation patterns that were observed during adduct formation. This reactivity was attributed to the high affinity of Si for oxygen and the attraction of the $\text{Si}(\text{CH}_3)_3^+$ ion to the formal negative charge of oxygen in a nitro group. These results also suggested that reactions of this type could prove useful in a detection scheme for common explosives using mass spectrometry.

Both RDX and TNT are nitro explosives: they contain $-\text{NO}_2$ groups, where the nitro group is connected to another nitrogen or carbon. Another major class of explosives is the nitrate esters, which contain the $-\text{ONO}_2$ group connected to a carbon atom. Two representative members of this class are ethylene glycol dinitrate (EGDN, **III**) and pentaerythritol tetranitrate (PETN, **IV**). PETN is of considerable interest, since



it can be used in sheet form or mixed with RDX to make SEMTEX,² a plastic explosive. Since our previous work with RDX and TNT suggested that $\text{Si}(\text{CH}_3)_3^+$ could be a useful chemical ionization reagent for the mass spectrometric detection of nitro explosives, it is

possible that $\text{Si}(\text{CH}_3)_3^+$ could similarly be used to identify nitrate esters. We report here an investigation of the reactivity of EGDN and PETN with $\text{Si}(\text{CH}_3)_3^+$, both to examine the usefulness of $\text{Si}(\text{CH}_3)_3^+$ as a chemical ionization reagent for the detection of nitrate esters in the gas phase and to allow us to compare the behavior of nitro and nitrate ester explosives with $\text{Si}(\text{CH}_3)_3^+$.

Experimental

Overview. Fourier transform ion cyclotron resonance (FT-ICR) mass spectrometry is a well-established technique and its experimental aspects have been discussed previously in the literature.³ Only details relevant to this experiment are presented here. A 1-in. cubic trapping cell is located between the poles of a Varian 15-in. electromagnet maintained at a field of 2.0 T. Data were collected with an IonSpec Omega/386 FT-ICR data system and associated electronics. Tetramethylsilane (TMS), $\text{Si}(\text{CH}_3)_4$, and EGDN were introduced into the cell from vacuum inlet lines by separate leak valves, and their pressures were measured with a Schultz-Phelps (SP) ion gauge calibrated against an MKS 390 HA-00001SP05 capacitance manometer. PETN was introduced to the ICR cell with a previously described solid sample probe.¹ A 0.1 mg/mL solution of PETN in methanol was injected into a 1.5 mm O.D. glass capillary tube and the solvent evaporated. The sample was then introduced to the ICR cell. Generation of PETN vapor required heating the sample tube to approximately 80 °C, significantly below the melting point (142 °C)⁴ and decomposition point (155 °C)⁵ of PETN. We were unable to produce enough PETN vapor to calibrate the SP ion gauge against the capacitance manometer. However, assuming that the SP gauge exhibits similar sensitivities to EGDN and PETN provided an estimate of the pressure of PETN.

Uncertainties in the absolute pressure limited rate constants to an accuracy of $\pm 20\%$ ($\pm 30\%$ for PETN). TMS (99.9% pure) was obtained commercially from Aldrich. PETN was obtained commercially from AccuStandard Inc. EGDN was synthesized by

the nitration of ethylene glycol.⁶ TMS and EGDN were both further purified by freeze-pump-thaw cycling.

Trimethylsilyl cation was generated by electron impact of TMS at a partial pressure of about $(9-10) \times 10^{-8}$ Torr. We found that a nominal electron energy of 22 eV was the most favorable energy for the formation of $\text{Si}(\text{CH}_3)_3^+$ ions. We then introduced either EGDN at pressures in the range of $(3-6) \times 10^{-7}$ Torr or PETN at estimated pressures in the range of $(2-3) \times 10^{-7}$ Torr. $\text{Si}(\text{CH}_3)_3^+$ was isolated by ejecting unwanted ions from the cell using frequency sweep excitation.⁷ Subsequent reactions of either EGDN or PETN with $\text{Si}(\text{CH}_3)_3^+$ were then observed. Rate constants were determined in a straightforward manner, from slopes of semilog plots of the decay of reactant ion abundance versus time and the pressure of the neutral reactant. For PETN an estimate of its rate constant was calculated using its estimated pressure. The reported rate constants are averages of several sets of experimental data taken at different pressures of the neutral gases. The cell temperature is somewhat higher for the PETN experiments due to the close proximity of the probe, operated at 80 °C. For the EGDN experiments the cell was operated at ambient temperature.

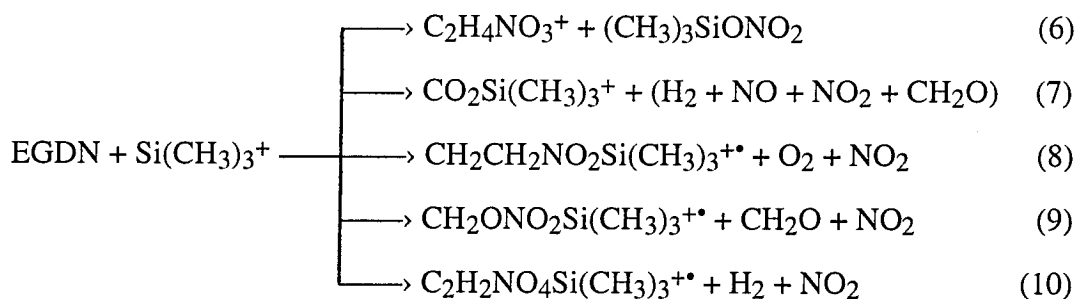
Sector Mass Spectrometer Experiments. Several additional chemical ionization experiments were performed on a VG/Fisons Prospec E magnetic sector mass spectrometer of EBE geometry. 0.75 μg samples of EGDN in 1.5 mm O.D. metal capillary tubes were prepared by injecting in each tube 1 μL of EGDN. The probe tip was heated to ≈ 80 °C to produce a burst of EGDN vapor. 1 μg samples of PETN in 1.5 mm O.D. glass capillary tubes were prepared by injecting in each tube 10 μL of a 0.1 mg/mL solution of PETN in methanol. The solvent was then evaporated. PETN vapor was produced by ramping the probe tip to 140 °C. TMS was present in the source region at a pressure of 4×10^{-6} Torr. The pressure is higher in the chemical ionization region, but we were unable to directly measure the pressure there. $\text{Si}(\text{CH}_3)_3^+$ was generated by electron impact with 22 eV electrons and allowed to react with EGDN or PETN vapor in

the chemical ionization region. Low resolution spectra were performed at 1000 resolution ($m/\Delta m$). Accurate mass measurements were performed on selected ions by voltage scanning at 7000-10,000 resolution.

Collision Induced Dissociation Experiments. CID experiments were performed on major fragment ions in the FT-ICR mass spectrometer to characterize the observed fragmentation patterns and determine if the fragment ions could serve as a "fingerprint" for either explosive. We used sustained off-resonance irradiation (SORI)⁸ to achieve the CID of the ions of interest. The collision energy for both EGDN and PETN fragments was varied between 0 and 4 eV in the laboratory frame of reference. The TMS gas and EGDN or PETN vapor present in the cell served as the collision gas.

Results

Reaction of $\text{Si}(\text{CH}_3)_3^+$ with EGDN. Reactions 6-10 were observed when



$\text{Si}(\text{CH}_3)_3^+$ reacted with EGDN (Figure 1). The compositions shown in reactions 7-10 are the only compositions consistent with the observed masses. The neutral products in reaction 7 are shown in parentheses, indicating that the neutral products of this reaction are uncertain. Figure 2 shows a time plot of the relative abundances of reactants and products for a single experiment. For the reaction of $\text{Si}(\text{CH}_3)_3^+$ with EGDN the total bimolecular rate constant $k = 0.91 \times 10^{-10} \text{ cm}^3\text{s}^{-1}\text{molecule}^{-1}$ and the reaction efficiency $k/k_{\text{Langevin}} = 0.10$.⁹⁻¹¹

CID of EGDN Fragments. CID experiments were performed on the $\text{CO}_2\text{Si}(\text{CH}_3)_3^+$ ion since the formation of CO_2 as a fragment was unexpected. The only ionic product seen from the CID of this fragment occurred at m/z 90 (see Figure 3). We

Figure 1a. Isolation of the $\text{Si}(\text{CH}_3)_3^+$ ion at $t = 0$ ms.

Figure 1b. Spectrum of the products of the reaction of $\text{Si}(\text{CH}_3)_3^+$ with EGDN at $t = 1200$ ms. The pressure of EGDN in the cell is 3.7×10^{-7} Torr.

Figure 1c. Spectrum of the products of the reaction of $\text{Si}(\text{CH}_3)_3^+$ with EGDN at $t = 3000$ ms.

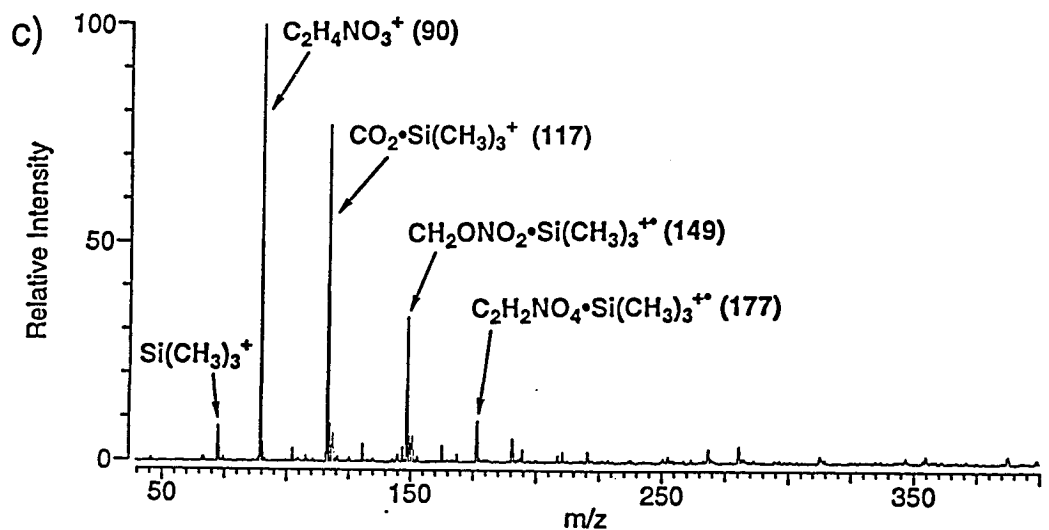
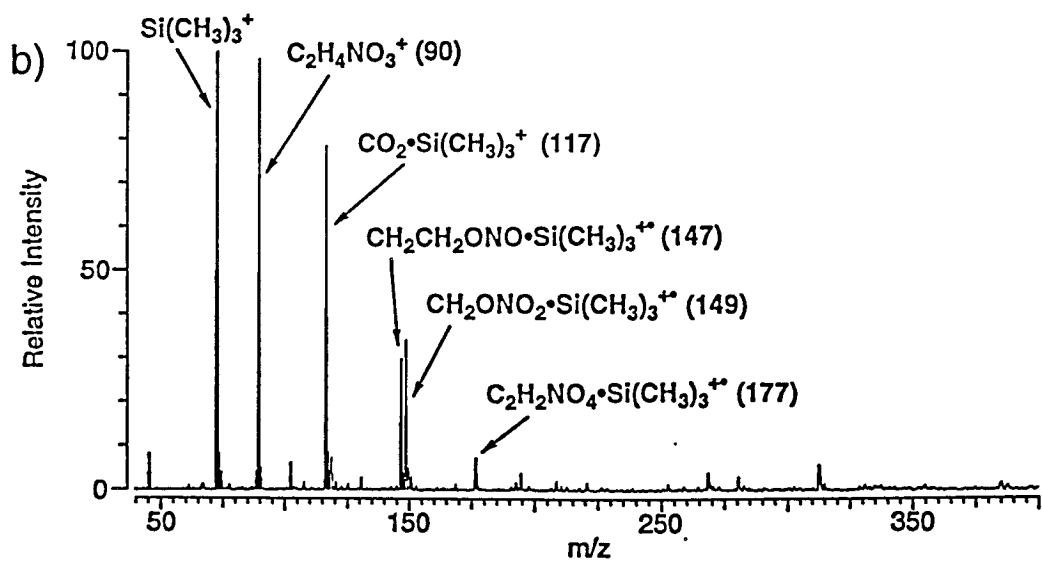
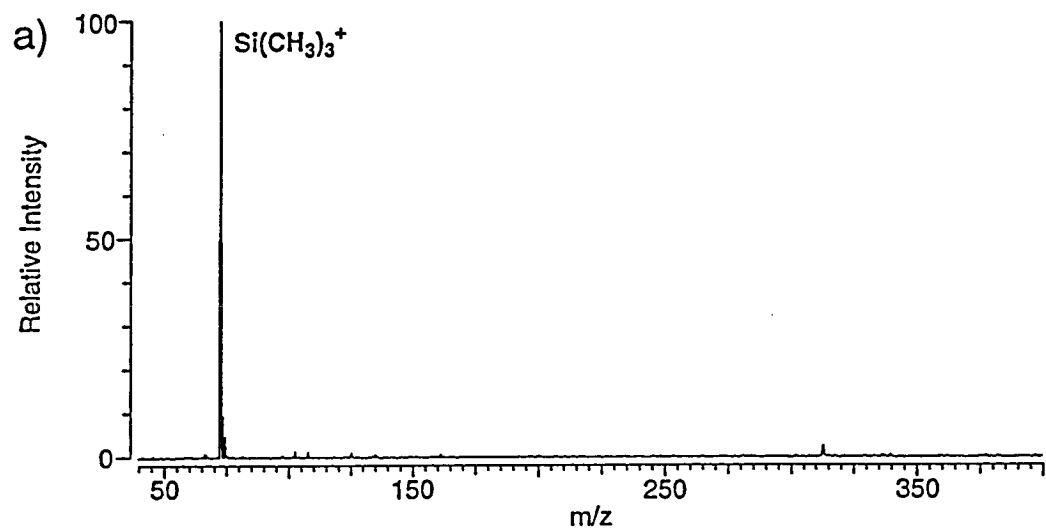
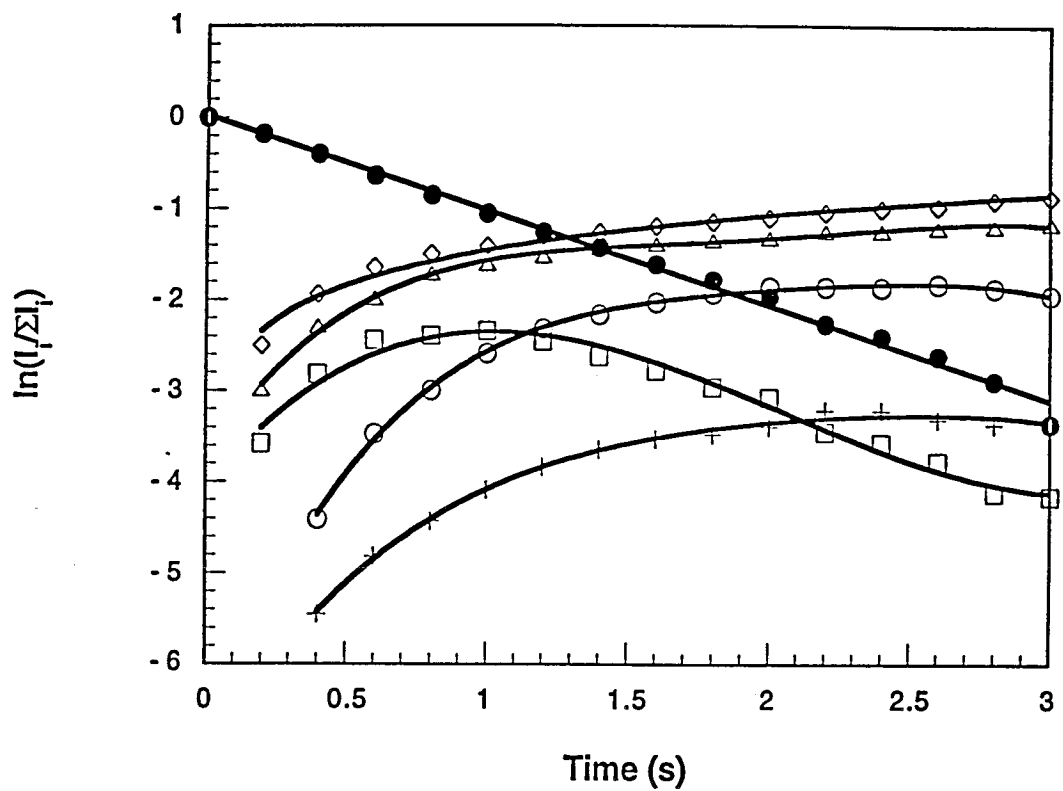


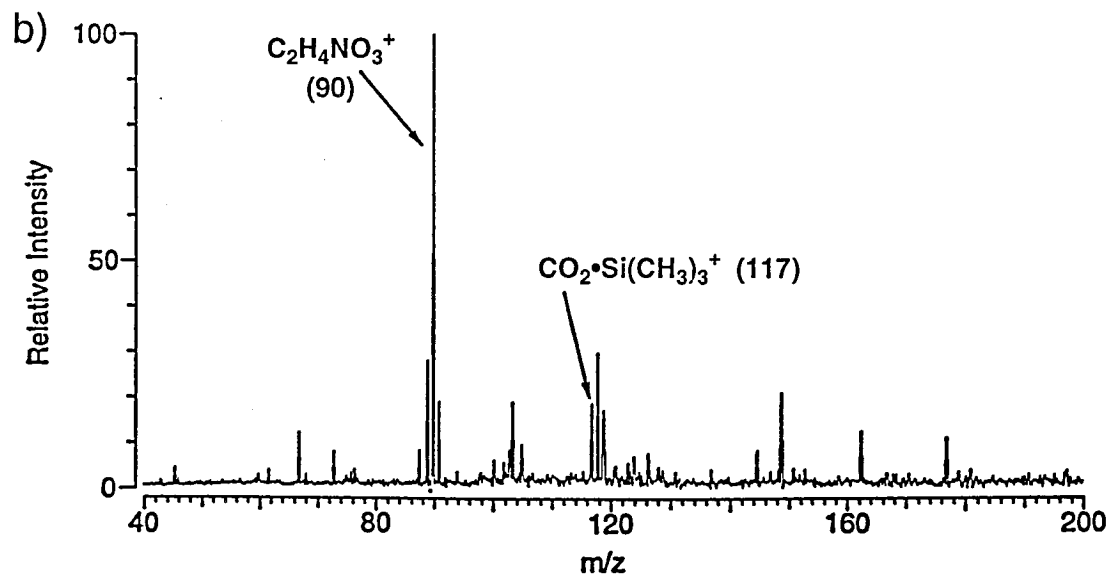
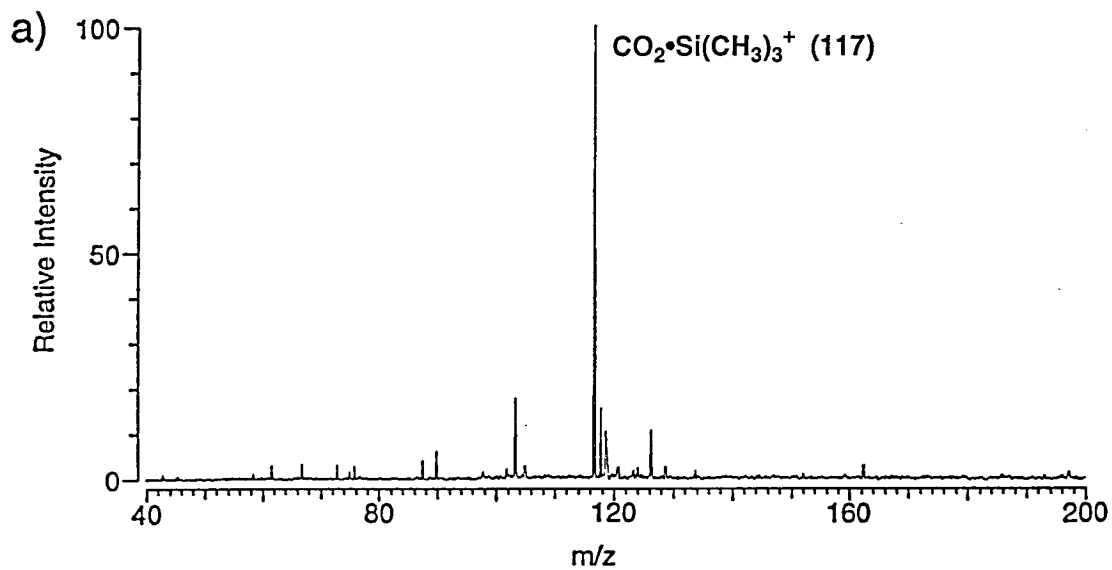
Figure 2. Semilog time plot of the products of the reaction of $\text{Si}(\text{CH}_3)_3^+$ with EGDN. The number in parentheses by each formula is the m/z value of each ion. The spectra in Figure 1 were taken from this time plot.



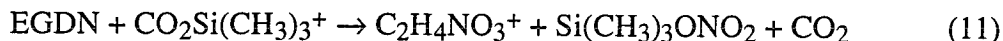
- | | |
|--|---|
| ● $\text{Si}(\text{CH}_3)_3^+$ (73) | ○ $\text{CH}_2\text{ONO}_2\cdot\text{Si}(\text{CH}_3)_3^{++}$ (149) |
| ◇ $\text{C}_2\text{H}_4\text{NO}_3^+$ (90) | + $\text{C}_2\text{H}_2\text{NO}_4\cdot\text{Si}(\text{CH}_3)_3^{++}$ (177) |
| △ $\text{CO}_2\cdot\text{Si}(\text{CH}_3)_3^+$ (117) | |
| □ $\text{CH}_2\text{CH}_2\text{ONO}\cdot\text{Si}(\text{CH}_3)_3^{++}$ (147) | |

Figure 3a. Isolation of the $\text{CO}_2\text{Si}(\text{CH}_3)_3^+$ ion at m/z 117 at $t = 0$ ms, after the $\text{Si}(\text{CH}_3)_3^+$ ion has had 1000 ms to react with EGDN.

Figure 3b. CID spectrum of the $\text{CO}_2\text{Si}(\text{CH}_3)_3^+$ ion. The collision gas is a mixture of EGDN and TMS is a 2:1 ratio. Ions were excited at a frequency approximately 2200 Hz above the resonant frequency of the ion (approximately 1 m/z low) for 2000 ms. The average collision energy was 1.5 eV for the $\text{CO}_2\text{Si}(\text{CH}_3)_3^+$ ion in the center-of-mass frame of reference.



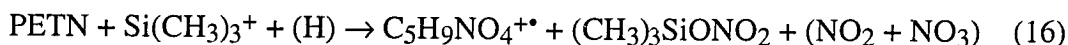
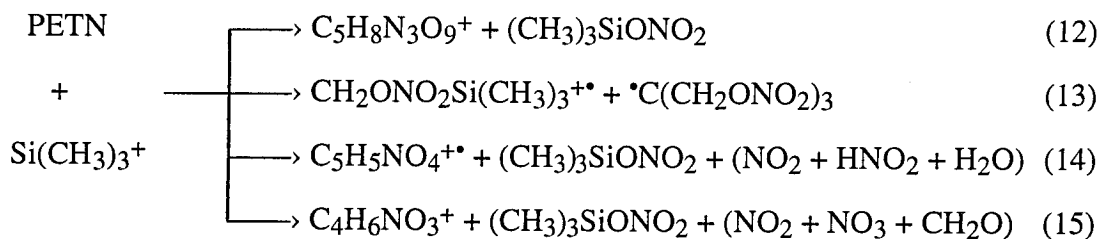
also attempted to react $\text{Si}(\text{CH}_3)_3^+$ with CO_2 in a separate experiment, but no adduct formation was observed. These results suggest that $\text{CO}_2\text{Si}(\text{CH}_3)_3^+$ is a fragment from the reaction of $\text{Si}(\text{CH}_3)_3^+$ with EGDN and that subsequent collisions with EGDN in the CID experiments displace CO_2 . The excited $\text{Si}(\text{CH}_3)_3^+$ ion then abstracts the nitrate group from EGDN, which was also observed in the direct reaction of $\text{Si}(\text{CH}_3)_3^+$ with



EGDN. Reaction 11 shows the overall process that occurs when CID is performed on $\text{CO}_2\text{Si}(\text{CH}_3)_3^+$.

Since the $\text{C}_2\text{H}_4\text{NO}_3^+$ ion occurs at m/z 90, it could also have the formula $\text{Si}(\text{CH}_3)_3\text{OH}^+$. However, the isotope pattern of the observed peak (see Figure 1) was inconsistent with the presence of Si. Therefore we conclude that the ionic product of reaction 10 has the composition $\text{C}_2\text{H}_4\text{NO}_3^+$.

Reaction of $\text{Si}(\text{CH}_3)_3^+$ with PETN in the FT-ICR Mass Spectrometer. Reactions 12-16 were observed when $\text{Si}(\text{CH}_3)_3^+$ reacted with PETN (see Figure 4). The



compositions shown in reactions 12, 13, 15 and 16 are the only compositions consistent with the observed masses, while the composition shown in reaction 14 is the only reasonable composition consistent with its observed mass. The composition of the $\text{C}_5\text{H}_9\text{NO}_4^{+\bullet}$ ion in reaction 16 implies that a hydrogen atom must be abstracted at some point during the formation of $\text{C}_5\text{H}_9\text{NO}_4^{+\bullet}$ from a source within the ICR cell. The H atom in reaction 16 is shown in parentheses, since we are unable to identify its source. The neutral products in reactions 14-16 are also shown in parentheses, indicating that the neutral products in these reactions are uncertain. Figure 5 shows a time plot of the

Figure 4a. Isolation of the $\text{Si}(\text{CH}_3)_3^+$ ion at $t = 0$ ms.

Figure 4b. Spectrum of the products of the reaction of $\text{Si}(\text{CH}_3)_3^+$ with PETN at $t = 240$ ms. The estimated pressure of PETN in the cell is $(3 \pm 0.5) \times 10^{-7}$ Torr. The peaks marked with asterisks are due to noise.

Figure 4c. Spectrum of the products of the reaction of $\text{Si}(\text{CH}_3)_3^+$ with PETN at $t = 600$ ms. The peaks marked with asterisks are due to noise.

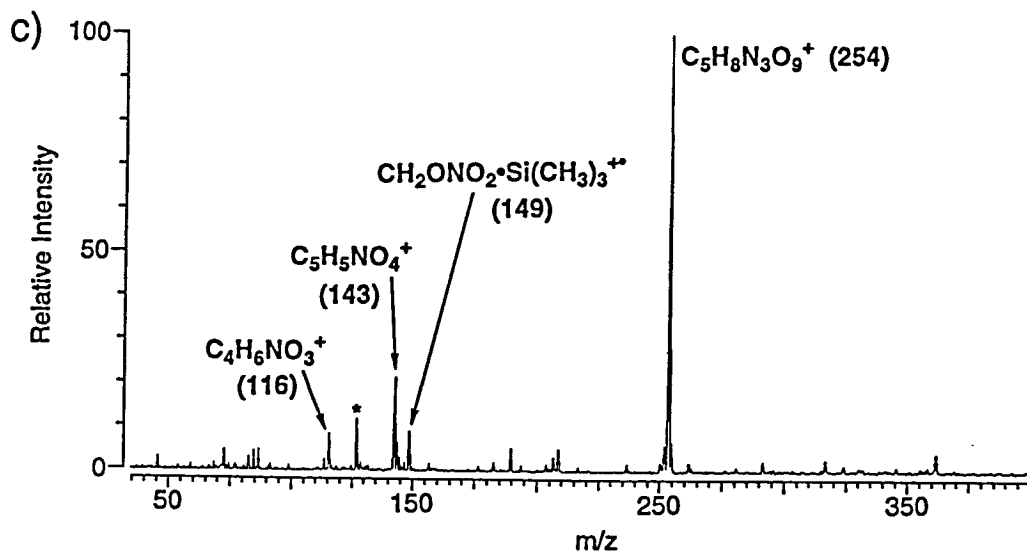
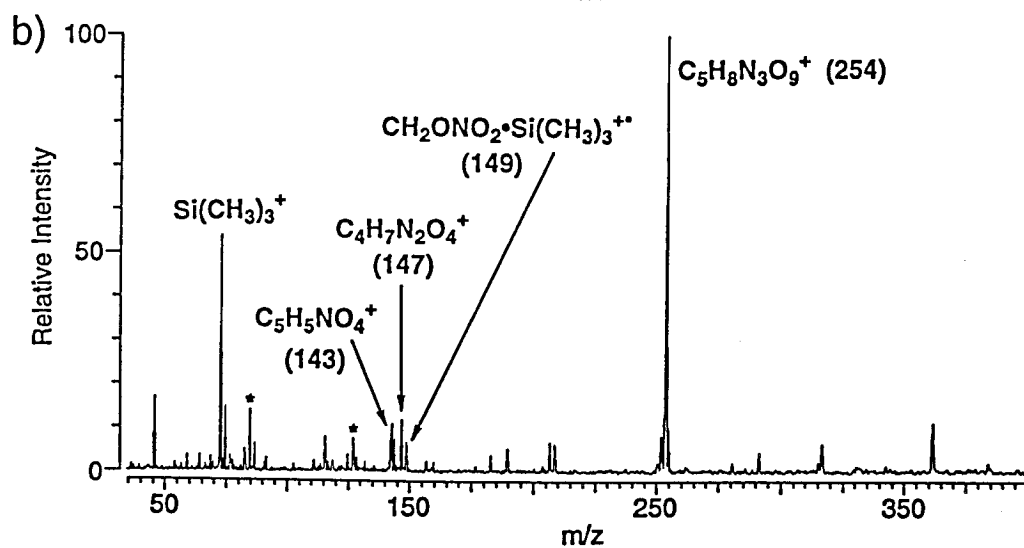
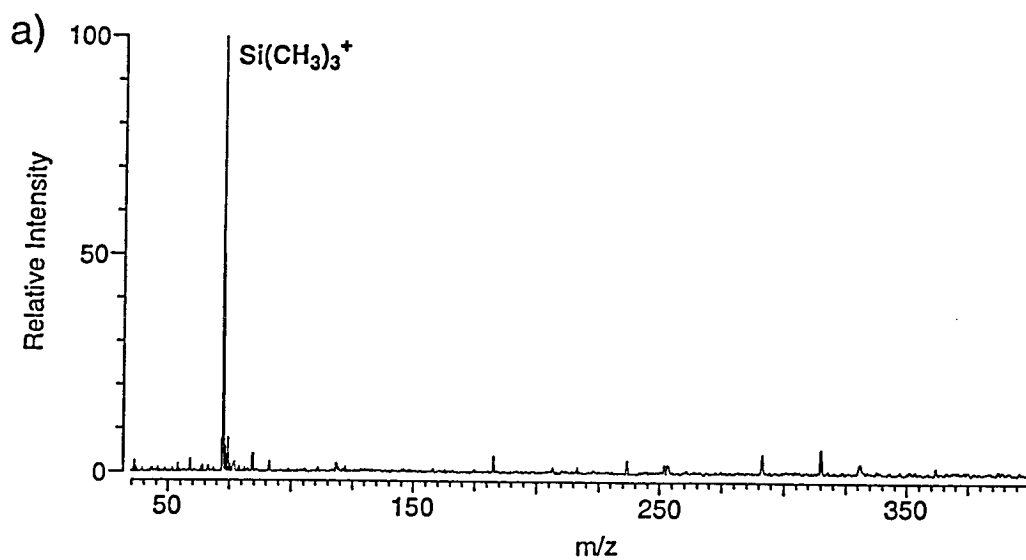
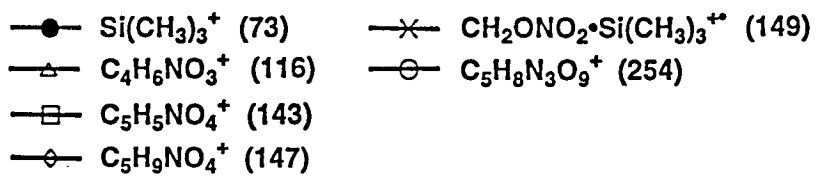
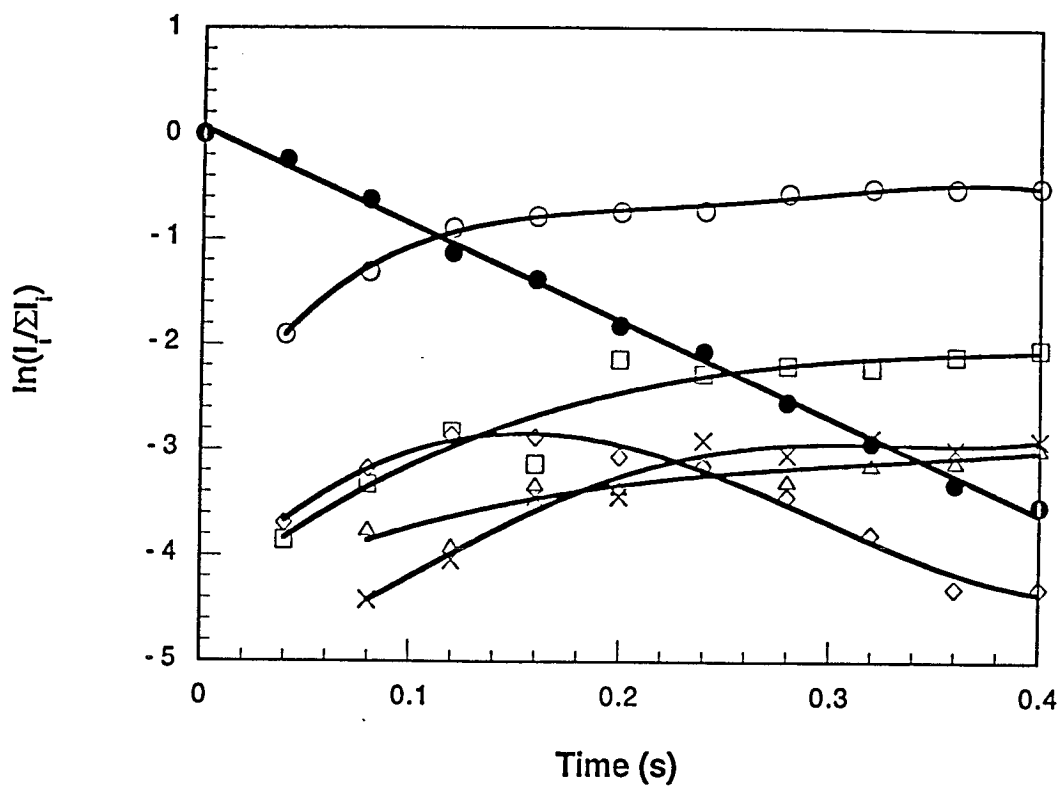
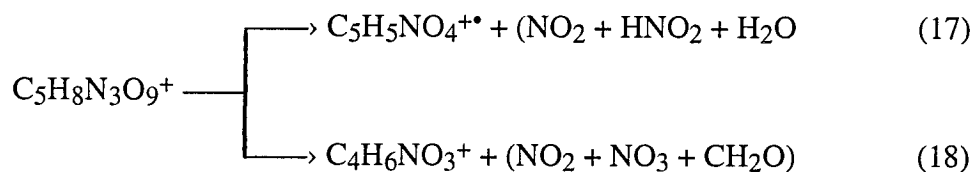


Figure 5. Semilog time plot of the products of the reaction of $\text{Si}(\text{CH}_3)_3^+$ with PETN. The number in parentheses by each formula is the m/z value of each ion. The spectra in Figure 4 were taken from this time plot.



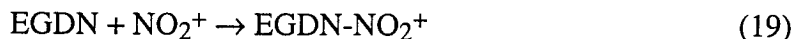
relative abundances of reactants and products for a single experiment. The time plot exhibited some pressure dependence: decreasing the pressure of PETN (from approximately 3×10^{-7} Torr to approximately 1.5×10^{-7} Torr) would decrease the yield of $C_5H_8N_3O_9^+$ and increase the amount of products from reactions 13-16. However, the $C_5H_8N_3O_9^+$ ion was the major product at all pressures observed. For the reaction of $Si(CH_3)_3^+$ with PETN the total bimolecular rate constant k is estimated to be $8 \times 10^{-10} \text{ cm}^3\text{s}^{-1}\text{molecule}^{-1}$. We estimate that the reaction efficiency $k/k_{\text{Langevin}} \approx 0.6$.^{9,11,12}

CID of PETN Fragments. Reactions 17 and 18 were observed when the

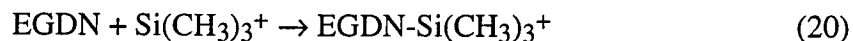


$C_5H_8N_3O_9^+$ ion at m/z 254 underwent CID (see Figure 6). The fragments observed from CID of $C_5H_8N_3O_9^+$ were also seen as minor products in the direct reaction of PETN with $Si(CH_3)_3^+$.

Reaction of $Si(CH_3)_3^+$ with EGDN and PETN in the Magnetic Sector Mass Spectrometer. When $Si(CH_3)_3^+$ was allowed to react with EGDN in the magnetic sector mass spectrometer, the main products were $C_2H_4NO_3^+$ from reaction 6 (70% of products) and $CO_2Si(CH_3)_3^+$ from reaction 7 (30% of products). Small amounts of $CH_2CH_2NO_2(CH_3)_3^{+\bullet}$ (reaction 8), EGDN- NO_2^+ at m/z 198 (reaction 19) and EGDN-



$Si(CH_3)_3^+$ at m/z 225 (reaction 20) were also observed. We should note that large



amounts of NO_2^+ are observed in the sector instrument when the EGDN vapor is subjected to electron impact and that the NO_2^+ and EGDN- NO_2^+ abundances are coupled, supporting our assignment of the composition EGDN- NO_2^+ to the ion at m/z 198. A typical mass spectrum is shown in Figure 7. The $C_2H_4NO_3^+$, $CO_2Si(CH_3)_3^+$ and $CH_2CH_2NO_2(CH_3)_3^{+\bullet}$ ions observed in the sector instrument were also seen in the

Figure 6a. Isolation of the $C_5H_8N_3O_9^+$ ion at m/z 254 at $t = 0$ ms, after the $Si(CH_3)_3^+$ ion has had 500 ms to react with PETN. The peaks marked with asterisks are due to electrical noise.

Figure 6b. CID spectrum of the $C_5H_8N_3O_9^+$ ion. The collision gas is a mixture of PETN and TMS in a 3:1 ratio. Ions were excited at a frequency approximately 1500 Hz above the resonant frequency of the ion (approximately 3.4 m/z low) for 1000 ms. The average collision energy was 1.7 eV for the $C_5H_8N_3O_9^+$ ion in the center-of-mass frame of reference. The peaks marked with asterisks are due to noise.

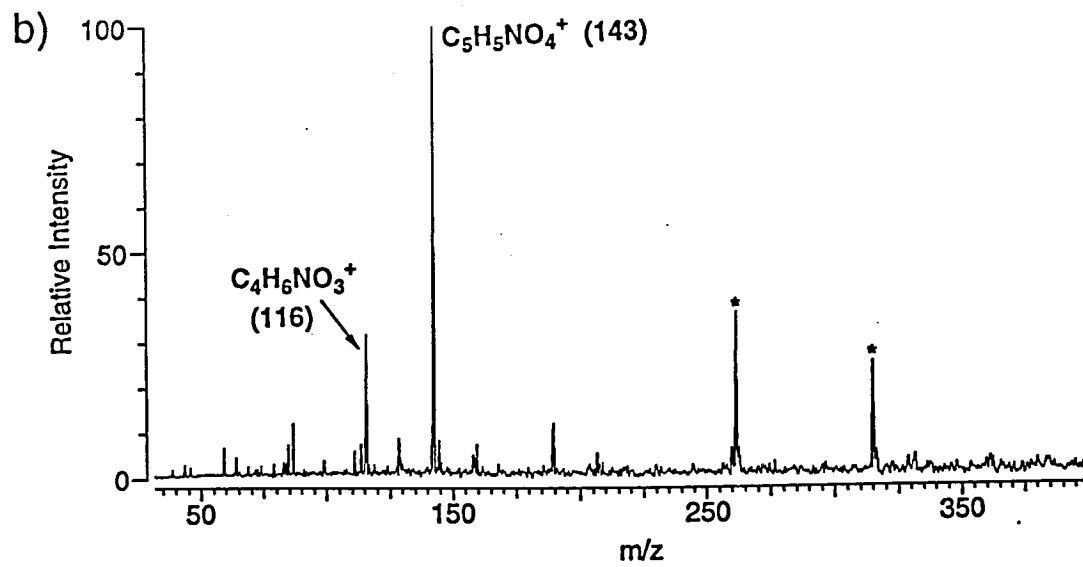
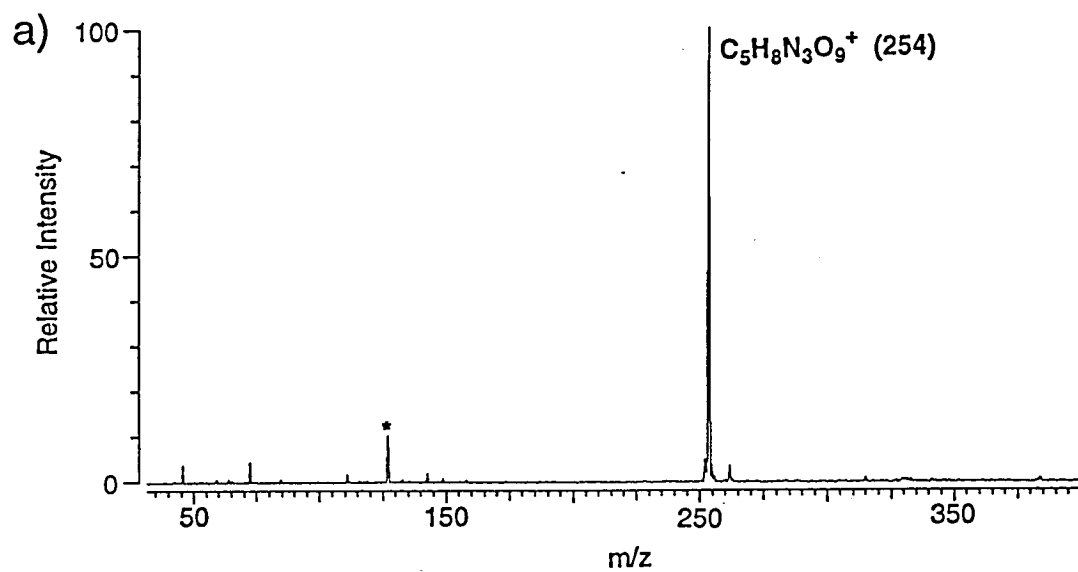
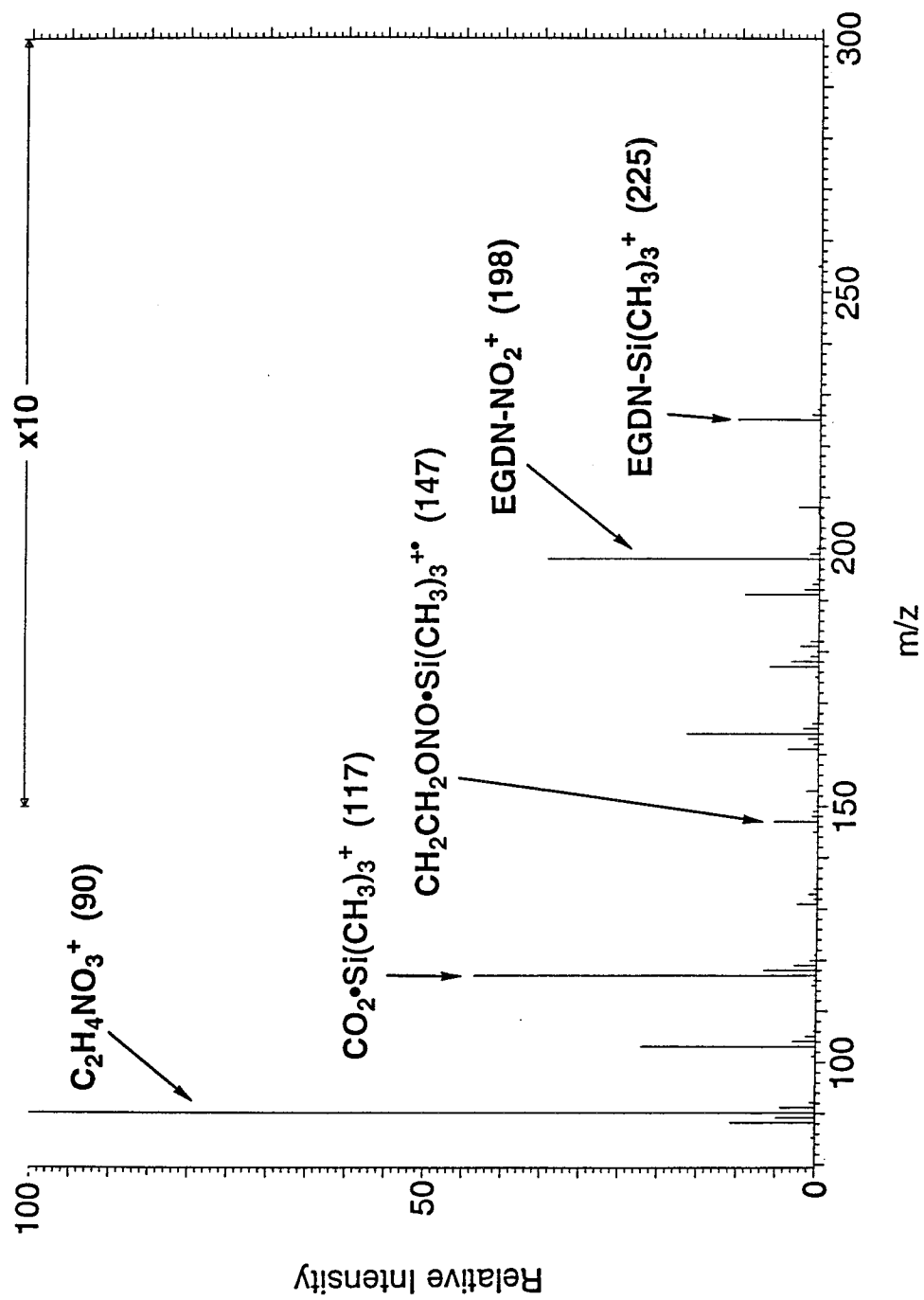
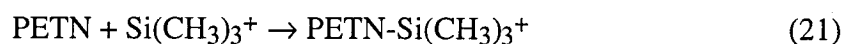


Figure 7. Spectrum of the products of the reaction of $\text{Si}(\text{CH}_3)_3^+$ with EGDN in a magnetic sector mass spectrometer. The peaks from m/z 150 to m/z 300 have been multiplied by a factor of 10.



FT-ICR experiments. Furthermore, in both the FT-ICR and sector instrument experiments $C_2H_4NO_3^+$ was the most abundant product, followed by $CO_2Si(CH_3)_3^+$. However, no $EGDN-Si(CH_3)_3^+$ was seen in the FT-ICR, while a small amount of it was observed in the sector instrument. The pressure of TMS was 1-2 orders of magnitude higher in the sector mass spectrometer than in the FT-ICR mass spectrometer, so it appears that the increased collisional stabilization at these higher pressures allows small amounts of the $EGDN-Si(CH_3)_3^+$ adduct to be directly observed.

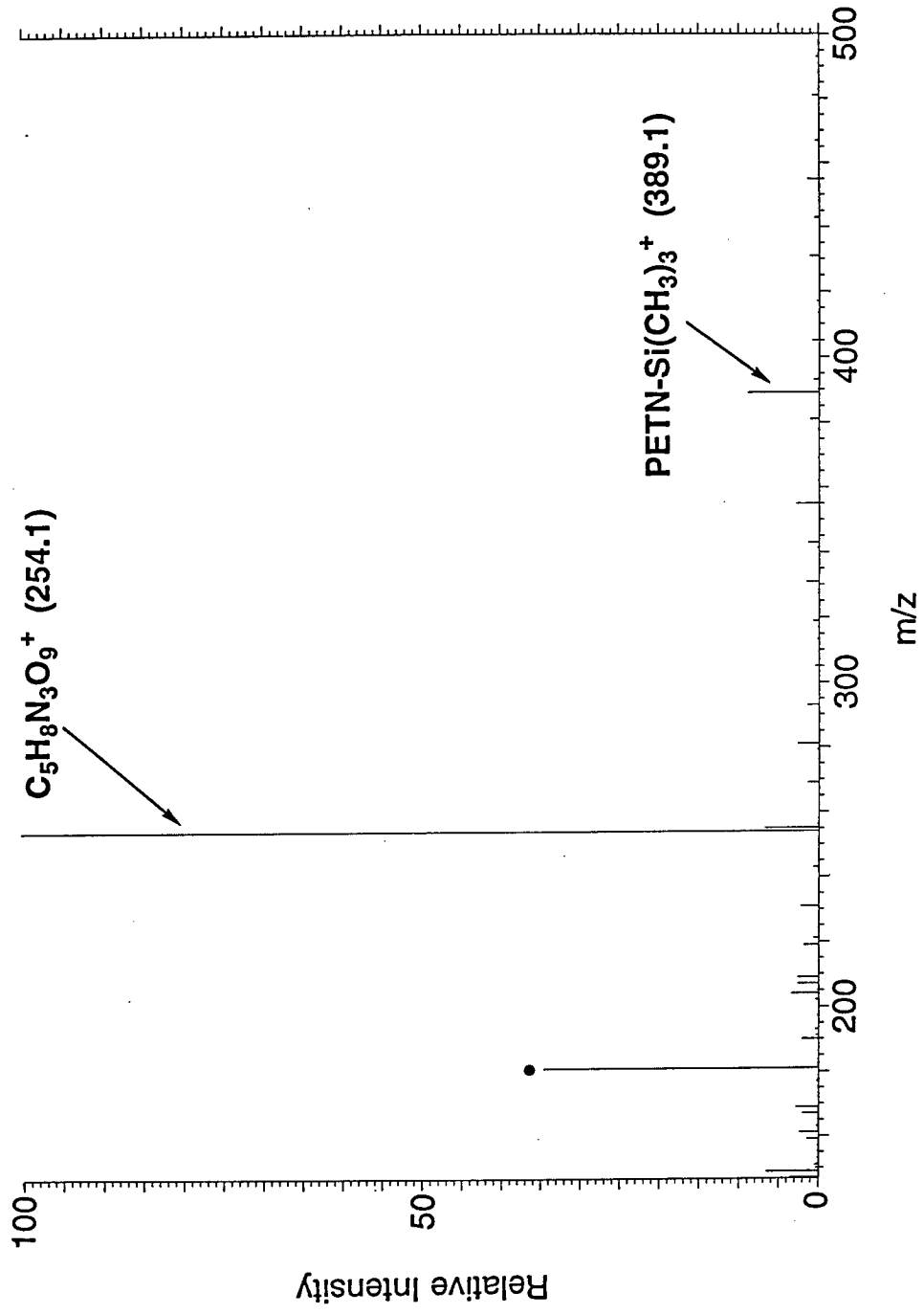
When $Si(CH_3)_3^+$ was allowed to react with PETN in the magnetic sector mass spectrometer, two products were observed: $C_5H_8N_3O_9^+$ from reaction 12 (90% of products) and the $PETN-Si(CH_3)_3^+$ adduct from reaction 21 (10% of products) observed.



A typical mass spectrum is shown in Figure 8. No fragmentation products from $C_5H_8N_3O_9^+$ were observed in the sector instrument mass spectra. Again, since the pressure of TMS was higher in the sector mass spectrometer than in the FT-ICR mass spectrometer, it is likely that the $C_5H_8N_3O_9^+$ ion is completely collisionally stabilized in the sector instrument. This would explain the observed lack of fragmentation of the $C_5H_8N_3O_9^+$ ion in the sector instrument spectra. Furthermore, a small amount of the initial $PETN-Si(CH_3)_3^+$ adduct at m/z 389 apparently receives enough collisional stabilization at these higher pressures to be directly observed. Collisional stabilization effects were also observed in the FT-ICR instrument, where the relative intensity of the $C_5H_8N_3O_9^+$ ion increased as the total pressure was increased. However, pressures in the FT-ICR instrument were apparently never high enough to produce the amount of collisional stabilization necessary to observe the $PETN-Si(CH_3)_3^+$ adduct.

The ion at m/z 254 was found to have an experimental m/z ratio of 254.02583, which is within 0.9 ppm of the m/z ratio of $C_5H_8N_3O_9^+$ (254.02605). Thus we conclude that the ion of m/z 254 observed in the sector mass spectrometer has the composition $C_5H_8N_3O_9^+$, as previously written.

Figure 8. Spectrum of the products of the reaction of $\text{Si}(\text{CH}_3)_3^+$ with PETN in a magnetic sector mass spectrometer. The spectrum has been baseline subtracted to suppress background peaks from perfluorokerosene (which was used to calibrate the magnet). The peak marked with a bullet at m/z 181.0 corresponds to C_4F_7^+ . It is the most abundant ion produced from perfluorokerosene in this mass range.



Semi-Empirical Calculations. To assist us in the elucidation of the relative energetics of EGDN, PETN, their adducts with $\text{Si}(\text{CH}_3)_3^+$, and their major fragment ions, we used semi-empirical calculations to study the relevant species. These semi-empirical calculations were performed at the PM3 level¹³ with HyperChem.¹⁴ We will discuss these calculations in greater detail later in this chapter.

Discussion

Reactivity of $\text{Si}(\text{CH}_3)_3^+$ with EGDN and PETN. Both EGDN and PETN were found to react efficiently with $\text{Si}(\text{CH}_3)_3^+$. Unfortunately, no parent adduct was observed with either explosive in our FT-ICR experiments; with both explosives only fragment ions were observed. For both EGDN and PETN the major product was a fragment ion formed by the loss of $(\text{CH}_3)_3\text{SiONO}_2$ ($\text{C}_2\text{H}_4\text{NO}_3^+$ at m/z 90 for EGDN, $\text{C}_5\text{H}_8\text{N}_3\text{O}_9^+$ at m/z 254 for PETN). Loss of NO_3^- has also been observed in thermal decomposition studies of nitrate ester explosives.¹⁵ With EGDN several additional product ions containing $\text{Si}(\text{CH}_3)_3^+$ were observed in significant amounts along with the $\text{C}_2\text{H}_4\text{NO}_3^+$ ion, but with PETN the $\text{Si}(\text{CH}_3)_3\text{ONO}_2$ loss channel dominated the other minor fragmentation pathways by an order of magnitude. In addition, CID of the $\text{C}_5\text{H}_8\text{N}_3\text{O}_9^+$ ion from the reaction of PETN with $\text{Si}(\text{CH}_3)_3^+$ produced the same ions that were seen as minor fragments in the direct reaction. Reaction of $\text{Si}(\text{CH}_3)_3^+$ with PETN thus yields mainly a single product, $\text{C}_5\text{H}_8\text{N}_3\text{O}_9^+$, which gives characteristic CID products. Although this ion is not the parent adduct from the association of PETN with $\text{Si}(\text{CH}_3)_3^+$, it appears that the reaction of $\text{Si}(\text{CH}_3)_3^+$ with PETN could be useful in the analytical detection and identification of PETN.

It is particularly interesting to note that the reaction of EGDN with $\text{Si}(\text{CH}_3)_3^+$ and PETN with $\text{Si}(\text{CH}_3)_3^+$ in a magnetic sector mass spectrometer produced the same major product ions that were observed in the FT-ICR mass spectrometer under very different conditions. Furthermore, conditions in the sector mass spectrometer allowed us to form the EGDN- $\text{Si}(\text{CH}_3)_3^+$ and PETN- $\text{Si}(\text{CH}_3)_3^+$ adducts. This suggests that

detection of explosives by chemical ionization with $\text{Si}(\text{CH}_3)_3^+$ could be implemented on many types of mass spectrometers and under a variety of conditions.

The time plot in Figure 2 for the reaction of EGDN with $\text{Si}(\text{CH}_3)_3^+$ shows that all of the products grow in monotonically over time except for the $\text{CH}_2\text{CH}_2\text{NO}_2\text{Si}(\text{CH}_3)_3^+$ ion at m/z 147, which initially grows in and then decays away. The $\text{C}_2\text{H}_2\text{NO}_4\text{Si}(\text{CH}_3)_3^+$ ion at m/z 177 and the $\text{CH}_2\text{ONO}_2\text{Si}(\text{CH}_3)_3^+$ ion at m/z 149 grow in at later times, indicating that they may not be nascent products. We should note that $\text{C}_2\text{H}_2\text{NO}_4\text{Si}(\text{CH}_3)_3^+$ and $\text{CH}_2\text{ONO}_2\text{Si}(\text{CH}_3)_3^+$ only comprise about 20% of the products after the $\text{Si}(\text{CH}_3)_3^+$ ion has been consumed.

The time plot in Figure 5 for the reaction of PETN with $\text{Si}(\text{CH}_3)_3^+$ shows that all products except $\text{C}_5\text{H}_9\text{NO}_4^+$ at m/z 147 grow in monotonically over time. Figure 6 shows that the CID of $\text{C}_5\text{H}_8\text{N}_3\text{O}_9^+$ at m/z 254 produced $\text{C}_5\text{H}_5\text{NO}_4^+$ at m/z 143 and $\text{C}_4\text{H}_6\text{NO}_3^+$ at m/z 116, which were also seen in the time plot data. This indicates that small amounts of the $\text{C}_5\text{H}_8\text{N}_3\text{O}_9^+$ ion fragment further to form $\text{C}_5\text{H}_5\text{NO}_4^+$ and $\text{C}_4\text{H}_6\text{NO}_3^+$ in the direct reaction. The $\text{C}_5\text{H}_9\text{NO}_4^+$ ion at m/z 147 grows in and then decays away in the direct reaction, while $\text{C}_4\text{H}_6\text{NO}_3^+$ continues to grow in as $\text{C}_5\text{H}_9\text{NO}_4^+$ disappears. Thus we suggest that as the $\text{C}_5\text{H}_9\text{NO}_4^+$ ion forms it can quickly lose CH_2OH to form $\text{C}_4\text{H}_6\text{NO}_3^+$. The $\text{CH}_2\text{ONO}_2\text{Si}(\text{CH}_3)_3^+$ ion (which was also seen with EGDN) once again grows in at later times, indicating that it may not be a nascent product. In this case the $\text{CH}_2\text{ONO}_2\text{Si}(\text{CH}_3)_3^+$ ion only comprises about 5% of the products after the $\text{Si}(\text{CH}_3)_3^+$ ion has been consumed.

The composition of $\text{C}_5\text{H}_9\text{NO}_4^+$ shows that it or one of its precursors must have gained a hydrogen atom from a source within the vacuum chamber. However, the specific mechanism by which $\text{C}_5\text{H}_9\text{NO}_4^+$ forms is uncertain. The $\text{C}_5\text{H}_9\text{NO}_4^+$ ion was not seen as a CID product from $\text{C}_5\text{H}_8\text{N}_3\text{O}_9^+$, but it can apparently easily fragment to $\text{C}_4\text{H}_6\text{NO}_3^+$. Thus we are unable to say whether or not $\text{C}_5\text{H}_9\text{NO}_4^+$ is a fragmentation product of $\text{C}_5\text{H}_8\text{N}_3\text{O}_9^+$.

Reaction Coordinate Diagrams for the Reaction of $\text{Si}(\text{CH}_3)_3^+$ with EGDN and PETN. In an effort to better evaluate the relative energetics of the reaction of $\text{Si}(\text{CH}_3)_3^+$ with EGDN or PETN to form the major product ions, we performed PM3 calculations on the species of interest. The calculated heats of formation for the lowest energy conformation of each species are shown in Table 1.¹⁶ However, some calculated values for the heats of formation were corrected as follows.

The $\Delta H_{\text{f},298}^\circ$ of nitroglycerine, $\text{CH}_2\text{ONO}_2\text{CHONO}_2\text{CH}_2\text{ONO}_2$, is known to be $-64.7 \text{ kcal mol}^{-1}$.¹⁷ However, the $\Delta H_{\text{f},298}^\circ$ calculated for nitroglycerine at the PM3 level of theory was $-75.3 \text{ kcal mol}^{-1}$. Apparently PM3 calculations do not properly account for crowding of the $-\text{ONO}_2$ groups on adjacent carbons. Thus we expect that the PM3 calculated $\Delta H_{\text{f},298}^\circ$ for EGDN will be underestimated by a similar amount. Therefore we adjusted the calculated $\Delta H_{\text{f},298}^\circ$ for EGDN upward by 11 kcal mol^{-1} . Such an adjustment was not necessary for PETN, since there are no adjacent carbons containing $-\text{ONO}_2$ groups. The PM3 calculated $\Delta H_{\text{f},298}^\circ$ of $-88.4 \text{ kcal mol}^{-1}$ for PETN is in good agreement with the experimental value of $-92.5 \text{ kcal mol}^{-1}$.¹⁷

Using the calculated heats of formation in Table 1 we have constructed reaction coordinate diagrams for the reaction of $\text{Si}(\text{CH}_3)_3^+$ with EGDN and PETN (shown in Figures 9 and 10, respectively). The reaction coordinate diagrams of Figures 9 and 10 show that the overall ΔH for the loss of $(\text{CH}_3)_3\text{SiONO}_2$ from either EGDN- $\text{Si}(\text{CH}_3)_3^+$ or PETN- $\text{Si}(\text{CH}_3)_3^+$ is quite exothermic. Thus it is not surprising that no parent adduct was observed with either explosive in our FT-ICR experiments. The reaction coordinate diagrams indicate that we would need to dissipate at least 20 kcal mol^{-1} of energy in collisions to allow for the formation of parent adduct, and apparently the pressures used in our FT-ICR experiments were too low to provide enough collisions to stabilize the parent adducts. In contrast to this, the experiments with EGDN and PETN in the magnetic sector mass spectrometer (at pressures 1-2 orders of magnitude higher than we had in the FT-ICR mass spectrometer) did produce a small amount of the EGDN-

Table 1. PM3 Heats of Formation of Species Involved in the Reactions of $\text{Si}(\text{CH}_3)_3^+$ with EGDN and PETN.

Species	$\Delta H^\circ_{f,298}$ (kcal mol ⁻¹) ^a
$\text{Si}(\text{CH}_3)_3^+$	141.3
EGDN	-41.4 ^b
EGDN- $\text{Si}(\text{CH}_3)_3^+$	61.7
$\text{Si}(\text{CH}_3)_3\text{ONO}_2$	-106.6
$\text{C}_2\text{H}_4\text{NO}_3^+$	185.4
PETN	-88.4
PETN- $\text{Si}(\text{CH}_3)_3^+$	15.8
$\text{C}_5\text{H}_8\text{N}_3\text{O}_9^+$	135.5

^aThe uncertainty of each value is estimated to be ± 10 kcal mol⁻¹. ^bCorrected by 11 kcal mol⁻¹ from the PM3 value of -52.4 kcal mol⁻¹. Discussion in text.

Figure 9. Reaction coordinate diagram for the reaction of EGDN with $\text{Si}(\text{CH}_3)_3^+$ to form the major product ions. We estimate the uncertainty in the derived enthalpy values to be $\pm 10 \text{ kcal mol}^{-1}$.

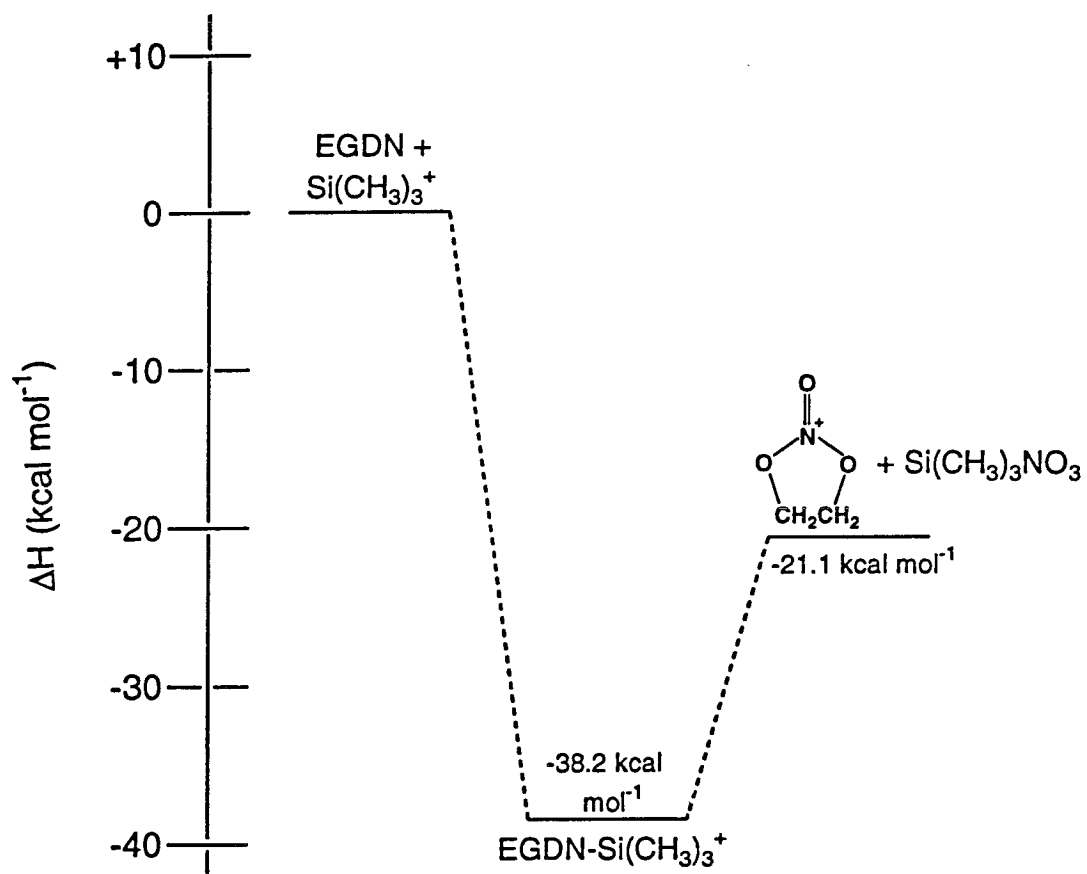
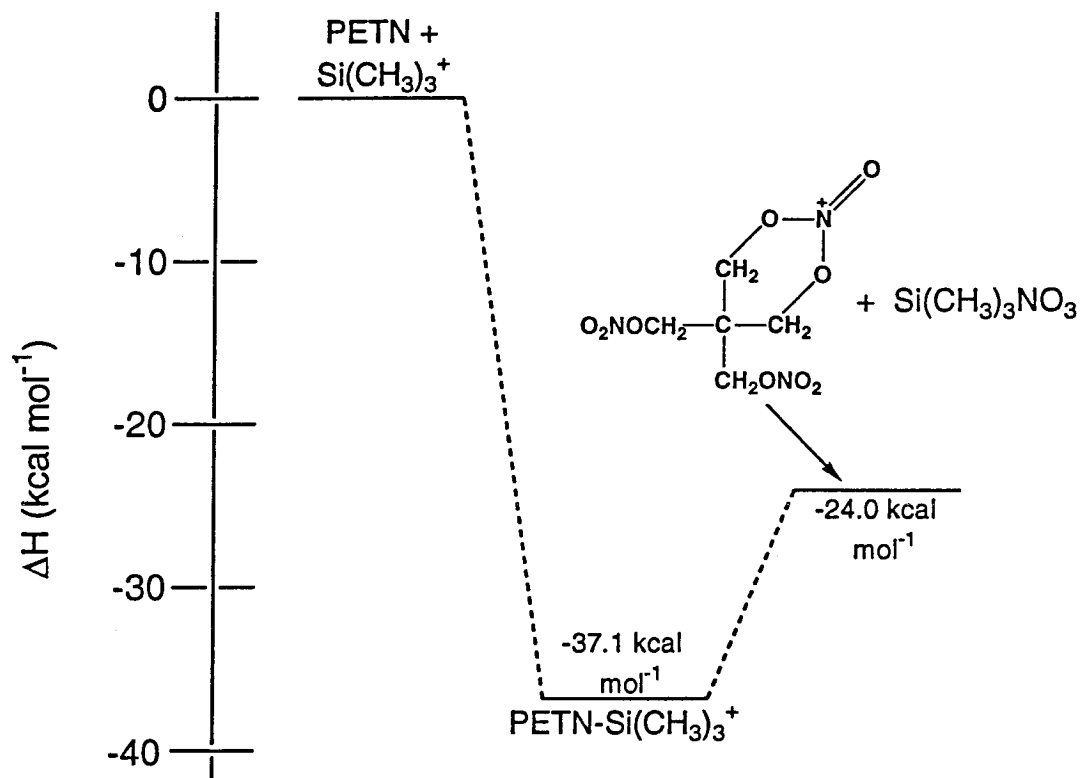


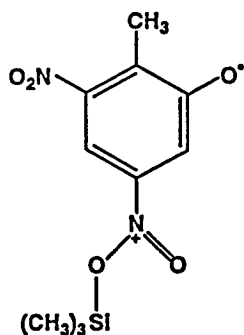
Figure 10. Reaction coordinate diagram for the reaction of PETN with $\text{Si}(\text{CH}_3)_3^+$ to form the major product ion. We estimate the uncertainty in the derived enthalpy values to be $\pm 10 \text{ kcal mol}^{-1}$.



$\text{Si}(\text{CH}_3)_3^+$ and $\text{PETN-Si}(\text{CH}_3)_3^+$ adducts. The higher pressure in the sector mass spectrometer is apparently able to provide the number of collisions needed to dissipate 20 kcal mol⁻¹ of energy and stabilize the $\text{EGDN-Si}(\text{CH}_3)_3^+$ and $\text{PETN-Si}(\text{CH}_3)_3^+$ adducts. Furthermore, the number of collisions is apparently enough to stabilize the $\text{C}_5\text{H}_8\text{N}_3\text{O}_9^+$ ion and suppress further fragmentations.

Comparison of the Reactivity of Nitrate Ester and Nitro Explosives Toward $\text{Si}(\text{CH}_3)_3^+$. We have found that both nitro¹ and nitrate ester explosives will react efficiently with $\text{Si}(\text{CH}_3)_3^+$ to form characteristic product ions. However, two significant differences are also observed: 1) with nitrate esters, no parent adduct was observed in the low pressure FT-ICR experiments, while significant amounts of parent adduct were seen with nitro explosives and 2) the fragmentation seen with the nitrate ester explosives is more complex than the fragmentation observed with the nitro explosives. EGDN in particular exhibits significant amounts of odd-electron fragments (accompanied by NO_2 loss). In contrast to this behavior, RDX only produced even-electron fragments from its reaction with $\text{Si}(\text{CH}_3)_3^+$. No NO_2 loss was observed.¹

TNT is an interesting case with respect to the second difference. Like nitrate esters, it forms an odd-electron fragment from an even-electron parent adduct. However, TNT loses NO rather than NO_2 , as shown in structure V (an example of one of the



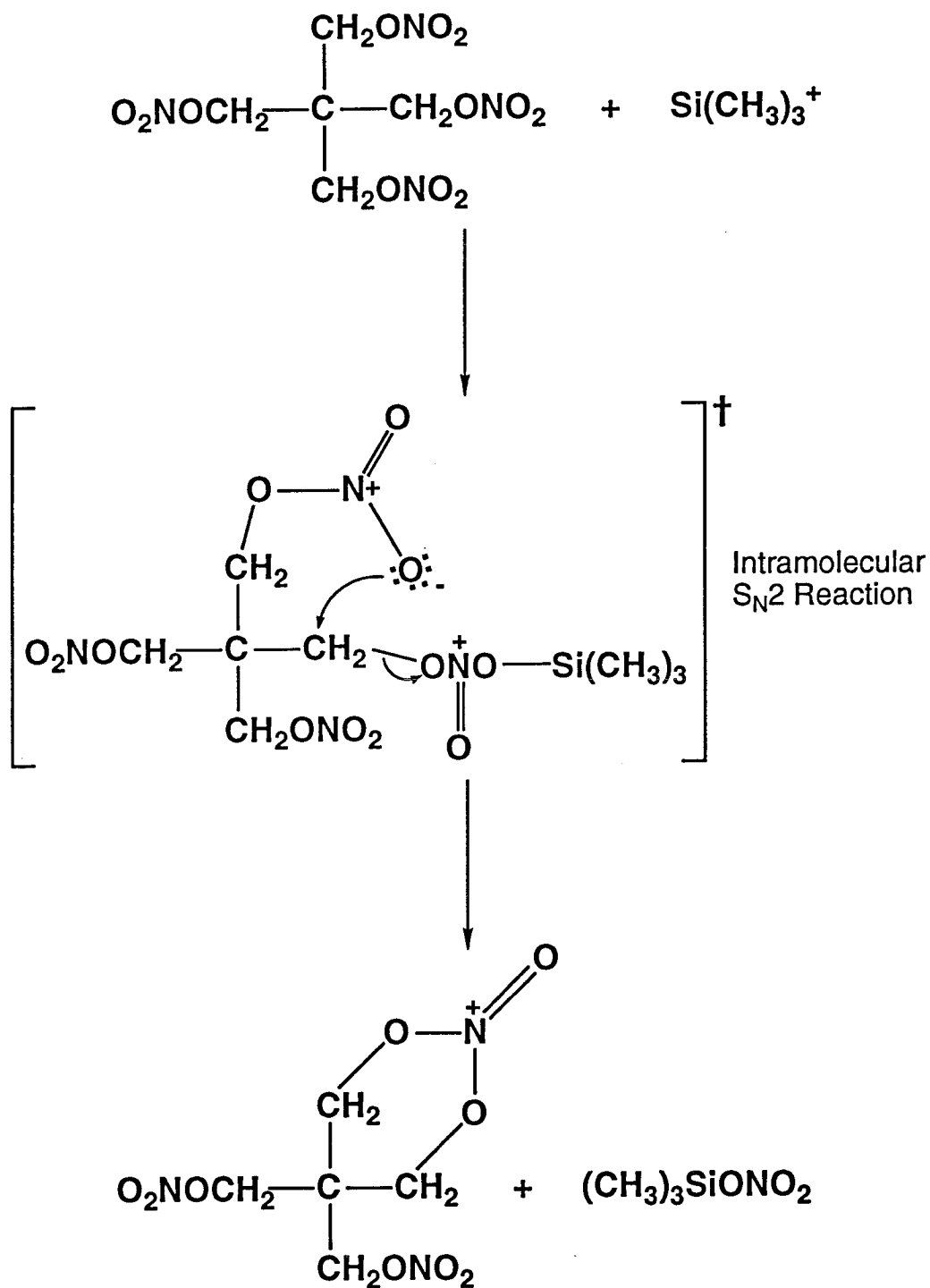
V

possible isomers for this species). But unlike the nitrate esters, no additional fragmentation is seen with TNT.¹ Both steric and thermodynamic factors could

contribute to these observed differences in reactivity, and we will consider these effects in detail.

First we will consider steric effects. Because of their ring shaped geometries, RDX and TNT are comparatively rigid molecules, while nitrate esters are not constrained in such a fashion and are "floppier." This will allow PETN and EGDN to access more conformational states and it might be expected that this would leave the nitrate esters more susceptible to fragmentation. This factor almost certainly plays a role in the formation of the cyclic organic cations $C_2H_4NO_3^+$ and $C_5H_8N_3O_9^+$ from EGDN and PETN, respectively. Scheme I shows the specific mechanism for the formation of the $C_5H_8N_3O_9^+$ ion from PETN and $Si(CH_3)_3^+$; however, this mechanism can be generalized to any nitrate ester containing at least two $-ONO_2$ groups (such as EGDN). The flexible nature of both EGDN and PETN allow a "free" $-ONO_2$ group to intramolecularly attack the carbon containing the $-ONO_2Si(CH_3)_3^+$ group and displace the $-ONO_2Si(CH_3)_3^+$ group by an intramolecular S_N2 reaction. Apparently most of the adduct formed between EGDN or PETN and $Si(CH_3)_3^+$ fragments in this way, and the parent adducts are consequently not seen in our FT-ICR mass spectra. In contrast, the comparatively rigid TNT and RDX molecules cannot fragment in such a way, and their parent adducts are observed in the FT-ICR mass spectrometer.¹

Thermodynamic effects are another important contributing factor in the easy formation of the $C_2H_4NO_3^+$ and $C_5H_8N_3O_9^+$ ions. Since the nitrate group to be lost has been chemically ionized by $Si(CH_3)_3^+$, no explicit separation of charge is required to form $C_2H_4NO_3^+$ or $C_5H_8N_3O_9^+$. Furthermore, as the C-O bond to the $-ONO_2Si(CH_3)_3^+$ group is breaking, another C-O bond with a "free" $-ONO_2$ group is simultaneously forming. Although the bond being formed is not identical to the bond being broken, they are similar and thus ΔH for this process should be small compared to the bond energy between EGDN or PETN and $Si(CH_3)_3^+$. This behavior is seen in our reaction coordinate diagrams of Figures 9 and 10, where bond formation between $Si(CH_3)_3^+$ and



Scheme I

EGDN or PETN liberates about 40 kcal mol⁻¹, while losing (CH₃)₃SiONO₂ only requires about 15 kcal mol⁻¹. On the other hand, with RDX fragmentation of the parent adduct requires almost all of the energy liberated by bond formation with Si(CH₃)₃⁺. In this case, even a single collision will dissipate enough energy to stabilize the parent adduct. Thus, even at the comparatively low pressures used in the FT-ICR mass spectrometer, enough collisions occur to stabilize the RDX-Si(CH₃)₃⁺ adduct.

Thermodynamic effects also play a second role in the differences between nitro and nitrate ester explosives. For aromatic nitro compounds the average R-NO₂ bond energy is 69±2 kcal mol⁻¹,¹⁸ while in RDX the N-NO₂ bond energy is estimated to be 47.8 kcal mol⁻¹.¹⁹ But the average Si⁺-O single bond energy in adducts of Si(CH₃)₃⁺ with oxygen-containing molecules is about 40 kcal mol⁻¹.^{1,20,21} For both TNT and RDX it takes more energy to generate NO₂ than is gained by adduct formation with Si(CH₃)₃⁺. Thus no loss of NO₂ is seen with TNT or RDX.¹ In contrast, the average RO-NO₂ bond energy in nitrate esters is 40.7±2 kcal mol⁻¹.¹⁸ This is about the same as the average Si⁺-O single bond energy in adducts of Si(CH₃)₃⁺ with oxygen-containing molecules. Thus for EGDN and PETN the loss of NO₂ should be approximately thermoneutral. If the EGDN or PETN molecule has any excess vibrational or rotational energy, then loss of NO₂ should be slightly exothermic. This loss of NO₂ is not as energetically favorable as the loss of Si(CH₃)₃ONO₂ and formation of the C₂H₄NO₃⁺ or C₅H₈N₃O₉⁺ ion, but it can occur and accounts for most of the other minor odd-electron fragments observed.

Although TNT can't lose NO₂, it does lose NO to form an odd-electron fragment, of which one possible isomer is shown in structure V.¹ The resulting cation is resonance stabilized by delocalization of the radical electron through the aromatic π system. The ability to form a resonance stabilized cation explains why TNT is able to lose NO so easily, and also explains why no further fragmentation is observed. Apparently it is the presence of the aromatic ring that allows TNT to behave in a fashion intermediate

between the reactivity of the nitro explosive RDX and the nitrate ester explosives EGDN and PETN.

These differences in the reactivity of nitro and nitrate ester explosives towards $\text{Si}(\text{CH}_3)_3^+$ do have an impact on the usefulness of $\text{Si}(\text{CH}_3)_3^+$ as a selective chemical ionization reagent for explosives. Although both EGDN and PETN form characteristic ions upon reaction with $\text{Si}(\text{CH}_3)_3^+$, no parent adduct is generated within the FT-ICR mass spectrometer. We were able to generate the EGDN- $\text{Si}(\text{CH}_3)_3^+$ and PETN- $\text{Si}(\text{CH}_3)_3^+$ parent adducts in a magnetic sector mass spectrometer. Thus the $\text{Si}(\text{CH}_3)_3^+$ ion may still be a useful reagent for the detection and identification of nitrate ester explosives in certain mass spectrometers. However, it would be convenient to find a reagent that would be ideal for both nitro and nitrate ester explosives under a wider variety of conditions. Therefore we are currently testing reagents related to the $\text{Si}(\text{CH}_3)_3^+$ ion in the hope of finding a reagent that will produce more stable adducts with nitrate ester explosives.

Conclusions

We have used FT-ICR mass spectrometry to investigate the reactivity of trimethylsilyl cations with the nitrate ester explosives EGDN and PETN. Both EGDN and PETN react quickly and efficiently with $\text{Si}(\text{CH}_3)_3^+$. No parent adduct was observed to form, but characteristic fragment ions were seen. The major product in each case is a cyclic ion formed by an intramolecular $\text{S}_{\text{N}}2$ reaction which ejects of $(\text{CH}_3)_3\text{SiONO}_2$. We also investigated the reactions of EGDN and PETN with $\text{Si}(\text{CH}_3)_3^+$ in a magnetic sector mass spectrometer, and there we were able to observe the formation of the EGDN- $\text{Si}(\text{CH}_3)_3^+$ and PETN- $\text{Si}(\text{CH}_3)_3^+$ adducts. CID experiments on selected fragment ions allowed us to elucidate the various fragmentation processes seen in the reactions of $\text{Si}(\text{CH}_3)_3^+$ with EGDN and PETN. The differences between the reactivity of the nitro and nitrate ester explosives toward $\text{Si}(\text{CH}_3)_3^+$ are well explained by steric

and thermodynamic effects. Under the proper conditions, $\text{Si}(\text{CH}_3)_3^+$ could still be a useful reagent for the analytical detection and identification of nitrate ester explosives.

Acknowledgments

We wish to acknowledge the Federal Aviation Administration for support of this work under grant 93-G-060, and the Beckman Foundation and Institute for continuing support of the FT-ICR research facility. We also wish to acknowledge Professor William A. Goddard, III, and the Beckman Institute Materials and Process Simulations Center for supporting some of our theoretical calculations.

References

- ¹Crellin, K. C.; Widmer, M.; Beauchamp, J. L. *Anal. Chem.* **1997**, *69*, 1092.
- ²Fainberg, A. *Science* **1992**, *255*, 1531.
- ³(a) Marshall, A. G. *Acc. Chem. Res.* **1985**, *18*, 316. (b) Comisarow, M. B. *Anal. Chim. Acta* **1985**, *178*, 1.
- ⁴Huang, C.-C.; Wu, T.-S. *Thermochim. Acta* **1992**, *204*, 239.
- ⁵Huang, C.-C.; Ger, M.-D.; Lin, Y.-C.; Chen, S.-I. *Thermochim. Acta* **1992**, *208*, 147.
- ⁶Oxley, J. C., personal communication.
- ⁷Comisarow, M. B.; Marshall, A. G. *Chem. Phys. Lett.* **1974**, *26*, 489.
- ⁸(a) Gauthier, J. W.; Trautman, T. R.; Jacobsen, D. B. *Anal. Chim. Acta* **1991**, *246*, 211. (b) Marzluff, E. M.; Campbell, S.; Rodgers, M. T.; Beauchamp, J. L. *J. Am. Chem. Soc.* **1994**, *116*, 7787.
- ⁹Collision rates are calculated using Langevin theory: Su, T.; Bowers, M. T. *Gas Phase Ion Chemistry*, Vol. 1, M. T. Bowers, Ed., 1979, Academic Press, New York.
- ¹⁰The dipole moment and polarizability of EGDN were calculated at the Hartree-Fock level with a 6-31** basis set to be 0 D and 7.98 Å³, respectively. The geometry optimization, dipole moment and polarizability calculations were performed with PS-GVB (see reference 11).
- ¹¹Ringnalda, M. N.; Langlois, J.-M.; Greeley, B. H.; Murphy, R. B.; Russo, T. V.; Cortis, C.; Muller, R. P.; Marten, B.; Donnelly, R. E., Jr.; Mainz, D. T.; Wright, J. R.; Pollard, W. T.; Cao, Y.; Won, Y.; Miller, G. H.; Goddard, W. A. III; Freisner, R. A. *PS-GVB, v2.1*, Schrödinger, Inc., 1995.
- ¹²The dipole moment and polarizability of PETN were calculated at the Hartree-Fock level with a 6-31** basis set to be 0 D and 16.26 Å³, respectively. The geometry optimization, dipole moment and polarizability calculations were performed with PS-GVB (see reference 11).
- ¹³(a) Stewart, J. J. P. *Method J. Comput. Chem.* **1989**, *10*, 209. (b) Stewart, J. J. P. *Method J. Comput. Chem.* **1989**, *10*, 221.
- ¹⁴*HyperChem™ Computational Chemistry Software Package, Version 4.0*, Hypercube Inc., 1994.
- ¹⁵Hiskey, M. A.; Brower, K. R.; Oxley, J. C. *J. Phys. Chem.* **1991**, *95*, 3955.
- ¹⁶The structural parameters for these species are presented in the appendix at the end of this chapter.

¹⁷Cox, J. D.; Pilcher, G. *Thermochemistry of Organic and Organometallic Compounds*, 1970, Academic Press, New York.

¹⁸Batt, L.; Robinson, G. N. *The Chemistry of Amino, Nitroso and Nitro Compounds and Their Derivatives*, Part 2, S. Patai, Ed., 1982, John Wiley & Sons, Chichester, England.

¹⁹Melius, C. F.; Binkley, J. S. *Symp. (Int.) Combust., [Proc.]* **1986**, 21, 1953.

²⁰Clemens, D.; Munson, B. *Anal. Chem.* **1985**, 57, 2022.

²¹Hendewerk, M. L.; Weil, D. A.; Stone, T. L.; Ellenberger, M. R.; Farneth, W. E.; Dixon, D. A. *J. Am. Chem. Soc.* **1982**, 104, 1794.

Appendix

The structural parameters obtained from the geometry optimizations of the lowest energy conformations of $\text{Si}(\text{CH}_3)_3^+$, EGDN, EGDN- $\text{Si}(\text{CH}_3)_3^+$, $\text{Si}(\text{CH}_3)_3\text{ONO}_2$, $\text{C}_2\text{H}_4\text{NO}_3^+$, PETN, PETN- $\text{Si}(\text{CH}_3)_3^+$ and $\text{C}_5\text{H}_8\text{N}_3\text{O}_9^+$ are given in the following Tables 1A-8A, respectively.

Table 1A. PM3-Optimized Bond Distances (Å) and Angles (deg) for the Lowest Energy Conformation of Si(CH₃)₃⁺.

Bond Length	
Si1-C2	1.8001
Si1-C3	1.8002
Si1-C4	1.8003
C2-H5	1.1060
C2-H6	1.0989
C2-H7	1.0995
C3-H8	1.1057
C3-H9	1.0997
C3-H10	1.0989
C4-H11	1.1060
C4-H12	1.0989
C4-H13	1.0994
Bond Angle	
C2-Si1-C3	120.02
C2-Si1-C4	119.99
C3-Si1-C4	119.96
Si1-C2-H5	110.11
Si1-C2-H6	113.61
Si1-C2-H7	113.41
H5-C2-H6	106.05
H5-C2-H7	105.91
H6-C2-H7	107.21

Table 1A. (Continued)

Bond Angle

H6-C2-H7	107.21
Si1-C3-H8	110.15
Si1-C3-H9	113.37
Si1-C3-H10	113.62
H8-C3-H9	105.90
H8-C3-H10	106.08
H9-C3-H10	107.19
Si1-C4-H11	110.21
Si1-C4-H12	113.58
Si1-C4-H13	113.37
H11-C4-H12	106.03
H11-C4-H13	105.90
H12-C4-H13	107.21

Table 2A. PM3-Optimized Bond Distances (Å) and Angles (deg) for the Lowest Energy Conformation of EGDN.

Bond Length	
C1-C2	1.5403
C1-O3	1.4168
C1-H4	1.1066
C1-H5	1.1066
C2-O6	1.4168
C2-H8	1.1069
C2-H9	1.1069
O3-N7	1.5265
O6-N10	1.5265
N7-O11	1.1848
N7-O12	1.1925
N10-O13	1.1848
N10-O14	1.1925
Bond Angle	
C2-C1-O3	104.96
C2-C1-H4	111.48
C2-C1-H5	111.48
O3-C1-H4	110.49
O3-C1-H5	110.49
H4-C1-H5	107.95
C1-C2-O6	104.96
C1-C2-H8	111.53

Table 2A. (Continued)

Bond Angle

C1-C2-H9	111.53
O6-C2-H8	110.47
O6-C2-H9	110.47
H8-C2-H9	107.91
C1-O3-N7	117.38
C2-O6-N10	117.34
O3-N7-O11	107.76
O3-N7-O12	117.86
O6-N10-O13	107.72
O6-N10-O14	117.90
O11-N7-O12	134.38
O13-N10-O14	134.38

Table 3A. PM3-Optimized Bond Distances (Å) and Angles (deg) for the Lowest Energy Conformation of EGDN-Si(CH₃)₃⁺.

Bond Length		Bond Length	
C1-C2	1.5417	O14-Si15	1.7861
C1-O3	1.3975	Si15-C16	1.8592
C1-H4	1.1079	Si15-C17	1.8579
C1-H5	1.1079	Si15-C18	1.8579
C2-O7	1.4643	C16-H19	1.0992
C2-H8	1.1064	C16-H20	1.0959
C2-H9	1.1064	C16-H21	1.0951
O3-N6	1.6384	C17-H22	1.1004
N6-O10	1.1713	C17-H23	1.0948
N6-O11	1.1804	C17-H24	1.0959
O7-N12	1.3543	C18-H25	1.1003
N12-O13	1.1806	C18-H26	1.0959
N12-O14	1.2732	C18-H27	1.0948
Bond Angle		Bond Angle	
C2-C1-O3	104.38	O14-Si15-C18	106.93
C2-C1-H4	111.35	C16-Si15-C17	114.64
C2-C1-H5	111.35	C16-Si15-C18	114.64
O3-C1-H4	110.92	C17-Si15-C18	114.21
O3-C1-H5	110.92	Si15-C16-H19	109.12
H4-C1-H5	107.95	Si15-C16-H20	112.70
C1-C2-O7	103.54	Si15-C16-H21	112.72
C1-C2-H8	112.37	H19-C16-H20	107.16

Table 3A. (Continued)

Bond Angle		Bond Angle	
C1-C2-H9	112.37	H19-C16-H21	107.17
O7-C2-H8	109.59	H20-C16-H21	107.69
O7-C2-H9	109.59	Si15-C17-H22	109.02
H8-C2-H9	109.23	Si15-C17-H23	112.99
C1-O3-N6	118.11	Si15-C17-H24	113.26
O3-N6-O10	104.67	H22-C17-H23	106.68
O3-N6-O11	114.78	H22-C17-H24	106.66
O10-N6-O11	140.55	H23-C17-H24	107.85
C2-O7-N12	120.06	Si15-C18-H25	109.02
O7-N12-O13	116.26	Si15-C18-H26	113.26
O7-N12-O14	117.56	Si15-C18-H27	112.99
O13-N12-O14	126.18	H25-C18-H26	106.66
N12-O14-Si15	132.01	H25-C18-H27	106.72
O14-Si15-C16	97.44	H26-C18-H27	107.85
O14-Si15-C17	106.93		

Table 4A. PM3-Optimized Bond Distances (Å) and Angles (deg) for the Lowest Energy Conformation of Si(CH₃)₃ONO₂.

Bond Length

O1-N2	1.3453
O1-Si3	1.7317
N2-O4	1.2010
N2-O5	1.2103
Si3-C6	1.8874
Si3-C7	1.8836
Si3-C8	1.8836
C6-H9	1.0947
C6-H10	1.0940
C6-H11	1.0932
C7-H12	1.0955
C7-H13	1.0942
C7-H14	1.0940
C8-H15	1.0950
C8-H16	1.0940
C8-H17	1.0942

Table 4A. (Continued)

Bond Angle		Bond Angle	
<hr/>		<hr/>	
N2-O1-Si3	125.08	Si3-C7-H13	111.55
O1-N2-O4	114.11	Si3-C7-H14	111.75
O1-N2-O5	116.35	Si3-C8-H15	110.23
O4-N2-O5	129.54	Si3-C8-H16	111.75
O1-Si3-C6	100.29	Si3-C8-H17	111.55
O1-Si3-C7	111.28	H9-C6-H10	107.93
O1-Si3-C8	111.28	H9-C6-H11	107.94
O4-N2-O5	129.54	H10-C6-H11	107.78
C6-Si3-C7	110.94	H12-C7-H13	107.59
C6-Si3-C8	110.94	H12-C7-H14	107.67
C7-Si3-C8	111.61	H13-C7-H14	107.89
Si3-C6-H9	110.40	H15-C8-H16	107.62
Si3-C6-H10	111.32	H15-C8-H17	107.61
Si3-C6-H11	111.34	H16-C8-H17	107.89
Si3-C7-H12	110.21		

Table 5A. PM3-Optimized Bond Distances (Å) and Angles (deg) for the Lowest Energy Conformation of C₂H₄NO₃⁺.

Bond Length	
N1-O2	1.1602
N1-O3	1.3768
N1-O4	1.3757
O3-C5	1.4497
O4-C6	1.4496
C5-C6	1.5378
C5-H7	1.1055
C5-H8	1.1062
C6-H9	1.1063
C6-H10	1.1056
Bond Angle	
O2-N1-O3	124.15
O2-N1-O4	124.25
O3-N1-O4	111.60
N1-O3-C5	109.41
N1-O4-C6	109.46
O3-C5-C6	104.78
O3-C5-H7	106.10
O3-C5-H8	106.07
C6-C5-H7	115.09
C6-C5-H8	115.05
H7-C5-H8	108.89

Table 5A. (Continued)

Bond Angle

O4-C6-C5	104.75
O4-C6-H9	106.09
O4-C6-H10	106.08
C5-C6-H9	115.07
C5-C6-H10	115.06
H9-C6-H10	108.92

Table 6A. PM3-Optimized Bond Distances (Å) and Angles (deg) for the Lowest Energy Conformation of PETN.

Bond Length		Bond Length	
C1-C2	1.5669	N7-O10	1.1842
C1-C3	1.5526	N7-O11	1.1956
C1-C12	1.5422	C12-O14	1.4126
C1-C13	1.5462	C12-H26	1.1093
C2-O4	1.4096	C12-H27	1.1091
C2-H22	1.1082	C13-O15	1.4126
C2-H23	1.1079	C13-H28	1.1091
C3-O5	1.4103	C13-H29	1.1093
C3-H24	1.1100	O14-N16	1.5204
C3-H25	1.1092	O15-N17	1.5204
O4-N6	1.5643	N16-O18	1.1851
O5-N7	1.5268	N16-O20	1.1955
N6-O8	1.1805	N17-O19	1.1850
N6-O9	1.1900	N17-O21	1.1955
Bond Angle		Bond Angle	
C2-C1-C3	103.34	O5-N7-O10	108.68
C2-C1-C12	106.83	O5-N7-O11	117.62
C2-C1-C13	106.83	O10-N7-O11	133.70
C3-C1-C12	112.87	C1-C12-O14	110.28
C3-C1-C13	112.87	C1-C12-H26	109.45
C12-C1-C13	113.23	C1-C12-H27	109.84
C1-C2-O4	109.14	O14-C12-H26	109.57

Table 6A. (Continued)

Bond Angle		Bond Angle	
C1-C2-H22	112.37	O14-C12-H26	109.53
C1-C2-H23	110.15	H26-C12-H27	108.14
O4-C2-H22	109.74	C1-C13-O15	110.28
O4-C2-H23	109.76	C1-C13-H28	109.89
H22-C2-H23	107.93	C1-C13-H29	109.45
C1-C3-O5	110.67	O15-C13-H28	109.52
C1-C3-H24	109.46	O15-C13-H29	109.57
C1-C3-H25	109.48	H28-C13-H29	108.10
O5-C3-H24	109.60	C12-O14-N16	116.72
O5-C3-H25	109.62	C13-O15-N17	116.72
H24-C3-H25	109.62	O14-N16-O18	108.62
C2-O4-N6	117.13	O14-N16-O20	117.80
C3-O5-N7	116.64	O18-N16-O20	133.58
O4-N6-O8	107.06	O15-N17-O19	108.69
O4-N6-N9	117.06	O15-N17-O21	117.80
O8-N6-O9	135.88	O19-N17-O21	133.51

Table 7A. PM3-Optimized Bond Distances (Å) and Angles (deg) for the Lowest Energy Conformation of PETN-Si(CH₃)₃⁺.

Bond Length		Bond Length	
C1-C2	1.5505	C13-H28	1.1067
C1-C3	1.5626	C13-H29	1.1101
C1-C12	1.5526	O14-N16	1.6282
C1-C13	1.5509	O15-N17	1.6542
C2-O4	1.4488	N16-O18	1.1741
C2-H22	1.1096	N16-O20	1.1865
C2-H23	1.1090	N17-O19	1.1716
C3-O5	1.3822	N17-O21	1.1793
C3-H24	1.1084	Si30-C31	1.8583
C3-H25	1.1094	Si30-C32	1.8580
O4-N6	1.3710	Si30-C36	1.8575
O5-N7	1.6459	C31-H33	1.0996
N6-O8	1.2611	C31-H34	1.0947
N6-O9	1.1852	C31-H35	1.0960
N7-O10	1.1730	C32-H40	1.0999
N7-O11	1.1818	C32-H41	1.0958
O8-Si30	1.7861	C32-H42	1.0951
C12-O14	1.3857	C36-H37	1.0990
C12-H26	1.1082	C36-H38	1.0955
C12-H27	1.1082	C36-H39	1.0954
C13-O15	1.3819		

Table 7A. (Continued)

Bond Angle		Bond Angle	
C2-C1-C3	103.34	O15-C13-H28	102.15
C2-C1-C12	106.83	O15-C13-H29	112.07
C2-C1-C13	108.28	H28-C13-H29	107.83
C3-C1-C12	111.56	C12-O14-N16	119.37
C3-C1-C13	111.57	C13-O15-N17	120.12
C12-C1-C13	113.79	O14-N16-O18	105.71
C1-C2-O4	115.11	O14-N16-O20	115.67
C1-C2-H22	111.51	O18-N16-O20	138.51
C1-C2-H23	111.94	O15-N17-O19	104.15
O4-C2-H22	96.12	O15-N17-O21	115.15
O4-C2-H23	111.86	O19-N17-O21	140.54
H22-C2-H23	109.20	O8-Si30-C31	105.47
C1-C3-O5	114.66	O8-Si30-C32	107.72
C1-C3-H24	109.49	O8-Si30-C36	97.83
C1-C3-H25	109.60	C31-Si30-C32	114.20
O5-C3-H24	102.63	C31-Si30-C36	114.90
O5-C3-H25	112.08	C32-Si30-C36	114.62
H24-C3-H25	107.97	Si30-C31-H33	109.07
C2-O4-N6	121.49	Si30-C31-H34	113.23
C3-O5-N7	120.02	Si30-C31-H35	112.89
O4-N6-O8	107.47	H33-C31-H34	106.79
O4-N6-O9	125.42	H33-C31-H35	106.61
O8-N6-O9	127.07	H34-C31-H35	107.88
O5-N7-O10	104.43	Si30-C32-H40	108.97

Table 7A. (Continued)

Bond Angle		Bond Angle	
O5-N7-O11	115.56	Si30-C32-H41	112.97
O10-N7-O11	139.92	Si30-C32-H42	113.26
N6-O8-Si30	133.43	H40-C32-H41	106.65
C1-C12-O14	115.17	H40-C32-H42	106.73
C1-C12-H26	109.44	H41-C32-H42	107.87
C1-C12-H27	110.19	Si30-C36-H37	109.31
O14-C12-H26	102.34	Si30-C36-H38	112.63
O14-C12-H27	111.37	Si30-C36-H39	112.63
H26-C12-H27	107.83	H37-C36-H38	107.14
C1-C13-O15	115.29	H37-C36-H39	107.20
C1-C13-H28	109.57	H38-C36-H39	107.65
C1-C13-H29	109.47		

Table 8A. PM3-Optimized Bond Distances (Å) and Angles (deg) for the Lowest Energy Conformation of C₅H₈N₃O₉⁺.

Bond Length		Bond Length	
C1-C2	1.5310	C5-H13	1.1062
C1-C4	1.5542	O6-N7	1.6708
C1-C5	1.5626	N7-O8	1.1684
C1-C20	1.5332	N7-O9	1.1776
C2-O3	1.4488	O14-N15	1.6664
C2-H10	1.1082	N15-O16	1.1685
C2-H11	1.1085	N15-O17	1.1761
O3-N24	1.3581	C20-H21	1.1081
C4-O14	1.3922	C20-H22	1.1067
C4-H18	1.1083	C20-O23	1.4491
C4-H19	1.1079	O23-N24	1.3651
C5-O6	1.3799	N24-O25	1.1673
C5-H12	1.1104		
Bond Angle		Bond Angle	
C2-C1-C4	109.09	O6-C5-H12	113.54
C2-C1-C5	113.01	O6-C5-H13	105.39
C2-C1-C20	107.92	H12-C5-H13	107.09
C4-C1-C5	108.35	C5-O6-N7	120.92
C4-C1-C20	109.08	O6-N7-O8	103.42
C5-C1-C20	109.34	O6-N7-O9	114.26
C1-C2-O3	114.09	O8-N7-O9	142.32
C1-C2-H10	114.45	C4-O14-N15	138.51

Table 8A. (Continued)

Bond Angle		Bond Angle	
C1-C2-H11	113.37	O14-N15-O16	103.03
O3-C2-H10	98.88	O14-N15-O17	114.10
O3-C2-H11	105.74	O16-N15-O17	142.87
H10-C2-H11	109.07	C1-C20-H21	113.71
C2-O3-N24	118.95	C1-C20-H22	113.93
C1-C4-O14	109.12	C1-C20-O23	113.64
C1-C4-H18	109.35	H21-C20-H22	109.08
C1-C4-H19	109.15	H21-C20-O23	106.21
O14-C4-H18	109.95	H22-C20-O23	99.07
O14-C4-H19	110.98	C20-O23-N24	118.88
H18-C4-H19	108.28	O3-N24-O23	123.96
C1-C5-O6	111.43	O3-N24-O25	118.30
C1-C5-H12	109.13	O23-N24-O25	117.59
C1-C5-H13	110.09		